Communauté
UNIVERSITÉ Grenoble Alpes

THÈSE

Pour obtenir le grade de

DOCTEUR DE LA COMMUNAUTÉ UNIVERSITÉ GRENOBLE ALPES

Spécialité: **Physique des matériaux**
Arrêté ministériel : 25 mai 2016

Présentée par

Lidia MAZZUCA

Thèse dirigée par **Dr. Juan RODRÍGUEZ-CARVAJAL**
codirigée par **Dr. Óscar FABELO**

préparée au sein **du laboratoire Institut Laue-Langevin**
et de **l'École doctorale de Physique de Grenoble**

Préparation, détermination de la structure et des propriétés physiques de composés moléculaires basées sur le formiate

Preparation, structure determination and physical properties of formate-based molecular compounds

Thèse soutenue publiquement le **26 Janvier 2018,**
devant le jury composé de:

Dr. Virginie SIMONET
Institut Néel, CNRS & Université Grenoble Alpes, Président

Dr. Gwenaëlle ROUSSE
Collège de France & Université Pierre et Marie Curie, Rapporteur

Dr. Jorge PASÁN GARCÍA
Universidad de La Laguna, Rapporteur

Dr. María Teresa FERNÁNDEZ-DÍAZ
Institut Laue-Langevin, Examinateur

Dr. Javier CAMPO
ICMA & Universidad de Zaragoza, Spain, Examinateur

Dedication

I dedicate this thesis to
David, to my family, and to
the memory of my
grandfather Ciccio.

Acknowledgement

My PhD journey ends after three amazing years of deep and hard formative experiences accompanied by a very good group of people forming a pleasant scientific environment at the Institute Laue Langevin (ILL). In this regard, I want to thank the ILL for the financial support and for providing me with an excellent PhD program as well as the high-level experimental resources.

I express my greatest gratitude to my supervisors Óscar Fabelo and Juan Rodríguez-Carvajal, for the opportunity conceded the patient and gentle supervision through the twisted path of the scientific research. Always with a positive attitude in the most difficult moments making me feel at ease and integral part of this group. In particular thanks for carefully correcting this manuscript.

My profound thanks go to Alberto Rodríguez Velamazán and Laura Cañadillas-Delgado which their support and scientific suggestions made possible to easier overcoming any issue. Moreover, I thank the diffraction group for the friendly environment and for the scientific work.

I would like to express my sincere gratefulness to my thesis committee: Dr. Gwenaelle Rousse, Dr. Jorge Pasán García, Dr. María Teresa Fernández-Díaz, Dr. Virginie Simonet and Dr. Javier Campo.

Along the way of my PhD I met a lot of people and friends sharing with me happy and crazy moments as well as stimulating and deep thoughts. I would like to thank Inés Puente Orench, for being always frankly and friendly with me, supportive, and often providing me the affection and the comprehension needed, but also speaking with me about the importance of being woman, and being woman in science.

I want to thank all my PhD colleagues that made possible to live this experience also under an amusing profile. I start from my beloved officemates Annalisa for welcoming me since the first day here in Grenoble and for all the deep dialogues about life, science, and religion. Thanks to: Frederic, for the crazy moments shared in the office, to Javier for being my

“best-friend” whom, a part to share with me huge quantity of “caffé napoletano originale”, he supported me in many moments, often creating together hilarious sketch that marked forever our memories (for example the unforgettable moments learning to ski “gallinando”). I would like to deeply thank Emilie, for being the best officemate ever, for saving me in any situation, and especially for becoming my beloved friend. I say thank you for the strong support to Analía, the last student arrived in the diffraction group, which in few months become a sincere and close friend. Thanks to the last Post-doc leaving, Margarida, because she has been a colleague but then the sister I never had.

So although they won't probably read this, I like to mention all of them: Rafal, Marco, Adrián, Philipp, Simon A., Hugo, Marco P., Andrea, Robin, Veronica, Stash, Jerome, Joseph, Kristjan, Umberto Luca, Eron, Ketty, Tetiana (piccolina), Jennifer, Lindsay, Dominik, Lucia, John, Giovanna, Soufiane, Sandrine, Alejandro, Jaime…..I would like to give a special thank you to Brigitte, Serge, and many other people that make ILL a nice place where to work, because of their professionalism.

Of course, I would like to apologize to all of those whom I forgot above or could not mention personally here.

I would like to thank my parents and my brother, so far away from me, but always present and careful not to miss their affection and support. Without you, nothing would make sense!

And, in conclusion an infinite thank you to David, the person that changed and improved my life, for his immense support, for becoming my family for the endless love and the many encouragements to go on, the suggestions (that I have always appreciated but I never applied). Thanks for believing in me, this over everything made possible to conclude this chapter of my life, sure that we will share the forthcoming one together. And last, but not least thanks for your precious professional support as lab responsible, without chemistry nothing would have happened!

Abstract in English

The synthesis and the characterization of new functional materials are key challenges in chemistry and physics. In particular, *metal–organic frameworks* (*MOFs*) with two or more coupled functionalities are still rare and very attractive candidates because of their wide variety of properties and promising applications interesting in many disciplines. The impact of the development of new fascinating materials on our day life might be considerable. This is also one of the reason explaining the intense increase of research in material science and condensed matter physics and chemistry.
This thesis is focused on the synthesis and the physical characterization of magnetic metal formate frameworks using the combination of neutron and synchrotron X-Ray diffraction as well as other techniques. Metal-formate compounds belong to a specific subgroup of *metal-organic frameworks* where the metal centres are linked by the formate molecules to form an anionic framework. The negative charge of the framework is balanced by a counter-cation which is located in the cavities of the framework. In this thesis, the counter-cation molecules are constituted by protonated amines. Typically, these compounds are synthesized by reacting formate or formic acid with a metal salt under solvo-thermal conditions or by slow evaporation or diffusion techniques.

In this work, I have investigated the crystal structure, phase transitions and magnetic properties of two families of metal formate frameworks. The first family is represented by hetero-metallic or mixed-valence compounds adopting a niccolite-like structure, and the second family is constituted by homo-metallic compounds adopting a perovskite-like (ABX_3) structure.The compounds synthesized and characterized in this thesis are: $[(CH_3)_2NH_2][Fe^{III}M^{II}(HCOO)_6]$ (M^{II} = Mg^{II}, Mn^{II}, Fe^{II}, Co^{II} and Ni^{II}), $[(CH_3CH_2NH_3][Fe^{III}Fe^{II}(HCOO)_6]$, $[(CH_3NH_3)[M(HCOO)_3]$ (M^{II} = Co^{II}, Mn^{II}, Fe^{II}, Ni^{II} and Cu^{II}), and $[(NH_4)[Mn(HCOO)_3]$.

The choice of using specific metal ions has been motivated by their different electronic configuration and therefore different physical behaviours, i.e. a large difference in the magnetic anisotropy is well known among the different divalent ions used in this study. Beside the effects on the properties when different divalent metal ions are introduced within the framework, the effects of the nature of the counterions has also been investigated. Even though there is not a clear correlation between the selected counterion and the change of the magnetic behaviour, neutron diffraction allows elucidating the differences in the crystal and in the magnetic structure when different counterions are used. Moreover, the work done in the thesis has helped us to interpret the bulk magnetometry measurements in the light of our results obtained with neutron diffraction, which is a complementary and more precise technique. A variety of magnetic phenomena, such as ferromagnetic behaviour, antiferromagnetic ordering and spin canting, have been observed in the studied compounds. Furthermore, from the crystallographic point of view, different kind of phase transitions were detected involving, for instance, the order-disorder of the counter-ion as in $[(CH_3)_2NH_2][Fe^{III}Fe^{II}(HCOO)_6]$ or $[(NH_4)[Mn(HCOO)_3]$, or the occurrence of modulated crystal structures, as for example in the $[(CH_3NH_3)[M(HCOO)_3]$ compounds.

Keywords: Neutron diffraction, X-ray diffraction, Metal-organic frameworks, Magneto-electric compounds, Antiferromagnetism.

Résumé en français

La synthèse et la caractérisation de nouveaux matériaux fonctionnels sont des enjeux majeurs en chimie et en physique. En particulier, les réseaux organométalliques (*metal –oganic frameworks :* MOFs) avec deux ou plusieurs fonctionnalités couplées, encore rares, sont très attractifs en raison de leur grande variété de propriétés et de leurs applications prometteuses connectant de nombreuses disciplines. Le développement de nouveaux matériaux fascinants peut avoir un impact considérable sur notre vie quotidienne, ce qui explique en partie l'intensification de la recherche dans le cadre de la science des matériaux et de la physique et chimie de la matière condensée.
Cette thèse se concentre sur la synthèse et la caractérisation des propriétés structurales et physiques de composés magnétiques basés sur des formiates métalliques en utilisant la combinaison de la diffraction de neutrons et de rayons X ainsi que d'autres techniques. Les réseaux de métal-formiate sont un sous-groupe spécifique des réseaux organométalliques, typiquement synthétisés en faisant réagir un ligand organique avec un sel métallique sous des conditions solvo-thermiques ou par des techniques d'évaporation ou de diffusion lente. Les centres métalliques sont liés par des molécules de formiate formant un cadre anionique qui peut être équilibré électriquement par des amines protonées.

Dans ce travail, j'ai étudié la structure cristalline, les transitions de phases et les propriétés magnétiques de deux familles de composés qui sont représentés par des composés hétéro-métalliques, ou à valence mixte, adoptant une structure de type niccolite et des composés homo-métalliques adoptant une structure pérovskite (ABX_3). Les composés suivants ont été synthétisés et caractérisés: $[(CH_3)_2NH_2][Fe^{III}M^{II}(HCOO)_6]$ (M^{II} = Mg^{II}, Mn^{II}, Fe^{II}, Co^{II} et Ni^{II}), $[CH_3CH_2NH_3][Fe^{III}Fe^{II}(HCOO)_6]$, $[(CH_3NH_3)[M(HCOO)_3]$ (M^{II} = Co^{II}, Mn^{II}, Fe^{II}, Ni^{II} et Cu^{II}), et $[(NH_4)[Mn(HCOO)_3]$.

Le choix d'utiliser des ions métalliques spécifiques a été motivé par leur configuration électronique différente et, par conséquent, par les différents comportements physiques, par exemple une grande différence bien connue dans l'anisotropie magnétique des différents ions divalents utilisés dans cette étude. Outre les effets sur les propriétés lorsque différents ions métalliques divalents sont introduits dans la structure, un autre aspect intéressant est l'effet produit en changeant la nature des contre-ions. Même s'il n'y a pas de corrélation claire entre le contre-ion sélectionné et le changement de comportement magnétique, la diffraction des neutrons permet d'élucider les différences dans la structure cristalline et dans la structure magnétique lorsque différents contre-ions sont utilisés. Par ailleurs, ce travail, nous aide à interpréter les mesures complémentaires de magnétométrie à la lumière de nos résultats de la diffraction neutronique. Une variété de phénomènes magnétiques, tels que le comportement ferromagnétique, l'ordre antiferromagnétique et le basculement de spin, ont été observés dans les composés étudiés. De plus, du point de vue de la structure cristalline, différentes transitions de phases ont été détectées impliquant par exemple l'ordre-désordre du contre-ion comme dans les composés $[(CH_3)_2NH_2][Fe^{III}Fe^{II}(HCOO)_6]$ ou $[(NH_4)[Mn(HCOO)_3]$, ou le passage d'une phase commensurable à une phase incommensurable donnant lieu à une modulation de la structure comme dans les composés de formule $[(CH_3NH_3)[M(HCOO)_3]$.

Mots clés : Diffraction de neutrons, Diffraction de rayons X, Réseaux organométalliques, Composés magnéto-électriques, Antiferromagnétisme.

TABLE OF CONTENTS

INDEX OF CRYSTAL STRUCTURE COMPOUNDS

1. $[(CH_3)_2NH_2][Fe^{III}Fe^{II}(HCOO)_6]$

2. $[(CH_3)_2NH_2][Fe^{III}Co^{II}(HCOO)_6]$

3. $[(CH_3)_2NH_2][Fe^{III}Mn^{II}(HCOO)_6]$

4. $[(CH_3)_2NH_2][Fe^{III}Ni^{II}(HCOO)_6]$

5. $[(CH_3)_2NH_2][Fe^{III}Mg^{II}(HCOO)_6]$

6. $[CH_3CH_2NH_3][Fe^{III}Fe^{II}(HCOO)_6]$

7. $[CH_3NH_3][Co(COOH)_3]$

8. $[CH_3NH_3][Fe(COOH)_3]$

9. $[CH_3NH_3][Ni(COOH)_3]$

10. $[CH_3NH_3][Mn(COOH)_3]$

11. $[CH_3NH_3][Cu(COOH)_3]$

12. $[NH_4][Mn(HCOO)_3]$

Chapter 1

General concepts

Introduction

The first chapter of this thesis has the purpose to guide the readers through the general concepts concerning the most salient topics investigated in this thesis project. It can be considered as a very concise compendium about molecular-based magnetic materials giving particular attention to the subject of metal-organic frameworks and magnetoelectric multiferroics. The essential feature, which is moving many scientists to spend their efforts in this field, is that the mutual coupling of certain properties can make a compound functional and this has as a consequence that the target compound can be usable in applications[1]. In order to explore multiferroic systems it is indispensable reviewing the basics of ferromagnetism and ferroelectricity.

1.1 Magnetic ordering

The magnetic behaviour of an atom has its origin in two components: the orbital moment of the electrons and the spin moment of unpaired electrons. When a material contains transition metal or rare earth ions with partially filled *d* or *f* electron shells will show a magnetic moment. The spin, $\boldsymbol{s}_i$ and orbital angular momentum, $\boldsymbol{l}_i$ of the individual electrons combine to give the total spin, $\boldsymbol{S} = \sum_i \boldsymbol{s}_i$ and total orbital angular momentum, $\boldsymbol{L} = \sum_i \boldsymbol{l}_i$. The orbital magnetic moment, $\boldsymbol{\mu_l}$ associated to the electron given by:

$$\boldsymbol{\mu_l} = -\frac{|e|}{2\,m_e}\,\hbar\boldsymbol{l} = -\mu_B\,\boldsymbol{l} \qquad (1.1)$$

where *e* represents the electron charge, m_e the electron rest mass, and $\mu_B = e\,\hbar/2\,m_e$ is the Bohr magneton, which is a physical constant (9.27×10^{-24} J T^{-1}).

The electron also possesses an intrinsic angular momentum, the electron spin ***s***. The associated magnetic moment $\boldsymbol{\mu_s}$ is

$$\boldsymbol{\mu_s} = -g_e\,\frac{|e|}{2m_e}\,\hbar\,\boldsymbol{s} = -g_e\mu_B\,\boldsymbol{s} \qquad (1.2)$$

where g_e is the spectroscopic splitting factor (or the Landé *g*-value) is a dimensionless quantity characterizing the magnetic moment and gyromagnetic ratio of a particle and it is equal to 2,

$$\boldsymbol{\gamma} = -g_e\,\frac{\mu_B}{\hbar} \qquad (1.3)$$

The interaction between the orbital and spin components, ***L*** and ***S*,** is called *Russell-Saunders coupling*[2], ***J*** = ***L*** + ***S*** (see, Figure 1).

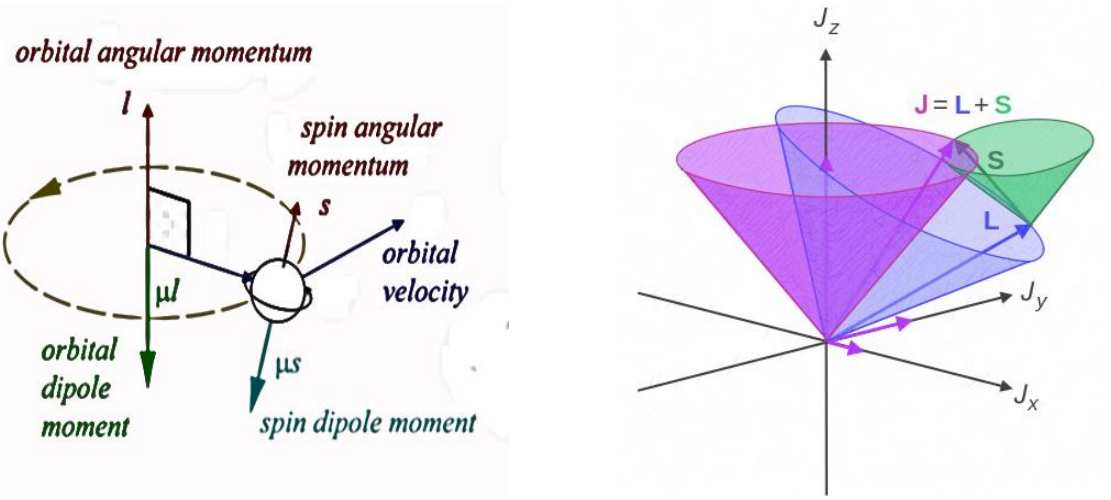

Figure 1: On the left the representation of the electronic orbital and spin angular momentum and the correspondent magnetic dipoles; on the right the vector cones of total angular momentum **J** (purple), orbital **L** (blue), and spin **S** (green).

The symbol *J* refers to the modulus of total angular momentum of the spin-orbit interaction. The effective magnetic moment is calculated from the spin-orbit interaction as:

$$\mu_{eff} = g_j \mu_b \sqrt{J(J+1)} \tag{1.4}$$

Ions with filled shells do not participate in the magnetic ordering because the spins of the electrons sum to zero, therefore only unfilled shells contribute.

Long-range magnetic ordering within the material occurs arise from the exchange interactions between the partially filled *d*-shells of different ions. The type of ordering (*i.e.* ferromagnetic, antiferromagnetic, etc.) relies on the nature of the different exchange interactions.

1.1.1 Exchange Interactions

In nature, the coupling of magnetic moments to another one is a quantum mechanical phenomena that contribute to magnetically ordered states and it is known as exchange interaction. The exchange terms are due to Coulomb interactions between two neighbouring spin moments and they are described by the overlap of electron wavefunctions of two adjacent atoms, in agreement with Pauli's exclusion principle. The Heisenberg Hamiltonian for the exchange interaction terms is given by:

$$\mathcal{H} = -\sum_{ij} J_{ij}\, \boldsymbol{S_i} \cdot \boldsymbol{S_j} \qquad (1.5)$$

which is a sum over all pairs of spins *i* and *j* where J_{ij} is the exchange interaction between the i^{th} and j^{th} spins. If $J < 0$ between two isolated ions, the energy minimization makes the alignment of the magnetic moments antiparallel (antiferromagnetic), while if $J > 0$ the alignment is parallel (ferromagnetic)[3].

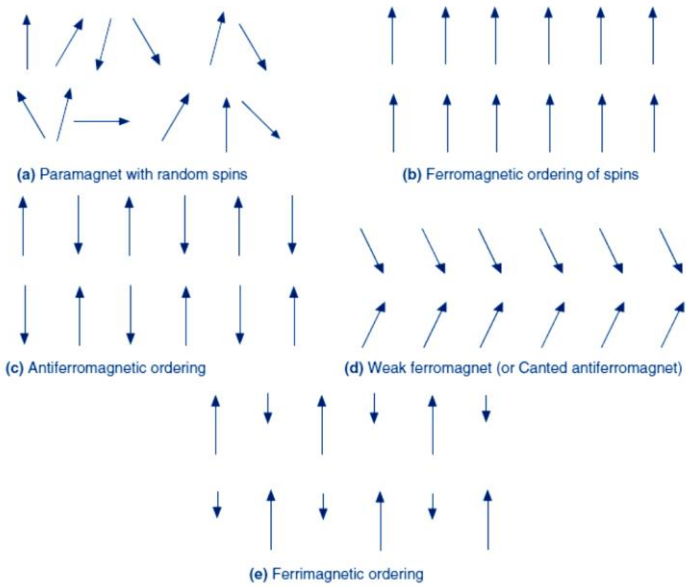

Figure 2 : Ordering of the magnetic dipoles in magnetic materials. From reference [9].

In a ferromagnet, all the spins are aligned parallel with a resultant net magnetic moment. If all spins have an antiparallel disposition, giving rise to an antiferromagnet, the net magnetic moment is cancelled to zero. In a ferrimagnet, the spins oppose each other yet the opposing moments are unequal so there is a spontaneous magnetization.

In the case of a weak ferromagnet (or canted antiferromagnet) the spins are tilted by a small angle about their principal axis, and they produce a small net magnetic moment. Moreover, magnetic order can be commensurate, where the magnetic unit cell is equal or an integer multiple of the crystallographic unit cell, or incommensurate where this is not the case. The three types of exchange that is possible to observe in insulators or semiconductors are: a) direct exchange, b) double exchange and c) superexchange.

The so-called *direct exchange interaction* operates between moments, which are close enough to have sufficient overlap of their wavefunctions, ant it occurs without intermediary. It gives a strong but short range coupling which decreases rapidly with the increase of the distance between ions. In the *double exchange*, ferromagnetic exchange

interactions are favoured as the magnetic ions can show mixed valence allowing the electrons to hop into a vacancy without having to change spin direction. This model is lightly similar to *superexchange* except that the hopping process is not virtual. Materials with double exchange are really semiconductors or become metals below the magnetic ordering temperature. In *superexchange*, the interaction between moments on ions is too far to be connected by direct exchange, so the interaction occurs between two atoms having ligands that participate in the exchange process giving rise to a net coupling between the separated ions[4]. Another important interaction can occur between magnetic ions in metals mediated by conduction electrons, this the case of the *RKKY Interaction*, named after Ruderman, Kittel, Kasuya and Yoshida. A local moment spin polarizes the conduction electrons, which then couple to neighbouring local moments.

In general the interaction constants appearing in equation (1.5) are not simply scalars (J_{ij}) but have a tensorial form ($J^{\alpha\beta}_{ij}$ coupled with spin components S_α and S_β, with $\alpha,\beta = x, y, z$) due ultimately to the spin-orbit interaction. This is known as the anisotropic exchange interaction. The antisymmetric part of the tensor is known as the Dzyaloshinsky-Moriya interaction[3]. The magnetic ordering in zero field (spin configuration) is finally determined by the minimum energy of the system described by a generalization of the Hamiltonian (1.5) adding single ion anisotropy terms.

1.2 Ferroelectricity

Ferroelectricity is referred to as spontaneous polarization that occurs in certain materials and can be reversed by the application of an external electric field. The observation of polarization-electric field (*P-E*) hysteresis loops is considered necessary to establish if a material is ferroelectric. These measurements allow the switching of the direction of spontaneous polarization by an applied electric field to be observed. When a system has a non-centrosymmetric arrangement of ions, it can exhibit spontaneous polarization, the ferroelectricity is determined by the equilibrium between short-range repulsions that favour centro-symmetric structures, and long range Coulomb forces that favour the ferroelectric state[5].

The definition of the ferroelectric order parameter $\boldsymbol{P}$ as dipole moment $\boldsymbol{p}$ per unit volume V is described by the following equation:

$$\boldsymbol{P} = \frac{d\boldsymbol{p}}{dV} \tag{1.6}$$

The short-range repulsions between adjacent electron clouds need to be countered by bonding that stabilises shifts in ion arrangements. In some materials, at high temperatures, the short-range repulsions dominate resulting in an unpolarised state. However, when the temperature decreases the stabilizing forces become stronger than the repulsions and the non-centrosymmetric, ferroelectric state becomes stable. This local off-centring of ions can form long range cooperative ordering yielding a net polarization through the dipole-dipole interaction. Sometimes competing effects overcome this interaction and the dipoles cancel each other out so there is no net polarization, this state is known as antiferroelectric.

1.3 Molecule-Based Magnetic Materials

The use of magnets in different materials for technological applications, nowadays, cover a big industrial area that goes from magnetic machines to acoustic devices, passing through ferroelectric photovoltaics, nano-electronics elements to telecommunication and informatics[6,7]. The interest of the scientific community for these materials arises not only because of the technological applicability but rather from the possibility to control the functional properties, especially if it is possible to combine one of them with another property. Recently, the development of more complex magnetic materials has been possible due to the tunability of their properties at molecular level[8]. Commonly, an inorganic magnetic unit is representative of a classical magnet (also called "atom-based inorganic solid"), and it is characterized of a high density of *d* or *f* orbital metal spin sites; while an organic magnetic material is made of atoms with *s* and *p* orbitals. The combination of both can play an essential role in the final magnetic behaviour of a multifunctional compound. When molecules are incorporated in such structures instead of a solely inorganic magnetic unit, one can speak of a so-called "molecule-based magnet". Generally, their peculiarity is the possibility to tune the magnetic properties changing the organic and/or inorganic constituents of the molecule by synthetic methods. Moreover, they can exhibit (in combination or not), magnetic properties normally associated with inorganic material, *e.g.* magnetic ordering, electric conductivity, optical properties *etc*. One of the inspiring challenges in this research field is to discover molecular materials with hysteresis and residual magnetization at zero-field for a critical temperature as high as possible, below which all spins of the magnetic units are ordered. The ordering of spins may give rise roughly to three different types of magnetic behaviours ranging from ferromagnetism, ferrimagnetism to

antiferromagnetism[9].The lack of interaction between spin sites produce a dynamic random distribution of spins called paramagnetic state. In the case of ferromagnetism, all the spins are parallel coupled in the same direction. Whereas in antiferromagnets there is an antiparallel alignment of the spins and their complete cancelation leads to a zero net moment. When the individual magnetic moments are different, the result is a non-zero total magnetic moment of the bulk and the material results ferrimagnetic. Another case, in which a complete cancelation cannot occur, is the canted antiferromagnet (or weak ferromagnet) that shows a net residual moment, see Figure 2. Design and the preparation of molecular based-magnetic materials is different from that of classical ones. The conventional organic synthesis together with the use of relatively low-temperatures, is one of the most relevant characteristic opposed to the high temperature metallurgic processes adopted for the synthesis of the classical magnets[7,10]. Certainly, the last method provides thermodynamic stability[9] but it also limits the chemical flexibility, which is a peculiar advantage offered by using the first method cited above. In fact, the possibility of controlling the properties like the interactions between building blocks, or changing the structure of the molecules, makes it possible to design functional materials as desired for specific applications. Basically, they are two possible ways for synthesizing molecule-based magnets: the organic and the metal-organic routes[11,12]. With the first method, purely organic magnets can be obtained using free radicals or radical ions in which magnetic interactions are mediated by non-covalent bonds generally dominated by a weak nature and with magnetic order shown at very low temperature. The pioneer in this field was *McConnell*[13] and later *Ovchinnikov*[14] and co-workers. Their idea was to take a biradical monomer with two stable nitroxide radical side groups and polymerize it. By changing the type and position of the hydrogen bonding substituents, it has been possible to tune the magnetic interaction of a-nitronyl nitroxide-based materials. *Miller et al.*[7,10], synthesized a ferromagnetic compound of formula $[Fe(C_5Me_5)_2][TCNE]$ (Me,C = penta-methylcyclopentadienyl; TCNE = tetracyano-ethylene) that represents from a structural point of view an ionic diamagnetic donor/acceptor complex. It orders as a bulk 3-D ferromagnet at 4.8 K and it is sufficiently strongly magnetic that at low temperature a pellet of it can be attracted by a strong magnet[6].

1.4 The Metal-Organic- Frameworks (MOFs) compounds

All those materials under the name of metal-organic frameworks are generally built up from a metal centre that represents the inorganic unit and a bridging organic part. The discovery of molecule-based magnetic materials and the persistent research of these rare materials allowed the scientific community to step on a new class of compounds characterized by voids with molecular dimensions in which shape and size of these empty spaces establish the limits of tunability of MOFs properties[15]. There are many variables that the coordination chemistry offers in order to template the framework of a MOF compound and consequently to obtain an electric and/or a magnetic response by making the appropriate choices from the starting reactants. For this reason, it is common to refer to this category of compounds also with the adjective of hybrid-materials[15, 17]. MOFs can show physical properties like magnetism, ferroelectricity, luminescence, optical features, and for this reason they can also be labelled as multifunctional materials[18,19,20]. In the synthesis of MOFs, the principal goal is to obtain a well-defined geometry, but it is also important to get a good crystallinity of the material in order to be able to determine the crystal structure as well as the physical properties eventually present and correlated them. Therefore, the qualities of porous materials, related to the controlled and flexible assembly of the inorganic and organic blocks, has produced a growth in this scientific research field that touch many different applications in technology. The emergent field of MOFs represented, and it still represents, a meeting point of interdisciplinary research since the 1990s[21], when scientists with a background in zeolite synthesis contributed to the expansion of the synthetic adapted-MOFs methods[22]. The different scientific knowledge explains the wide variety of methods employed for the synthesis of MOFs, like for example the use of solvo-thermal reactions, which will be discussed in *chapter 2*, achieved from zeolite porous material chemistry. The typical framework shown by natural and synthetic zeolites is based on four-connected tetrahedral networks due to the sp^3 hybridization at silicon producing tetrahedral Si–O bonds. Their thermal, hydrothermal and chemical stability depends of the strong Si–O bond presence, while polarity and the charge balance is defined by the Si/Al ratio[15]. The fact that alumino-silicate zeolites has ensured a considerable success for the industrial market encouraged the academic community even more to pursuit new MOFs compounds. In this regard, the contribution of *Robson* and *Hoskins* provided with their works[21,23,24] enriched the research area of MOFs. The concept of framework solids built up by metal centres with tetrahedral or octahedral valence linked by rod-like polydentate ligands, generating a “regular array

of cavities interconnected by windows"[21] could be extended to infinite networks via coordination chemistry. But, it was thanks to *Yaghi* et *al.* that the term MOF started to be widely spread[17,25,26] for the investigation on a Co-carboxylate layer with porous occupied by aromatic guest molecules with reversible sorption behaviour[27]. About the specific classification of these materials, there have been controversial discussions[28,29], especially for those MOFs possessing a multiferroic behaviour there is still a kind of uncertainty for not being identified in a specific category. In fact, they are in between two big systems in which metal-organic-frameworks may also be magnetoelectric materials.

1.5 Multiferroics and Magnetoelectrics materials

Multiferroics, as defined by Hans Schmid[30], are single phase materials that simultaneously possess two or more "ferroic" order parameters, in absence of external electric and magnetic fields. The main four primary ferroic parameters are ferroelectricity, ferromagnetism, ferrotoroidicity and ferroelasticity. Already J.C. Maxwell, long before, intuited and proposed the combination of electric field, magnetic field and electric charge dynamics using four equations. Despite this, it has been common to think that electric and magnetic ordering in solids were most often appearing separated simply because the electric charges of electrons are responsible for the electric effects, while electron-spins govern the magnetic properties. The term multiferroic is most often used to refer to a system with magnetic and ferroelectric order, as is the case in the materials studied in this thesis. From an application point of view, the interest in multiferroic materials lies in the possibility of strong magnetoelectric coupling and the possibility to create new functionalities in materials.

The magnetoelectric effect has the characteristic of controlling electrical properties with a magnetic field and magnetic properties with an electric field. It exists a very small number of materials showing magnetism or electrical polarization and exhibiting both ferroelectric and ferromagnetic order parameters simultaneously. As shown in Figure 3 magnetoelectricity is an independent phenomenon but it can also be observed in multiferroic materials[31].

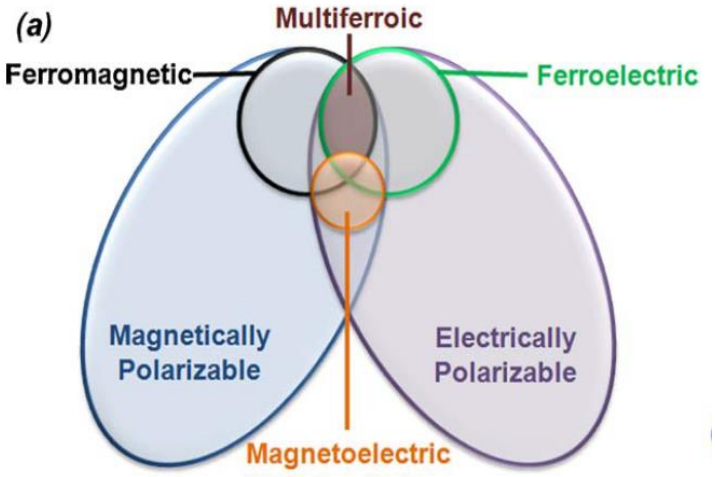

Figure 3 : Multiferroics combine the properties of ferroelectrics and magnets. Figure from reference [40].

The poor existence of magnetoelectric-multiferroics, and particularly ferroelectric-ferromagnetic multiferroics, can be understood by considering a number of factors like, for example, symmetry and electronic properties.

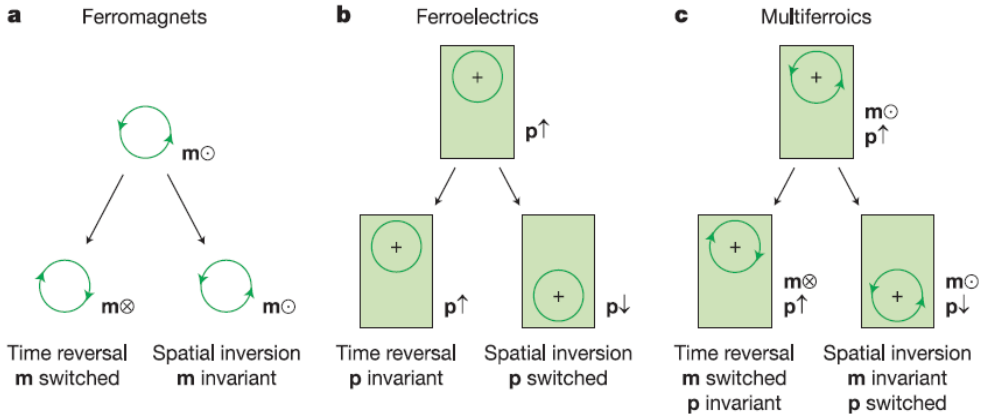

Figure 4: Spatial and time inversion symmetry in multiferroics. Figure from reference [33].

The difference in filling the *d* shells required for ferroelectricity (empty *d* orbitals) and magnetism (partially filled *d* orbitals) makes these two ordered states mutually exclusive[32]. Moreover, the magnetic moment in a ferromagnet, described as a current loop, is unchanged under spatial inversion, however, the direction of the current and

therefore the magnetic moment changes under time inversion. The opposite is true for a ferroelectric[33] (see Figure 4).

Considering a ferroelectric material as a positive point charge lying asymmetrically in a crystal unit cell, spatial inversion reverses the polarisation while time inversion has no effect. Consequently, a multiferroic shows no spatial or time invariance[34].

One central feature in the investigation of multiferroics is the production of high quality samples, and considering that multiferroics behaviour do not follow any specific rule[35] it is very hard to create a new multiferroic material. Surely, an appealing approach towards multiferroics are metal-organic frameworks because as reported by *Rogez et al.*[33] they have the advantage of showing a weak ferromagnetism in coexistence with antiferroelectric order and for this reason their properties can be exploitable in many applications[36]. Therefore, MOFs tunability can be a useful tool for controlling the ferroelectric properties[37].

1.5.1 Multiferroics Type I

In order to understand the basic phenomena of multiferroics it is necessary to classify multiferroics by the microscopic mechanism that determines their properties. There are various pathways for achieving multiferroism in materials that can be enclosed in type *I and II* as described by *Khomskii*[38].

Type I multiferroics are materials in which ferroelectricity and magnetism have different sources and appear largely independent of each other. They are often good ferroelectrics and the onset temperatures of the magnetic and ferroelectric transitions can be well above room temperature. The most common mechanisms in the *type I* are described below.

1.5.1.1 Electronic Lone Pair generates ferroelectricity

The $6s^2$ lone pairs, possessed by the ions such as Tl^{1+}, Pb^{2+} and Bi^{3+} have a high polarizability and are the source of ferroelectricity. In model systems like the perovskites type ABO_3 the active $6s^2$ lone pair causes the empty $6p$ orbital of *A* to become closer in energy to the oxygen $2p$ orbital. Then a hybridization between the two *p* orbitals occurs, inducing a structural distortion and ferroelectricity while the magnetism comes from the partially filled *d* shells of the *B*-site cation. This mechanism is reported for materials like $BiFeO_3$ and $BiMnO_3$ [38].

1.5.1.2 Ferroelectricity due to charge ordering

This mechanism is often observed in transition metal ions with different valence where the electric dipole depends on the electron correlations instead of the covalent bonding between anions and cations[39]. The ferroelectricity mechanism can be explained as the mixture of site centred and bond-centred charge ordering: when charges order in a non-centrosymmetric mode, induce electric polarization[32] and if magnetic ions are present, a magnetic order may be coupled to ferroelectricity and coexisting.

1.5.1.3 Geometric Ferroelectricity

In general, ferroelectric materials show a phase transition to a low-temperature phase that does not have a centre of symmetry. The multiferroic phase appears only at cryogenic temperatures when antiferromagnetic order due to spin frustration arises. However, the ferroelectric instability arise from the topology of the chemical structure, and the ferroelectric distortions are driven by ionic size effects, the space-filling, breaks inversion symmetry and does not implicate any significant re-hybridization effects[35]. The first material[40] that was identified as geometric ferroelectric is the hexagonal manganite $YMnO_3$ (Figure 5).

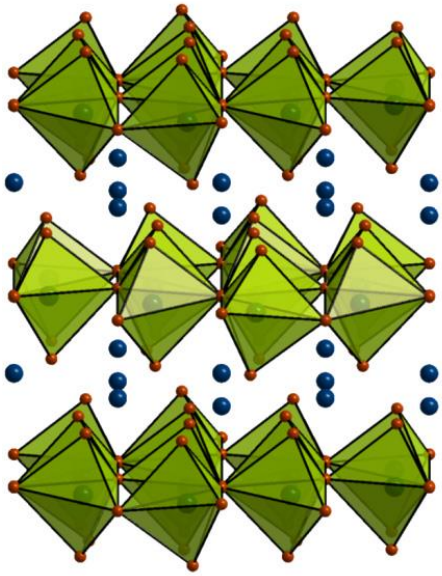

Figure 5: Crystal structure of $YMnO_3$, classified as a geometric ferroelectric, crystallizes in a layered hexagonal structure, consisting of a two-dimensional arrangement of connected oxygen bi-pyramids surrounding the Mn^{3+} cations that are separated by layers of Y^{3+} cations. Figure obtained from reference [39].

Ferroelectricity in $YMnO_3$ arises from the rotation of MnO_5 bipyramids, which separate two-dimensional triangular planes of Y ions. Because of the topology of differently charged ions in the chemical lattice, this rotation leads to ferroelectric polarization even in the absence of charge transfer from one ion or bond to another.

1.5.2 Multiferroics Type II

Multiferroic materials for which ferroelectricity is induced by magnetism, implying a strong coupling between the two order parameters, are defined as multiferroics of *type II*. The prototypical examples of this sort of behaviour are, for instance, the compounds $TbMnO_3$ and $TbMn_2O_5$ where ferroelectricity is induced by the formation of a symmetry-lowering magnetic ground state that lacks inversion symmetry[31]. Roughly, this classification can be grouped into materials with spiral/cycloidal magnetic configurations (Figure 6) coming from the spin-orbit interaction or special collinear magnetic orderings where all the magnetic moments align along a particular axis.

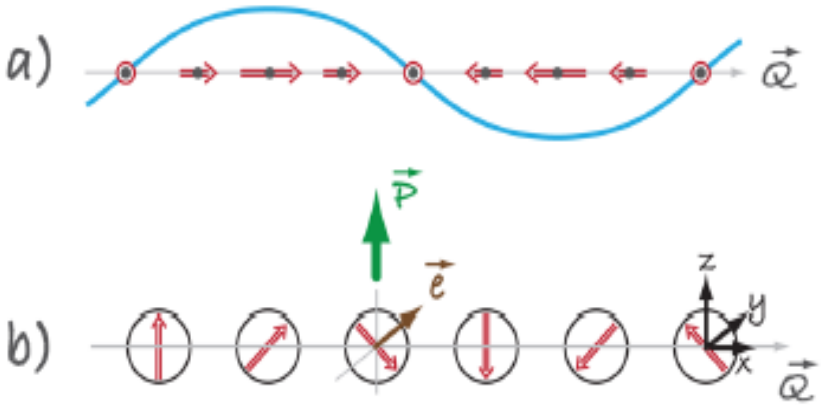

Figure 6: a) sinusoidal spin density wave in which spins lie along one direction but they show different magnetic moment magnitude b) cycloidal spin configuration. Figure obtained from reference [37].

Most of the *type-II* multiferroics known up to now are belonging to the spiral group where ferroelectricity appears in conjunction with a spiralling magnetic phase, mostly of the cycloid type. Magnetic frustration in general is the source of spiral magnetic ordering in an insulator[38].

In the second group, ferroelectricity appears in collinear magnetic structures, without the necessary involvement of the spin-orbit interaction. Polarization can appear in these materials as consequence of exchange restriction because the magnetic coupling varies with the atomic positions[38].

1.6 Applications of Magnetoelectric Multiferroics Materials

The challenge for scientists working in this field during the last years has been to recreate a mutual coupling between the properties of a material. Therefore, the heart of the problem is to find new examples of multiferroic-magnetoelectric materials by the appropriate synthesis methods. An important distinction has to be made between systems exhibiting independent electric and magnetic orders and those presenting a magneto-electric coupling, both of which are promising in terms of applications. However, the highest expectations rise from magneto-electric compounds, because they give access to a new type of control of magnetization by an electric field in spintronic devices[41]. Furthermore, technological applications, such reading magnetic storage devices, have been suggested for multiferroics. Magnetization and polarization could both encode information, by combining the best qualities of FeRAMs (ferroelectric random-access memories) and MRAMs (magnetoresistive random-access memories): fast low-power electrical write operation, and non-destructive magnetic read operation[42]. The advantage in this case, would be the ability for data to be written electrically and read magnetically[43]. Nevertheless, it should be highlighted that the magnetic ordering temperature in current materials is still too low to expect immediate applications, and that the search for stable room-temperature multiferroics sufficiently insulating to maintain a large macroscopic polarization is a major challenge. In this scenario, MOF-based compounds offer very attractive perspectives as central model multiferroic systems, because ligands, metal ions, and organic cations can be varied to drive single-phase compounds towards technological applications. A few hybrid or molecule-based materials are currently emerging. In fact, MOFs provide an impressive number of applications, such as gas storage, exchange or separation, drug delivery, catalysis, optics, and magnetism and they are also good candidates for obtaining multiferroics. A compromise between the size of the ligand and the strength of the exchange coupling can be an essential requisite. Following these developments, MOFs appear to be an appealing way to combine magnetic and electric orders within a single structure and they seem to be designated to enhance discoveries in the fields of materials science and chemistry.

Aims of the thesis

This thesis focuses on the design and the synthesis of multifunctional magnetic molecular materials. More precisely, the studied compounds involved in the investigation are metal-organic frameworks (MOFs) in which we intend to produce multiferroic properties, where the magnetic and electric behaviour depends on the intrinsic nature of the metal and of the organic ligand as well as the particular geometry due to the union of metal-ligand. One of the reason that moved our interest to study this specific group of multiferroics is certainly their rarity. Another more general motivation, that also attracted many scientists, is the versatility of coordination chemistry knowledge that allows to synthesize MOFs with more than one ferroic property. The strategy consists of applying some modifications to the metal, or/and of the ligands, or/and of the counter ion, in order to obtain a multifunctional material. This flexibility is an interesting aspect, which leads every year to the synthesis of new compounds[44]. MOFs are also known as coordination polymers because they typically form extended structures via ligands that form coordination bonds with metal centres. Extending in three dimensions this structural model it is possible to produce MOF materials with high porosity. This last property represents another motivation that took extensive attention owing to their high surface area, low density, high porosity, thermal stability and flexible chemical functionalities. In fact, researchers rapidly predicted that these porous materials would demonstrate advantageous potential uses as gas storage, separations, catalysis and other applications.

The main goal of the thesis has been not only to determine and characterize the crystal structure of the synthesized compounds, but especially to understand how these solid materials behave. This effort involved together many different concepts from many areas of physics and coordination chemistry that makes it, a fascinating multidisciplinary project.

Here, the systems studied are metal-formate frameworks, composed of homo or hetero-metallic *3d* metal centres, connected via formate and via protonated amine, located in the cavities to balance the charge of the framework. By incorporating magnetic moment carriers, such as paramagnetic metals, in known metal-formate frameworks, it is possible to study and control their magnetic behaviour. In general, in these materials, long-range

antiferromagnetic ordering[45,46], accompanied with weak ferromagnetism or ferrimagnetism[47], usually occurs at low temperature.

Metal-formate frameworks such as $[(CH_3)_2NH_2][M^{II}Fe^{III}(HCOO)_6]$, $[CH_3CH_2NH_3][M^{II}Fe^{III}(HCOO)_6]$, $[NH_4][M(HCOO)_3]$ and $[CH_3NH_3][M^{II}(HCOO)_3]$, with M = Mn^{II}, Fe^{II}, Co^{II} , and Ni^{II}, have shown promising electric behaviours mostly due to their order–disorder transition and the coexistence of magnetic and electric orderings enclosure them in the uncommon category of MOF-multiferroics.

However, the development of room temperature MOFs is still far. Therefore, the future investigation of the design, synthesis and assembly of MOFs will be crucial for the development of room temperature multiferroics, especially for those having an important magnetoelectric coupling.

Bibliography

(1) Kreisel, J.; Kenzelmann, M. 2009, pp 17–20.

(2) *Wikipedia*; 2017.

(3) Blundell, S. *Magnetism in Condensed Matter*; Oxford Master Series in Physics; Oxford University Press: Oxford, New York, 2001.

(4) Goodenough, J. B. *Magnetism And The Chemical Bond*; John Wiley And Sons, 1963.

(5) Rabe, K.; Ahn, C. H.; Triscone, J.-M. *Physics of Ferroelectrics - A Modern Perspective*; Springer, 2007.

(6) Miller, J. S. *Inorg. Chem.* **2000**, *39* (20), 4392.

(7) Miller, J. S.; Epstein, A. J. *Angew. Chem. Int. Ed. Engl.* **1994**, *33* (4), 385.

(8) Coronado, E.; Gatteschi, D. *J. Mater. Chem.* **2006**, *16* (26), 2513.

(9) Schröder, M. *Functional Metal-Organic Frameworks: Gas Storage, Separation and Catalysis*; Springer, 2010.

(10) Miller, J. S. *Materials Today* **2014**, *17* (5), 224.

(11) Gatteschi, D.; Sessoli, R. *J. Mater. Chem. Magn. Mater.* **1992**, *104*, 2092.

(12) Caneschi, A.; Gatteschi, D.; Sessoli, R.; Rey, P. *Acc. Chem. Res.* **1989**, *22* (11), 392.

(13) Harden M. McConnell, H. M. M. *J. Chem. Phys.* **1963**, *39* (7), 1910.

(14) Korshak, Y. V.; Medvedeva, T. V.; Ovchinnikov, A. A.; Spector, V. N. *Nature* **1987**, *326* (6111), 370.

(15) Rosseinsky, M. J. *Microporous and Mesoporous Materials* **2004**, *73* (1–2), 15.

(16) Kuppler, R. J.; Timmons, D. J.; Fang, Q.-R.; Li, J.-R.; Makal, T. A.; Young, M. D.; Yuan, D.; Zhao, D.; Zhuang, W.; Zhou, H.-C. *Coord. Chem. Rev.* **2009**, *253* (23–24), 3042.

(17) Rowsell, J. L. C.; Yaghi, O. M. *Microporous and Mesoporous Materials* **2004**, *73* (1–2), 3.

(18) Wang, Z.; Hu, K.; Gao, S.; Kobayashi, H. *Adv. Mater.* **2010**, *22* (13), 1526.

(19) Zhang, W.; Xiong, R.-G. *Chem. Rev.* **2012**, *112* (2), 1163.

(20) Singh, M. K.; Yang, Y.; Takoudis, C. G. *Coord. Chem. Rev.* **2009**, *253* (23–24), 2920.

(21) Hoskins, B. F.; Robson, R. *J. Am. Chem. Soc.* **1990**, *112* (4), 1546.

(22) Stock, N.; Biswas, S. *Chem. Rev.* **2012**, *112* (2), 933.

(23) Robson, R.; Hoskins, B. F. *J. Am. Chem. Soc.* **1989**, *111*, 5962.

(24) Robson, R. *Dalton Trans.* **2008**, No. 38, 5113.

(25) Kim, J.; Chen, B.; Reineke, T. M.; Li, H.; Eddaoudi, M.; Moler, D. B.; O'Keeffe, M.; Yaghi, O. M. *J. Am. Chem. Soc.* **2001**, *123* (34), 8239.

(26) Li, H.; Eddaoudi, M.; Groy, T. L.; Yaghi, O. M. *J. Am. Chem. Soc.* **1998**, *120* (33), 8571.

(27) Yaghi, O. M.; Li, G.; Li, H. *Nature* **1995**, *378* (6558), 703.

(28) Ramesh, R. *Nature* **2009**, *461* (7268), 1218.

(29) Férey, G. *Chem. Soc. Rev.* **2007**, *37* (1), 191.

(30) Schmid, H. *Ferroelectrics* **1994**, *162* (1), 317.

(31) Martin, L. W.; Chu, Y.-H.; Ramesh, R. *Materials Science and Engineering: R: Reports* **2010**, *68* (4–6), 89.

(32) Cheong, S.-W.; Mostovoy, M. *Nat Mater* **2007**, *6* (1), 13.

(33) Rogez, G.; Viart, N.; Drillon, M. *Angewandte Chemie International Edition* **2010**, *49* (11), 1921.

(34) W. Eerenstein; N. D. Mathur; J. F. Scott. *Nature* **2006**, *442* (7104), 759.

(35) Picozzi, S.; Ederer, C. *J. Phys.: Condens. Matter* **2009**, *21* (30), 303201.

(36) Lin, Z.-J.; Lü, J.; Hong, M.; Cao, R. *Chem. Soc. Rev.* **2014**, *43* (16), 5867.

(37) Stroppa, A.; Jain, P.; Barone, P.; Marsman, M.; Perez-Mato, J. M.; Cheetham, A. K.; Kroto, H. W.; Picozzi, S. *Angew. Chem.* **2011**, *123* (26), 5969.

(38) Khomskii, D. *Physics Online Journal* **2009**, *2*, 20.

(39) Ikeda, N.; Ohsumi, H.; Ohwada, K.; Ishii, K.; Inami, T.; Kakurai, K.; Murakami, Y.; Yoshii, K.; Mori, S.; Horibe, Y.; Kitô, H. *Nature* **2005**, *436* (7054), 1136.

(40) Van Aken, B. B.; Palstra, T. T. M.; Filippetti, A.; Spaldin, N. A. *Nat Mater* **2004**, *3* (3), 164.

(41) Ramesh, R.; Spaldin, N. A. *Nat Mater* **2007**, *6* (1), 21.

(42) Martin, L. W.; Ramesh, R. *Acta Materialia* **2012**, *60* (6–7), 2449.

(43) Hill, N. A. *J. Phys. Chem. B* **2000**, *104* (29), 6694.

(44) Qin, W.; Xu, B.; Ren, S. *Nanoscale* **2015**, *7* (20), 9122.

(45) Xu, G.-C.; Zhang, W.; Ma, X.-M.; Chen, Y.-H.; Zhang, L.; Cai, H.-L.; Wang, Z.-M.; Xiong, R.-G.; Gao, S. *J. Am. Chem. Soc.* **2011**, *133* (38), 14948.

(46) Cañadillas-Delgado, L.; Fabelo, O.; Rodríguez-Velamazán, J. A.; Lemée-Cailleau, M.-H.; Mason, S. A.; Pardo, E.; Lloret, F.; Zhao, J.-P.; Bu, X.-H.; Simonet, V.; Colin, C. V.; Rodríguez-Carvajal, J. *J. Am. Chem. Soc.* **2012**, *134* (48), 19772.

(47) Mazzuca, L.; Cañadillas-Delgado, L.; Rodríguez-Velamazán, J. A.; Fabelo, O.; Scarrozza, M.; Stroppa, A.; Picozzi, S.; Zhao, J.-P.; Bu, X.-H.; Rodríguez-Carvajal, J. *Inorg. Chem.* **2017**, *56* (1), 197.

Chapter 2

Theory and Experimental Methods

Introduction

In the second chapter all the experimental techniques used for identifying and characterizing the studied compounds are reported as well as the synthetic methods used to prepare the samples of interest. This thesis has been successfully concluded thanks to the great opportunity of carrying out the majority of experiments at the *Institut Laue Langevin*, the most important neutron science facility in the world, providing a wide selection of instruments and techniques that will be described later on in this chapter. Beside neutron experiments, for this thesis it has been made use of other complementary instruments like High Resolution Synchrotron X-Ray diffractometers, superconducting quantum interference device (SQUID), DSC calorimeters, etc. The main concepts regarding Neutron and X-ray scattering will be outlined, in particular diffraction techniques that have been principally used to investigate the crystal and magnetic structures of the synthesized compounds.

2.1 General aspects on Sample Preparation

There are several aspects to take into account when approaching the synthesis of a new compound. Especially when the compounds are belonging to the family of multiferroic MOFs in which a big problem is to maintain the integrity of the starting reactants in order to preserve the coordination bonds. The principal goal is to obtain a good crystal quality for proceeding then with the structural analysis. The general approach consists of choosing metal unit with unpaired electrons, because they are at the origin of magnetic phenomena. The solubility of the precursors is important but not a limiting feature, because as known in solvo-thermal conditions this obstacle is easily bypassed. Before reaching the suitable product, many tests are indispensable for identifying the correct method. Habitually playing with some “synthetic variables” as concentration, solvent polarity, pH, or temperature, lead to obtain better crystal’s quality. Once the procedure for a compound is established, in general, the same method is also used for synthesizing the isostructural compounds, even if sometimes identical conditions do not provide the desired phase and the conditions should be changed. Concerning the synthesis methods used for the topic studied in this thesis, many efforts have been spent for improving slow

evaporation, slow diffusion and solvo-thermal synthesis. MOFs were mainly synthesized by combining an organic ligand and a metal salt in solvo-thermal conditions at moderated temperatures under autogenous pressure.

2.1.1 Solvo-thermal method

Solvo-thermal reactions, take place in closed vessels under autogenous pressure created from heating the solvent above its boiling point. It exploits the self-assembling of poor soluble reagents during a process that has a working temperature range of 80-140 ˚C.

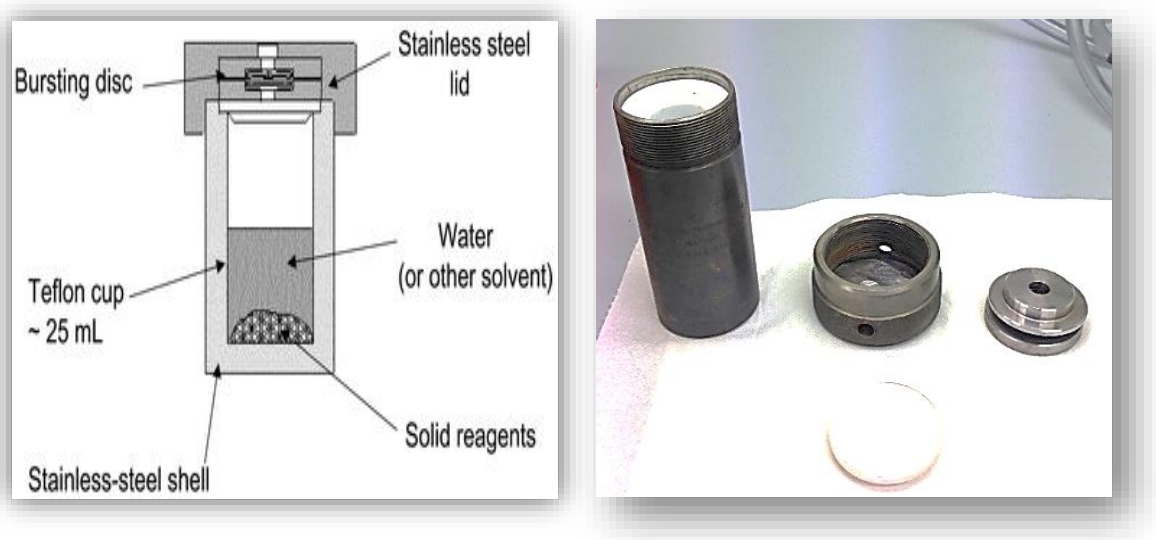

Figure 1: Typical configuration of a vessel autoclave

The solvo-thermal method was originally used for the synthesis of zeolites, but has been well adapted for the synthesis of MOFs. The system in Figure 1 is made up of a sealed Teflon-lined –*PARR Instrument Company*, contained in a stainless steel autoclave. The Teflon tube is able to hold the reaction up to 140ºC. The most important parameter to respect is that it must not be filled with more than 2/3 of the solution when used at high temperature to avoid overpressure. The reaction is carried in an oven set at the desired temperature, and after the reaction the mixture solution is left to cool down at room temperature under controlled conditions. The product is in general filtered and washed several times with a solvent, in order to remove eventual impurities or non-reacting precursors.

2.1.2 Slow evaporation method

It is the simplest technique for growing crystals and it involves the preparation of a solution in a suitable solvent. Then the solution is kept undisturbed, waiting for the evaporation of the solvent in the solution up to the saturation. If the appropriate conditions

occur, it is easy to obtain single crystals of suitable size in at least two of the three dimensions by the crystallization of few seeds from the solution. A number of factors can influence the crystals size, for example the solubility of the sample in the chosen solvent, the number of nucleation sites and time, temperature, pH, etc. If possible, a solvent should be chosen in which the sample is soluble. The crystal-growing glass should be clean because dust or defects in the surface can provides numerous nucleation sites (too many seeds) and may avoid the crystal growth of one or few crystals by competition between different crystallites. Vibration or frequent movement to check the sample tends to lead to poor quality crystals. The sample can then be left in a sample vial that has a perforated cap. The size of the perforations is an experimental variable that depends to some extent on the volatility of the sample. Other variations on this method are to transfer some of the solution to a crystallization dish and cover with perforated aluminium foil. If nucleation happens too fast, too many small crystals can grow.

2.1.3 Liquid- liquid Diffusion method

The principle of this method is to diffuse slowly two solutions into each other, Figure 2. Containing different reactants and prepared with the same solvent or using miscible solvents For example, in a narrow mono-tube, the solution with the lower density is carefully layered on the top of the solution with higher density previously placed at the bottom. This practise is better done with a syringe or in general by use of a Pasteur pipette. Over a certain period, the two solutions are slowly mixing and, if the reactants form an insoluble product it may be obtained as single crystals. It is possible to separate the two solutions with by a third solvent layer that permits a slower diffusion of the reactants. A variation of this method can be performed by freezing the lower layer before adding the second liquid. Another possible approach is to diffuse a pure solvent in which the final product is moderately or completely insoluble, and let it diffuse into a solution of a different solvent containing the reactants or product to be

Figure 2: Liquid-liquid diffusion between two methanolic solution. The methanolic solution of a copper salt was layered on top of the methanolic solution of methylamine and formic acid.

crystallized. The same principle is also used in the vapour diffusion technique, in which the pure solvent diffuses into the solution via gas phase and the separation between them is applied by using physical barrier: in a larger tube with the pure solvent, a smaller sample tube is placed which contains the solution with the reactant. The method works better if the solution is less volatile than the pure solvent in order that the latter diffuses into the sample solution.

2.2 SQUID: magnetization measurements

Superconducting **Q**uantum **I**nterference **D**evice (SQUID) magnetometer is a device with remarkable sensitivity[1] used for investigating extremely small variations in magnetic flux at different temperatures in two ways. In the static *DC* mode, a direct current is crossing the insulator in the absence of any external electromagnetic field, owing to tunnelling. In the dynamic *AC* mode if a voltage is applied across the junction; a small oscillating current starts flowing back and forth through the Josephson junction[2], that can be described as the tunnelling of a pairs of electrons from one superconductor to another through the insulating junction between them. By monitoring the current flowing in the loop it is possible to detect very small changes in flux, allowing the measurement of very weak magnetic fields. The quantized flux allows the detection of very small changes in the magnetic field associated with the flux quantum. The threshold detection limit[3] for SQUID's is 10^{-14} T, which is smaller than the magnetic fields of the human heart (10^{-10} T) or brain (10^{-13} T). The measurement procedure can foresee a measure in which the magnetization is dependent of magnetic field at fixed temperature for observing possible hysteresis behaviour for example. Another procedure is to measure the magnetization as a function of temperature for detecting eventual magnetic transitions, which are characterized by a deviation of the magnetic susceptibility defined as $\chi = \frac{\delta M}{\delta H}$. The law that governs the evolution of the paramagnetic magnetization as function of the temperature is the Curie-Weiss law: $\chi(T) = \frac{C}{T-\theta}$. When $\theta = 0$ the exchange interactions are negligible and only isolated paramagnetic centres exist in the sample, when $\theta > 0$ the algebraic sum of the exchange interaction is positive and rough ferromagnetic behaviour is expected and, finally when $\theta < 0$ for the exchange interactions are antiferromagnetic. The magnetic susceptibility can also be measured following the **Z**ero **F**ield **C**ooled (*ZFC*)- **F**ield **C**ooled (*FC*) procedure. This allows to probe phenomena such as magnetic viscosity or the presence of magnetic domains. In such cases, a difference

between the ZFC and FC curves will be observed. All the superconducting elements have to be surrounded by liquid helium to keep the temperature such that all the components are in the superconducting regime. The sample moves through a system of superconducting detection coils which are connected to the SQUID with superconducting wires, allowing the current from the detection coils to inductively couple to the SQUID sensor. This configuration produces an output voltage which is proportional to the current flowing in the input coil. In the ring, a periodic critical current flows due to the interference effects of the electrons pairs wave function. In the superconductor loop, the circulating current can only have certain values. It means that a magnetic flux contained in the loop is quantized in units of the flux quantum

$$\Phi_0 = \frac{2\pi\eta}{2e} = 2 \text{ x}10^{-15} \text{ T/m}^2, \qquad (2.1)$$

where e is the absolute value of the electron charge. The current I flowing through a junction depends on the phase difference $\delta = \theta_2 - \theta_1$ in the two superconductor regions:

$$I = I_0 \sin\delta = I_0 \sin(\theta_2 - \theta_1) \qquad (2.2)$$

where I_0 is the critical current (maximum zero-voltage current) that can pass through the junction.

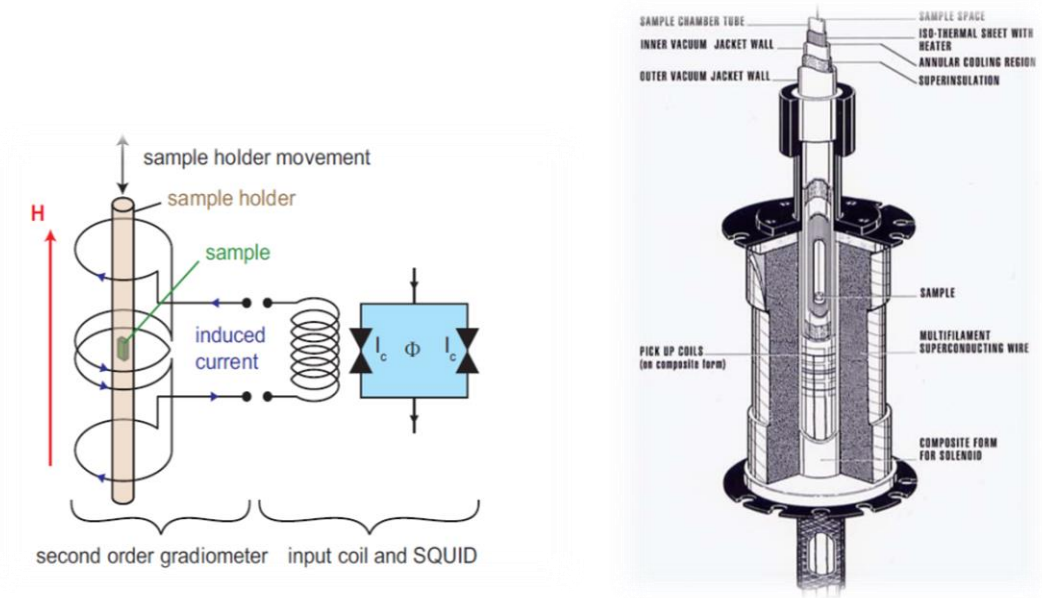

Figure 3: Characteristic configuration of a SQUID

Furthermore, in the presence of a voltage V between the electrodes, δ evolves with time t according to $\delta(t)=\delta(0)-\frac{2eVt}{\eta}$. The superconducting current is then given by the expression :

$$I = I_0 \sin\left[\delta(0)-\frac{2eVt}{\eta}\right] \qquad (2.3)$$

from where it is clear that the current oscillates with a frequency $\omega = 2eV/\hbar$. Equations (2) and (3) describe the static (direct current: DC) and dynamic (alternate current: AC) properties of a Josephson junctions, named DC and AC Josephson junctions respectively. The main part of SQUID magnetometer, is shown in the Figure 3.

2.3 Difference scanning calorimetry (DSC)

In this thesis differential scanning calorimetry[4] has been used in order to detect structural phase transitions in the sample of interest. The principle of the DSC, see Figure 4, is to measure the heat flow into the sample by the difference between it and the flow into an empty crucible reference, while scanning the temperature a constant rate.

Figure 4: Differential Scanning Calorimeter DSC131 (ILL) and on the left above the typical crucible where lodging the sample.

Depending on the type of transition, more or less heat must flow into the sample to keep it at the same temperature as the reference. From the observed difference in heat flow, differential scanning calorimeters can not only detect the transition temperature but also measure the amount of heat released (exothermic process) or absorbed (endothermic process) during a transition. The amount of sample necessary can be approximately from 1 to 200 mg and it is placed in alumina crucibles, designed to ensure thermal transfer between the sample and the sensor

2.4. Neutron Scattering Theory

2.4.1 Properties of Neutrons

A neutron is a subatomic particle, with no electric charge, with mass $m_n = 1.67493 \cdot 10^{-27}$ kg and a nuclear spin $S = {}^1/_2$ and with a lifetime of 880(1) s. Since they have a nuclear magnetic moment, expressed in nuclear magnetons: $\mu_n = -\gamma \mu_N \sigma = = -1.913 \mu_N$, where $\mu_N = \frac{e\hbar}{2m_p}$, with m_p representing the proton mass, they also respond to magnetic fields. Because, as mentioned before, they are electrically neutral, neutrons

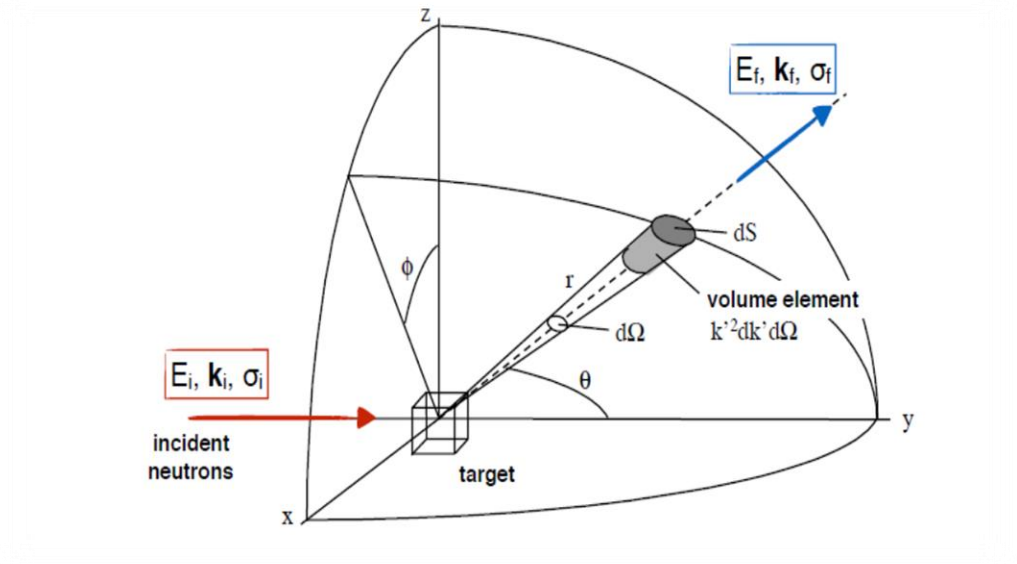

Figure 5: Diagram of the scattering process of neutrons by a target. Figure Taken from reference [8].

interact weakly and deeply with matter [5].The process that govern the interaction between neutrons and the matter is a difficult subject surely better described in many articles, manuscripts and books[5–8].The dual nature of neutrons permits to consider them as particles and as waves. It is conventional that the energy E of a neutron corresponds to a temperature T: $E = k_B T$ where k_B is the Boltzmann constant. The De Broglie

wavelength of a neutron is defined by $\lambda = \frac{h}{m_n v}$ so that the wave vector is defined as $\boldsymbol{k} = \frac{m}{\hbar}\boldsymbol{v}$.

2.4.2 The scattering Cross Section

The following is a brief description about the interaction between neutrons and a scattering system, the full details are reported in several books[5,7].

In an experiment, a neutron endowed with an initial wavevector $\boldsymbol{k}_i$, with initial energy E_i and initial spin σ_i is scattered by the sample into a small solid angle $d\Omega$ with final wavevector $\boldsymbol{k}_f$, final energy E_f and final spin σ_f as shown in Figure 5. The momentum transferred to the sample is $\hbar\boldsymbol{Q}$ where $\boldsymbol{Q}$ is the scattering wavevector defined as $\boldsymbol{Q} = \boldsymbol{k}_i - \boldsymbol{k}_f$, and $\hbar\omega$ is the energy of excitation of the sample defined as $\hbar\omega = E_i - E_f$. In the case of elastic scattering $\hbar\omega = 0$, in inelastic scattering neutrons gain or lose energy, and the conservation of this one is defined as $E_i - E_f = \hbar\omega = \frac{\hbar^2}{2m_n}\left(k_i^2 - k_f^2\right)$. In this process, the numbers of neutrons scattered into the solid angle $d\Omega$ are measured by a detector in a given direction per second as a function of their energy E.

The *partial differential cross section* is described by the following equation:

$$I_{scattered} = \frac{d^2\sigma}{d\Omega dE} = \frac{flux\ scattered\ into\ the\ solid\ angle\ d\Omega\ \text{with}\ E_f\ and\ E_f+dE_f}{initial\ flux\ onto\ the\ sample\ with\ energy\ E_i} \qquad (2.4)$$

Supposing that the energy of scattered neutron is not analysed but that just all the neutrons scattered in the solid angle $d\Omega$ are counted, to this expression corresponds the *differential cross section:*

$$\frac{d\sigma}{d\Omega} = \int \left(\frac{d^2\sigma}{d\Omega dE}\right) dE' = \left(\frac{m}{2\pi\hbar}\right)^2 \left|\langle \lambda_f \boldsymbol{k}_f | V | \lambda_i \boldsymbol{k}_i \rangle\right|^2 = |f(\Omega)|^2 \qquad (2.5)$$

Where $f(\Omega)$ is the so-called scattering amplitude and it depends on the kind of interaction potential: nuclear or magnetic.

The *total cross section* is defined by the equation:

$$\sigma_{tot} = \frac{total\ number\ of\ neutrons\ scattered\ per\ second}{\phi} \qquad (2.6)$$

where Φ is the flux of the incident neutrons. The Born approximation of neutron scattering supposes that the change of the incident neutron wave by scattering centre is almost negligible and can be treated as a perturbation. Considering this approximation, the differential scattering cross section, describing the ensemble of the process in which the scattering system changes from λ to λ' and the neutron state from $\boldsymbol{k}_i$ to $\boldsymbol{k}_f$, is derived from *Fermi's golden rule* , defining the *differential cross section* :

$$\left(\frac{d^2\sigma}{d\Omega dE}\right)_{\lambda_i \to \lambda_f} = \frac{k_f}{k_i}\left(\frac{m}{2\pi\hbar^2}\right)^2 \left|\langle \lambda_f \boldsymbol{k}_f | V | \lambda_i \boldsymbol{k}_i \rangle\right|^2 \delta\left(E_i - E_f + E_{\sigma_i} - E_{\sigma_f}\right) \tag{2.7}$$

The parameter V represents the scattering potential that is related to the type of interactions involved: with the nuclei of an atom and with the magnetic field generated by electrons. Using the *Fermi pseudo-potential* it is possible to describe the interaction between the neutron and the atomic nucleus and its potential can be modelled by delta function as following:

$$V(\boldsymbol{r}) = \frac{2\pi\hbar^2}{m_n} b_j \delta(\boldsymbol{r} - \boldsymbol{R}_j) \tag{2.8}$$

where $\mathbf{r}$ is the neutron position, $\boldsymbol{R}_j$ is the position of the scattering center j, and b_j is the scattering length that it depends on the respective element considered on the isotope and on the spin state of the nucleus, and where δ is a Dirac delta and m_n is the neutron's mass. The scattering amplitude of a neutron, due to the nuclei of the atoms, is related to the *Fourier transform* of the potential function and is given by:

$$f(\Omega) = \sum_i b_i \, e^{i\boldsymbol{Q}\cdot\boldsymbol{r}_i} \tag{2.9}$$

Where b_i and $\boldsymbol{r}_i$ are the scattering length and the position of the i nucleus respectively.

Consequently, the *differential cross-section* can be written as:

$$\frac{d\sigma}{d\Omega} = |f(\Omega)|^2 = \sum_{i,j} b_j^* b_i \, e^{\mathrm{i}\mathbf{Q}\cdot(\mathbf{r}_i - \mathbf{r}_j)} \tag{2.10}$$

In a periodic system, such that the atomic nuclei related by a lattice vector have the same value of the scattering length, the scattering cross section is non-zero only for values of the scattering vectors equal to a reciprocal scattering vector.

2.4.3 The Neutron Coherent Elastic Scattering Cross Section

The differential cross section is composed of a *coherent* and *incoherent* part.

$$\left(\frac{d^2\sigma}{d\Omega dE}\right)_N = \left(\frac{d^2\sigma}{d\Omega dE}\right)_N^{Coh} + \left(\frac{d^2\sigma}{d\Omega dE}\right)_N^{Incoh} \tag{2.11}$$

In the *coherent* scattering neutron waves, scattered from different nuclei, interfere with each other. The nature of the coherent scattering depends on the distances between atoms and from $\boldsymbol{Q}$ scattering vector. The equilibrium of a structure is described by the Elastic *coherent* scattering ($E = 0$) whereas inelastic coherent scattering ($E \neq 0$) provides information about the collective motions of the atoms. In the *incoherent* scattering, there is no interference between waves scattered by different nuclei. In fact, the intensities scattered from each nucleus add up independently. It is possible to describe the *incoherent* scattering, as for the coherent one, in *incoherent elastic* scattering which results to be in all directions the same while the *incoherent inelastic* scattering is given by the interaction of a neutron with the same atom at different positions and different times, thus providing information about atomic diffusion. The *differential cross-section* decomposed in coherent and incoherent components has this form:

$$\left(\frac{d\sigma}{d\Omega}\right)_{Coh} = N\frac{(2\pi)^2}{v_0}\sum_{\boldsymbol{\tau}}(\boldsymbol{Q}-\boldsymbol{\tau})\,|F_N(\tau)|^2 \tag{2.12}$$

$$\left(\frac{d\sigma}{d\Omega}\right)_{incoh} = N\sum_d\{\overline{b_d^2} - \bar{b}_d^2\} \tag{2.13}$$

Where $\boldsymbol{\tau}$ represents a reciprocal lattice vector, d is the index of an atom in the unit cell; v_0 is the unit cell volume and F_N is the nuclear structure factor:

$$F_N(\boldsymbol{\tau}) = \sum_d \bar{b}_d e^{-i\boldsymbol{\tau}\cdot\boldsymbol{r}_d} \tag{2.14}$$

The intensity peaks of the coherent scattering are the so-called Bragg peaks. The Bragg law and the diffraction method is described in the paragraph 2.5.

2.4.4 Magnetic contribution

Until now, the discussion focused on the interactions among neutrons and atomic nuclei. Nonetheless, as mentioned before, it exists another interaction between neutrons and matter that results from the fact the neutron spins ($\boldsymbol{\sigma}$) are sensitive to magnetic field ($\boldsymbol{H}$) produced by unpaired electrons, because they possess a magnetic dipole moment. One difference between the two types of scattering, however, is that the magnetic interaction, unlike the nuclear interaction is not isotropic. For neutrons, the dipolar nature of the magnetic interaction means that only the component of the sample's magnetization that is perpendicular to the scattering vector $\boldsymbol{Q}$, is effective in scattering neutrons. The dipole moment of a neutron is given by:

$$\mu_n = -\gamma \mu_N \boldsymbol{\sigma} \tag{2.15}$$

where μ_N represents the nuclear magneton, γ is a numerical constant and σ is *Pauli* spin operator which has eigenvalues ±1. The interaction potential between the neutrons and the local magnetic field from the unpaired electrons, is given by using:

$$V_m(\boldsymbol{r}) = -\boldsymbol{\mu}_n \cdot \boldsymbol{H} = \gamma \mu_N \boldsymbol{\sigma} \cdot \boldsymbol{H} \tag{2.16}$$

The magnetic field generated by a system in which *n* electrons at $\boldsymbol{r}$ positions with a spin $\boldsymbol{s}$ is described as:

$$\boldsymbol{H}(\boldsymbol{r}) = \sum_i^n \nabla \times \left\{ \frac{-2\mu_B \boldsymbol{s_i} \times \boldsymbol{R_i}}{\boldsymbol{R_i^3}} \right\} - \frac{2\mu_B}{\hbar} \frac{\boldsymbol{p} \times \boldsymbol{R}}{\boldsymbol{R_i^3}} \tag{2.17}$$

Where $\boldsymbol{R} = \boldsymbol{r} - \boldsymbol{r_i}$ and μ_B is the Bohr Magneton.

At this point is essential to define the spin and orbital magnetization densities $\mathbf{M_S}(\mathbf{r})$ and $\mathbf{M_L}(\mathbf{r})$ respectively as:

$$\boldsymbol{M_S}(\boldsymbol{r}) = -2\mu_B \sum_i^n \boldsymbol{s} \delta\,(\boldsymbol{r} - \boldsymbol{r_i}) \tag{2.18}$$

$$\boldsymbol{\nabla} \times \boldsymbol{M_L}(\boldsymbol{r}) = -\frac{e}{m_0 c} \sum_i^n \boldsymbol{p_i} \delta\,(\boldsymbol{r} - \boldsymbol{r_i}) \tag{2.19}$$

Therefore the expression of the total magnetization density $\mathbf{M}(\mathbf{r})$ is:

$$\boldsymbol{M}\,(\boldsymbol{r}) = \boldsymbol{M_S}(\boldsymbol{r}) + \boldsymbol{M_L}(\boldsymbol{r}) \tag{2.20}$$

The diffusion amplitude, considering the case of neutron diffraction by magnetic field generated by electrons, is given as following:

$$f(\Omega) = \langle \sigma | \boldsymbol{\sigma} \cdot \boldsymbol{F}_{\boldsymbol{M}\perp}(\boldsymbol{KQ}) | \sigma' \rangle \tag{2.21}$$

Where $\boldsymbol{F}_{\boldsymbol{M}}(\boldsymbol{Q})$ is the magnetic structure factor, the Fourier transform of magnetization and ⊥ represents the component perpendicular to the scattering vector $\boldsymbol{Q}$**:**

$$\boldsymbol{F}_{M}(\boldsymbol{Q}) = p \sum_i \boldsymbol{M}_i e^{i\boldsymbol{Q}\cdot\boldsymbol{r}_i} e^{-Wi} \tag{2.22}$$

where p is a constant ($2.696\ 10^{-13}$ cm/μ_B)

2.4.4.1 The magnetic propagation vector

The magnetic structure does not automatically have the same periodicity and symmetry as its associated crystal structure (see Figure 6). The relation between a magnetic moment and its equivalent in the unit cell is expressed by the propagation or wave vector **k**:

$$\boldsymbol{m}_{\boldsymbol{jl}} = \sum_{\boldsymbol{k}} \boldsymbol{m}_j^k e^{i\boldsymbol{kl}} \tag{2.23}$$

where j means an atom of the nuclear unit cell and $\boldsymbol{l}$ is a lattice vector.

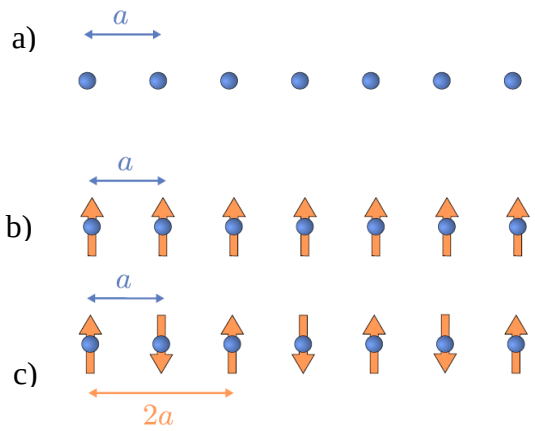

Figure 6: From above a) It represents the crystal periodicity, b)It is an example in which magnetic periodicity coincide with nuclear unit cell (**k** = 0), c) The magnetic periodicity is two times the nuclear one: **k** = (1/2).

The magnetic cross section is equivalent to the expression given in the equation (2.12) and is expressed as following:

$$\left(\frac{d\sigma}{d\Omega}\right) = N\frac{(2\pi)^2}{v_0}\sum_{\boldsymbol{k}} \sum_{\boldsymbol{\tau}} \delta(\boldsymbol{Q} - \boldsymbol{k} - \boldsymbol{\tau}) \left|\langle \sigma | \boldsymbol{\sigma} \cdot \boldsymbol{F}_{M\perp}(\boldsymbol{Q}) | \sigma' \rangle\right|^2 \tag{2.24}$$

2.5 Diffraction Method

The simplest type of *coherent* scattering to understand is ***diffraction***, which represents also the main neutron and X-ray technique employed for the study of the compounds investigated in this thesis. Neutron and X-ray scattering are an important source of information for the study of the crystal and magnetic structure of a sample. The basic principle of diffraction techniques is the same for neutrons and X-rays (shown schematically in Figure 5, but due to their different scattering properties neutrons and X-rays provide complementary information X-ray scattering factor, *f*, of an atom is quite different to the neutron scattering factor, *b*, of the same atom (see Figure 7). The reason is that X-ray diffraction results from scattering by the electrons of an atom while neutron (non-magnetic) diffraction is due to scattering from the nucleus of an atom[9]. The contribution to the diffracted X-ray intensity is thus dependent on the atomic number *(Z)* and is consequently larger for atoms with larger *Z*. Neutrons, on the other hand, interact directly with the nucleus of the atoms, and the contribution to the diffracted intensity is determined by the nature of the isotope; for example, hydrogen and deuterium contribute differently because the neutron scattering lengths of H is b_H = -3.7406(11) fm whereas that one of D is b_D = 6.671(4) fm.

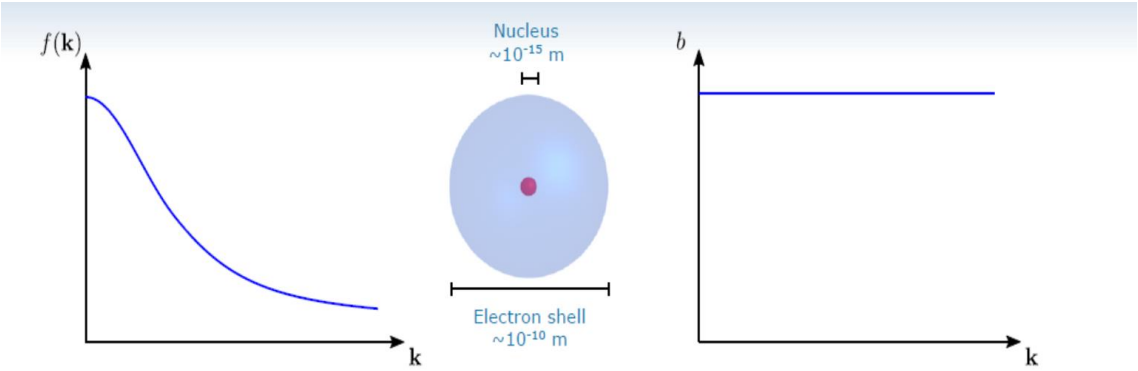

Figure 7: The amplitude of the scattered wave (the Fourier transform of the potential function) is called the atomic **form factor** f (X-rays) or **scattering length** b (neutrons).

H and D respectively, have opposite sign, and consequently they can be distinguished by neutron diffraction. In general, it is desirable to work with a moderately concentration of H atoms in a sample, as the H-nuclei scattering has a large incoherent component, contributing to a large continuous background.

One advantage of neutron diffraction over X-ray diffraction is that the second one is rather unaffected by the presence of the hydrogen atoms in a structure, whereas the nuclei of ^{1}H and D and its thermal motions, can be determined in a crystal with greater precision by neutron diffraction because they have a greater scattering power.

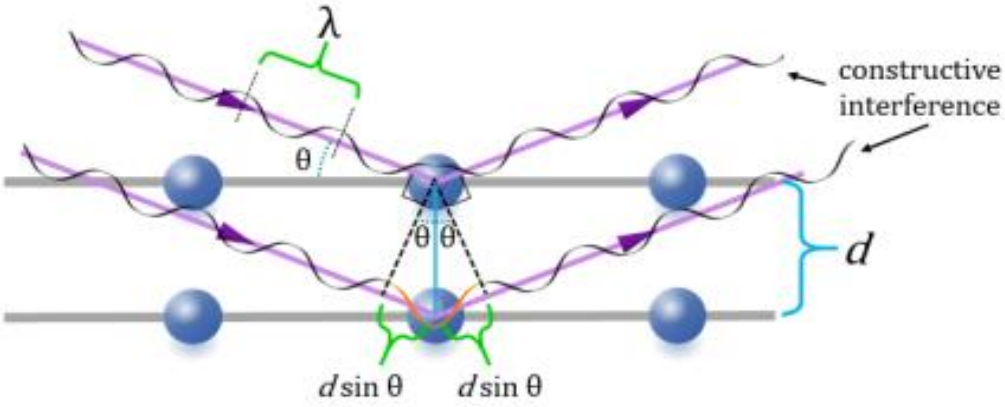

Figure 8: Diffraction phenomenon occurring when a wave interact with the matter according with the Bragg's law.

During diffraction experiments, only the elastic part ($\hbar\omega = E_i - E_f$) of the scattering cross section is taken in account. The elastic pattern typically consists of sharp Bragg reflections if the sample is crystalline. A diffraction experiment is realized according to *Bragg's law*[5], (see Figure 8). The Bragg law is a consequence of the Laue condition for periodic systems: a beam is diffracted only when the scattering vector is proportional to a reciprocal lattice vector, $\boldsymbol{Q} = \boldsymbol{\tau} = 2\pi\,\mathbf{h}$. The reciprocal lattice vector coordinates $\mathbf{h} = (hkl)$ (Miller indices) is always perpendicular to the lattice planes with spacing $d_{hkl} = 1/|\mathbf{h}|$, from the geometry of the scattering it is easily deduced that:

$$\lambda = 2d_{hkl}sin\theta \qquad (2.25)$$

This law can also be deduced considering that, the incident radiation is "reflected" selectively by the lattice planes as explained in the next paragraph. A monochromatic neutron beam with incident wavelength $\lambda = \frac{2\pi}{k_i}$, with k_i the modulus of the incident wavevector, is directed on lattice atoms, arranged in lattice planes, with distance, $d = \frac{2\pi}{Q}$, the diffracted beams with wave vector k_f interfere with each other constructively or destructively, so that only when the incident angle with respect to the planes θ verifies the Bragg law (2.25) the interference is constructive (see Figure 9).

Each time that the condition of the equation 2.25 is matched a so-called Bragg peak appears. The intensity of each of these peaks depends on the scattering power of the atoms in the unit cell, each peak is characterized by the scattering vector $\boldsymbol{Q} = 2\pi\ \mathbf{h}$ with components 2π (hkl). In the case of X-Rays, electrons orbiting the nucleus are scattered, so heavier atoms are those who scatter the most. Such intensity (I_{hkl}) can be shown to be proportional to the structure factor F_{hkl}, which is the Fourier transform of the unit cell scattering potential:

$$I_{hkl} \propto |F_{hkl}|^2 = \sum_{j=1}^{N} f_j e^{i2\pi(hx_j+ky_j+lz_j)} \text{ (for X-rays)} \qquad (2.26)$$

$$I_{hkl} \propto |F_{hkl}|^2 = \sum_{j=1}^{N} b_j e^{i2\pi(hx_j+ky_j+lz_j)} \text{ (for Neutrons)} \qquad (2.27)$$

where x_j, y_j and z_j represent the atomic positions of the j^{th} atom, f_j its atomic scattering factor (or b_j the scattering length).

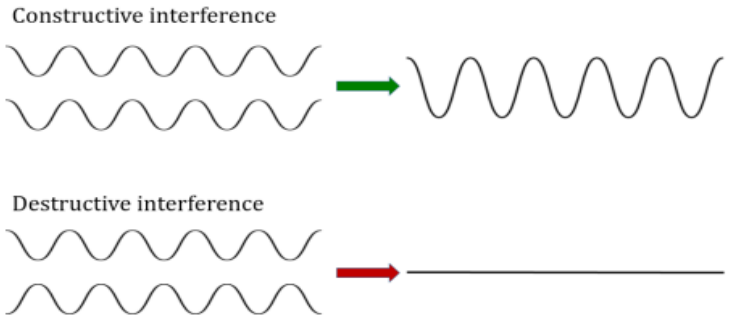

Figure 9 : If two waves that are in phase, then they experience constructive interference and result in one wave of a larger amplitude. If two waves are out of phase, then they destructively interfere and cancel out.

2.5.1 Neutron and X-Ray Synchrotron sources

While the Synchrotron radiation sources used, in order to evaluate the structural model and properties, are the *SOLEIL* Synchrotron (Paris), the *ALBA* Synchrotron (Barcelona), and the *ESRF* Synchrotron (Grenoble). Neutron scattering and synchrotron radiation are complementary methods for the investigation of structure and dynamics of condensed matter. But, the typical specificity of neutrons are the localization of light elements, isotopic substitution and the distinction between neighbouring elements in the periodic table.

A brief description of the instruments and beam lines is the theme of the following section. Two kind of techniques have been employed during this thesis project: single crystal and powder diffraction. Below, a brief description of the used instruments is reported.

2.6 Single crystal neutron diffractometers used at ILL facility

2.6.1 D9 Diffractometer

The instrument D9 is a four-circle diffractometer[10] located at the Instiut Laue Langevin, used for the measurement of single crystal samples, (see Figure 10). It is used for accurate and precise measurements of Bragg intensities up to very high momentum transfer. The sample is placed in an Eulerian cradle as shown in the Figure 10 and, in order to orient it, it is possible to rotate the three angles of the Eulerian cradle.

Due to the availability of short wavelengths, the instrument is suited for high-resolution structure determination because a large volume of reciprocal space can be explored. The wavelength can be chosen between 0.25 and 0.85 Å. The monochromator is a Cu crystal in transmission geometry using the (220) planes. The detector covers 32 x 32 pixels, and records the intensity of the diffracted beam of the selected Bragg reflection in relation with the sample rotation around the vertical axis. One Bragg reflection measurement typically takes a few minutes, and recording of a full set of data a few days.

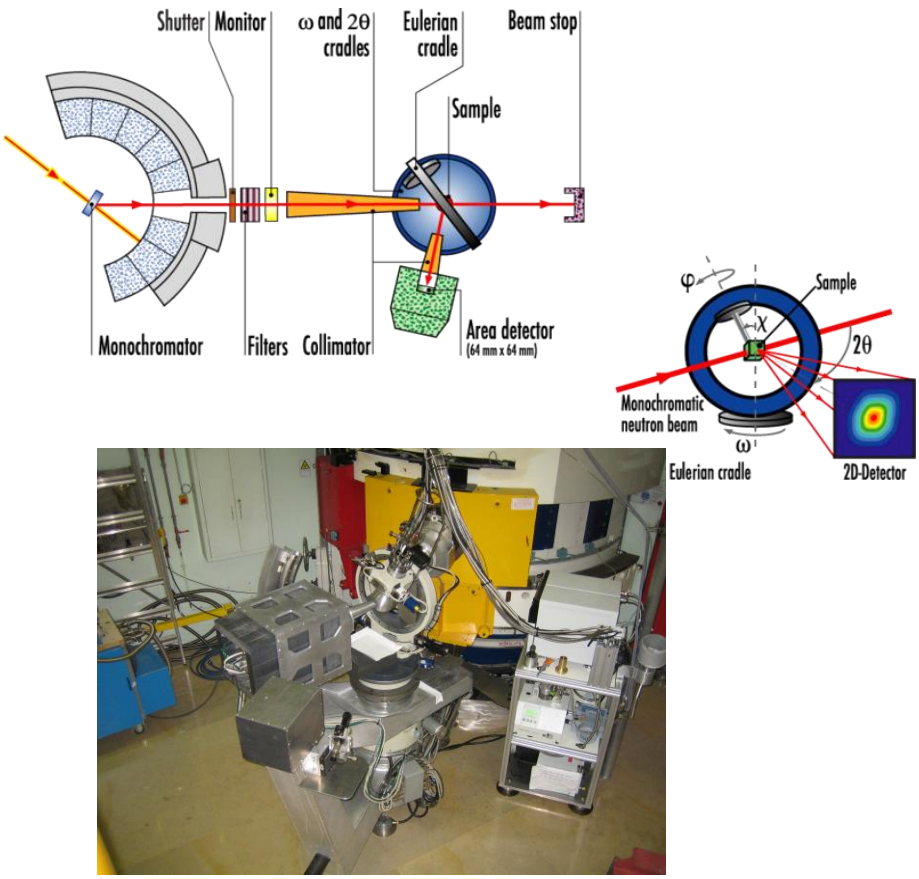

Figure 10: The D9 four-circle diffractometer geometry at ILL neutron hot source.

2.6.2 D19 Diffractometer

D19 is a single-crystal and fibre diffractometer, which incorporates a very large (120° x 30°) position-sensitive detector (PSD), and works best in the wavelength range 0.8 to 2.4 Å, (see Figure 11). D19 works most efficiently for unit cell volumes between 1000 and 100,000 $Å^3$ i.e. cell edges from say 10 to 50 Å. Experiments requiring wavelengths below 0.8 Å are best performed on the hot-source D9 diffractometer, unless D19's large PSD is required. D19 shares the H11 thermal beam tube with the two powder diffractometers D2B and D20. Important features of D19 are:

- D19 "sees" the neutrons first (from part of the H11 beam tube: diameter 20 cm at the core end),
- the D19 monochromator position is relatively close to the core giving high flux, and also has high resolution due to a maximum monochromator take-off angle of 90°,

- any one of four monochromators may be rotated into diffracting position using an ILL box-shaped monochromator mount so that the wavelength choice can be matched to the user's sample.

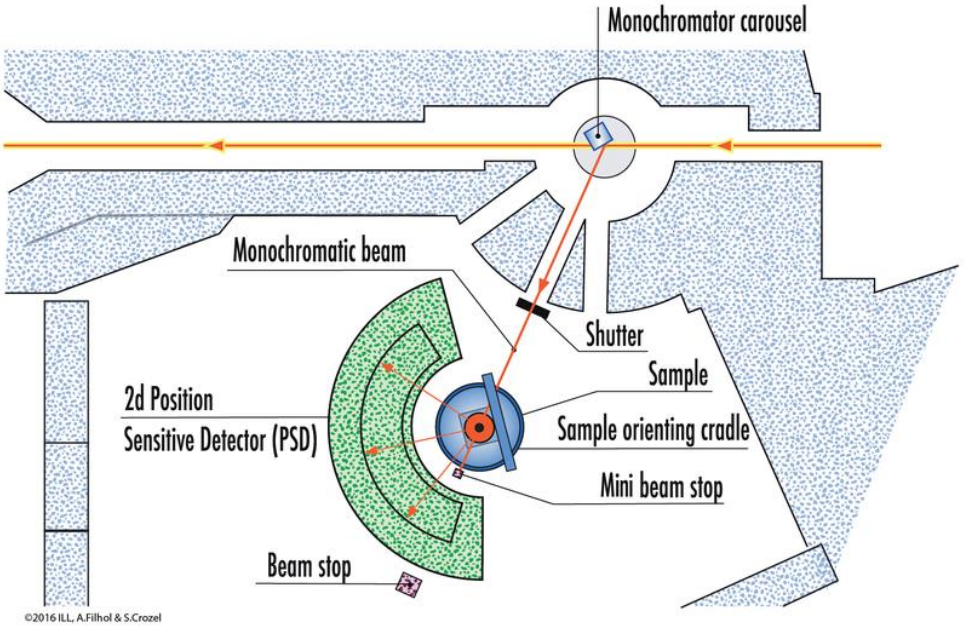

Figure 11: D19 diffractometer in a schematic view.

The horizontally mounted "banana" detector is set symmetrically about the equatorial plane, with the sample at the centre of horizontal curvature. The detector rotates on a gamma-arm ($\gamma = 2\theta$ in the equatorial plane), on air cushions. The present sample orienter is a C-shaped Eulerian cradle with offset phi axis. This allows a larger range in omega than a conventional cradle, and easy installation of a compact 2-stage Displex which can cool below 2 K. Installation of a kappa cradle is planned to further reduce blind regions.

2.7 Powder neutron diffractometers used at *ILL* facility

2.7.1 D1B Diffractometer

D1B is a medium resolution high-flux powder diffractometer[11] (see Figure 12). It is an instrument suitable for exploring a large variety of polycrystalline materials but it is especially designed for magnetic structural studies[12]. The high-flux instrument optimization results in high-resolution loss at high Q. With such instrumental design, fixed take-off angle at $2\theta_m = 44.22^o$, the best resolution (sharper peaks) is obtained at angles close to $2\theta_m$. In recent years[11], some technological updating of the instrument, like

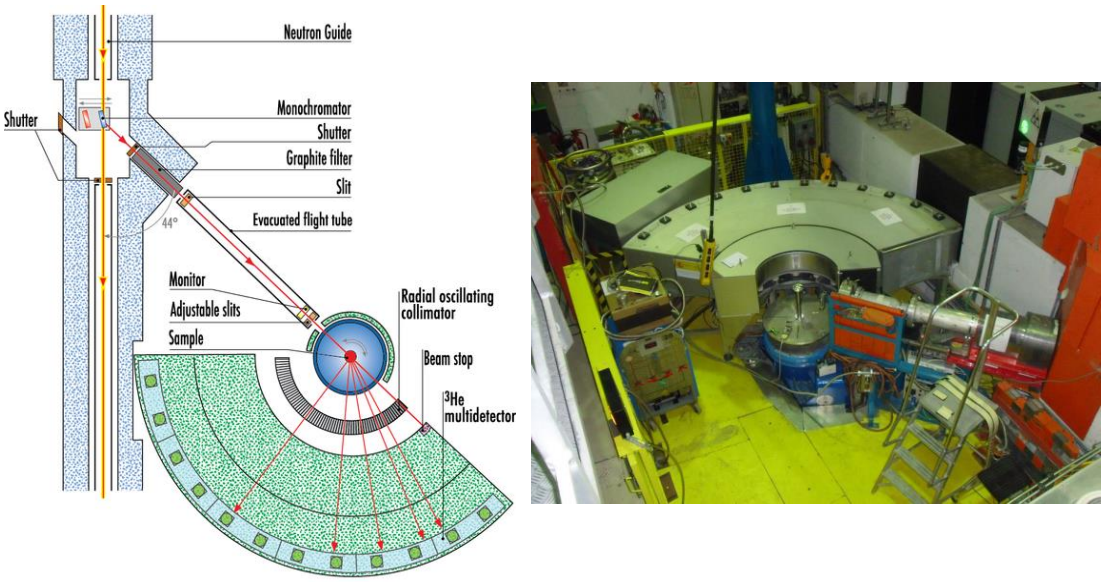

Figure 12: D1B high flux powder diffractometer at ILL.

a new position sensitive detector (PSD) and a radial oscillating collimator (ROC) have made it an even more valuable tool. The detector covers an angular range of 128º and is made of 1280 gold wires providing a neutron detection point every 0.1º. The ROC instead, is made of 198 gadolinium-based absorbing collimation blades. The polychromatic beam from the thermal guide H22 is diffracted by the monochromator at a take-off angle of 44.22º. Three pyrolytic graphite (HOPG) monochromators focusing onto the sample position provide a flux of $6.5 \cdot 10^6$ n $cm^{-2}s^{-1}$ and a wavelength of 2.52 Å which is the most often used for the experiments on magnetic structures. A second wavelength with = 1.28 Å, giving rise to a higher Q-range for refining crystal structures, is available by using a germanium monochromator; however the neutron flux at the sample position is ten times lower. D1B offers different conditions and setups for carrying out the experiments: there are an orange cryostat (2 K< T <300 K) with a vanadium tail of ϕ =24 mm, a furnace (T <1000 ºC) with a vanadium resistor ϕ=50mm and a 4-circle Eulerian cradle goniometer. D1B is especially designed for having low background, which permits to observe small intensities scattered by the sample. Other sample environments are cryomagnets, pressure cells, dilution cryostats etc. A great number of experiments performed on D1B concern the determination of magnetic structures; nevertheless, for its characteristics it is possible to investigate a different variety of scientific problems as for example the in “situ” studies. Collecting a diffraction pattern with sufficient statistics in few minutes is one of the advantage (1-5 min) of this

instrument. The D1B's data are reduced and analysed, with LAMP[13] or the FullProf suite[14] software.

2.7.2 D2B Diffractometer

D2B is a high-resolution powder diffractometer[15] designed to achieve optimal resolution ($\Delta d/d = 5 \cdot 10^{-4}$). The definition "high-resolution" refers to the fact that the instrumental resolution function results in narrow peaks at high scattering angle (see Figure 13).

This is achieved by a large monochromator take-off angle as shown in the Figure 13, which is specifically for this instrument 135°. The angular range is $5° < 2\theta < 165°$. A typical experiment is made by filling a vanadium cylindrical container (cans of diameter 6.5 mm or higher) with the powder to be measured; it is possible to measure very small quantity of sample like about 200 mg.

A complete diffraction pattern is obtained after about 25 steps of 0.05° in 2θ, since the 128 detectors are spaced at 1.25° intervals. Such scans take typically 30 minutes; and they are repeated to improve statistics. Wavelengths can easily be changed under computer control since they are changed by a simple rotation of the Ge-monochromator making accessible the (*hhl*) Ge-reflections. D2B was also designed for working on magnetism and high resolution at large *d*-spacings using wavelengths between 2.4 Å and 6 Å.

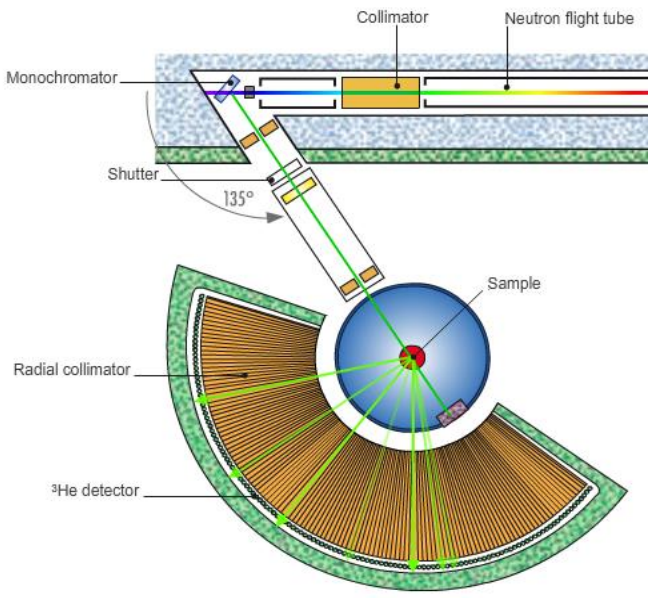

Figure 13*:* D2B high-resolution powder diffractometer at ILL.

For accessing the reciprocal space at high *Q*, suitable for crystal structure refinement, it is needed to use a short wavelength as 1.59 Å (optimal wavelength).

2.8 Powder diffractometer at the ALBA Synchrotron

Some of synchrotron radiation XRPD measurements in this thesis were carried out at the Materials Science Powder Diffraction (MSPD) beamline at ALBA[16] synchrotron facility in Cerdanyola del Valles, Barcelona (see Figure 14). The setup of the beamline in our experimental case has been the following: the experiments were carried out using an Oxford nitrogen cryostream 700 working from RT down to 80 K and the helium-based cryostat from 130 down to 25 K temperature range. Below 80 K, data were collected with

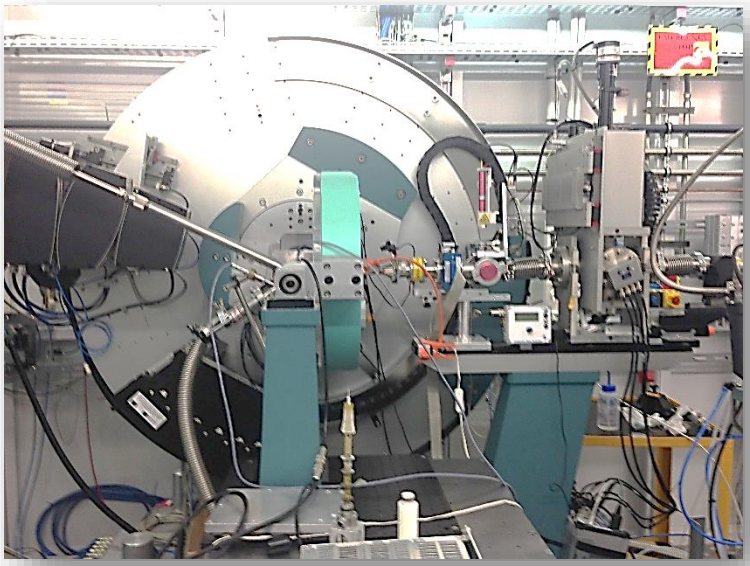

Figure 14: Materials Science Powder Diffraction (MSPD) diffractometer at ALBA.

a MAD detector plus an analyser crystal at λ= 0.4948 Å, in the 5°- 50° 2θ angular range (energy resolution of 5 KeV). This combination implies a long acquisition time but it permits to improve the quality of the data and the resolution, in order to obtain patterns with enough statistics suitable for structure solution and refinement. Moreover, with a wavelength of 0.4948 Å, we obtained a good compromise between instrumental resolution, data completeness and the overlapping of neighboring reflections. From RT down to 80K, the data acquisitions (time ca. 30 minutes) were carried out using the sample environment set-up provided by a MYTHEN detector since it opens a ≈ 40 angular 2θ range. This setup allows faster data acquisition with very good statistics and angular resolution.

2.9 Single crystal diffractometer at the SOLEIL Synchrotron

Synchrotron radiation experiments were also carried out at the CRISTAL beamline of the SOLEIL[17] synchrotron in Saint-Aubin (Paris) (see Figure 15). CRISTAL is a high performance undulator-based beam line dedicated to single crystals and powders between 4 and 30 keV. Our experiment was performed using single crystal samples measured in the 4-circle diffractometer, using the Kappa goniometer-geometry, allowing an easy, fast and precise data collection.

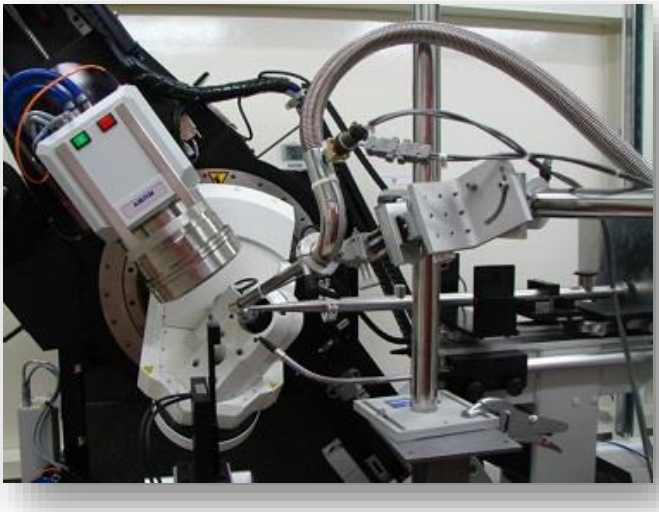

Figure 15: CRYSTAL diffractometer at the Synchrotron of SOLEIL.

The range of energy chosen for our case it was between 15 and 22 KeV with λ= 0.66951 Å in order to obtain high quality data. The diffraction patterns were measured using the oscillation method: for each image acquisition, the diffraction signal is measured while the sample is rotating at constant speed over a small angular range. Data collection were acquired with an Agilent 2D CCD detector consisting of 1024 x 1024 pixels, 13x13 μm^2 pixel size. In order to perform low temperature measurements a helium-based cryostream was used. For indexing and integrating the recorded data the CysAlis PRO software program was used.

Bibliography

(1) Swithenby, S. J. *J. Phys. [E]* **1980**, *13* (8), 801.

(2) SQUID Magnetometer and Josephson Junctions http://hyperphysics.phy-astr.gsu.edu/hbase/Solids/Squid.html.

(3) SQUID Magnetometer and Josephson Junctions (II) http://hyperphysics.phy-astr.gsu.edu/hbase/Solids/Squid2.html.

(4) Mihalik jr., M.; Mihalik, M.; Fitta, M.; Vavra, M.; Zentková, M.; Vilarinho, R.; Mota, D. A.; Tavares, P.; Moreira, J. A.; Almeida, A. *J. Phys. Conf. Ser.* **2015**, *592* (1), 012119.

(5) Squires, G. L. *Introduction to the Theory of Thermal Neutron Scattering*; Cambridge University Press, 2012.

(6) Schober, H. *J. Neutron Res.* **2014**, *17* (3–4), 109.

(7) Lovesey, S. W. *Theory of Neutron Scattering from Condensed Matter: Volume II: Polarization Effects and Magnetic Scattering*; International Series of Monographs on Physics; Oxford University Press: Oxford, New York, 1986.

(8) Lefrançois, E. Synthesis and study of iridium oxide compounds for entangled spin-orbit physics, UNIVERSITÉ GRENOBLE ALPES: Grenoble, 2016.

(9) Properties of the Neutron http://pd.chem.ucl.ac.uk/pdnn/inst3/neutrons.htm.

(10) ILL. D9-Four circle,single crystal diffractometer https://www.ill.eu/instruments-support/instruments-groups/instruments/d9/characteristics/.

(11) Orench, I. P.; Clergeau, J. F.; Martínez, S.; Olmos, M.; Fabelo, O.; Campo, J. *J. Phys. Conf. Ser.* **2014**, *549* (1), 012003.

(12) ILL. D1B-Powder diffractometer https://www.ill.eu/instruments-support/instruments-groups/instruments/d1b/description/instrument-layout/.

(13) LAMP, the Large Array Manipulation Program. https://www.ill.eu/instruments-support/computing-for-science/cs-software/all-software/lamp/.

(14) Rodríguez-Carvajal, J. *Phys. B Condens. Matter* **1993**, *192* (1), 55.

(15) ILL. D2B-High resolution diffractometer https://www.ill.eu/instruments-support/instruments-groups/instruments/d2b/description/instrument-layout/.

(16) ALBA Synchrotron. MSPD-BEAMLINE INFORMATION https://www.cells.es/en/beamlines/bl04-mspd.

(17) SOLEIL, French national synchrotron facility. CRISTAL, beam line https://www.synchrotron-soleil.fr/en/beamlines/cristal.

Chapter 3

Heterometallic compounds of the mixed-valence metal-formate

Introduction

This chapter enters into the heart of the experimental study carried out during the work of this thesis and it provides a deep description about the results of the investigation realized on different compounds belonging to the $[(CH_3)_2NH_2][Fe^{III}M^{II}(HCOO)_6]$ family. This family is a particular case of MOF compounds described in the first chapter of this document. Here we modify the framework that is constituted by metal-formate anions conserving the counterion formed by dimethylammonium and we study the $Fe^{III}Fe^{II}$ compound replacing the counterion by ethylammonium.

Neutrons in combination with synchrotron X-Ray diffraction have proved to be an important tool to determine the nuclear and the magnetic structures and consequently the physical properties of these heterometallic compounds.

Of the first-row transition metals, iron possesses a particular appealing due to its coordination chemistry, multivalence states and redox behaviour, which made it the ideal candidate for synthesizing such heterometallic compounds with interesting magnetic properties accompanied by order-disorder phase transition[1–4]. In the wake of enthusiasm for the results obtained by *Hagen et al.*[1], where the mixed-valence framework $[(CH_3)_2NH_2][Fe^{III}Fe^{II}(HCOO)_6]$ (**1**) was explored and characterized, along this chapter we are going to explore the substitution of the divalent ion into the $[Fe^{III}Fe^{II}(HCOO)_6]^-$ network. Therefore, hereafter we will present the synthesis and physical characterization of the bimetallic $Fe^{III}M^{II}$ series.

The strategy was replacing the divalent iron with others divalent metals of the fourth row in the periodic table, in order to obtain isostructural compounds that they might exhibit close or similar properties of compound **1**. This study is based on the investigation of the nuclear and magnetic structures of the $[(CH_3)_2NH_2][Fe^{III}M^{II}(HCOO)_6]$ compounds where M^{II} is Co^{II} (**2**), Mn^{II} (**3**), Ni^{II} (**4**) and Mg^{II} (**5**). It deserves to be noted that the latter element Mg^{II} is not a fourth row transition metal, but the earth alkaline metal in the third row of the periodic system. However, the diamagnetic behaviour of this ion will be help us to obtain a better understanding of the full series. Through this study, the prefixed aim has been to improve the understanding of the physical properties of these molecular materials.

The obtained results will be presented and discussed by comparison with the earliest example reported[1–6]. Finally, to investigate the influence of the counterions in the physical properties of these compounds, we have prepared and characterized the mixed valence $[CH_3CH_2NH_3][Fe^{III}Fe^{II}(HCOO)_6]$ formate compound (**6**) in which the dimethylammonium cation was substituted by the ethylammonium , a similar counterions with three non-hydrogen atoms. Compound **6** has in common with its analogue compound **1,** the fact of exhibiting large negative magnetization, but contrary to compound **1**, this compound does not show any structural phase transition. Therefore, a detailed structure characterization is needed in order to identify the differences.

3.1 Overview of the $[(CH_3)_2NH_2][Fe^{III}M^{II}(HCOO)_6]$family

In the $[(CH_3)_2NH_2][Fe^{III}M^{II}(HCOO)_6]$ compounds the metal ions and the bridging ligands favour a niccolite-like structure arrangement, generally represented by the nickel-arsenide (NiAs) mineral Figure 1. In this array, the nickel atoms occupy the octahedral sites while the arsenic atoms are disposed in a distorted hexagonal close-packed structure where each As atom lies at the centre of a trigonal prism made of Ni atoms[7]. From a topological point of view, all compounds assuming similar topology are referred to this archetype of solids. This is the reason why this series of compound are termed as niccolite-like.

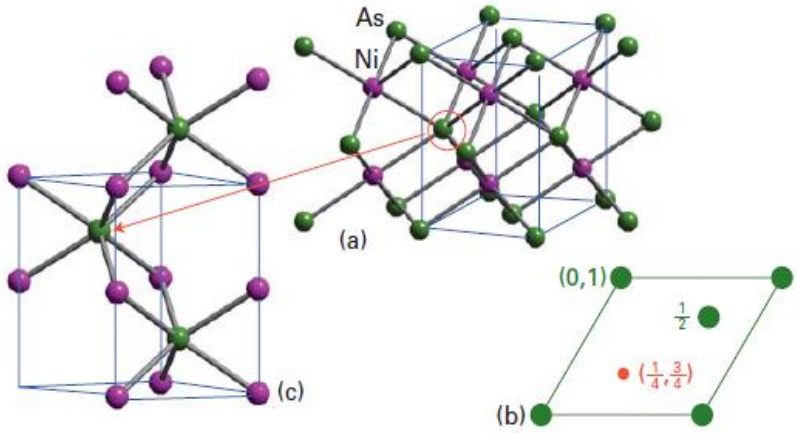

Figure 1: (a) The nickel-arsenide structure, (b) the projection representation of the unit cell, and (c) the trigonal prismatic coordination around As. Figure obtained from reference[7].

The construction of the $[(CH_3)_2NH_2][Fe^{III}M^{II}(HCOO)_6]$ compounds can be described as an anionic formate framework, in which two metals have divalent and trivalent state, balanced by the presence of a counterion, in this case dimethylammonium cation. The counterions can influence the formation of the framework. For example, the counterions can modify the framework due to the size effects or by charge balance due to the different

protonation state of the selected counterion, finally the weak interactions play also an important role. Van der Waals or hydrogen bond network can induce or preclude the occurrence of a particular phase.

The chemical nature of the formate ligand $(HCOO)^-$ plays a double role. Due to the reduced size, it is able to mediate the magnetic exchange interaction between the metal centres. Moreover, the rigidity of the formate ligand, the smallest and simplest carboxylate, gives rise to well-known coordination modes, and therefore help to do a rational design of the metal-organic framework. The coordination modes that the formate ligands can assume are: *syn−syn, anti−anti* or *syn−anti*[8,9], as shown in Figure 2.

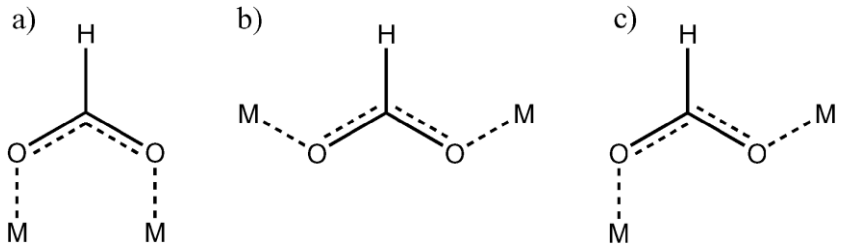

Figure 2: Possible coordination modes of the formate anion: a) *syn–syn*, b) *anti–anti* and c) *syn–anti*. Figure obtained from [8].

In the last ten years[1,9], the formate started to attract the interest of the scientific community in the synthesis of magnetic MOFs, resulting in a very good replacement of the more studied ligands as cyanide[10], azide[11], oxalate[12], and also acetate[13].

Different metal-formate frameworks topologies are reported[9]. A simple identification of the topology of the 3d periodic nets of MOFs is provided by three-letter symbols of the Reticular Chemistry Structure Resource (RCSR) database. In case of the perovskite like structures, the framework can be described as a **pcu** net (primitive cubic topology), a six-connected net based on a primitive cubic packing. The niccolite like structures, adopting the classical inorganic NiAs structure, are also forming a six-connected net. Its three-letter symbol in the RCSR database is **nia** (nickel arsenide topology). Other possibilities to describe 3d periodic nets are the Vertex Symbol (VS) and the Point Symbol (PS), both of which are often improperly termed as Schläfli Symbols. Listing the rules for deriving the symbols goes beyond the scope of the introductory part of this thesis, for more details can be useful to consult the article by V. A. Blatov , M. O'Keeffe and D. M. Proserpio[9a].

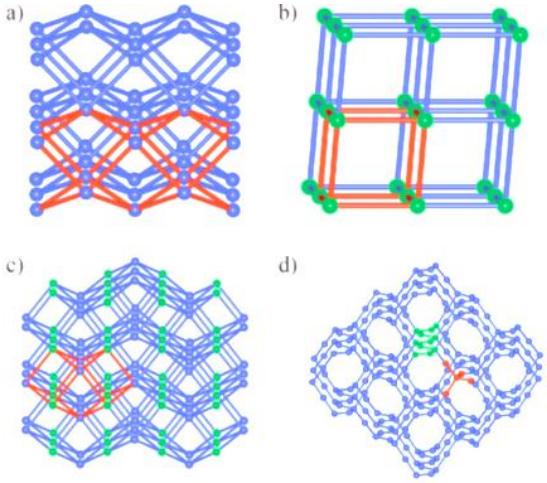

Figure 3: Representation of the topologies of metal nodes *a)* ($4^9\,6^6$) network of $[NH_4][M^{II}(HCOO)_3]$ b) ($4^{12}\,6^3$) network of $[(CH_3)_2NH_2][M^{II}(HCOO)_3]$, c) ($4^{12}\,6^3$) ($4^9\,6^6$) Network of $[(CH_3)_2NH_2][Fe^{III}M^{II}(HCOO)_6]$ and d) 6^6 network of $[M^{II}{}_3(HCOO)_6]$. The connection is highlighted and enclosed by red sticks, with green spheres ($4^{12}\,6^3$) nodes and blue spheres ($4^9\,6^6$) nodes. Figure obtained from reference [9].

For example in the chiral multiferroic compound $[NH_4][M^{II}(HCOO)_3]$ is observed a $(4^9 \cdot 6^6)$-**pcu** topology. The perovskite frameworks $[A][M^{II}(HCOO)_3]$ (where A is the $[(CH_3)_2NH_2]^+$, or $[CH_3NH_3]^+$, or $[CH_3CH_2NH_3]^+$) showing a $(4^{12} \cdot 6^3)$-**pcu** topology[9,14]. The formation of bi-nodal metal-formate framework is characterized by $(4^{12} \cdot 6^3)$ $(4^9 \cdot 6^6)$-**nia** which corresponds for example to the $[(CH_3)_2NH_2][Fe^{III}M^{II}(HCOO)_6]$ compound object of discussion in this chapter and related to the minerals of niccolite (NiAs)[9,14]. Finally, another topology is given by the porous diamond framework characterized by 6^6-**dia** (diamond topology), which is the case of the following compound $[M^{II}{}_3(HCOO)_6]$. The cited topologies are reported below in Figure 3. Regarding a general description of the family of compounds with the general formula $[(CH_3)_2NH_2][Fe^{III}M^{II}(HCOO)_6]$ (with M^{II} = Fe, Co, Mn, Ni and Mg) it is important to know that it crystallizes in the $P\bar{3}1c$ space group at room temperature (RT)[1–5]. The Fe^{II}-based compound present a nuclear phase transition at 155 K, mainly involving a reorientation of the counterion. The space group at low temperature (LT) is the $R\bar{3}c$, keeping invariant the origin of the unit cell, in the phase transition the *a* and *b* axes rotate 30° around the *c*-axis, while their values change from 8.2550(12), 8.2550(12) and 13.891(3) Å to 14.2600(17), 14.2600(17) and 41.443(8) Å for *a*, *b* and *c*, respectively. The value of the c^{LT} axis is about $3 \cdot c^{RT}$, while the value of a^{LT} is very close to $3^{1/2}a^{RT}$ (see Figure 8); therefore V^{LT} = 7290.3Å^3, almost equal to $9\,V^{RT}$ [$P\bar{3}1c$ to $R\bar{3}c$ $\boldsymbol{a}' = 2\boldsymbol{a} + \boldsymbol{b}$, $\boldsymbol{b}' = -\boldsymbol{a} + \boldsymbol{b}$, $\boldsymbol{c}' = 3\boldsymbol{c}$]. It should be noted, that the copper-based framework has been recently reported by Ciupa *et al.*[5], however the structural studies shown that this compound is not isomorph to the other members of this series, probably due to the large

Jahn Teller effect of the copper ion. The reported compound[5] crystallize in the monoclinic system with the following unit cell parameters a = 8.3771(8) Å, b = 14.095(2) Å, c = 13.635(2) Å, and β = 92.96(6) exhibiting stronger hydrogen bonds than the trigonal analogues.

3.2 Objectives

The first member of the mixed-valence formate family reported in literature[2,3,5] is the $[(CH_3)_2NH_2]Fe^{III}Fe^{II}(HCOO)_6]$ compound **1**. Later, many works published have revealed the existence of heterometallic analogues[4,5,15,16]. Our goal is to investigate possible isostructural compounds in order to determine the structural and magnetic properties as well as to discover the similarities and differences of all the compounds object of study. From the synthetic point of view, along this chapter our objective has been to preserve the crystal structure of the $Fe^{III}Fe^{II}$ compound and replace the divalent metal ion Fe^{II}, with other different divalent metals ions. The choice of using specific metal ions has been motivated by their different electronic configuration and therefore different physical behaviours, i.e. a large difference in the magnetic anisotropy is well known among the different divalent ions used along this study. Since this investigation involve neutron characterization, in the selection of the divalent ions was also taken into account the neutron absorption of each element. The influence of the substitution of the divalent ions in the macroscopic magnetic behaviour have been recently reported[14,19]. These works help us to compare our neutron results with the magnetometry measurements, which is a complementary technique. Beside the effects on the properties when different divalent metal ions were introduced within the framework, another interesting effect is produced by changing the nature of the counterions. Although there is not a clear correlation between the selected counterion and the magnetic behaviour[6,18–20], the exploration of this scenario using neutron diffraction can help us to elucidate the differences in the nuclear and in the magnetic structure when different counterions are used.

3.3 Experimental section

3.3.1 Synthesis of compounds 2 to 5

The synthesis of the compounds **2** to **5** has been performed under solvothermal conditions, which is one of the most used synthetic route for the preparation of metal-organic compounds. The fundamentals of this method are reported in chapter 2. Compounds **2**

and **3** were prepared by mixing $FeCl_3 \cdot 6H_2O$ (0.75 mmol) and $CoCl_2 \cdot 6H_2O$ or $MnCl_2 \cdot 4H_2O$ (0.75 mmol) in dimethylformamide (7.5 ml) and formic acid (7.5 ml). The mixture was sealed in a Teflon-line stainless steel vessel, and heated at 140 °C, for 48 hours. During this period, under autogenous pressure the reactives dissolve slowly with the increasing of temperature and react to form crystalline products. Once cooled to room temperature, dark red crystals for **2**, dark yellow crystals for **3** harvested with a yield of about 60% for **2** and **3**. For the synthesis of compounds, **4** and **5** important variations have been applied in order to obtain better quality of crystalline product because following the compounds **2** and **3** synthesis route, the crystals quality was not satisfactory as expected. The synthesis of **4**, has been carried out using anhydrous $NiCl_2$ (0.4 mmol) and $Fe(NO_3)_3\ 9H_2O$ (0.4 mmol) instead of $FeCl_3\ 6H_2O$ and a reaction time of in dimethylformamide (7.5 ml) and formic acid (7.5 ml) then heated at 140 °C, for 24 hours. Therefore, many variations in the synthetic route were carried out to improve the yield, purity and quality of the samples. For compound **5** $MgCl_2 \cdot 6H_2O$ (0.5 mmol) was mixed with an excess of $FeCl_3$ (0.8 mmol). Dark green crystals for **4**, black crystals for **5** harvested with a yield of about 60% for **4**, and 80% for compound **5** based on the divalent metal salt. Also for this last case, many tests have been performed before obtaining the best results in relation with the size of the single crystals. All products were filtered, washed with methanol or ethanol and dried in air over night. Finally, we would like to note that all our attempts to synthesize copper-based compound have been unsuccessful. The synthesis reported by Ciupa *et al.*[5] as well as all the adaptations of the previous described syntheses give rise to a solid solution (Fe:Cu) of the previously reported homometallic compound with formula $[(CH_3)_2NH_3][M^{II}(HCOO)_3]$.

3.3.2 Single crystal X-ray Diffraction Measurements

Single-Crystal X-Ray data collection of compounds **2** and **3** was carried out using synchrotron radiation with $\lambda = 0.66951$ Å at the CRISTAL beamline at the SOLEIL synchrotron (Saclay, France), at 30, 45, 55, 65, 75 85, 95 and 105 K using a He-cryostream. The data were indexed, integrated and scaled using the CrysAlis PRO software program[21]. Data collection for **4** was carried out by using the same synchrotron radiation source but the measurement was performed only at 45 K, above the magnetic ordering temperature. The structures from **2** to **4** were solved by direct methods using the SHELXS[22] program. All non-hydrogen atoms were refined anisotropically by full-matrix least-squares technique based on F^2 using SHELXL[22]. The hydrogen atom of the formate

ligand was positioned geometrically refined with AFIX43 constraint code. The final geometrical calculations and the graphical manipulations were carried out with PARST9[23], PLATON[24] and DIAMOND[25] programs.

3.3.3 Neutron Powder Diffraction Measurements

Neutron powder diffraction experiments were performed on the high-intensity diffractometer D1B and on the high-resolution diffractometer D2B, both equipped with variable temperature environment, at the Institut Laue-Langevin. The samples were contained in a ∅6 mm cylindrical vanadium can and placed inside an Orange Cryostat. In order to obtain an accurate crystal structure of both compounds, diffraction patterns were acquired at 45 K at D2B (λ = 1.595 Å).

The measurements at D1B were recorded using λ = 2.521 Å wavelength, above and below the magnetic order temperature, at 45 and 2 K, respectively, with the aim of obtaining the magnetic structure of compounds **2** to **5**.

Data reduction was carried out using the LAMP software[26,27], while the data refinement and calculations were carried out using the FullProf Suite programs[27]. A joint refinement (multipattern fit) of the synchrotron single crystal and neutron powder diffraction data was carried out to determine contribution of the light atoms and discard any structural phase transition related with the order of the hydrogen atoms. Magnetic structure models were deduced from the output of the BasIreps program included in the FullProf Suite[28].

All DFT calculations[29] were performed using the generalized gradient approximation to exchange-correlation functional according to Perdew-Becke-Erzenhof (PBE)[30] The electronic structure was computed using the projector augmented wave method (PAW)[31] as implemented in the Vienna *ab initio* simulation package (VASP)[32,33] . The energy cut off was set to 400 eV and a sampling grid of 4 x 4 x 2 Monkhorst-Pack grid of k points. The GGA + U calculations within Dudarev's approach were performed with 3 and 5 eV U-values for Fe^{III}, Mn^{II} and Co^{II}. For the calculation we have considered the high temperature (HT) structure for the three compounds. Since the counterion molecule is disordered over three possible local configurations, we have selected an ordered arrangement of molecular dimethylammonium counter ions compatible with an antiferro-electric arrangement. This will not change our discussions as far as the magnetic properties are concerned.

3.3.4 Crystallographic tables for compounds from **1** to **5**

Experimental parameters and main crystallographic data for compounds from **1** to **5** obtained from the powder neutron diffraction.

Formula	**$[NH_2(CH_3)_2][Fe^{III}Fe^{II}(HCOO)_6]$ (1)**
Empirical Formula	$C_8H_{14}Fe_2NO_{12}$
M_r (g·mol-1)	427.88
Temperature (K)	220(2)
λ(Å)	0.71073
Crystal system	Trigonal
Space group (No.)	$P\bar{3}1c$ (163)
a (Å)	8.2550(12)
b (Å)	8.2550(12)
c (Å)	13.891(3)
V (Å^3)	819.8(3)
Z	2
ρ_c (g·cm^{-3})	1.733
Meas. Reflections/ (Rint)	15574 (0.2526)
Indep. ref. [I > 2σ(I)]	713
Parameters/ restraints	67/ 0
Hydrogen treatment	refall
Goodness of fit	1.513
Final R indices [I > 2σ(I)]: R1 / wR2	0.1800/0.2635
R indices (all data): R1 / wR2	0.2406/0.2777

Formula	**$[NH_2(CH_3)_2][Fe^{III}Co^{II}(HCOO)_6]$ (2)**
Empirical Formula	C8H14FeCoNO12
Mr (g·mol-1)	430.98
Temperature (K)	45(2)
λ(Å)	1.59465
Crystal system	Trigonal
Space group (No.)	$P\bar{3}1c$ (163)
a (Å)	8.22213(5)
b (Å)	8.22213(5)
c (Å)	13.68840(12)
V (Å3)	801.405(14)
Z	2
ρ_c (g·cm^{-3})	1.786
Meas. Reflections	3200
Parameters/ restraints	102/ 0
Hydrogen treatment	Refined with constraints
Goodness of fit	1.4
R_B (%)	7.22
R_F (%)	5.55
χ^2	2.034

Formula	$[NH_2(CH_3)_2][Fe^{III}Mn^{II}(HCOO)_6]$ (3)
Empirical Formula	$C_8H_{14}FeMnNO_{12}$
M_r (g·mol-1)	426.99
Temperature (K)	45(2)
λ(Å)	1.59465
Crystal system	Trigonal
Space group (No.)	$P\bar{3}1c$ (163)
a (Å)	8.2976(3)
b (Å)	8.2976(3)
c (Å)	13.8926(11)
V (Å^3)	13.8926(11)
Z	2
ρ_c (g·cm^{-3})	1.712
Meas. Reflections	3200
Parameters/ restraints	54/ 0
Hydrogen treatment	Refined with constraints
Goodness of fit	2.1
R_B (%)	12.4
R_F (%)	5.81
χ^2	4.40

Formula	$[NH_2(CH_3)_2]_n[Fe^{III}Ni^{II}(HCOO)_6]$ (4)
Empirical Formula	$C_8H_{14}FeNiNO_{12}$
M_r (g·mol-1)	426.98
Temperature (K)	45(2)
λ(Å)	1.59465
Crystal system	Trigonal
Space group (No.)	$P\bar{3}1c$ (163)
a (Å)	8.15994(10))
b (Å)	8.15994(10)
c (Å)	13.5997(3)
V (Å^3)	784.21(2)
Z	2
ρ_c (g·cm^{-3})	1.831
Meas. Reflections	3200
Parameters/ restraints	27 / 0
Hydrogen treatment	Refined with constraints
Goodness of fit	1.1
R_B (%)	4.4
R_F (%)	3.77
χ^2	1.53

Formula	$[NH_2(CH_3)_2]_n[Fe^{III}Mg^{II}(HCOO)_6]$ (5)
Empirical Formula	$C_8H_{14}FeMgNO_{12}$
M_r (g·mol-1)	426.98
Temperature (K)	45(2)
λ(Å)	2.520
Crystal system	Trigonal
Space group (No.)	$P\bar{3}1c$ (163)
a (Å)	8.1583(2)
b (Å)	8.1583(2)
c (Å)	13.7963(6)
V (Å^3)	795.23(5)
Z	2
ρ_c (g·cm^{-3})	1.397
Meas. Reflections	1280
Parameters/ restraints	57 / 0
Hydrogen treatment	Refined with constraints
Goodness of fit	3.1
R_B (%)	3.46
χ^2	10.3

Experimental parameters and main crystallographic data for compound **2** obtained from the single crystal X-ray diffraction as function of temperature.

Formula	$[NH_2(CH_3)_2][Fe^{III}Co^{II}(HCOO)_6]$ (2)							
Empirical Formula	$C_8H_{14}CoFeNO_{12}$							
***M*$_r$ (g·mol-1)**	430.98							
λ(Å)	0.66951							
Crystal size (µm)	60x70x90							
Crystal system	Trigonal							
Space group (No.)	*P*-31*c* (163)							
Temperature (K)	30(2)	45(2)	55(2)	65(2)	75(2)	85(2)	95(2)	105(2)
***a* (Å)**	8.21840(10)	8.21630(10)	8.21580(10)	8.21650(10)	8.21270(10)	8.21320(10)	8.21360(10)	8.21140(10)
***b* (Å)**	8.21840(10)	8.21630(10)	8.21580(10)	8.21650(10)	8.21270(10)	8.21320(10)	8.21360(10)	8.21140(10)
***c* (Å)**	13.6756(2)	13.6768(2)	13.6791(2)	13.6791(2)	13.6789(2)	13.6863(2)	13.6935(2)	13.6951(3)
***V* (Å^3)**	799.93(2)	799.59(2)	799.63(2)	799.76(2)	799.01(2)	799.54(2)	800.04(2)	799.71(3)
Z	2	2	2	2	2	2	2	2
ρ_c (g·cm^{-3})	1.789	1.790	1.790	1.790	1.791	1.790	1.789	1.790
μ(mm^{-3})	1.617	1.617	1.617	1.617	1.618	1.617	1.616	1.617
Meas. Reflections/ (Rint)	9220/ (0.0333)	9221/ (0.0341)	9187/ (0.0359)	9159/ (0.0407)	9110/ (0.0531)	9106/ (0.0725)	9172/ (0.0790)	9188/ (0.0789)
Indep. ref. [I > 2σ(I)]	994	997	980	991	997	997	962	966
Goodness of fit	1.078	1.097	1.117	1.227	1.181	1.143	1.230	1.228
Final *R* indices [*I* > 2σ(*I*)]:R1 / wR2	0.0238/ 0.0614	0.0245/ 0.0641	0.0256 / 0.0684	0.0295/ 0.0996	0.0321/ 0.1055	0.0394/ 0.1243	0.0431/ 0.1371	0.0432/ 0.1389
***R* indices (all data): R1 / wR2**	0.0241/ 0.0616	0.0249/ 0.0644	0.0259/ 0.0686	0.0301/ 0.1000	0.0328/ 0.1067	0.0402/ 0.1256	0.0447/ 0.1467	0.0462/ 0.1600

Experimental parameters and main crystallographic data for compound **3** obtained from the single crystal X-ray diffraction as function of temperature.

Formula	$[NH_2(CH_3)_2][Fe^{III}Mn^{II}(HCOO)_6]$ (3)							
Empirical Formula	$C_8H_{14}MnFeNO_{12}$							
***M*$_r$ (g·mol-1)**	426.98							
λ(Å)	0.66951							
Crystal size (µm)	80x70x60							
Crystal system	Trigonal							
Space group (No.)	*P*-31*c* (163)							
Temperature (K)	30(2)	45(2)	55(2)	65(2)	75(2)	85(2)	95(2)	105(2)
***a* (Å)**	8.277(10)	8.276(10)	8.275(10)	8.276(10)	8.274(10)	8.2726(2)	8.2722(2)	8.267(10)
***b* (Å)**	8.277(10)	8.276(10)	8.275(10)	8.276(10)	8.274(10)	8.2726(2)	8.2722(2)	8.267(10)
***c* (Å)**	13.895 (2)	13.897(2)	13.894(2)	13.891(2)	13.890(2)	13.888(3)	13.886(3)	13.876(2)
***V* (Å^3)**	824.55(2)	824.38(2)	824.05(2)	824.02(2)	823.60(2)	823.14(4)	822.95(4)	821.36(2)
Z	2	2	2	2	2	2	2	2
ρ_c (g·cm^{-3})	1.720	1.720	1.721	1.721	1.722	1.723	1.723	1.726
μ(mm^{-3})	1.435	1.435	1.436	1.436	1.436	1.437	1.438	1.440
Meas. Reflections/ (Rint)	10382/ (0.0391)	10379/ (0.0385)	10354/ (0.0438)	10309/ (0.0500)	10311/ (0.0597)	10305/ (0.0696)	10388/ (0.0745)	10420/ (0.0799)
Indep. ref. [I > 2σ(I)]	1125	1128	1123	1120	1121	1124	1123	1126
Goodness of fit	1.252	1.219	1.229	1.222	1.186	1.184	1.143	1.133
Final R indices [I > 2σ(I)]: R1 / wR2	0.0242/ 0.0681	0.0246/ 0.0703	0.0262/ 0.0710	0.0305/ 0.0876	0.0354/ 0.1014	0.0397/ 0.1143	0.0433/ 1.143	0.0504/ 0.1502
R indices (all data): R1 / wR2	0.0257/ 0.0746	0.0261/ 0.0761	0.0285/ 0.0793	0.0327/ 0.0947	0.0387/ 0.1148	0.0439/ 0.1275	0.0472/ 0.1223	0.0550/ 0.1595

3.3.5 FTIR-Measurements

The infrared spectra of the compounds **2** to **5** have been collected using a JASCO FT/IR-4600 equipped with a single bounce ATR monolithic diamond top plate. All the spectra were recorded at room temperature, and they represented a useful tool to verify the presence of the dimethylammonium or formate group in the final product. Moreover, the shift in the IR bands can give us and idea if the obtained product is the desired one. For example, through the identification of the protonated amine vibrational modes in order to confirm its presence in the cavity of the framework and as well as the identification of the vibrational modes of the formate group.

Table 1. Vibration modes for compounds **2** to **5**.

	2	**3**	**4**	**5**
υ**HCOO**$^-$	2879*w*	2873*w*	2881*w*	2883*w*
υ_{as}**HCOO**$^-$	1556*s*	1556*s*	1556*s*	1575*s*
δCH$_3$	1455*w*	1455*w*	1455*w*	1455*w*
υ_s**HCOO**$^-$	1383*m*	1385*m*	1383*m*	1389*m*
υ**HCOO**$^-$	1327*s*	1331*s*	1325*s*	1328*s*
ρCH$_3$	1084*w*	1083*w*	1083*w*	1084*w*
υ_{as}**CNC**	1014*w*	1014*w*	1014*w*	1014*w*
υ_s**CNC**	884*w*	884*w*	884*w*	884*w*
ρNH$_2$	853*w*	850w	853*w*	851w
υ**HCOO**$^-$	810*s*	807*s*	814*s*	811*s*

Key codes: *w*: weak, *m*: medium, *s*: strong and **υ** stretching, **δ** bending, **ρ** rocking, $\upsilon_{as/s}$ asymmetric/symmetric stretching.

The infrared spectra are shown in the Figure 4, while the list of the assignments bands corresponding to the internal vibrations modes of the compounds **2** to **5** is reported in Table 1. The transmission bands are also compared with the spectra of the previously reported[4,5,15,18,34,35] compounds containing dimethylammonium (DMA^+) in which the vibrational modes coincide with the frequencies reported here. The results of these measurements carried out, show that the spectra are all very similar, however the different compounds show that some mode shifts among them approximately in the range of 1-5 cm^{-1}, while if we compare our results with those of Ciupa *et al.*[5] the mode can shift approximately in the range of 10-20 cm^{-1} . Here the stretching band υ(C−H), from the $HCOO^-$ group, is observed as a weak band around 2880 cm^{-1}, while the υ(C−O) asymmetric stretching is observed at *ca.* 1556 cm^{-1} with a very strong band except for

compound **5** that shows a higher frequency shifted of 19 cm^{-1}. The symmetric stretching of υ(C−O) appears at *ca.* 1328 cm^{-1} as a strong band. The in-plane υ(C−H) bending is given at approximately 1385 cm^{-1} and the out-plane υ(OCO) bending is observed as a strong band at *ca.* 811 cm^{-1} . Regarding the vibrational bands of the amine, the δ(CH_3) bending (scissoring) appeared as a weak band at 1455 cm^{-1} and at 1083 cm^{-1} (rocking).

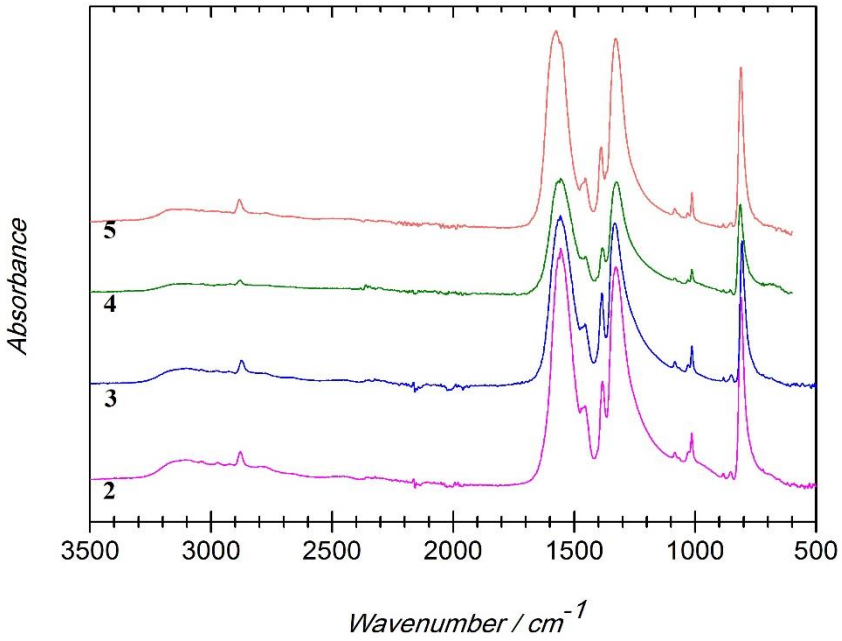

Figure 4: Infrared spectra of compounds from **2** to **5** recorded at room temperature.

The υ(C−N), symmetric and asymmetric stretching frequencies are at 1014 cm^{-1} and 884 cm^{-1} resulting with weak intensities bands. However, this technique is not powerful enough to discriminate between the solid-solution homometallic phase and the heterometallic phase. An example of this is the IR spectra of the synthetized $Fe^{III}Cu^{II}$ compound (not reported here), which is very similar to the other members of this series, but the crystal structure, once solved by diffraction methods, has shown a complete different structural arrangement.

3.4 Crystal structures of the compounds **2** to **5**

Along this section we are going to describe the crystal structure of the $[(CH_3)_2NH_2][Fe^{III}M^{II}(HCOO)_6]$ compounds (**2** to **5**) (see Figure 5). These compounds have been characterized via neutron and synchrotron X- Ray diffraction techniques and finally compared with **1**. The presented results have been derived from the joint refinements of the synchrotron X-Ray diffraction together with neutron data. The combination of powder neutron diffraction and single crystal or powder X-Ray diffraction in a multipattern approach, allowed performing the refinement of the crystal structures

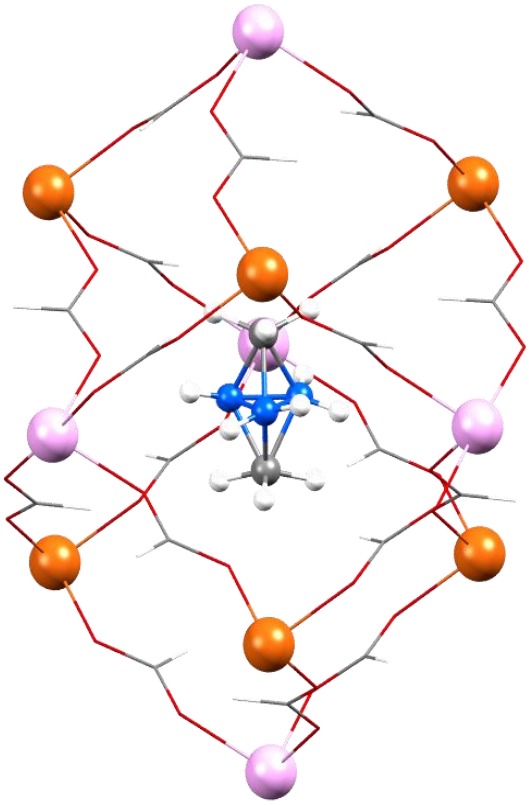

Figure 5: Detail of the crystal structure of the $[(CH_3)_2NH_2][Fe^{III}M^{II}(HCOO)_6]$ niccolite-like compound [with M^{II} = Fe^{II}(**1**), Co^{II} (**2**) and Mn^{II} (**3**) Ni (**4**) and Mg(**5**) ions]. The $[(CH_3)_2NH_2]^+$ counterion is disordered over three different positions due to the 3-fold axis running thought the carbon atoms of the methyl-groups. The three possible positions within the $[Fe^{III}M^{II}(HCOO)_6]^-$ framework have been represented simultaneously. The M^{II} is in pink, Fe^{III} is orange the oxygen is red, nitrogen is blue, carbon grey and hydrogen white.

with high precision. The crystal structures of the full series crystallize with a niccolite-like topology as have been previously described. Therefore, the **2** to **5** compounds are isomorphs to **1** at room temperature. All of them crystallize into the trigonal space group $P\bar{3}1c$ at high temperature. In the crystal structures, the metal ions have an octahedral coordination geometry: Fe^{III} is surrounded by six M^{II} ions (and vice versa) through the coordination of six oxygen atoms of the formate ligand, which is arranged in *anti-anti* configuration mode generating a 3D anionic network. The framework take the form of a bi-nodal niccolite-like structure $(4^{12} \cdot 6^3)$ $(4^9 \cdot 6^6)$-**nia** in which M^{II} is connected to the six neighbouring metal ions in an arrangement of a trigonal prism and it is a $(4^9 \cdot 6^6)$-**pcu** node (see Figure 3), while Fe^{III} has its six neighbours arranged in an octahedron, being a $(4^{12} \cdot 6^3)$ node. Their combinations give rise to a bi-nodal $[(CH_3)_2NH_2][Fe^{III}M^{II}(HCOO)_6]$ framework. A detailed view of the structure network topology of the metal centres is given in Figure 6. In this configuration, the

$Fe^{III}\cdots M^{II}$ distances are 5.882(1), 5.8516(2), 5.9176(3), 5.8098(1) and 5.8370(9) Å for **1** to **5**, respectively. A comparison of the hydrogen bonds distances for compounds **2** to **5**, and the key bond lengths and angles are summarized in Table 2 .

Zhao et al.[2] reported that the two independent metal atoms in the asymmetric unit can be distinguished by the Fe^{III}–O bond distance. The summary of these observations is that the bond lengths of Fe^{II}–O and Fe^{III}–O decrease proportionally with the decrease of the temperature, leading the authors to suppose the existence of a weak electronic interaction between the two metal centres. For Example, the Fe^{III}–O bonds lengths in **2** to **5** are 2.0046(10), 2.0143(14), 2.009(2), 2.0226(11) and 1.9526(1) Å, respectively. While the bonds distances between the M^{II}–O are longer as is expected for a less electronegative interaction, with values of 2.1199(13), 2.0761(17), 2.155(3), 2.0322(13) and 2.1282(1) Å, for compound **2** to **5**, respectively.

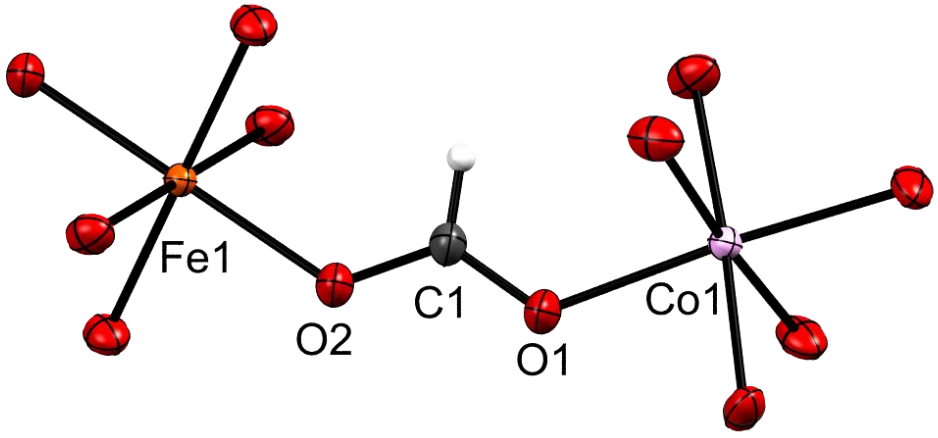

Figure 6: ORTEP- representation of a framework fragment of **2** consisting of a FeO_6 and CoO_6 octahedron bridged by a formate ligand in *anti-anti* conformation**.** Ellipsoid probability 50%.

Table 2: Selected geometric parameters of **1** to **5** from neutron data. At 175 K using single crystal neutron diffraction for **1** in Reference [3], at 45 K using a multipattern refinement for compounds **2** to **4** and at 45 K powder neutron diffraction for **5**.

Compound	$Fe^{III}Fe^{II}$ **1**	$Fe^{III}Co^{II}$ **2**	$Fe^{III}Mn^{II}$ **3**	$Fe^{III}Ni^{II}$ **4**	$Fe^{III}Mg^{II}$ **5**
Temperature [K]	175	45	45	45	45
Distances [Å]					
$M^{(II)}$–O1	2.1199(13)	2.0761(17)	2.1550(3)	2.0322(13)	2.0368(2)
$Fe^{(III)}$–O2	2.0046(10)	2.0143(14)	2.009(2)	2.0226(11)	2.0281(1)
C1−O1	1.2326(15)	1.2401(2)	1.2450(4)	1.2467(18)	1.2451(1)
C1−O2	1.2606(15)	1.2610(3)	1.2660(4)	1.2536(2)	1.2507(1)
C1−H1	1.085(4)	1.068(12)	1.050(2)	0.941(3)	1.070(3)
N−C2	1.499(10)	1.486(11)	1.601(2)	1.481(13)	1.4778(1)
C2−H2	0.995(11)	1.108(3)	0.970(6)	0.980(3)	1.01(1)
Angles [°]					
$O1-M^{(II)}-O1^{(I)}$	93.01(5)	93.48(7)	93.35(9)	93.01(5)	92.41(5)
$O1^{(I)}-M^{(II)}-O1^{(II)}$	89.44(5)	89.44(6)	89.31(9)	89.72(5)	90.41(6)
$O1-M^{(II)}-O1^{(II)}$	84.62(5)	83.73(6)	84.10(10)	84.38(5)	84.87(5)
$O1^{(I)}-M^{(II)}-O1^{(III)}$	176.68(5)	176.08(7)	176.42(11)	176.32(6)	176.18(5)
$O2-Fe^{(III)}-O2^{(IV)}$	91.20(4)	91.39(7)	91.26(10)	91.36(5)	90.80 (6)
$O2-Fe^{(III)}-O2^{(V)}$	88.80(4)	88.61(7)	88.74(10)	88.64(5)	89.20(5)
$O2^{(IV)}-Fe^{(III)}-O2^{(V)}$	180.00(6)	180.00(11)	180.00(15)	180.00(7)	180.00(14)
O1−C1−O2	124.64(11)	124.18(18)	124.0(3)	124.20(14)	124.22(11)

Symmetry codes: (I): 1−*y*, *x*−*y*, *z*; (II): *x*, *x*−*y*, 1/2−*z*; (III): 1−*y*, 1-*x*, 1/2−*z*; (IV): 1−*y*, −1+*x*-*y*, *z*; (V): 1+*y*, 1-*x*+*y*, −*z*

Moreover, according to the order of the periodic table, it results that the M^{II}–O bond lengths decrease with the increase of the atomic number *Z* (see also the Table 2). In the Figure 6, for more clarity there is represented a framework fragment of **2,** consisting of a FeO_6 and CoO_6 octahedron, bridged by a formate ligand which shows the *anti-anti* conformation. This is a representative illustration of the compounds **1** to **5** studied here.

The anionic frameworks form cavities that are occupied by dimethylammonium cations $[(CH_3)_2NH_2]^+$, indispensable to achieve the electro-neutrality of the compound, shown in Figure 7. Significant is the role assumed by the dimethylammonium cation in the cavity, affected by an important disordered due the presence of a 3-fold axis.

The 3-fold axis passes through the carbon, generating the nitrogen positions statistically distributed over three equivalent sites, while simultaneously a 2-fold axis is passing perpendicular to them, and giving rise to a second atom of carbon.

As clarified by *Cañadillas-Delgado et al.*[3] for compound **1,** at low temperature, the counterion undergoes an order-disorder phase transition (*ca.* 155 K) that implies a change in the space group from $P\bar{3}1c$ (high temperature) to $R\bar{3}c$ (low temperature). From the crystallographic point of view, this transition produces quite different cell parameters values ($a = b$ = 14.26, c = 41.44 Å) compared to those recorded at high temperature. In fact, at low temperature, when the compound transited from $P\bar{3}1c$ to the $R\bar{3}c$ space group, the loss of some of the 3-fold axes leads to an increase of the unit cell size and in particular generating the triplication of the *c*-axis. In addition, the order−disorder phase transition is triggered by the presence of an extensive network of hydrogen bonds involving the nitrogen and the carbon of the dimethylammonium as donors and the formate oxygen atoms as acceptors. This feature is important for the interpretation of the electric properties. Moreover, in the same work[3], the measurement of the temperature dependence of the relative permittivity shows an electric transition, which has been assigned to a paraelectric to antiferroelectric phase transition.

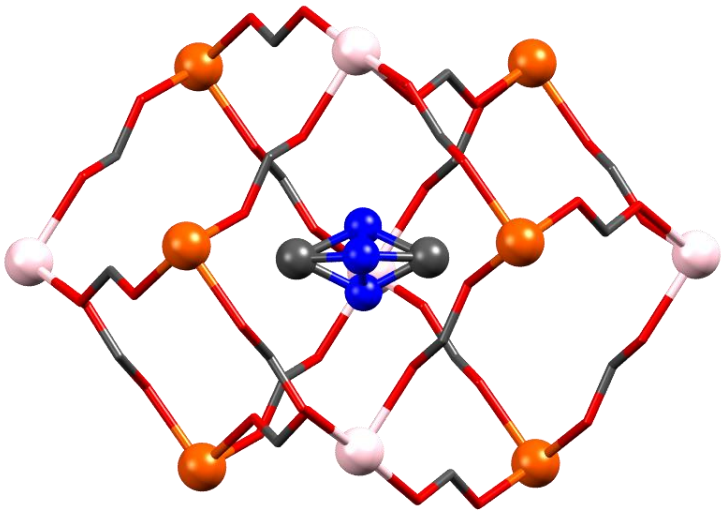

Figure 7: Disordered dimethyl ammonium cation in a cavity of the anionic $[Fe^{III}Co^{II}(HCOO)_6]^-$ framework. Hydrogens omitted for clarity. Atoms: Carbon (grey), oxygen (red), nitrogen (blue), cobalt (pink) and iron (orange).

This transition occurs is concomitant with the structural transition, and therefore, it is triggered by the order−disorder transition of the dimethylammonium counterions, shown in Figure 8.

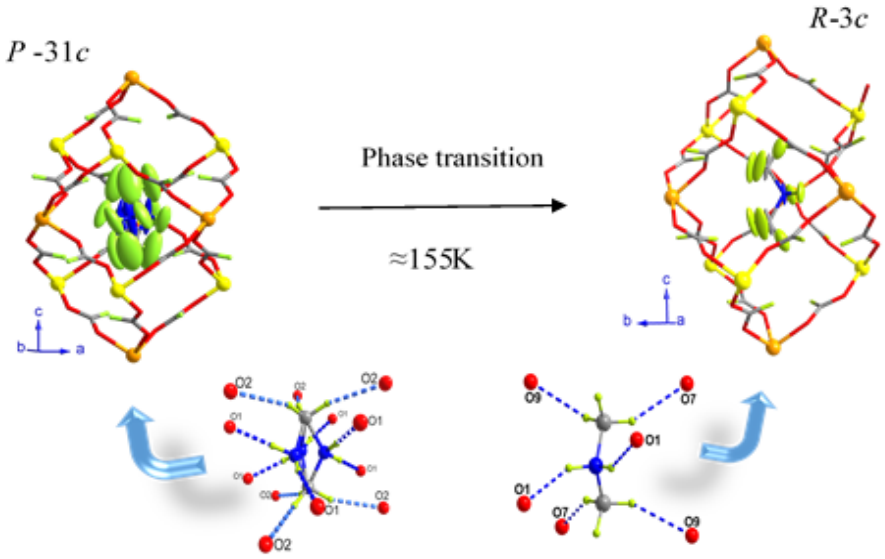

Figure 8: View of the *b*-axis of compound **1** together with the magnetic moment of each Fe^{II} and Fe^{III} sites, yellow/blue and orange/green, for nuclear/magnetic structure, respectively.

However, from our X-Ray crystallographic studies carried out at different temperatures, for compound **2** and **3** between 30 and 105 K, and for compound **4** at 45 K, it results that all of them are isostructural with the previously reported **1** at RT (compound **5** was not measured by synchrotron X-Ray diffraction due to lack of time; the investigation is still going on). Therefore, compounds from **2** to **5** are not subjected to any structural phase transition involving the hydrogen atoms, they retain the trigonal $P\bar{3}1c$ space group[2, 5,15] at high and low temperature. Probably because the DMA^+ is weakly anchored within the cavities, as suggested from the size and the direction of thermal ellipsoids (see Figure 9). On the contrary, the anisotropic displacement parameters in **1** indicate that at high temperature this molecule is not well anchored in the cavities but it has some freedom of motion around its set of positions[3]. In the compounds **2** to **5** the electrical properties do not undergo any change[2,4,5,16] as it is observed in

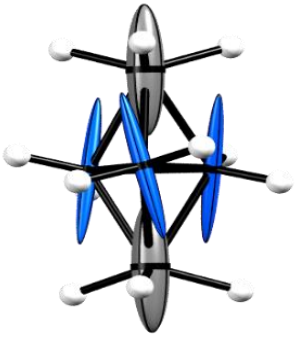

Figure 9: View of the dimethylammonium counterion using the ORTEP representation. Ellipsoid probability 50%. Hydrogens fixed-size sphere at 0.15 Å.

compound **1**. For these reasons, the structural transition is an exclusive behaviour observed only in compound **1**, where the donor-acceptor/H-acceptor distances are shorter in the low temperature (LT) phase than at room temperature (RT) [3.042(16)/2.16(10) and 3.043(8)/2.16(8) Å at RT and 2.9121(9)/1.982(3) and 2.920(1)/1.982(3) Å at LT]. The shortening of the hydrogen bonds upon cooling should be the responsible element of the structural phase transition observed in **1**. In general, by diffraction experiments it is possible to identify when an H-atom is involved in some kind of interactions. Many different classifications of the H-bond have been given based on different properties[36–38]. However, here we consider the H-bonds defined through geometrical parameters given by the crystal structure (distances and angles). In a typical H-bond the donor interacts with one acceptor ("two-centred"); but a donor can interact at the same time with more than one acceptor.

Table 3: Hydrogen bonds distances and angles.

D	**H**	**A**	**D−H**	**H···A**	**D···A**	**D−H···A**
$[(CH_3)_2NH_2][\ Fe^{III}Co^{II}(HCOO)_6$, **2**						
N1	H101	O1$^{(I)}$	0.863(5)	2.178(4)	3.029(5)	168.37(5)
C2	H100	O2$^{(II)}$	1.109(3)	2.4181(3)	3.502(4)	165.17(2)
C2	H100$^{(II)}$	O1$^{(III)}$	1.109(3)	2.667(2)	3.305(2)	115.87(2)
(I) : *x*,1+*x*-*y*, 1/2−*z* (II) : 1−*y*, 1+*x*-*y*, *z* (III) : −*x*+*y*, 1−*x*, *z*						
$[(CH_3)_2NH_2][\ Fe^{III}Mn^{II}(HCOO)_6$, **3**						
N1	H101	O1$^{(I)}$	1.056(7)	2.087(8)	3.038(1)	148.58(5)
C2	H100	O2$^{(II)}$	0.969(7)	2.551(7)	3.507(8)	168.83(5)
(I) : *x*,1+*x*-*y*, 1/2−*z* (II) : 1−*y*, 1+*x*-*y*, *z*						
$[(CH_3)_2NH_2][\ Fe^{III}Ni^{II}(HCOO)_6$, **4**						
N1	H101	O1	1.024(3)	2.082(7)	3.030(1)	152.85(1)
N1	H101	O1$^{(I)}$	1.024(3)	2.583(9)	3.375(1)	133.82(9)
C2	H100	O2	0.983(5)	2.521(4)	3.480(4)	165.01(5)
(I) : *x*,1+*x*-*y*, 1/2−*z*						
$[(CH_3)_2NH_2][\ Fe^{III}Mg^{II}(HCOO)_6$, **5**						
N1	H101	O1$^{(I)}$	1.006(4)	2.105(1)	3.020(1)	150.25(2)
C2	H100	O2	1.005(2)	2.505(1)	3.483(1)	164.13(2)
(I) : *x*,1+*x*−*y*, 1/2−*z*						

Generally, the terms “bifurcated” (“three- centred”) or “trifurcated” (“four- centred”)[36] are used if two or three acceptors are involved, respectively. A detailed view of the H-bonds of the counterion for the compounds from **2** to **5** is shown in Figure 10 and hydrogen bonds distances and angles are given in Table 3**.**

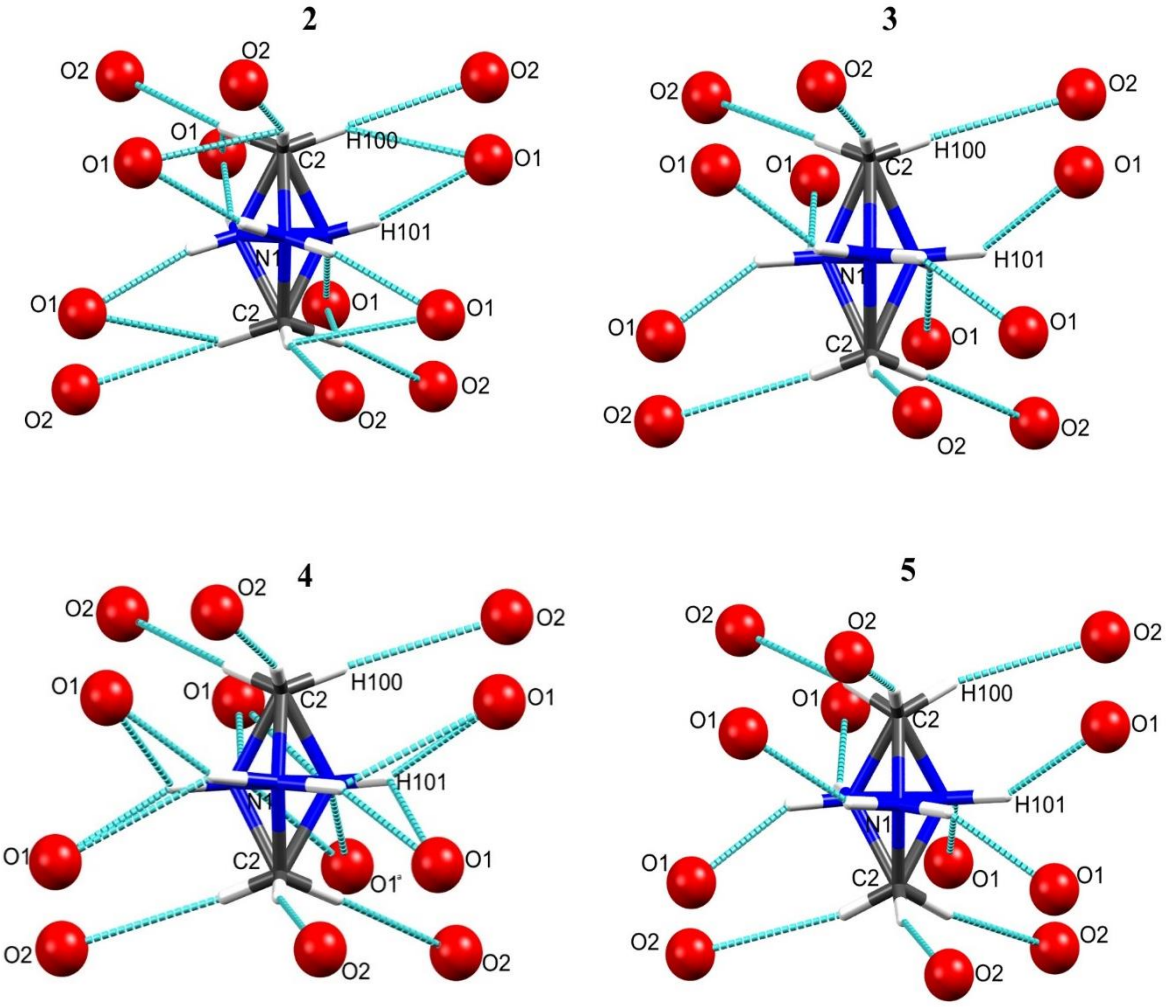

Figure 10: Detailed view of the hydrogen bonds involving the disordered dimethyl ammonium counterion in **2** to **5** (Top: **2** left, **3** right. Bottom: **4** left, **5** right). Note that the hydrogen bonding systems in **3** and **5** are equivalent.

The H-bonds occur between the DMA^+ counterions and the oxygen atoms of the formate framework. DMA^+ acts as hydrogen bond-donor via N−H and C−H groups while the oxygen atoms of the formate act as acceptors. The N−H···O bonds usually show shorter donor acceptor distances if compared to the non-classical C−H···O bonds, as the nitrogen donor is more electronegative than carbon. The H-bonds of compound **2** are characterized by the presence of one moderate H-bond that is mostly electrostatic $N1^{(I)}–H101^{(I)}\cdots O1^{(II)}$ and other two $C2^{(I)}–H100^{(I)}\cdots O2^{(III)}$ and $C2^{(I)}–H100^{(III)}\cdots O1^{(IV)}$, [with (I): *x*, *y*, *z*; (II): *x*,1+*x*−*y*, 1/2−*z*; (III) : 1−*y*, 1+*x*−*y*, *z*; (IV) : −*x*+*y*, 1−*x*, *z*], which fall in the range of

the weak H-bonds. The general properties of these categories are listed by T. Steiner[37] and resumed by E. Kwan[34] and are used as reference for this thesis. The disordered dimethylammonium located in the cavity, confers a not optimal geometry of the N−H bonds and to H−N−H angles. In fact, the N1−H101 bonds in **2** are out of plane, and the angle H−N−H is 112°, an aspect which seems to influence the surrounding environment in terms of H-interactions. In particular, it is interesting to observe that the C2−H100 bond shares the same acceptor (O1) with the hydrogen of N1−H101, giving rise to a bifurcated H-bond. A Comparison between N1−H101···O1, the C2−H100···O2 and C2−H100···O1 of the H···A and D···A distances, confirms that the shorter bond is the N1−H101···O1 one, which is more favoured with respect to the other two H-bonds with a weaker manners. In compound **4**, (Figure 10, below left) it is possible to distinguish a moderate H-bond for N1−H101···O1 and two weak H-bonds, N1−H100···O1$^{(I)}$ and C2−H100···O1 [with (I) : *x*,1+*x*−*y*, 1/2−*z*]. The N1−H101···O1$^{(I)}$ bond shows a bifurcation, in which every N−H bond establish a double contact with the acceptor O1, shared at the same time with the next N1−H101 bond. Angles and distances measured corresponds to the standard definitions[37]. But, surprisingly, the H−N−H angle with *ca.* 126° is particularly larger than usual values[39,40]; and N−H bond are slightly out of the plane if compared with **2**.

Moreover, the hydrogen bonding systems observed in **3** and **5** are similar with slightly different angles and distances, where N1$^{(I)}$−H100$^{(I)}$···O1$^{(II)}$ is a medium H-bond and C2−H100···O1$^{(II)}$ (**3**) and C2−H100···O (**5**) [(I): *x*,1+*x*−*y*, 1/2−*z*; (II): 1−*y*, 1+*x*−*y*, *z*], correspond to a weak interaction, both of them show two-centred H-bonding. No particular distortions are observed, and the H−N−H angles are 94° and 98° (for **3** and **5** respectively). If we consider that when dimethylammonium cation is not affected by disorder this value corresponds to circa 107°, so that the angles H−N−H measured in **2**, **3** and **5** appears more reasonable, because closer to it, than the value of **4**. As seen until now, the disorder plays an important role, affecting the geometry and consequently the bonds, and the angles of the structure, as well as the potential H-bonds. The studied structures **2** to **5**, have differences that once evaluated, help to better understand and distinguish their characteristics. The counterion accommodated in the cavity of the anionic framework occupying an empty space that corresponds to a volume (Å^3) of *ca.* 235.9 for compound **2**, 239.9 for **3**, 219.2 for **4** and 234.3 for **5,** corresponding to 29.5, 29.1, 27.9, 29.5 percent of the unit cell volume, respectively.

However, with the presence of dimethylammonium, the remaining available volume (Å^3) is 14.5 for **2**, 14.1 for **3**, 14.7 for **4**, 14.7 for **5** corresponding to 1.8 %, 1.7 %, 1.9 %, and 1.8 %, respectively. The position of the hydrogen atoms of the structures **2** to **4** were determined combining X-Ray synchrotron and powder neutron diffraction data (see Figure 11 below, for compound **2** and Figure 12 for compound **3**), both collected at the temperature of 45 K, above the magnetic phase transition (*ca.* 32, 35, 42, 13.5 K respectively*).*

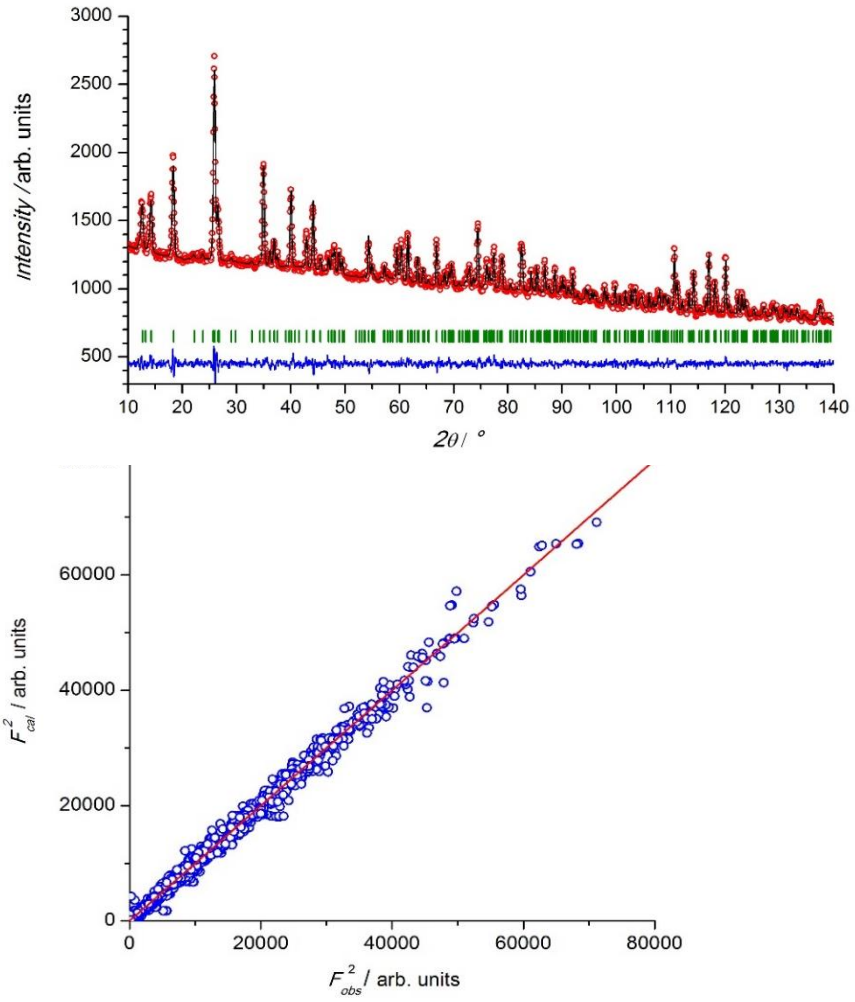

Figure 11: (Top) Experimental (open red circles) neutron powder diffraction data and calculated Rietveld refinement (black solid line) pattern for $[(CH_3)_2NH_2][Fe^{III}Co^{II}(HCOO)_6]$ compound (data collected at 45 K using the D2B instrument with λ=1.59465 Å). The difference between observed and calculated patterns has been represented in blue. The vertical green marks represent the position of the Bragg reflections. (Bottom) Plot of the observed *vs* calculated square structure factors collected, corresponding to the data collected at 45 K at the CRISTAL beamline. The experimental data are represented as open blue circles and the ideal case ($F_{cal}^2 = F_{obs}^2$) is represented as a solid red line. The refinement has been done in the space group *P*-31*c* with the associated cell parameters $a = b = 8.22225(6)$ Å, $c = 13.68859(16)$ Å, $\alpha = \beta = 90°$ and $\gamma = 120°$. The multi-pattern data refinement gives the following agreement factors $\chi^2 = 2.03$ and $R_B = 7.09$ % for neutron and $R_F = 5.75$ % for X-ray data.

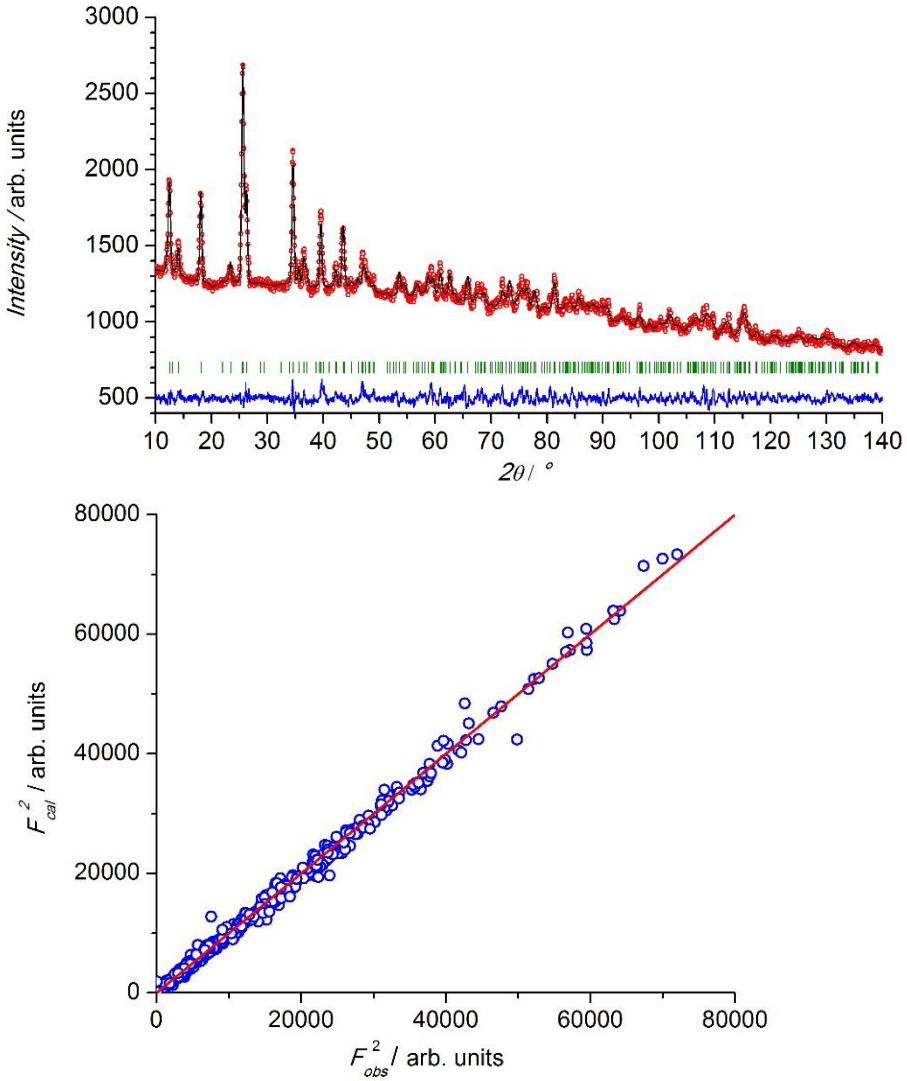

Figure 12: (Top) Experimental (open red circles) neutron powder diffraction data and calculated Rietveld refinement (black solid line) pattern for $[(CH_3)_2NH_2][Fe^{III}Mn^{II}(HCOO)_6]$ compound (data collected at 45 K using the D2B instrument with λ=1.59465 Å). The difference between observed and calculated patterns has been represented in open blue circles. The vertical green marks represent the position of the Bragg reflections. (Bottom) Plot of the observed *vs* calculated square structure factors collected, corresponding to the data collected at 45 K at the CRISTAL beamline. The experimental data are represented as open blue circles and the ideal case ($F_{cal}^2 = F_{obs}^2$) is represented as a solid red line. The refinement has been done in the space group *P*-31*c* with the associated cell parameters $a = b = 8.2976(5)$ Å, $c = 13.8983(14)$ Å, $\alpha = \beta = 90°$ and $\gamma = 120°$. The multipattern data refinement gives the following agreement factors $\chi^2 = 4.40$ and $R_B = 12.4$ % for D2B and $R_F = 5.81$ % for CRISTAL beamline data.

In the last years, a work on the characterization of novel niccolite compounds[4,5] with formula $[(CH_3)_2NH_2][Fe^{III}M^{II}(HCOO)_6]$ where M^{II}= Ni^{2+} and Mg^{2+} has been published reporting interesting evidences. In these specific cases, disorder affects not only the counterion inside the cavity but also the metal ions positions. Compounds **4** and **5**, in contrast with the others members of this family of compounds, have the metal ions statistically distributed over the two octahedral sites with equal probability[5] giving rise to a disorder on the metal sites positions that it is in agreement with our neutron diffraction

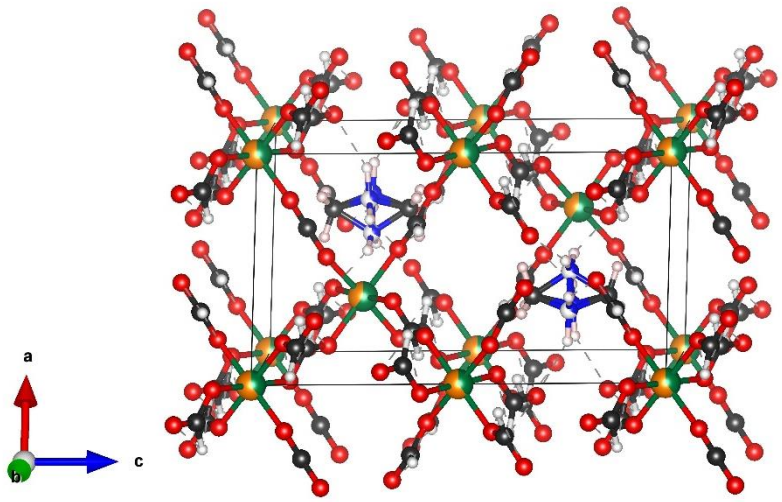

Figure 13: Crystal structure view of compound **4** affected by disorder on the metal positions. The disorder for the occupation of the site *1* (Wyckoff position 2*c*) resulting in a mix of Ni1/Fe1 is characterized by 59.66% / 40.34% respectively and for site *2* (Wyckoff position 2*b*) Fe2/Ni2, is 59.66% / 40.34%. The colour code is green for nickel and orange for iron. The oxygen, nitrogen, carbon and hydrogen atoms are represented red, grey, blue and white respectively.

refinements combined with X-Ray synchrotron data. For compound **4**, the best refinement carried out, with the neutron and X-Ray synchrotron data, recorded at 45 K and combined in a multipattern approach, revealed a disordered metal coordination sites involving both metals. The occupation of the site *1* (Wyckoff position 2*c*) made a mix of Ni1/Fe1 is characterized by 59.66% / 40.34% respectively and for site *2* (Wyckoff position 2*b*) Fe2/Ni2, is 59.66% / 40.34%. This unexpected mixed distribution influences the length of the M-O distances (see Figure 13). In general, the distance of Fe^{III}–O is *c.a.* 2.02 Å while the M^{II}–O is c.a. 2.09 Å. As shown in Table 2 the distances of Fe−O and Ni−O are 2.0226(11) and 2.0322(13), respectively. Both lengths, surprisingly, have close values to the typical M^{III}–O bond length. Probably suggesting that in the site 1, the divalent site for the well-ordered compounds (M^{II}), there is in reality a mix between $Ni^{II}/Fe^{II}/Fe^{III}$. A powerful tool to use in order to try to distinguish between divalent and trivalent metal centres is certainly given by using the bond valence calculation. From this calculation the valence of the site *1* (Wyckoff position 2*c*) referred to nickel ion instead to be as expected close to two is in reality a value closer to three [2.681 (4)]. While in the site *2* (Wyckoff position 2*b*) there is observed the expected mix between Fe^{III}/Ni^{II}.

Our results about compound **5** are quite different from those described by *Ciupa et al.*[4]. The authors reported a disorder in site *1* (Wyckoff position 2*c*) of Mg1/Fe1 of the 68% / 32% and in the site *2* (Wyckoff position 2*b*) Mg2/Fe2 of 32%/68%. Our best refinement performed on a high flux neutron diffraction data at 45 K, gives for site *1*

(Wyckoff position 2*c*) Mg1/Fe1 84% / 16% and for site *2* (Wyckoff position 2*b*) Mg2/Fe2 7% / 93%. It is clear that, from these values, site *1* shows a disorder among the metal positions of Mg/Fe, while the site 2 (Wyckoff position 2*b*) is almost fully occupied by Fe^{III} metal ions. In order to achieve the electroneutrality under this new configuration, the

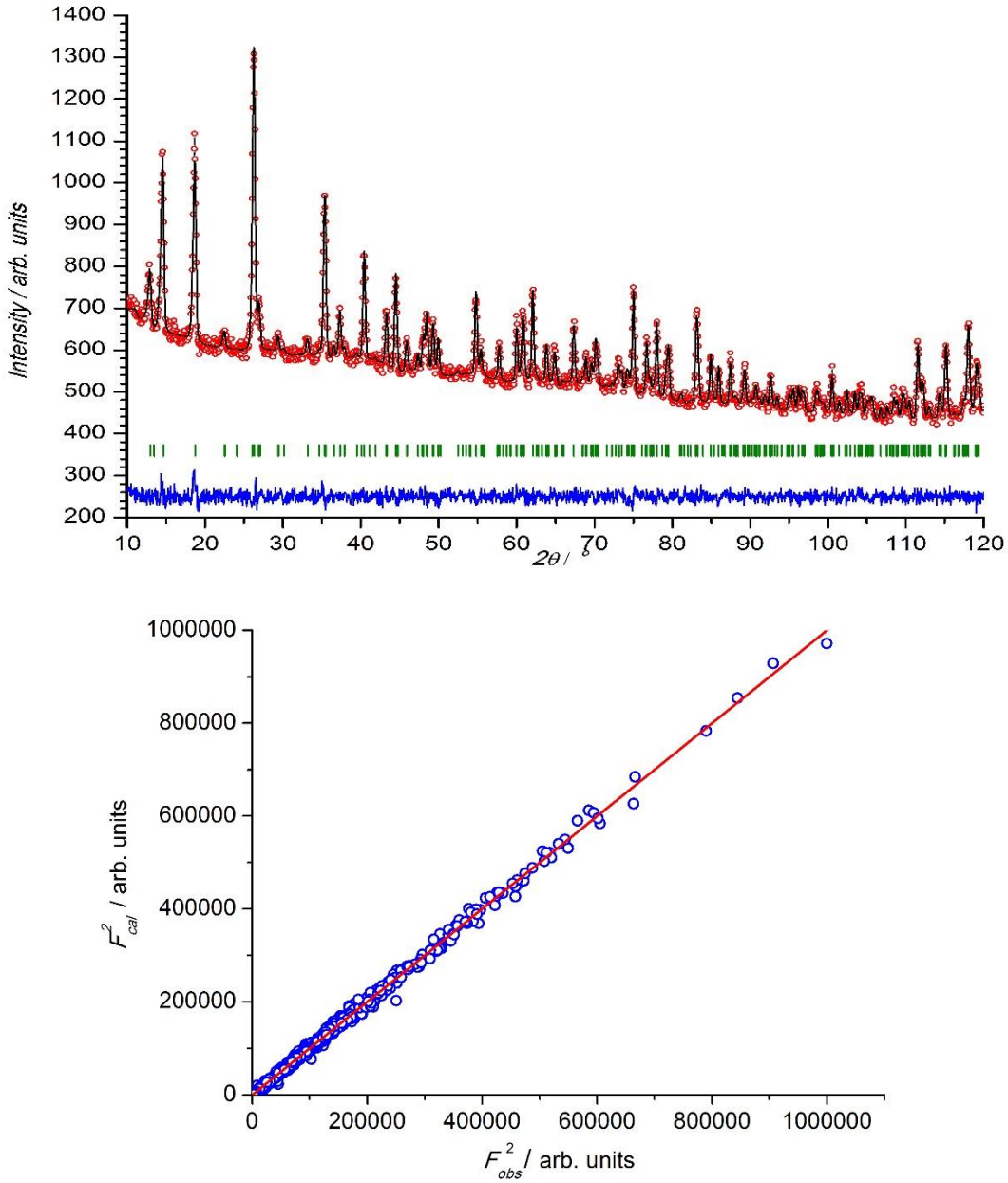

Figure 14: Experimental (open red circles) neutron powder diffraction data and calculated Rietveld refinement (black solid line) pattern for $[(CH_3)_2NH_2][Fe^{III}Ni^{II}(HCOO)_6]$. Data compound **4** were collected at 45 K using the D2B instrument with λ= 1.59465 Å. The difference between observed and calculated patterns has been represented in blue. The vertical green marks represent the position of the Bragg reflections. The multi-pattern data refinement gives the following agreement factors χ^2 = 1.53 and R_B = 4.39%, for neutron (D2B) and R_F = 3.00 % for X-ray (for CRISTAL beamline data). The experimental data are represented as open blue circles and the ideal case ($F_{cal}^2 = F_{obs}^2$) is represented as a solid red line. The refinement has been done in the space group *P*-31*c* with the associated cell parameters $a = b$ = 8.1861 (2) Å, c = 13.6426 (15) Å, $\alpha = \beta$ = 90° and γ = 120°.

oxidation number of iron in site *1* (Wyckoff position 2c) must be changed to Fe^{II} giving rise to a mixed occupation with Mg^{II}. This latter explanation is certainly the most reliable; since otherwise we would have to observe a consequent decrease of the dimethylammonium cation of *ca.* 16% (by refining the occupation parameters related to the cation) in order to achieve electroneutrality in this way. In add, neutron coherent scattering length is not correlated with atomic number as for the case of X-Ray, for this reason it is possible to accurately identify the metal elements in the framework. In fact,

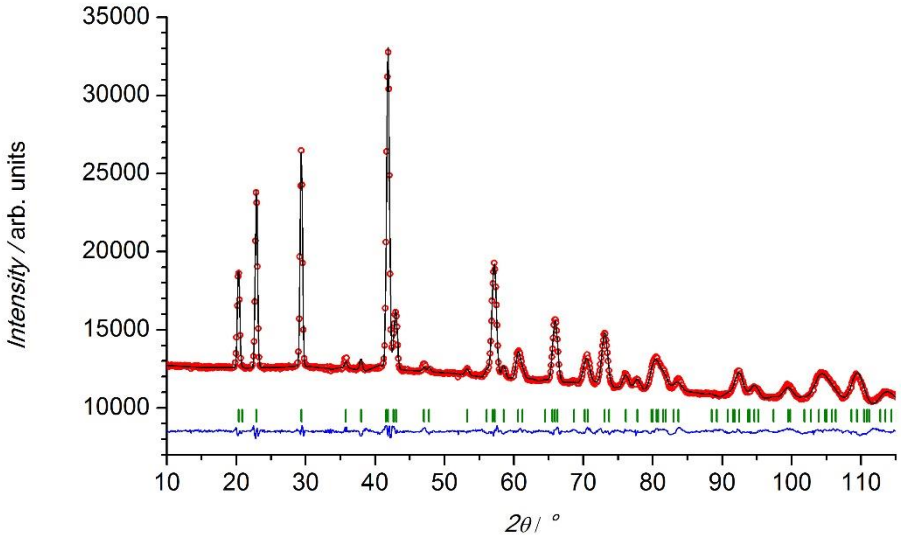

Figure 15: Experimental (open red circles) neutron powder diffraction data and calculated Rietveld refinement (black solid line) pattern for $[(CH_3)_2NH_2][Fe^{III}Mg^{II}(HCOO)_6]$. Data compound **5** were collected using D1B instrument with λ= 2.521 Å. The difference between observed and calculated patterns has been represented in blue. The vertical green marks represent the position of the Bragg reflections. Data refinement gives the following agreement factors for **5** (below) χ^2 =10.3 and R_B =3.47 %, for neutron (D1B) and R_F =3.11%.

Mg, Ni and Fe ions have the following neutron coherent scattering length values: 5.375, 10.3 and 9.45 fm, respectively. Which permit to obtain a good contrast between them. The neutron diffraction refinements for the compounds **2** and **3** give rise to a model in which the M^{II} sites do not show a significant metal disorder, the neutron coherent scattering length being 2.49 and −3.73 fm for Mn and Co respectively. The neutron powder diffractogram shown in Figure 14 corresponds to the fit of the crystal structure of compound **4**, performed by a joint refinement (multipattern fit) of the synchrotron single crystal and neutron powder diffraction D2B with λ= 1.59465 Å (χ^2= 1.53 and R_B = 4.39%, R_F = 3.00 %).

The crystal structure determined by this joint refinement is crucial to understand the magnetic structure described hereafter. Moreover, from this refinement we have discarded the occurrence of any possible structural phase transition related with the order of the hydrogen atoms which could not be determined based only on the X-Ray data. In the Figure 15 it is showed the fit of the neutron data for compound **5**, obtained by measurements at D1B recorded using λ = 2.521 Å wavelength. The structural model has been obtained using a joint refinement combining medium resolution neutron diffraction data with high resolution powder diffraction data at 45 K above the magnetic phase transition. Even thinking that we have used medium resolution neutron diffraction data, the contrast between Mg and Fe is large enough to unambiguously determine the disorder model for the metal sites. The best values of the agreement factors for the neutron diffraction fit (χ^2= 10.3 and R_B= 3.47%, R_F= 3.11%) are obtained considering the previous described disordered model.

3.5 Magnetic Studies of the compounds 2 to 5

The magnetic structure determination of the compounds **2** to **5**, at zero magnetic field, have been carried below the ordering temperature ($T_N \approx$ 32, 35, 42 K for **2**, **3** and **4**, respectively and $T_C \approx$ 13.5 K for **5**). A series of neutron diffraction measurements at different temperatures above and below the ordering temperature were carried out by using the high flux and medium resolution D1B powder diffractometer. The high flux neutron diffraction pattern collected in the paramagnetic phase (*ca.* 45 K) was used to refine the instrumental parameters. The determination of the magnetic structure of **2** to **5** was obtained performing the difference of patterns between the neutron data in the paramagnetic (*ca.* 45 K) and magnetically ordered regions. A Rietveld refinement in the paramagnetic phase was carried out using the previous obtained crystal structure model. The atomic parameters were fixed and only the instrumental and scale factor were refined. The values derived from this refinement were used in the difference refinements. The study about the magnetic structures of **2** to **5**, is compared with the previously reported study[3] on compound **1** ($T_N \approx$ 37 K). The magnetic structures can be described as two antiferromagnetic-coupled sublattices containing different spin carriers Fe^{III} and M^{II}. This evidence is supported by previous works[1,3–5,18] which are the starting points for our studies. From preliminary magnetic susceptibility measurements carried out by *Zhao et al.*[2] using FCM (field-cooled magnetization) under applied magnetic field it was revealed that compound **2** exhibits a minimum of $\chi_m T$ at 33 K (Figure 16). Below this

point $\chi_m T$ presents a sharp increase to reach a maximum value at 22 K, and it further drops reaching a value of *ca.* 9 cm^3Kmol^{-1} at 2.0 K. These features are typical for ferrimagnetic behaviour coming from the non-compensation of the interacting local spins, which are antiferromagnetically coupled. The ferrimagnetic state was confirmed by the isothermal magnetization measurements[2]. When the divalent metal ion was changed to Mn^{2+} the temperature dependence of χ_m and $\chi_m T$ is equal to 7.67 cm^3Kmol^{-1}, a value, which is well below that, expected for a pair of magnetically non-interacting high-spin Fe^{3+} and Mn^{2+} ions. In fact, it is fair to underline that this is a particular case, in which the spins of both metal ions are all 5/2, an antiferromagnetic behaviour would be expected. On the other hand, as shown in Figure **16**, weak ferromagnetism takes place. Upon cooling, $\chi_m T$ continuously decreases, and it reaches a minimum value of 3.16 cm^3Kmol^{-1} at 36 K. Below this temperature, $\chi_m T$ exhibits a sharp increase to reach a maximum value of 4.15 cm^3Kmol^{-1} at 32 K, and it further decreases to 0.33 cm^3Kmol^{-1} at 2.0 K. The magnetization measurements at 100 G reported by the same authors[2], shows that the ZFC-FC curves diverge at 35 K indicating the three-dimensional long-range antiferromagnetic ordering with weak ferromagnetism, probably due to a spin canting. Two mechanisms can give rise to this phenomenon: the antisymmetric exchange (Dzyaloshinsky-Moriya interaction) and the magnetic anisotropy. Commonly, Fe^{III} and Mn^{II} are isotropic, and for the current case, the Dzyaloshinsky-Moriya interaction would be responsible for the canting[19,41,42,42–45]. The principal cause could be the lack of the inversion centre in the $[Fe^{III}Mn^{II}(HCOO)]^-$ anionic framework. The *anti-anti* mode formate group in fact links the metal sites with a non-centrosymmetric bridges.

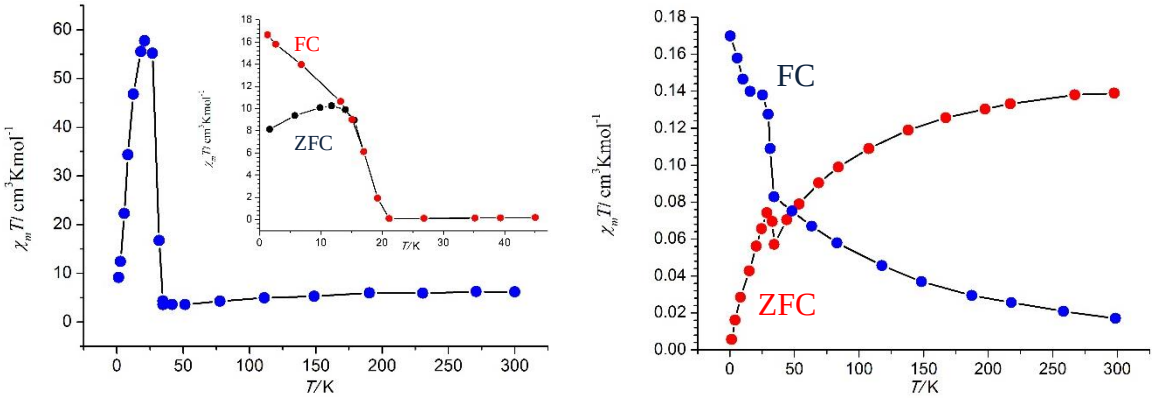

Figure 16: (Left) Thermal variation of $\chi_m T$ at 0.1 T. The inset shows the 100 G zero-field-cooled (ZFC) and 100 G field-cooled (FC) magnetization curves of compound **2**. (Right) Thermal variation of χ_m and χ_m with T at 0.1 T of compound **3**. Data obtained from Reference[2].

Concerning the magnetic properties of **4** and **5**, more recently *Ciupa et al.*[4,5] showed the temperature dependence of the magnetization *M* measured in an external magnetic field H of 100 Oe. Low temperature magnetic data, collected in zero-field-cooling (ZFC) and field-cooling (FC) conditions show that compound **4** exhibits an ordering below 42 K (see Figure 17), value which is the highest ordering temperature among this series. The large difference between the data collected in zero-field-cooling (ZFC) and field-cooling (FC) regimes suggest ferrimagnetic ordering, probably due to the non-compensation of the magnetic moments. The hysteresis observed in *M* (H) up to about 10 kOe (see the inset of Figure 17) is in agreement with this hypothesis. Furthermore the magnetization curve of **5** exhibits a magnetic order at T_C =13.5 K which is the smallest ordering temperature of this series, as the compound contains nonmagnetic magnesium ions. The outline of the σ(T) measured in the FC regime denote a ferromagnetic behaviour due to the very large difference between ZFC-FC curves and by a clear occurrence of hysteresis as shown in the inset of the Figure 17 (right). As for compound **3** the phenomena could be related to antisymmetric exchange or to single ion anisotropy[46], both leading to a small spin canting in the antiferromagnetic lattice, giving rise to a small ferromagnetic component perpendicular to the principal antiferromagnetic spin axis. Another, interesting detail is the observation of negative magnetization value in the ZFC regime that is similar to the first member of this family, compound **1**, being the first to have shown large negative magnetization value. In the previous works[1–3] it was demonstrated that **1** is characterized by a remarkable asymmetric magnetization reversal in the hysteresis loop, with a large negative magnetization and classified as Néel-type ferrimagnet. The magnetization of the two independent sites, Fe^{II} and Fe^{III} have different temperature dependencies, in fact, the site with smaller saturation magnetization orders more rapidly than the one with the larger value and consequently their magnetic moments

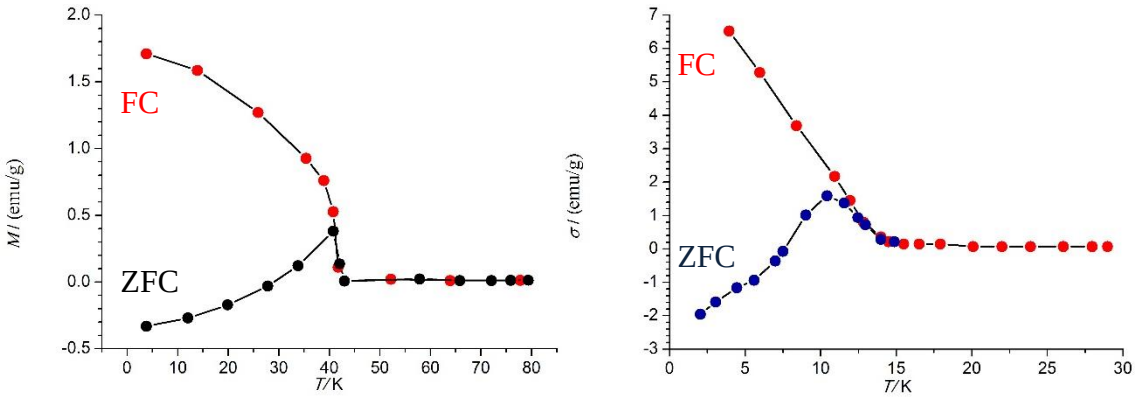

Figure 17: View of the magnetization *M* as a function of temperature measured in ZFC and FC regimes for **4** (left) and the magnetization *σ* as a function of temperature measured in ZFC and FC regimes for **5** (right) compound, respectively. Data obtained from reference[4, 5].

are not compensated among them producing a weak ferrimagnetism between sublattices coupled antiferromagnetically. The compound **5** shows a certain disorder of the metal ion positions leading to a mix occupation of Mg^{2+}/Fe^{2+} ions. It cannot be excluded that in some zones of the crystal different coupling interactions between the magnetic divalent metal (Mg^{II}/Fe^{II}) and Fe^{III} can occur. We carried out neutron experiments in order to reveal the expected effect of temperature on the magnetic coupling, but not magnetic signal was observed. We remark that the ordering temperature of **5** is 13.5 K, which is consistent with the observed dilution of the divalent site, and it is partially occupied by Mg^{II}/Fe^{II} with only a 15.6 % of Fe^{II} ions. Therefore, based on the neutron data, the most probable scenario for the Mg-based compound is that the ferromagnetic signal observed in the macroscopic magnetometry measurements are due to the short range order of the Fe^{III}-Fe^{II} region present in this compound, which is compatible with the absence of magnetic reflections below 13.5 K (Figure 18, bottom right).

3.5.1 Magnetic structures investigation of compounds **2**, **3** and **4**

The neutron diffraction patterns recorded from paramagnetic to *ca.* 2 K for **2**, **3** and **4** show the increase of intensity on some Bragg reflections, suggesting the occurrence of a long-range magnetic ordering (see Figure 18), which are in agreement with the magnetometry measurements shown earlier. The only exception is **5** (Figure 18 bottom right), that does not show any magnetic signal as has been explained in the previous section. The observed magnetic contribution, on top of nuclear reflections, suggests that the magnetic reflections can be indexed with the propagation vector **k** = (0, 0, 0). The k-Search program included in the FullProf Suite[28] was used in order to confirm the occurrence of a propagation vector **k** = (0, 0, 0)[43].

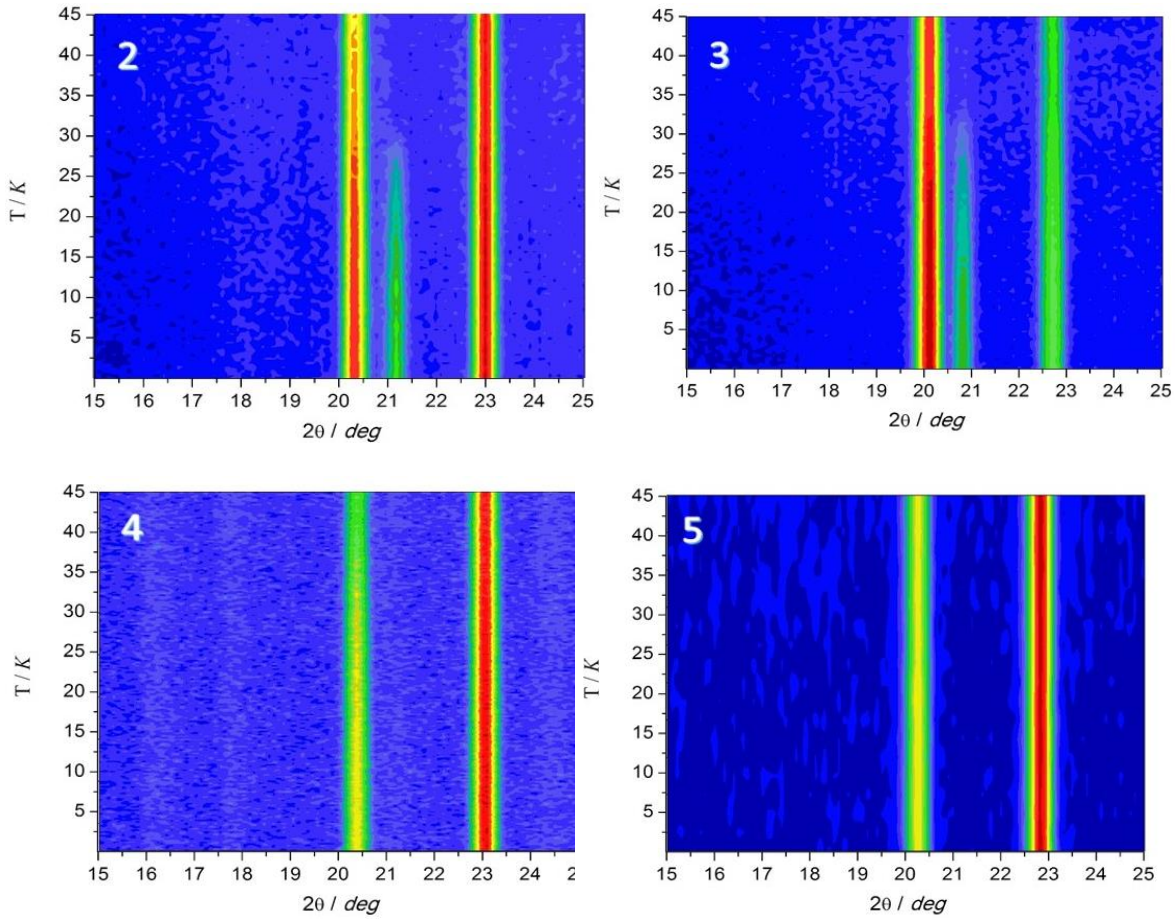

Figure 18: Detail of the mesh plot of the thermodiffractograms corresponding to compounds **2** (top left), **3** (top right), **4** (bottom left) and **5** (bottom right). All data are collected at D1B in the range temperature of 2- 45 K. A clear increase of the reflections (1 0 0) at 2θ = 20.4° for **2**, 20.2° for **3** while in the case of **4** the only clearly observed magnetic reflection correspond to the (1 −1 0) at 2θ = 20.5°. Then a new (0 0 2) reflection increase corresponding at 2θ value of 21.2° for **2**, 20.8° for **3**. And the last reflection (1 0 1) increase at 2θ of 23.0° for **2**, 22.7° for **3.**

The weak magnetic contribution observed on these materials, together with the high overlapping between nuclear and magnetic reflections, and the background produced by the high number of hydrogen atoms in these compounds (0.61 hydrogen atoms per non-hydrogen atom), precludes an accurate magnetic structure refinement directly from these patterns. These difficulties can partially be circumvented by working with difference patterns. For that, we must subtract the normalized nuclear intensity of the paramagnetic phase collected at 45 K from the ordered phase pattern (*ca.* 2 K). This difference pattern isolates the magnetic contribution and, therefore, a more accurate indexing of the magnetic reflections and magnetic structure determination can be undertaken (see Figure 19). The representational analysis technique described by Bertaut[48] has been used to determine the possible magnetic structures compatible with the $P\bar{3}1c$ space group and

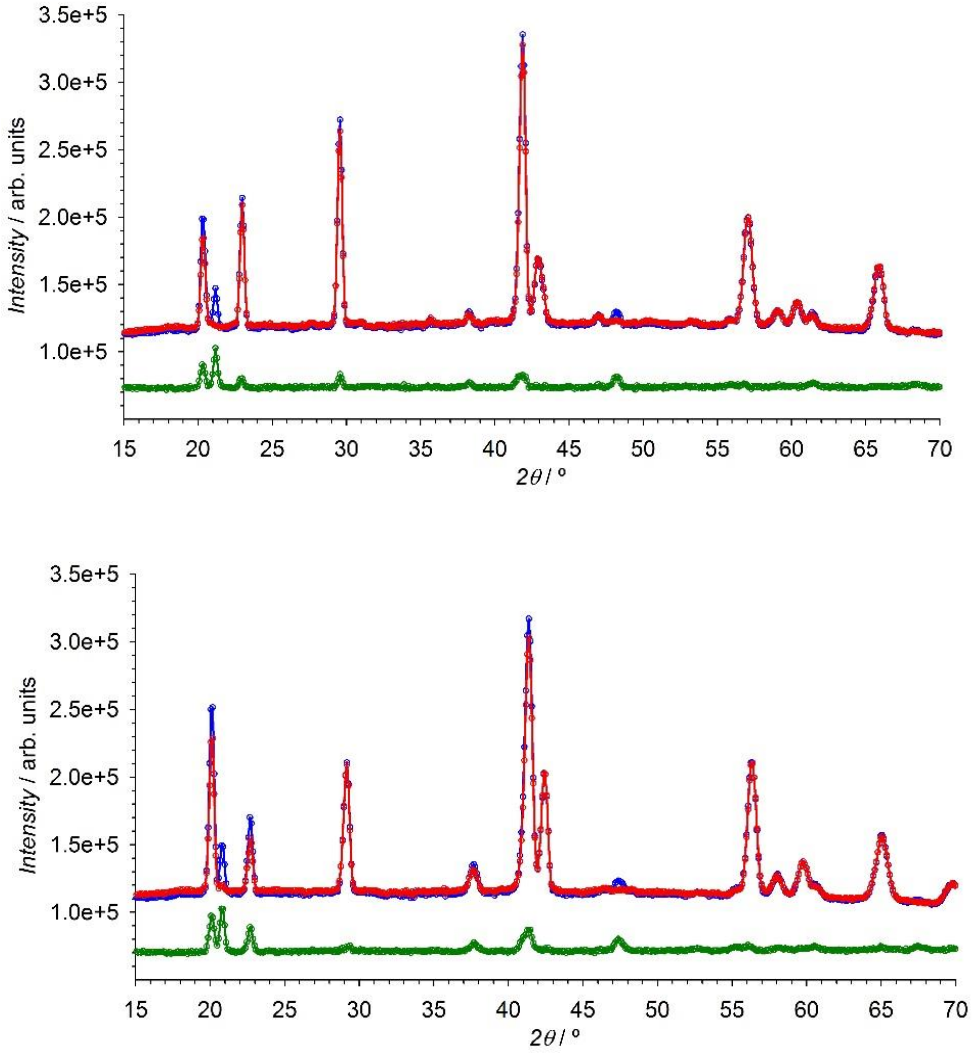

Figure 19: Neutron powder patterns of **2** (top) and **3** (bottom) collected at 1.5 K (blue) and 45 K (red) using the high flux D1B diffractometer. The difference diffraction pattern is represented in green. The intensity of the calculated difference pattern was shifted to an arbitrary value of ca. 58000 units in order to achieve a similar background as in the original patterns.

propagation vector **k** = (0, 0, 0) for **2** and **3** compounds. Six irreducible representations (*irreps*) of the group G_k, (Γ_1 to Γ_6) and the corresponding set of basis vectors for each irreducible representation was determined using the program BasIreps[49]. The representational analysis provides the expression of the magnetic moment Fourier components as linear combinations of basis vectors of the irreducible representations of the propagation vector group $G_{\mathbf{k}}$. The basis vectors describe the possible arrangements of magnetic structures. From the six possible *irreps* provided by BasIreps, Γ_1 to Γ_4 are real and one-dimensional, while Γ_5 and Γ_6 are complex and two-dimensional. The magnetic representation Γ_M for each magnetic site [Wyckoff position 2*b* for Fe(1) and for 2*c* for M^{2+}(1)] can be decomposed as direct sum of *irreps* by applying the great orthogonality

theorem. In the present case being where **k** = (0, 0, 0), all the Fourier coefficients must be real; therefore, the *irreps* from Γ_1 to Γ_4 are in principle direct possible solutions.

The complex 2D *irreps* should be converted to real giving rise to a new set of possible magnetic structures. Since both metallic networks (M^{II} and Fe^{III}) become magnetically ordered at the same temperature, it is expected that the magnetic structure is described within the same magnetic representation. Γ_3 is the only 1D *irrep* that appears in the magnetic representation Γ_M for both Wyckoff positions (2*b* and 2*c*). However, this solution, where all magnetic moments are strictly along the *c*-axis, is not able to reproduce the experimental data; consequently, we have to analyse the 2D *irreps*. An analysis of the complex representations shows that they can be transformed in two two-dimensional physically irreducible representations (PIR). We have used BasIreps in the mode reading the PIR database provided in reference[50]. In the present case the Γ_5 and Γ_6 *irreps*, which are complex and two-dimensional, can be transformed to real matrices (PIR: ${}^{p}\Gamma_6$ and ${}^{p}\Gamma_3$, respectively) by application of a unitary transformation (see Table 4).

Table 4: Physically Irreducible Representations of the space group $\boldsymbol{P\bar{3}1c}$ for **k** = (0, 0, 0)[a].

	$(1\|000)$	$(3^{+}_{00z}\|000)$	$(3^{-}_{00z}\|000)$	$(2_{2x0}\|00\frac{1}{2})$	$(2_{x2x0}\|00\frac{1}{2})$	$(2_{x-x0}\|00\frac{1}{2})$	$(-1\|000)$	$(-3^{+}_{00z}\|000)$	$(-3^{-}_{00z}\|000)$	$(m_{0yz}\|00\frac{1}{2})$	$(m_{x0z}\|00\frac{1}{2})$	$(m_{xxz}\|00\frac{1}{2})$
${}^{p}\Gamma_1$	1	1	1	1	1	1	1	1	1	1	1	1
${}^{p}\Gamma_2$	1	1	1	-1	-1	-1	1	1	1	-1	-1	-1
${}^{p}\Gamma_3$	$\begin{pmatrix}1 & 0\\0 & 1\end{pmatrix}$	$\begin{pmatrix}-a & -b\\b & -a\end{pmatrix}$	$\begin{pmatrix}-a & b\\-b & -a\end{pmatrix}$	$\begin{pmatrix}-a & -b\\-b & a\end{pmatrix}$	$\begin{pmatrix}1 & 0\\0 & -1\end{pmatrix}$	$\begin{pmatrix}-a & b\\b & a\end{pmatrix}$	$\begin{pmatrix}1 & 0\\0 & 1\end{pmatrix}$	$\begin{pmatrix}-a & -b\\b & -a\end{pmatrix}$	$\begin{pmatrix}-a & b\\-b & -a\end{pmatrix}$	$\begin{pmatrix}-a & -b\\-b & a\end{pmatrix}$	$\begin{pmatrix}1 & 0\\0 & -1\end{pmatrix}$	$\begin{pmatrix}-a & b\\b & a\end{pmatrix}$
${}^{p}\Gamma_4$	1	1	1	1	1	1	-1	-1	-1	-1	-1	-1
${}^{p}\Gamma_5$	1	1	1	-1	-1	-1	-1	-1	-1	1	1	1
${}^{p}\Gamma_6$	$\begin{pmatrix}1 & 0\\0 & 1\end{pmatrix}$	$\begin{pmatrix}-a & -b\\b & -a\end{pmatrix}$	$\begin{pmatrix}-a & b\\-b & -a\end{pmatrix}$	$\begin{pmatrix}-a & -b\\-b & a\end{pmatrix}$	$\begin{pmatrix}1 & 0\\0 & -1\end{pmatrix}$	$\begin{pmatrix}-a & b\\b & a\end{pmatrix}$	$\begin{pmatrix}-1 & 0\\0 & -1\end{pmatrix}$	$\begin{pmatrix}a & b\\-b & a\end{pmatrix}$	$\begin{pmatrix}a & -b\\b & a\end{pmatrix}$	$\begin{pmatrix}a & b\\b & -a\end{pmatrix}$	$\begin{pmatrix}-1 & 0\\0 & 1\end{pmatrix}$	$\begin{pmatrix}a & -b\\-b & -a\end{pmatrix}$

[a] The symmetry elements are written according to Seitz's notation. $a = 1/2$ and $b = \sqrt{3}/2$.
Notice that the ordering of PIR (database: PIR_data.txt, by Harold T. Stokes and Branton J. Campbell, 2013) is different than those obtained directly from the *irreps* calculations done by BasIreps[49].
The magnetic space groups of the 1D *irreps* (all of them maximal subgroups of *P*-31*c*1') are unambiguously determined as ${}^{p}\Gamma_1$: *P*-31*c*, ${}^{p}\Gamma_2$: *P*-31*c*'; ${}^{p}\Gamma_4$: *P*-3'1*c*'; ${}^{p}\Gamma_5$: *P*-3'1*c*. For the 2D *irreps* the magnetic space groups are of lower symmetry and depend on the particular basis vectors used to describe the magnetic structure.

The magnetic representation Γ_M for 2*b* and 2*c* Wyckoff positions (Fe^{III} and M^{II}, respectively) can be decomposed as a direct sum of PIR.

$$\Gamma_M(2b) = {}^{p}\Gamma_1 \oplus {}^{p}\Gamma_2 \oplus {}^{p}\Gamma_3$$

$$\Gamma_M(2c) = {}^{p}\Gamma_2 \oplus {}^{p}\Gamma_3 \oplus {}^{p}\Gamma_5 \oplus {}^{p}\Gamma_6$$

Considering that both sublattices should be ordered within the same magnetic representation, the possible PIR are those that appear simultaneously in the decomposition of the magnetic representation of 2*b* and 2*c* sites. Then the magnetic structure can only be described by $^{p}\Gamma_2$, $^{p}\Gamma_3$ or a combination of both PIR. In the case of the 2D *irrep* $^{p}\Gamma_3$ the associated magnetic structures are constrained to be in the *ab*-plane, while the 1D *irrep* $^{p}\Gamma_2$ gives a contribution strictly along the *c*-axis. The model described by $^{p}\Gamma_2$ is not able to fit the experimental data for compounds **2** and **3**, while the models associated with $^{p}\Gamma_3$ give reasonably good agreement with experimental data.

We have explored the possible solutions without taking into account the symmetry using the simulated annealing procedure implemented in FullProf [28] giving a small component along the *c*-axis. In order to account for this component, a combination of both PIR is necessary (see Table 5).

Table 5 : Basis vectors of the physically irreducible representations for the 2*b* and 2*c* sites, which give the best model for the magnetic structure. We have added the notation of the *irreps* provided in the Bilbao Crystallographic Server[51,52].

				$^{2}BV_1$			
$^{p}\Gamma_2(GM_2^{+})$	2*b* (0,0,0)	Fe^{III}	*x*, *y*, *z*	(0,0,1)			
			x, *x*−*y*, −*z*+1/2	(0,0,1)			
	2*c* (1/3,2/3,1/4)	M^{II}	*x*, *y*, *z*	(0,0,1)			
			−*x*, −*y*, −*z*	(0,0,1)			
				$^{3}BV_1$	$^{3}BV_2$	$^{3}BV_3$	$^{3}BV_4$
$^{p}\Gamma_3(GM_3^{+})$	2*b* (0,0,0)	Fe^{III}	*x*, *y*, *z*	(1,0,0)	(0,1,0)	(1, 2,0)	(−2, −1,0)
			x, *x*-*y*, −*z*+1/2	(−1,0,0)	(1,1,0)	(−1, −2,0)	(−1, 1,0)
	2*c* (1/3,2/3,1/4)	M^{II}	*x*, *y*, *z*	(1,2,0)	(1,0,0)		
			−*x*, −*y*, −*z*	(1,2,0)	(1,0,0)		

We have also used the program k-SUBGROUPMAG from the Bilbao Crystallographic Server[51,52] in order to determine the Shubnikov groups associated with the mixture of the two *irreps* $^{p}\Gamma_2$ and $^{p}\Gamma_3$. The only possible magnetic groups are: *P*-1 and *C*2'/*c*'. The use of basis vectors $^{3}BV_1(Fe^{III})$, $^{3}BV_2(Fe^{III})$, $^{3}BV_1(M^{II})$, $^{2}BV_1(Fe^{III})$ and $^{2}BV_1(M^{II})$ give rise to the *P*-1 magnetic space group (see Figure 20).

Using only five parameters we obtain a configuration (similar to that provided by *C*2'/*c*' but with the moments rotated 30º around the *c*-axis) showing good results; however, the convergence of the refinement is not achieved when all parameters of *P*-1 (six free parameters) are included. The use of basis vectors $^{3}BV_3(Fe^{III})$, $^{3}BV_4(Fe^{III})$, $^{3}BV_2(M^{II})$, $^{2}BV_1(Fe^{III})$ and $^{2}BV_1(M^{II})$ give rise to a configuration of five free parameters

corresponding to one of the three equivalent variants of the *C*2'/*c*' Shubnikov group (subgroups of $P\bar{3}1c1$'). The occurrence of the three variants of *C*2'/*c*' is due to the loss of the ternary axis at the magnetic transition in the parent group $P\bar{3}1c1$'. The three possible orientations, with respect to the unit cell of the parent group, of the magnetic structure described by the *C*2'/*c*' are shown in Figure 21.

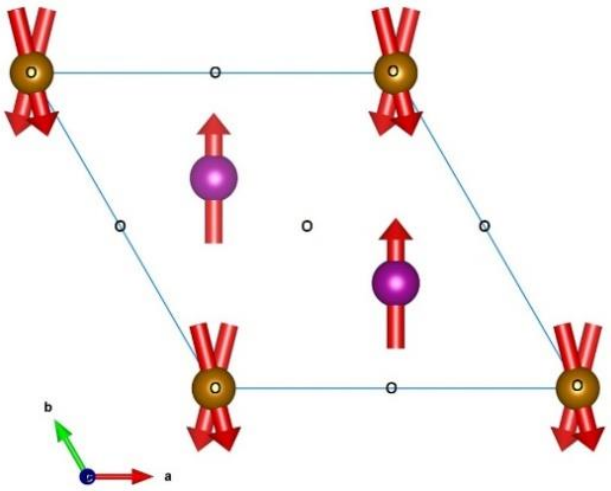

Figure 20: View along the *c*-axis, trigonal unit cell, of the magnetic structure solved in the *P*-1 Shubnikov group together with the symmetry elements.

These models correspond to three different domains within a single crystal, so that in neutron powder diffraction the three variants contribute as different crystallites to the pattern. The magnetic model described by *C*2'/*c*' Shubnikov group gives rise to a magnetic structure where the magnetic moments of both sites are mainly antiferromagnetically coupled in the *ab*-plane, with a small component along the *c*-axis. As a result of peak overlap in the trigonal crystal system, neutron powder diffraction is not able to distinguish the absolute direction of the magnetic moments within the *ab*-plane. Based on the *ab initio* calculations for compound **2**, the projection of the easy axis for the cobalt ions within the *ab*-plane gives a value of 60º from the *a*-direction (variant 1).

Moreover, according to the symmetry relations, the two symmetry related Fe^{III} ions are not strictly antiferromagnetically coupled with the M^{II} ions. The moments of the Fe^{III} ions are slightly tilted among them, with an angle of *ca.* 20 and 13º between adjacent Fe^{II} ions along the *c*-axis for the compound **2** and **3**, respectively. The Rietveld refinement of the difference pattern using the mentioned combination of PIR is shown in Figure 22.

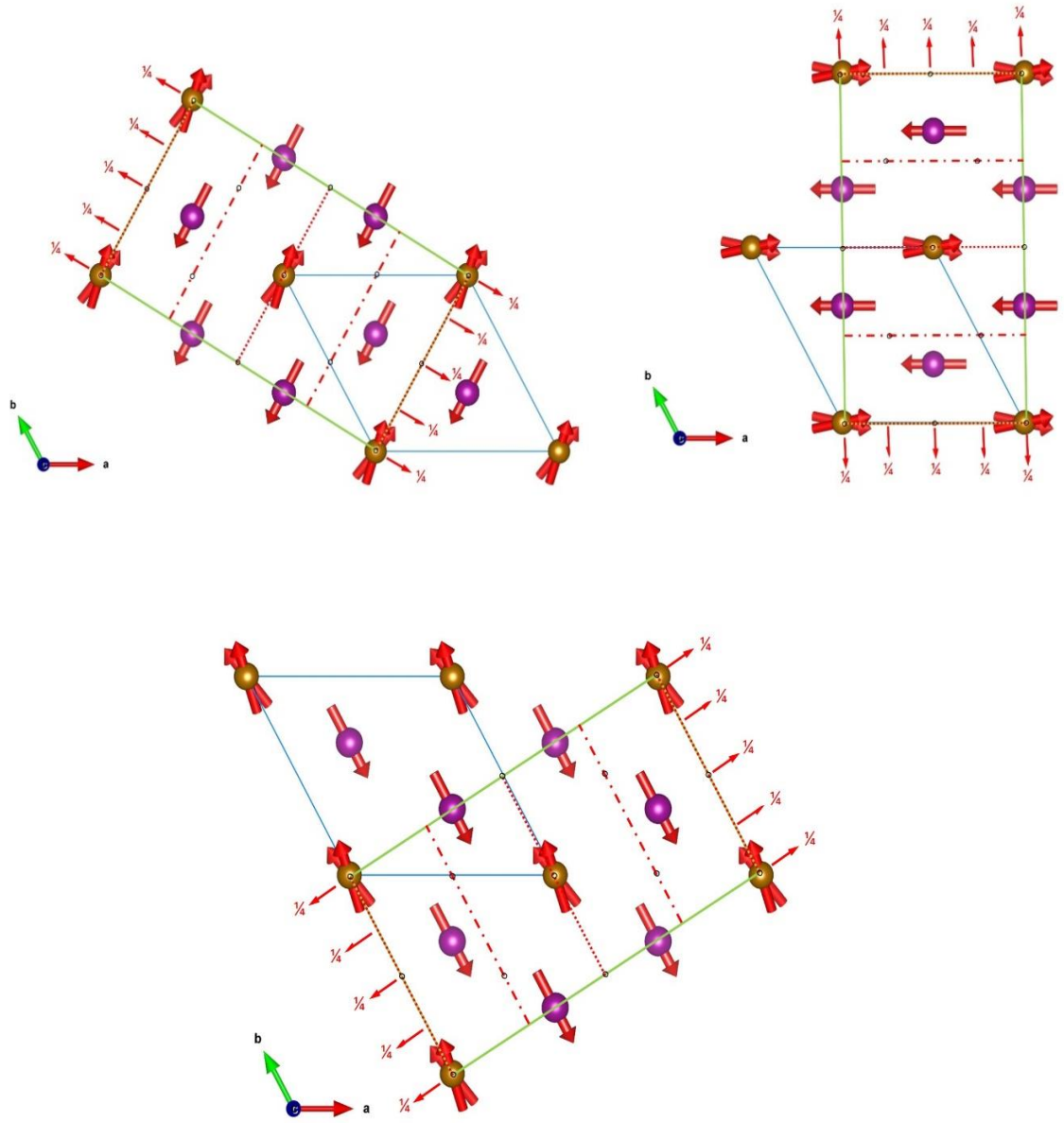

Figure 21: View along the *c*-axis, trigonal unit cell (blue), of the three possible variants compatible with the *C*2'/*c*' Shubnikov group. The monoclinic unit cell is represented in green together with the symmetry operations. The time reversal symmetry operation is represented following the Daniel B. Litvin notation (red). The unit cell transformations are $\boldsymbol{a}' = \boldsymbol{a}+\boldsymbol{b}$; $\boldsymbol{b}' = -\boldsymbol{a}+\boldsymbol{b}$; $\boldsymbol{c}' = \boldsymbol{c}$ for variant 1 (top left), $\boldsymbol{a}' = \boldsymbol{a}$; $\boldsymbol{b}' = \boldsymbol{a}+2\boldsymbol{b}$; $\boldsymbol{c}' = \boldsymbol{c}$ for variant 2 (top right) and $\boldsymbol{a}' = -\boldsymbol{b}$; $\boldsymbol{b}' = 2\boldsymbol{a}+\boldsymbol{b}$; $\boldsymbol{c}' = \boldsymbol{c}$ for variant 3 (bottom).

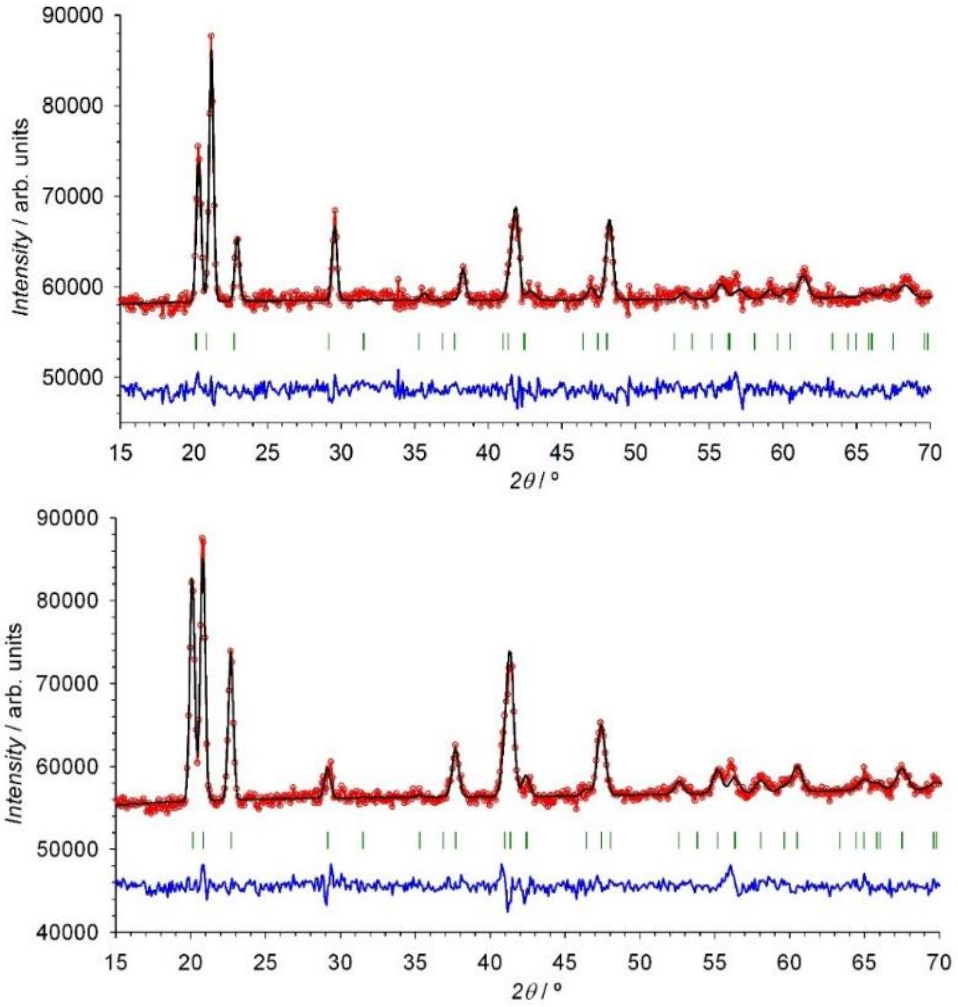

Figure 22: Fit of the difference pattern of compound **2** (top) and **3** (bottom) using the combination of both p-irreps (${}^{p}\Gamma_2 \oplus {}^{p}\Gamma_3$) (see main text). The Rietveld data refinement gives the agreement factors $\chi^2 = 3.87$, and magnetic $R_B = 12.9$ % for **2**, and $\chi^2 = 3.22$ and $R_B = 7.26$ % for **3**. The experimental data is represented by open red circles, the calculated Rietveld patterns are shown as solid black lines, and the differences between observed and calculated patterns is plotted as solid blue lines. The vertical green marks represent the positions of the Bragg reflections.

The Fe^{III} (2*b*) and the M^{II} (2*c*) atoms are connected through *anti-anti* carboxylate bridges. The Fe^{III}–M^{II} interaction through this bridge has an antiferromagnetic nature, as observed in magnetometry measurements. The antiferromagnetic coupling takes place mainly in the *ab*-plane (see Figure 23). Each carboxylate group connects two ions with different valence along the [2/3, 1/3, −1/4], [−1/3, −2/3, −1/4], [−1/3, 1/3, −1/4], [−2/3, −1/3, 1/4], [1/3, 2/3, 1/4] and [1/3, −1/3, 1/4] directions, giving rise to the final three-dimensional structure. It deserves to be noted that according to the crystal structure, all carboxylate groups are symmetry related and therefore equivalent. However, from the magnetic point of view the exchange coupling of these carboxylate groups should be slightly different, giving rise to the two different magnetic orientations of the Fe^{III} ions. This ultimately means that the magnetic space group has lower symmetry than the paramagnetic group.

We cannot refine the crystal structure in the monoclinic group because within our precision we do not see significant variation of the nuclear intensities.

The macroscopic magnetic measurements of **2** show the occurrence of an antiferromagnetic coupling between the neighbouring metal ions. Below T_N the susceptibility exhibits a sharp increase. This feature is compatible with a ferrimagnetic behaviour probably due to the non-compensation of the magnetic moments of the different ions present in this compound. From the neutron diffraction experiments, this scenario is confirmed; the refined magnetic moments of the Fe^{III}(2*b*) and the Co^{II}(2*c*) atoms are 4.33(9) and 2.5(1) μ_B, respectively. The modulus of the resultant magnetization calculated for a molecular unit $\mathbf{M} = \{[\mathbf{m}_{2b}(I) + \mathbf{m}_{2b}(II) + \mathbf{m}_{2c}(I) + \mathbf{m}_{2c}(III)]/2\}$ [with (I) : *x*, *y*, *z*; (II) : $-y$, $-x$, $-z+1/2$ and (III) : $-x$, $-y$, $-z$], is approximately 1.7 μ_B. This value is slightly low for a collinear ferrimagnet with opposite spins of S= 5/2 and S= 3/2 (2 μ_B). However, a small deviation of the value of 2 μ_B for completely polarized magnetic spins and antiferromagnetic coupling is possible when the magnetic moments are not strictly collinear or when a spin delocalization effect occurs. Therefore, this model produces a ferrimagnetic layered structure, where the layers formed by the magnetic moments of the Co^{II} are stacked following an *AAA* sequence, while the layers formed for the Fe^{III} are stacked following an *ABAB* sequence, both packed along the *c*-axis see (Figure 23). Along the *c*-axis, the magnetic contribution on the Co^{II} site is notably weaker than the component on the Fe^{III} site. Moreover, the refined structure give rise to a model where both sites are antiferromagnetically coupled along the *c*-axis. The magnetic measurements of **3** are slightly different from those of **1** or **2**, since both metallic centres have the same spin state, with s = 5/2. The electronic configurations of the high-spin Mn^{II} and Fe^{III} are also very similar, both being spin sextets with A_{1g} as orbital ground state in case of O_h symmetry and with Landé factors close to 2.0. Therefore, we expect a collinear antiferromagnetic coupling between both ions. The magnetometry measurements show a global antiferromagnetic behaviour, which was corroborated by the negative value of the Weiss constant after the Curie-Weiss fit of the experimental data. However, at T_N the susceptibility curve as function of the temperature presents a jump, which should be due either to the non-compensation of the magnetic moments of both networks or to the occurrence of a weak spin-canting. The refined magnetic moments for each magnetic site give a similar value, being slightly lower for Fe^{III} than for Mn^{II} ion [4.3(1) and 4.4(1) μ_B, respectively]. This feature, together with the packing sequence of the Fe^{III} ions, which

follow the same order as in compound **2**, produces a non-compensation of the magnetic moment within the *ab*-plane.

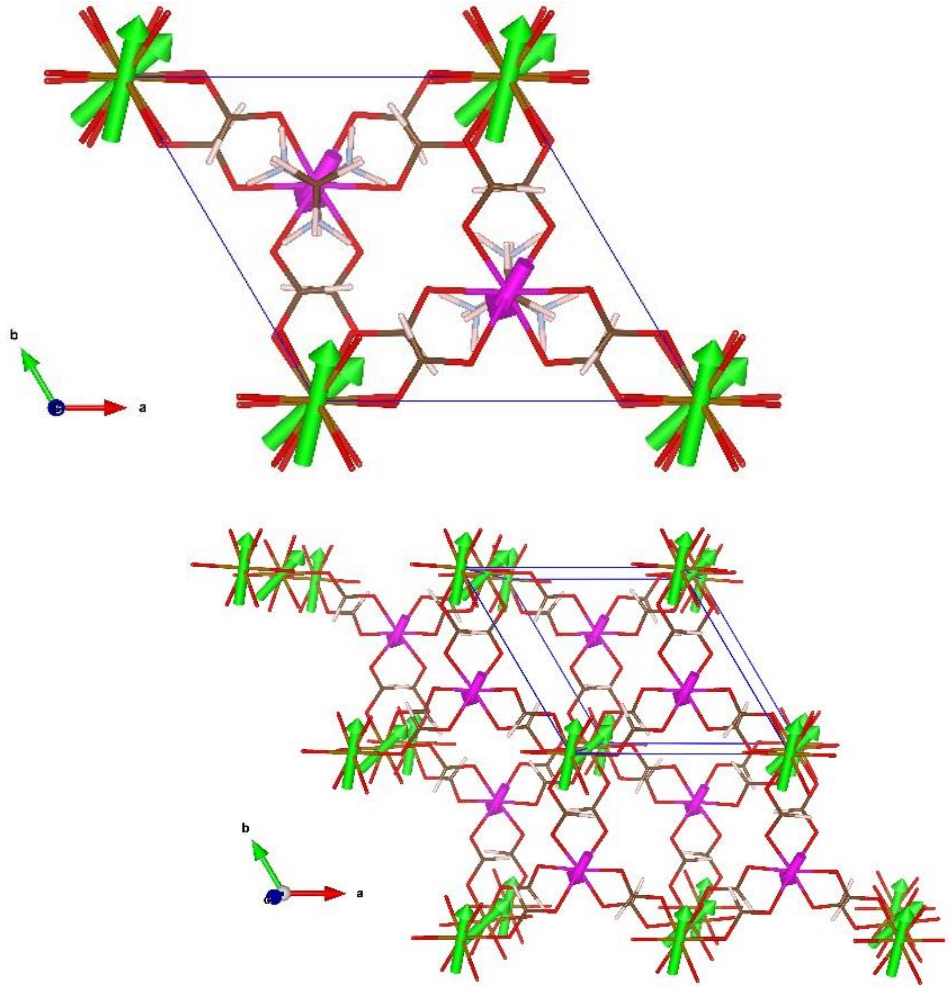

Figure 23: (Top) View along the *c*-axis of the unit cell of compound **2**, together with the magnetic moment of the Co^{II} and Fe^{III} ions represented as pink and green arrows respectively. (Bottom) Perspective view of a fragment of **2**, where the *ABAB* stacking sequence of the Fe^{III} ions along the *c*-axis is noticed. A single unit cell has been represented together with the magnetic structure as reference for the reader. For the sake of clarity, the $[(CH_3)_2NH_2]^+$ counterions have been omitted in this figure. The modulus of each arrow has been proportionally scaled to the magnetic moment of each magnetic site.

Moreover, the fit of the data gives a component of the magnetic moments along the *c*-axis for the Fe^{III} sites, which produces a tilting of the magnetic moment with respect to the *ab*-plane of around 15°(5) (see Figure 24). This tilting angle has the same sign for all Fe^{III} sites. However, the refined value of the magnetic contribution along the *c*-axis of the Mn^{II} ion is zero within the experimental error. Therefore, this model is compatible with the occurrence of a spin-canting.

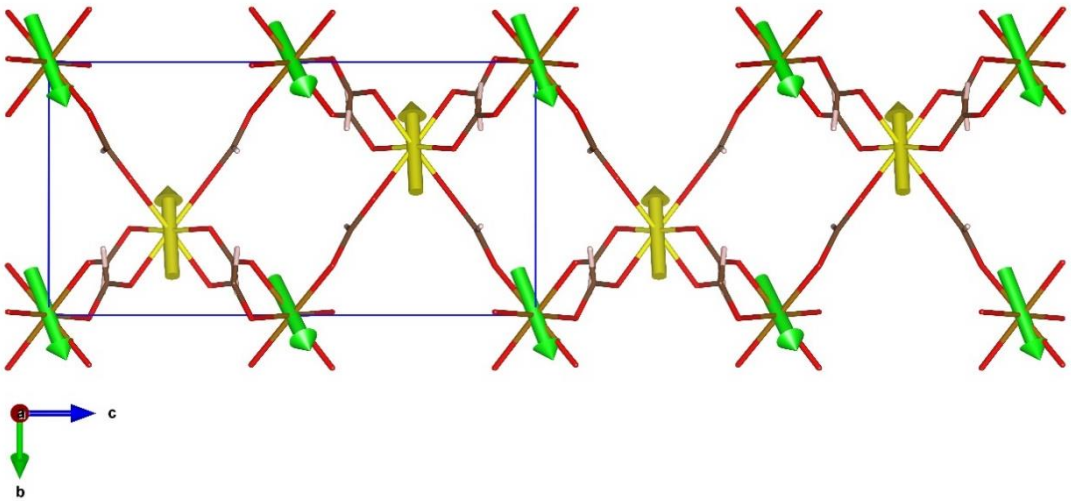

Figure 24: View along the *a*-axis of the unit cell of compound **3**, together with the magnetic moments of the Mn^{II} and Fe^{III} ions represented as yellow and green arrows respectively. The occurrence of a weak canting along the *c*-axis is clearly observed. For the sake of clarity, only the $[Fe^{III}Mn^{II}(HCOO)_6]^-$ framework has been represented, together with the magnetic structure obtained from the Rietveld refinement. The modulus of each arrow has been proportionally scaled to the magnetic moment of each magnetic site.

The magnetic moments obtained after the Rietveld refinement using the combination of ${}^{p}\Gamma_2$ and ${}^{p}\Gamma_3$, are listed in Table 5. The modulus of the resultant magnetization calculated for formula $\mathbf{M} = \{[\mathbf{m}_{2b}(\mathrm{I}) + \mathbf{m}_{2b}(\mathrm{II}) + \mathbf{m}_{2c}(\mathrm{I}) + \mathbf{m}_{2c}(\mathrm{III})]/2\}$ [with (I) : *x*, *y*, *z*; (II) : −*y*, −*x*, −*z*+1/2 and (III) : −*x*, −*y*, −*z*] is approximately 1.4 μ_B. The projections in the *ab*-plane of the magnetic moments of Fe^{III} and Mn^{II} are *ca*. 3.97(30) μ_B and 4.44(11) μ_B. The difference between them is 0.5 μ_B, value which is smaller than the component along the *c*-axis. Consequently, it is reasonable to think that the signal observed in magnetometry measurements should be mainly produced by the occurrence of a canting along the *c*-axis. The refined magnetic structures for **2** and **3** are therefore compatible with the macroscopic magnetic measurements; moreover, the refined values of the magnetic moments are in good agreement with other metal-organic compounds[53–57]. However, the values of the magnetic moments obtained for the Fe^{III} sites are slightly higher than those previously observed for compound **1**, suggesting that the possible delocalization of the magnetic moment into the bridging ligands is less important.

The magnetic structure of compound **4**, was analysed using the same procedure as for compounds **2** and **3** (see Tables 4 and 5). As described before, the magnetic structure can only be described by ${}^{p}\Gamma_2$, ${}^{p}\Gamma_3$ or a combination of both PIR. Experimentally the magnetic structure is well described by the ${}^{P}\Gamma_2$ irrep, whose list of basis vector is given in Table 5. The Shubnikov group corresponding to the irrep ${}^{P}\Gamma_2$ is $P\bar{3}1c'$ describing a magnetic structure with all magnetic moments strictly coupled along the *c*-axis.

The Rietveld refinement of the difference pattern, obtained between the paramagnetic phase and the low temperature (2 K) phase, using the mentioned irrep, is shown in Figure 25.

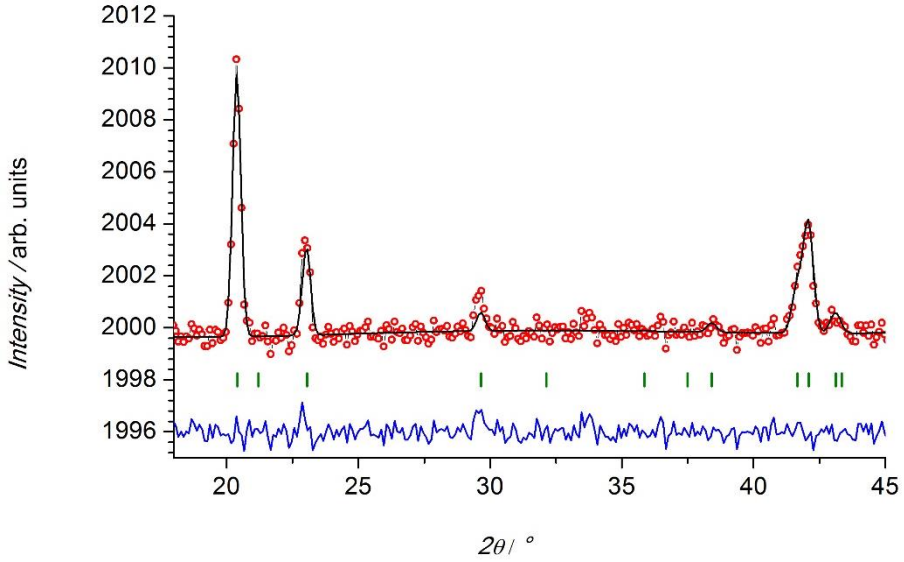

Figure 25. Fit of the difference pattern of compound **4** using the p-irreps ($^{p}\Gamma_2$). The Rietveld data refinement gives the agreement factors χ^2 =1.806, and magnetic R_B=8.28%. Experimental data are represented by open red circles, the calculated Rietveld patterns are shown as solid black lines, and the differences between observed and calculated patterns are plotted as solid blue lines. The vertical green marks represent the positions of the Bragg reflections.

The magnetic moments of the metal sublattices determined by the refinement of the D1B data at 2 K, using the difference patterns between the paramagnetic and the magnetically ordered phase, are listed below in the Table 6.

The non-compensation of the magnetic moments produces a net ferromagnetic component along the *c*-axis. The ferromagnetic moment obtained from neutron data recorded at 2 K is calculated as the vector sum of the magnetic moments along *c*-axis, and is *ca*. 0.6 μ_B, which is approximately twice the value obtained by macroscopic measurements (0.31 μ_B), see Figure 26.

The macroscopic magnetic measurements of **4** show the occurrence of an antiferromagnetic coupling between the neighbouring metal ions, together with a ferromagnetic signal which can be due to a weak spin-canting or a non-compensation of the magnetic moments. Based on the refinement of the magnetic structure the second option is the most plausible explanation.

Table 6: Magnetic moment components (μ_B) determined for each atom site through Rietveld refinement using the combination of ${}^{p}\Gamma_2$ (Shubnikov group $P\bar{3}1c'$)

		SOF	M_a	M_b	M_c	M_{total}	$M_{calculated}$	M_{sum}
Ni/Fe (2*c*)	Ni	60.66%	0	0	−3.36(1)	−3.36(1)	−1.193	3.21
	Fe	39.34%					−2.017	
Fe/Ni (2*b*)	Fe	62.82%	0	0	3.91(3)	3.91(3)	2.98	3.79
	Ni	37.18%					0.81	

Atomic positions: Fe^{III}: (0, 0, 0), and Ni^{II}: (1/3, 2/3, 1/4) corresponding to 2*b* and 2*c* of the Wyckoff positions.

In order to explain the difference between the macroscopic magnetization and the neutron diffraction results, it should be noted that the magnetization measurements were performed using a powder sample, and therefore there is a random distribution of the sample. This random distribution involve that only part of the magnetic moments are aligned with the external magnetic field and as consequence the macroscopic magnetization should be notable smaller than the value obtained from the neutron diffraction refinement.

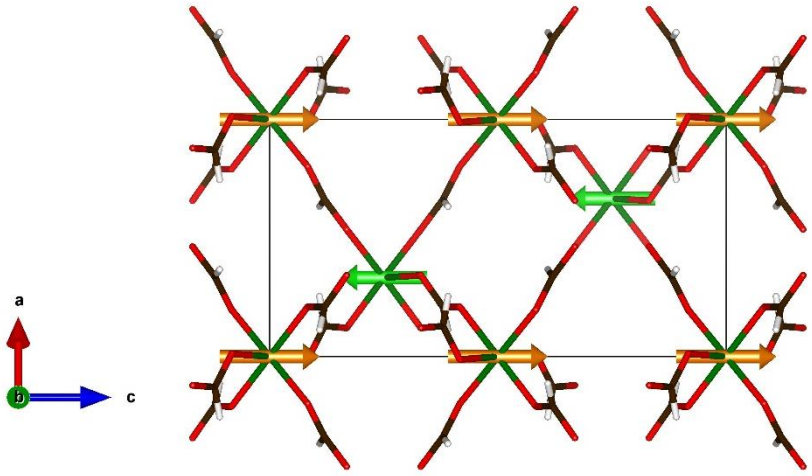

Figure 26. View along the *c*-axis of the unit cell of compound **4**, together with the magnetic moments of the Ni^{II} and Fe^{III} ions represented as green and orange arrows respectively. The occurrence of a weak ferromagnetism due to the non-compensation of the magnetic moments along the *c*-axis is observed. For the sake of clarity, only the $[Fe^{III}Ni^{II}(HCOO)_6]^-$ framework has been represented. The modulus of each arrow has been proportionally scaled to the magnetic moment of each magnetic site.

3.6 The $[(CH_3CH_2NH_3)][Fe^{III}Fe^{II}(HCOO)_6]$ compound, **6**

The investigation of the magneto structural correlations carried out until now, showed that magnetoelectric properties of the family of niccolite type compounds, can be significantly modified and changed by using various metal centres. It has been our goal to explore the structural and the magnetic effects of the compounds reported in the previous sections, by replacing the divalent iron atoms in the metal-organic framework of compound **1** with other divalent metal ions. To investigate the influence of the counterion on the $[Fe^{III}Fe^{II}(HCOO)_6]^-$ anionic framework it has been necessary to attempt a different synthesis in which the dimethylammonium counterion is replaced by another alkyl ammonium counterion. In this last case, our goal is to focus our efforts on the magnetic results and to compare them with the analogue compound **1**[1–3]. Recent works published by Macka *et al.*[16,58] proposed their results about the characteristics of novels heterometallic and mixed valence metal compounds, where the well know dimethylammonium have been replaced by other ammonium-based counterions [1-6,9,15,33,60]. In this section the investigation has been focused on the exploration of magnetic properties $[(CH_3CH_2NH_3)][Fe^{III}Fe^{II}(HCOO)_6]$ (**6**). We have selected the ethylammonium counterion because of its similarity with the dimethylammonium, in fact, both have three non-hydrogen atoms, same number of hydrogen and same geometry. Therefore, in order to compare with compound **1**, this is the most appropriate counterion.

3.6.1 Synthesis of compound **6**

The $[(CH_3CH_2NH_3)][Fe^{III}Fe^{II}(HCOO)_6]$ compound has been synthesized using the solvothermal method. The fundamentals of this method are reported in chapter 2. The synthesis consisted of mixing $FeCl_3 \cdot 6H_2O$ (1.5 mmol) and $FeCl_2 \cdot 4H_2O$ (1.5 mmol) in *N*-ethylformamide (8 ml) and formic acid (8 ml).

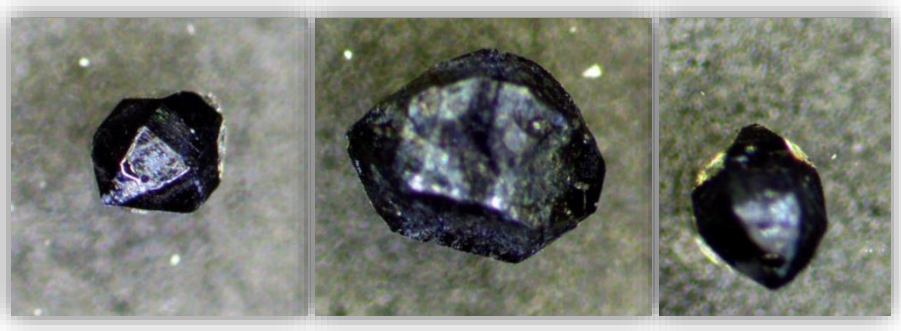

Figure 27: Picture of compound **6** obtained by the here described solvothermal method.

The mixture was sealed in a teflon-line stainless steel vessel and heated for 24 hours at 140°C. During this period, under autogenous pressure the reactive dissolve slowly with the increasing of temperature and react to form crystalline products. Once cooled to room temperature, the product was obtained in the form of a dark black polycrystalline powder. Some crystals (see Figure 27) may have been suitable for X-Ray diffraction, but were too small for single crystal neutron diffraction. The product was filtered, washed with methanol and dried in air over night. The obtained yield was around 60% based on the divalent metal salt.

3.6.2 FTIR-Measurements

The infrared spectrum of compound **6**, which matches with literature data, is shown in Figure 28. A list of the band assignments corresponding to the internal vibrations modes of **6** is given in Table 7. At 2880 cm^{-1} there is a weak absorption peak corresponding to the $\upsilon HCOO^-$ band due to the stretching of C−H. A strong band at 1557 cm^{-1} and weak at 1327 cm^{-1} represent the C−O stretching, while the absorption peak at 1382 cm^{-1} is due to the C−H in plane bending. The bands observed at 811 cm^{-1} and at 786 cm^{-1} arise from the O−C−O symmetric bending (scissor). For the ethyl-ammonium the band at 1485 cm^{-1} comes from the bending of the NH_3 group. A very weak absorption peak is visible for the bending of the CH_2 group at 1450 cm^{-1}. CH_2 rocking is observed at 1222 cm^{-1} and 1193 cm^{-1}. At 1049 cm^{-1} the CCN group corresponding the asymmetric stretching of the group. At 855 cm^{-1} there is a very weak band that can be assigned to NH_2 rocking and at 991 cm^{-1} and 961 cm^{-1} we observe the rocking of the NH_3 group.

Table 7: Vibrational modes assignments for compound **6**.

$\upsilon HCOO^-$	2880*w*
***υ*HCOO$^-$**	1557*s*
δNH_3	1485*m*
δCH_3	1450*w*
***υ*HCOO$^-$**	1382*m*
***υ*HCOO$^-$**	1327*s*
$\rho CH_2/CH_3$	1222*w*
$\upsilon_{as}CCN$	1049*w*
ρNH_3	991*w*
δNH_2	855*w*
***υ*HCOO$^-$**	811*s*

Key codes: (*w*: weak, *m*: medium, *s*: strong and υ: stretching, δ: bending, ρ: rocking, $\upsilon_{as/s}$: asymmetric/symmetric stretching)

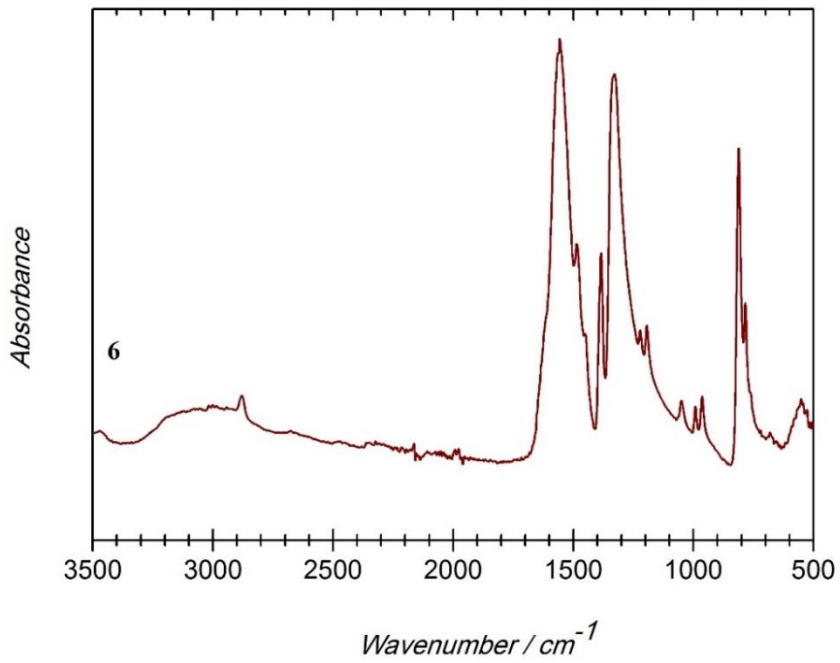

Figure 28: Infrared spectrum of compounds **6** recorded at room temperature.

3.7 $[(CH_3CH_2NH_3)][Fe^{III}Fe^{II}(HCOO)_6]$ crystal structure

The powder neutron and X-Ray diffraction data analysis for the $[(CH_3CH_2NH_3)][Fe^{III}Fe^{II}(HCOO)_6]$ compound, confirms a trigonal system with the space group $P\bar{3}1c$ space group. Unit cell parameters are 8.21037(1), 8.21037(1) 14.03720(2) Å. Also in this structure, the metal centres are linked by the formate group in the usual *anti-anti* configuration, as for the previous compounds. This compound is predicted to be isomorph to the previously presented compounds. Moreover, from the Rietveld refinement a well-ordered metal site is observed.

The $Fe^{III}\cdots Fe^{II}$ distance is 5.898 Å,the Fe^{II}/Fe^{III}–O distances are 1.993 Å and 2.101 Å, respectively. Which implies an ordered alternating distribution of Fe^{III} and Fe^{II} atoms in the $[Fe^{III}Fe^{II}(HCOO)_6]^-$ framework (see Figure 29 and Table 9). In addition, bond valence calculations demonstrate the unequivocal presence of the two metal atoms in the different oxidation states (see Table 8).

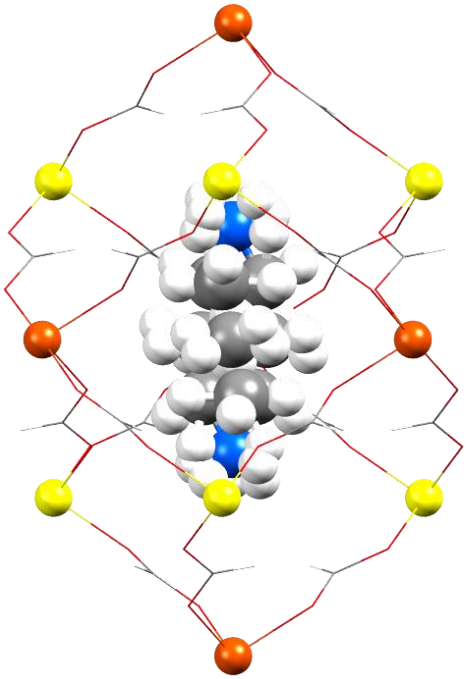

Figure 29: Detail of the crystal structure of the $[CH_3CH_2NH_3][Fe^{III}Fe^{II}(HCOO)_6]$ niccolite-like compound **6.** The $[CH_3CH_2NH_3]^+$ counterion is disordered into six different positions due to the 3-fold axis passing through the CH_3 group of the ethyl-groups. The possible positions within the $[Fe^{III}M^{II}(HCOO)_6]^-$ framework have been represented simultaneously. The Fe^{II}, Fe^{III}, oxygen, nitrogen, carbon and hydrogen atoms are represented in yellow, orange, grey, blue and white respectively.

Table 8: Bond-valence and coordination of atom Fe1 (Fe^{II}, with Wyckoff position *2c*) and Fe2 (Fe^{III} with Wyckoff position *2b*).

Calculated distances in [Å]						
Fe1−O1	2.0834(79)	2.0837(58)	2.0841(80)	2.0834(79)	2.0837(58)	2.0841(80)
Fe2−O1	2.0018(78)	2.0018(85)	2.0018(61)	2.0018(78)	2.0018(85)	2.0018(61)

Average distance [Å]	**Predicted distance [Å]**	**Valence**	**Sum**
2.0838(30)	2.1405	2.000	2.331(19)
2.0018(31)	2.0155	3.000	3.113(26)

The 3D anionic framework $[Fe^{III}Fe^{II}(HCOO)_6]^-$ forms cavities that are prolonged along the *c*-axis, in which the ethylammonium molecule (see Figure 30 and Figure 31) is accommodated for the charge balance. The space surrounding the cation together and the presence of a three-fold axis, produces an important disorder over six equivalent positions of the ethylammonium cation.

Table 9: Selected geometric parameters of **6** from neutron data. At 175 K using single crystal neutron diffraction for **1** see Reference [3], at 45 K using powder neutron diffraction.

Compound		**$[(CH_3)_2NH_2][Fe^{III}Fe^{II}(HCOO)_6]$**	**$[CH_3CH_2NH_3][Fe^{III}Fe^{II}(HCOO)_6]$**
Code		**1**	**6**
Temperature [K]		175	45
Distances [Å]	$Fe^{(I)}$–O1	2.1199(13)	2.084(7)
	$Fe^{(II)}$–O2	2.0046(10)	2.002(8)
	C1−O1	1.2326(15)	1.243(10)
	C1−O2	1.2606(15)	1.312(9)
	C1−H1	1.085(4)	0.936(15)
	N−C2	1.499(10)	1.405(16)
	C2−H	0.995(11)	1.108(3)
	N−H	0.99 (1)	0.90(2)
	N· · ·O1	3.046(2)	3.83(13)
Angles [°]	O1−$Fe^{(I)}$–O1	93.01(5)	94.1(3)
	O1−$Fe^{(I)}$–$O1^{(I)}$	89.44(5)	89.1(3)
	O1−$Fe^{(I)}$–$O1^{(I)}$	84.62(5)	84.5(3)
	O1−$Fe^{(I)}$–$O1^{(II)}$	176.68(5)	178.0(2)
	O2−$Fe^{(II)}$–$O2^{(III)}$	91.20(4)	90.9(3)
	O2−$Fe^{(II)}$–$O2^{(IV)}$	88.80(4)	87.4(3)
	$O2^{(III)}$–$Fe^{(II)}$–$O2^{(IV)}$	180.00(6)	180.00(5)
	O1−C1−O2	124.64(11)	123.5(6)

Symmetry codes: (I): *x*, *x*–*y*, 1/2–*z*; (II): 1–*y*, 1–*x*, 1/2-*z*; (III): 1–*y*, –1+*x*–*y*, *z*; (IV): 1+*y*, 1–*x*+*y*,–*z*

The site occupation factor is equal to 1/6 for each setting. The structural analysis has been performed using a powder sample on high resolution synchrotron and neutron diffractometers. The data from the powder X-Ray experiment, carried out with a wavelength of 0.4949 Å, allowed to refine a preliminary structural model using the Rietveld method. From this refinement we have obtained new structural information differing from the results previously reported[16]. The fit of the X-Ray data using as starting point the model proposed by Mącka *et al*.[18] give rise to a fit which is not satisfactory. An excess of density is observed inside the cavities, different strategies where used to determine the origin of this density. Our first attempt was to assign this density to a metal ion which occupied partially the cavities, however neither the environment of the metal

was observed nor the thermal parameter give us a physically reasonable result. A second option was to include a combination of formic acid and ethylammonium, but then this solution was discarded due to the obtained geometrical parameter for the formic acid, which are far from the ideal one. After many attempts, the best model was obtained when the occupancy of the ethylammonium molecule was refined in order to fit the excess of density. The expected value of the ethylammonium occupancy inside the cavities is 0.1666 due to symmetry relations. However, when the occupancy of the ethylammonium molecule is refined the best fit obtained is R_B= 4.74 and χ^2=2.33. The obtained refined value of the occupancy is 0.30839, which is notably larger than the expected one. This could be interpreted as if one ethylammonium and one ethylamine molecules are weakly anchored in each cavity of the framework, see Figure 31. Although the protonation state of the molecules inside the cavities cannot be determined using X-Ray diffraction. However, to obtain a charge balance, one of these molecules has to be necessarily unprotonated ethylamine while the second one should be an ethylammonium counterion. Therefore, based on this results we propose $[(CH_3CH_2NH_3)][Fe^{III}Fe^{II}(HCOO)_6]\cdot(CH_3CH_2NH_2)$ as the correct chemical formula for compound **6**. In order to confirm the results obtained from the high-resolution X-Ray powder data, which suggest the presence of ethylammonium and ethylamine molecules in the framework cavities, we have carried out high-resolution neutron powder diffraction at the same temperature, 45 K, on the D2B instrument.

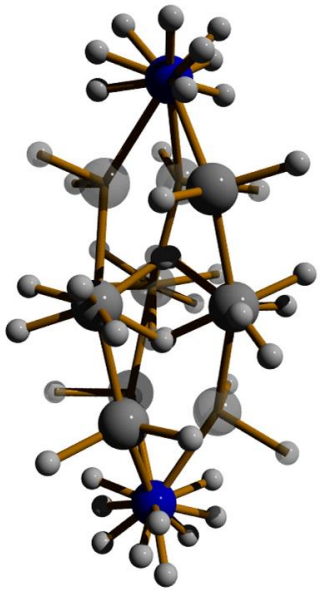

Figure 30: View of the disordered ethyl ammonium counterion over six possible configuration.

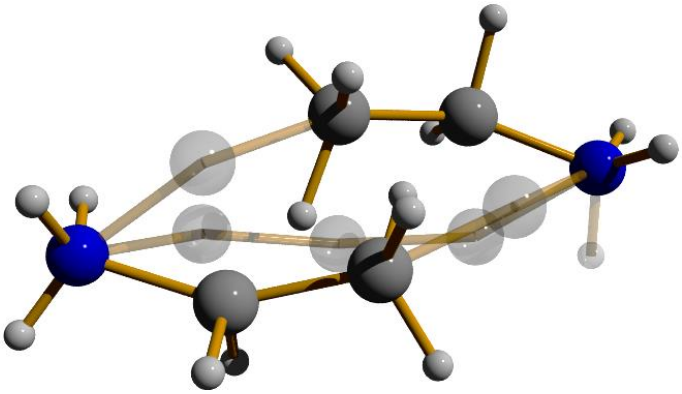

Figure 31: Another view of the disordered ethylammonium/ethylamine molecules over six possible configuration. The atoms and bonds are voluntary given in transparent colour, in order to make in evidence the two positions that EtA^+/EtA assume over the six possible orientations.

Formula	$[(CH_3CH_2NH_3)][Fe^{III}Fe^{II}(HCOO)_6]\cdot(CH_3CH_2NH_2)$ (6)
Empirical Formula	$C_{10}H_{21}Fe_2N_2O_{12}$
M_r (g·mol-1)	472.97
Temperature (K)	45(2)
λ(Å)	1.921
Crystal system	Trigonal
Space group (No.)	$P\bar{3}1c$ (163)
***a* (Å)**	8.21020(8)
***b* (Å)**	8.21020(8)
***c* (Å)**	14.03702(16)
***V* (Å^3)**	819.433(15)
Z	2
ρ_c (g·cm^{-3})	1.921
Meas. Reflections	3200
Parameters/ restraints	149/ 0
Hydrogen treatment	Refined with constraints
Goodness of fit	1.4
R_F (%)	1.67
χ^2	2.032

The best model obtained from the X-Ray refinements was used as starting point for the neutron diffraction fit. Using a Fourier map, it was possible to detect the negative density related to the hydrogens and to localize them one by one. The density surrounding the nitrogen atoms is the most distinguishable reason why the related hydrogens were easily located. The assignment of the hydrogens are harder in the case of the ethyl group that show an important disorder over six (two times three positions) positions. To obtain an

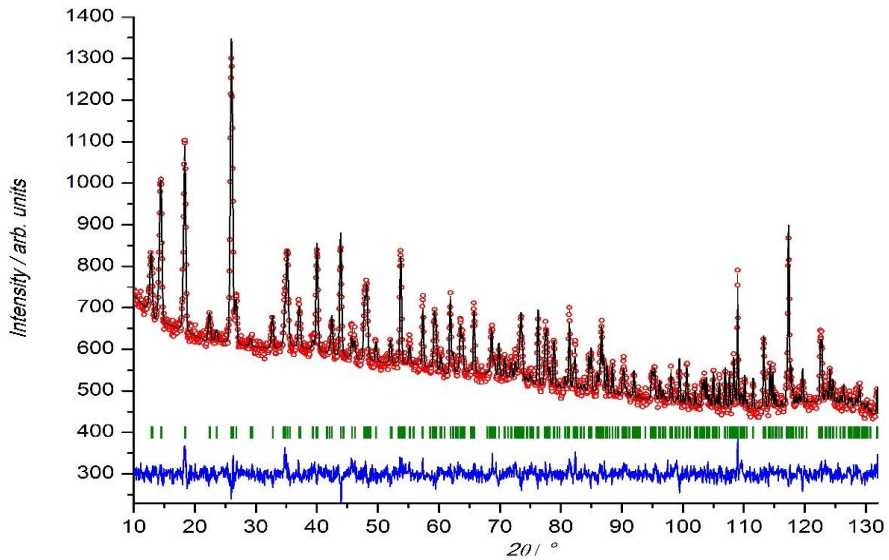

Figure 32: Experimental (open red circles) neutron powder diffraction data and calculated Rietveld refinement (black solid line) pattern for $[(CH_3CH_2NH_3)][Fe^{III}Fe^{II}(HCOO)_6]\cdot(CH_3CH_2NH_2)$ Data of compound **6** collected at 45 K using the D2B instrument with λ= 1.59465 Å. The difference between observed and calculated patterns is represented in blue. The vertical green marks represent the position of the Bragg reflections. The refinement has been done in the space group *P*-31*c* with the associated cell parameters, $a = b$=8.210202(5) Å, c = 14.0^{37}024 (13) Å with $\alpha = \beta = 90°$ and γ =120°. The D2B data refinement gives the following agreement factors for χ^2 = 2.032 and R_B =12.81 % for neutron.

acceptable model, and to detect precisely all the hydrogen atoms of the counterion, geometrical standard bond distances restrictions were used. The atomic coordinates were treated with an approximation of the rigid body method that does not reduce the number of free parameters, considering that in powder diffraction, the observations/number of variables ratio is lower than in an equivalent single crystal experiment for the same $sin\theta/\lambda$ range. In fact, for example, very small variations for testing the atomic model, produces considerable worsening on the quality of the fit. The best fit gives rise to this agreement factors R_B= 12.81 and χ^2= 2.032 and it is shown in Figure 32. The occupancy values calculated by neutron data refinements were circa two times of the expected one (0.1666 the occupancy value expected and 0.33322 concerning all the atoms of the molecules inside the cavity), results which are in good agreement with the synchrotron X-Ray data. The only difference to the X-Ray results is that, the neutron model gives slightly bigger values which are closer to the double of the theoretical occupancy factor. This slightly difference is due to the highest contrast of the neutron diffraction data. In the final refinement, the entire framework was refined anisotropically, while the molecules anchored in the cavities were refined isotropically. This unexpected result precludes a direct comparison of this compound with the compound **1**. The occurrence of two different molecules located in the cavity of the framework modifies notably the interactions with the framework and, therefore, this can be the origin of the absence of structural phase transition in this compound. This double check has been essential to support the hypothesis of the presence of two molecules inside the cavity. As mentioned above, to respect the charge balance, just one of the molecule can be protonated while the other species is electrically neutral. If this was not the case, the new spatial arrangement would have induced a symmetry breaking resulting in the appearance of prohibited Bragg

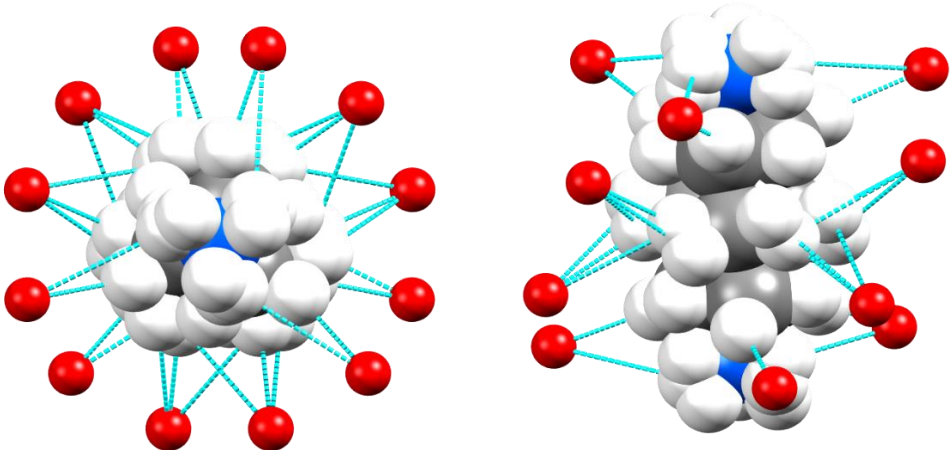

Figure 33: View of the possible hydrogen bonds between the disordered ethylammonium /ethylamine molecules in the cavity and the framework.

reflections for the space group used for solving the crystal structure ($P\bar{3}1c$). The size of the thermal parameters and the hydrogen bonds involved, suggest that the ethylammonium/ethylamine molecules are weakly anchored within the voids. The deep analysis of the hydrogen bonds is here omitted because the large disorder of the molecules inside the cavities. Nonetheless, we report a picture that shows an estimation of the all possible hydrogen bonds, Figure 33. The molecules, located in the cavity of the anionic framework, occupy an empty space that corresponds to a volume of *ca.* 237 $Å^3$ which is 28.9 % of the total unit cell volume. With the molecules in the cavity, the remaining volume is 14.3 $Å^3$ (1.7% of the total volume). The comparison between the reaming empty space in compound **1** at room temperature, (when the dimethyalmmonium is disordered), and that one in compound **6**, (where there are two molecules occupied almost the same volume than in **1**), gives rise surprisingly, to very similar results. The ethylammonium/ethylamine molecules occupy almost the same volume than one dimethylammonium counterion in the compound **1,** this feature can be explained by a chemical pressure effect. However, the distance between molecules are compatible with this packing, moreover the comparison of the thermal parameter of the framework for compound **1** and compound **6** show an interesting result. Those of obtained for compound **6** are notably larger than those of compound **1**. This can be interpreted in the case of compound **6** as a "distortion" within the framework, induced by the presence of more than one molecule in the cavity.

3.8 Magnetic studies of compound **6**

A recent study[18] about compound **6** informed about the magnetic properties observed by measuring the magnetization as function of temperature. The magnetic moments of the two sublattices Fe^{II} and Fe^{III} manifest the ordering temperature at 39 K, which is slightly higher than the T_{ord} of compound **1** (37 K). The variation of the magnetization is measured while increasing and decreasing the temperature in a constant magnetic field (100 Oe)[18], see Figure 34. By warming the system up the magnetization curve decreases until that the two sublattices compensate each other at the temperature at 26 K. Above this temperature point the magnetization assume negative values and a change of the sublattices orientation takes place at 39 K, after that it increases back to zero. This behaviour is similar to the magnetic properties reported for **1** that showed a compensation temperature at 29 K. In the cooling scan the magnetization keeps positive values until compensation temperature at 26 K is reached and becomes negative once below this value. The saturation of the

magnetization, in both processes, occurs at similar value (*ca.* 3 $emug^{-1}$) which it is typical of a full reversal of the total magnetization. In add, when a negative magnetization occurs, because of the anisotropy, there is a hurdle to overpass which is big enough to obstruct the pole reversal. It is necessary to apply a greater magnetic field in compound **6** (50 kOe, see reference[18]) to overcome the anisotropy barrier, while in compound **1** we have seen[2] that the reorientation of the sublattices occurred after applying a magnetic field above the 1.5 kOe. As reported by Zhao *et al.*[2] it marks a very exceptional circumstance in molecular-based magnets to discover a negative value of magnetization. Supported by these latter arguments, our goal has been to investigate the magnetic structure of this compound using high flux and medium resolution D1B powder neutron diffractometer

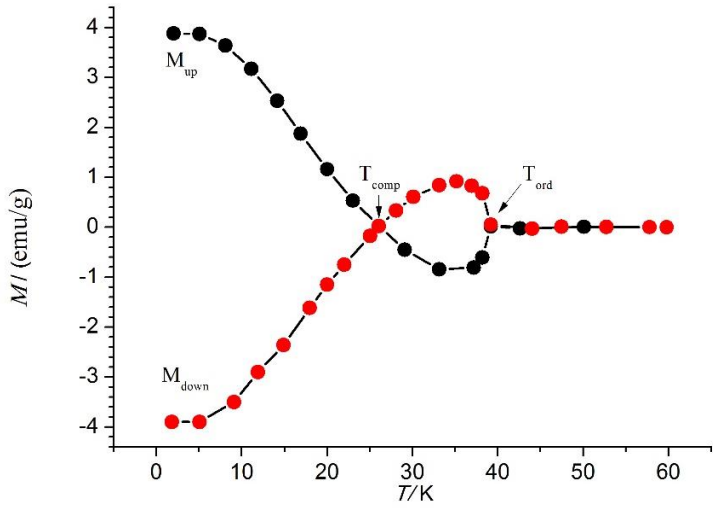

Figure 34: View of the magnetization M as a function of temperature measured in increasing and decreasing T in a constant magnetic field Inset: field dependence of M measured upon increasing and decreasing field. Data obtained from reference [18].

and compare the results with the ones obtained for compound **1**. We carried out different measurements above and below the ordering temperature (39 K). The diffraction pattern collected in the paramagnetic phase has been useful in order to refine the low-temperature instrumental parameters. The indexing of the observed magnetic reflections was done using K-search program[47] included in FullProf suite[28], confirming the occurrence of a **k** = (0, 0, 0) propagation vector. The neutron diffraction patterns of **6** recorded at *ca.* 2 K shows the increase of the intensity Bragg reflection (0 1 0) at $2\theta = 20.5^{o}$, then the reflection (0 0 2) at $2\theta = 20.7$, which are in agreement with a long-range magnetic order, see Figure 35.

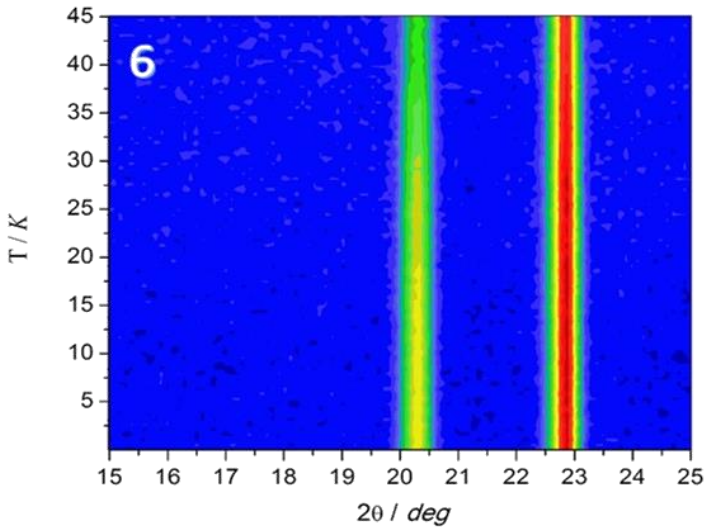

Figure 35: Detail of the mesh plot of the thermodiffractograms corresponding to compounds **6**. Data are collected at D1B in the range temperature of 2- 45 K. An increase of the Bragg reflections (0 1 0) at 2θ = 20.5°and (0 0 2) at 2θ = 20.7°.

The weak magnetic contribution together with the overlapping between nuclear and magnetic reflections, due to the occurrence of a **k** = (0, 0, 0) propagation vector, and the background produced by the high number of hydrogens atoms preclude an accurate magnetic structure refinement directly from this pattern. As in the previous examples, this problem has been bypassed using a difference patterns, subtracting the normalized nuclear intensity of the paramagnetic phase (45 K) from the ordered phase pattern (*ca.* 2 K). The symmetry analysis is the same as that done for compounds **2**-**4** previously described. As for compound **4**, the magnetic structure is well described by the $^{P}\Gamma_2$ irrep (see the fit of the difference pattern of 6 in Figure 36). The magnetic moments

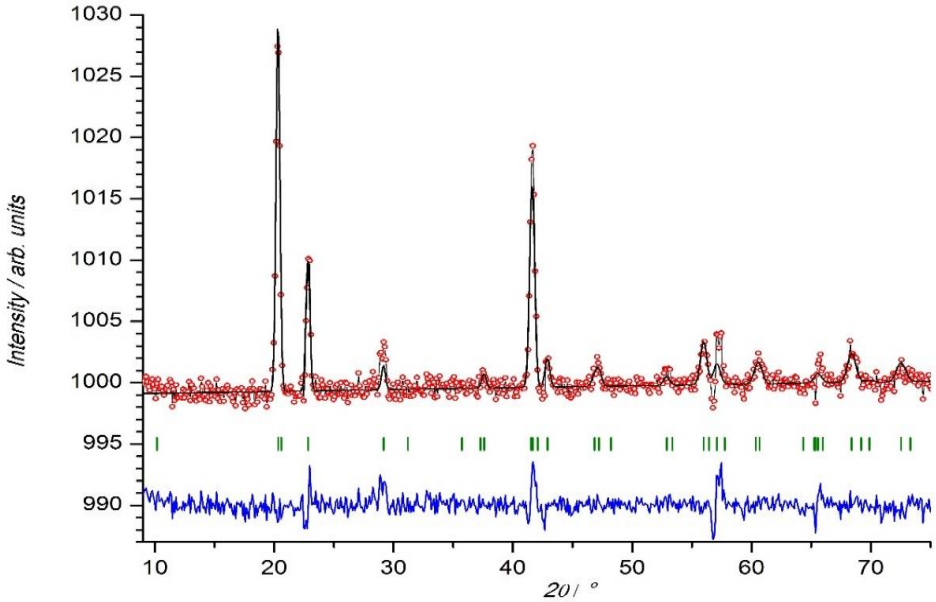

Figure 36: Fit of the difference pattern of compound **6** using the p-irreps ($^{P}\Gamma_2$). The data refinement gives the agreement factors χ^2 = 3.462, and magnetic R_B = 13.29% Experimental data are represented by open red circles, the calculated patterns are shown as solid black lines, and the differences between observed and calculated patterns are plotted as solid blue lines. The vertical green marks represent the positions of the Bragg reflections.

of the metal sublattices determined by the refinement of the D1B data at 2K, using the difference patterns between the paramagnetic and the magnetically ordered phase, are listed in the Table 10.

Table 10: Magnetic moment components determined for each atom site through Rietveld refinement using the combination of $^{p}\Gamma_2$ (Shubnikov group *P*-31/*c*')

	M_a	M_b	M_c	M_{total}
Fe(2c)	0	0	4.416 (6)	4.416 (6)
Fe(2b)	0	0	−4.005 (8)	−4.005 (8)

The macroscopic magnetic measurements of **6** show the occurrence of an antiferromagnetic coupling between the neighbouring metal ions, feature confirmed by our results. The magnetic structure shows a small ferromagnetic component that arises from the non-compensation of the $Fe^{III}Fe^{II}$ sublattices along the *c*-direction (Figure 37). The ferromagnetic moment is calculated as the vector sum of the magnetic moments obtained from neutron data recorded at circa 2 K along *c*-axis, and it is *ca.* 0.4 μ_B. This value is a bit bigger than the expected one (0.3 μ_B) shown in the magnetization data measured by SQUID magnetometer[18] because may be due to the use of polycrystalline sample which random distribution concur to produce different magnetic moment configuration. With this study, carried out using non-polarized neutron diffraction experiments, we can only obtain information about the magnetic moments resident on the iron sites and the not about those delocalized out of them. In order to analyse the magnitude of the magnetic moments and the distribution of the spin density could be interesting to use polarized neutron diffraction experiments.

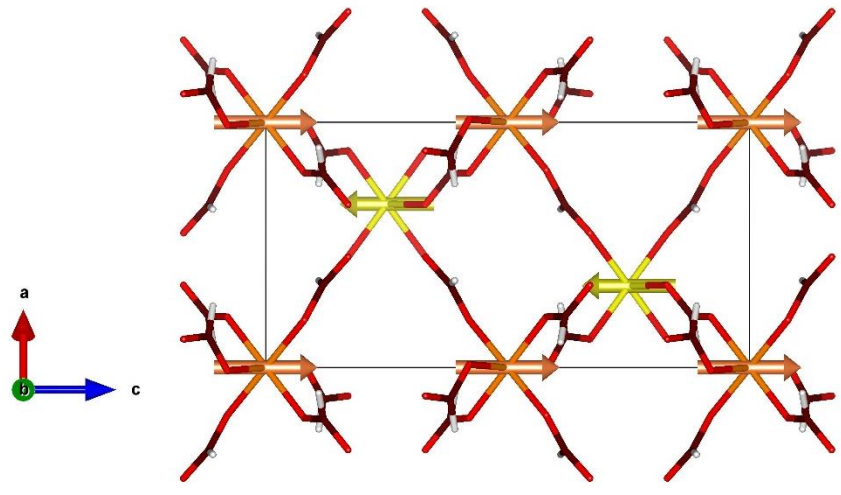

Figure 37: View along the *c*-axis of the unit cell of compound **6**, together with the magnetic moments of the Fe^{II} and Fe^{III} ions represented as yellow and orange arrows respectively. The occurrence of a weak ferromagnetism in the *c*-axis is observed. For the sake of clarity, only the $[Fe^{III}Mn^{II}(HCOO)_6]^-$ framework has been represented, together with the magnetic structure obtained from the Rietveld refinement.

Conclusion and discussion

In this work we have determined and refined the crystal structure of $[(CH_3)_2NH_2][Fe^{III}M^{II}(HCOO)_6]$ with M^{II} = Co^{II} (**2**), Mn^{II} (**3**), Ni^{II} (**4**) and Mg^{II} (**5**) ions, combining high resolution neutron diffraction together with synchrotron X-Ray diffraction at 45 K. This multipattern refinement, permitted the localization of the hydrogen atoms of the $[(CH_3)_2NH_2]^+$ counter ions, and discards the occurrence of a structural phase transition. The refined structural models have been used as starting point for the refinement of the magnetic structures. Based on the symmetry analysis, we have obtained two possible physically irreducible representations (p-irreps) that have been combined (magnetic space group *C*2'/*c*') to explain the experimental data. The magnetic structure of **2** consist in a non-compensated antiferromagnetic arrangement where the magnetic moments are contained in the *ab*-plane. In contrast, for compound **3** the magnetic structure is almost antiferromagnetic within the *ab*-plane with a spin-canting along the *c*-axis. The magnetic structure of **4**, has been solved in the magnetic subgroup $P\bar{3}1c$' with a unique physically irreducible representation. The magnetic behaviour is characterized by an antiferromagnetic coupling along *c*-axis among the random distribution of the metals ions. The non-compensation of the magnetic moments give rise to a small ferromagnetic component along the *c*-axis. This magnetic model is closer to the magnetic structure of compound **1**. In the case of compound **1**, the magnetic moment of Fe^{III} is symmetry constrained along the *c*-axis and the main contribution of the Fe^{II} ion is along the *c*-axis with a small component in the *ab*-plane. Moreover, compound **1** presents a tripling of the *c*-axis due to the occurrence of a structural phase transition giving rise to a variation in the staking sequence of the magnetic moments compared to those obtained for **2**, **3** and **4**. Furthermore, compound **1** is the only one presenting a negative magnetization under small external field. In the case of compound **3**, this effect is not expected due to both metal sites (Mn^{II} and Fe^{III}) having very similar electronic configuration. However, in the case of compound **2**, where the difference in the electronic configuration is notable, a negative magnetization effect could be expected. However, the absence of this negative magnetization in the cobalt compound can be explained taking into account that both metallic networks become ordered at the same time, and therefore there is no "inductive effect" from one network over the other. A specific mention has to be done in the case of compound **5**. In a recent work presented by Ciupa *et al.*[4] present

this compound of formula $[(CH_3)_2NH_2][Fe^{III}Mg^{II}(HCOO)_6]$ which crystallizes in the same space group that compound **2**, **3** and **4** even at low temperature, and presents a negative magnetization. For this reason and because of the partial substitution of Mg^{2+} by Fe^{2+} suggested a similar magnetic behaviour to **1**, but diluted. In reality, even after a long acquisition using high flux neutron powder diffraction, no magnetic signals were observed. Probably, due to the disorder distribution of the metal ions which preclude a real long range order. The contribution of the small $Fe^{III}Fe^{II}$ regions within the $Fe^{III}Mg^{II}$ framework is too small to be detected by neutron diffraction techniques. In the last section of this chapter, we decide to investigate the substitution of the counterion in the niccolite-like framework. In particular, the influence of the substitution of dimethylammonium by ethylammonium in the $[Fe^{III}Fe^{II}(HCOO)_6]^-$ framework. The previous reported results, suggest that the substitution of ethylammonium by diethylammonium cations gives rise to a compound isomorphous to **1**, and with similar magnetic behaviour. However, our experimental results suggest a different scenario. The crystal structure determination of compound **6**, shows that the preliminary model is not able to fit the experimental data. High-resolution synchrotron and neutron diffraction have been used to propose a new structural model. The crystal structure was solved in the $P\bar{3}1c$ space group, as the other members of the series. However, the only model that fit properly the experimental data suggest that two different molecules are weakly anchored into the framework cavities. Therefore, the final formula for this compound is $[(CH_3CH_2NH_3)][Fe^{III}Fe^{II}(HCOO)_6]\cdot(CH_3CH_2NH_2)$. The magnetic structure of **6,** has been solved in the magnetic subgroup $P\bar{3}1c$' with a unique physically irreducible representation. The magnetic behaviour is characterized by an antiferromagnetic coupling along the *c*-axis. The non-compensation of the magnetic moments give rise to a small ferromagnetic component along the *c*-axis. The magnetic structure of compound **6** is very similar to that obtained for compound **1**, in fact there is a group-subgroup relation between both. The negative magnetization observed in **6**, can be explained using a two network model. These data suggest that the Fe^{II} sublattice is the first one to be ordered and then induces the Fe^{III} sublattice to be coupled antiferromagnetically with it, mainly due to the antiferromagnetic interaction through the *anti-anti* formate bridge. Below T_{comp}, the proportion of the ordered magnetic moment increases more noticeably for the Fe^{III} sublattice, which a large magnetic moment, and a negative magnetization is observed due to the non-compensation of both Fe^{III} and Fe^{II} networks.

Bibliography

(1) Hagen, K. S.; Naik, S. G.; Huynh, B. H.; Masello, A.; Christou, G. *J. Am. Chem. Soc.* **2009**, *131* (22), 7516.
(2) Zhao, J.-P.; Hu, B.-W.; Lloret, F.; Tao, J.; Yang, Q.; Zhang, X.-F.; Bu, X.-H. *Inorg. Chem.* **2010**, *49* (22), 10390.
(3) Cañadillas-Delgado, L.; Fabelo, O.; Rodríguez-Velamazán, J. A.; Lemée-Cailleau, M.-H.; Mason, S. A.; Pardo, E.; Lloret, F.; Zhao, J.-P.; Bu, X.-H.; Simonet, V.; Colin, C. V.; Rodríguez-Carvajal, J. *J. Am. Chem. Soc.* **2012**, *134* (48), 19772.
(4) Ciupa, A.; Mączka, M.; Gągor, A.; Sieradzki, A.; Trzmiel, J.; Pikul, A.; Ptak, M. *Dalton Trans.* **2015**, *44* (19), 8846.
(5) Ciupa, A.; Mączka, M.; Gągor, A.; Pikul, A.; Ptak, M. *Dalton Trans.* **2015**, *44* (29), 13234.
(6) Zhao, J.-P.; Xu, J.; Han, S.-D.; Wang, Q.-L.; Bu, X.-H. *Adv. Mater.* **2017**, 1606966.
(7) Peter Atkins; Duward Shriver. *Inorganic Chemistry-5th Edition*; W.H. Freeman & Company, 2009.
(8) M. Bovill, S.; J. Saines, P. *CrystEngComm* **2015**, *17* (43), 8319.
(9) Wang, Z.; Hu, K.; Gao, S.; Kobayashi, H. *Adv. Mater.* **2010**, *22* (13), 1526.
a) V. A. Blatov, M. O'Keeffe and D. M. Proserpio, *CrystEngComm***,** 2010,**12**, 44

(10) Etaiw, S. E. H.; El-bendary, M. M. *Spectrochim. Acta. A. Mol. Biomol. Spectrosc.* **2013**, *110*, 304.

(11) Yang, E.-C.; Shi, X.-J.; Liu, Z.-Y.; Zhao, X.-J. *Inorg. Chem. Commun.* **2010**, *13* (6), 733.
(12) Mastropietro, T. F.; Marino, N.; Munno, G. D.; Lloret, F.; Julve, M.; Pardo, E.; Armentano, D. *Inorg. Chem.* **2016**, *55* (21), 11160.
(13) V. McGuire, C.; S. Forgan, R. *Chem. Commun.* **2015**, *51* (25), 5199.
(14) Wang, X.-Y.; Wang, Z.-M.; Gao, S. *Chem. Commun.* **2008**, *0* (3), 281.
(15) Mączka, M.; Gągor, A.; Pikul, A.; Trzebiatowska, M. *Vib. Spectrosc.* **2017**, *90*, 74.
(16) Mazzuca, L.; Cañadillas-Delgado, L.; Rodríguez-Velamazán, J. A.; Fabelo, O.; Scarrozza, M.; Stroppa, A.; Picozzi, S.; Zhao, J.-P.; Bu, X.-H.; Rodríguez-Carvajal, J. *Inorg. Chem.* **2017**, *56* (1), 197.
(17) Li, M.-Y.; Kurmoo, M.; Wang, Z.-M.; Gao, S. *Chem. – Asian J.* **2011**, *6* (11), 3084.
(18) Mączka, M.; Ciupa, A.; Gągor, A.; Sieradzki, A.; Pikul, A.; Ptak, M. *J. Mater. Chem. C* **2016**, *4* (6), 1186.
(19) Wang, Z.; Zhang, X.; Batten, S. R.; Kurmoo, M.; Gao, S. *Inorg. Chem.* **2007**, *46* (21), 8439.
(20) Overgaard, J.; Rentschler, E.; Timco, G. A.; Larsen, F. K. *ChemPhysChem* **2004**, *5* (11), 1755.
(21) Agilent Technologies UK Ltd. Agilent, CrysAlis PRO.
(22) Sheldrick, G. M. *Acta Crystallogr. Sect. C Struct. Chem.* **2015**, *71* (1), 3.
(23) Nardelli, M. *J. Appl. Crystallogr.* **1995**, *28* (5), 659.
(24) Spek, A. L. *J. Appl. Crystallogr.* **2003**, *36* (1), 7.
(25) Brandenburg & H. Putz. DIAMOND 2.1d, Crystal Impact GbR, CRYSTAL IMPACT, K.
(26) Richard, D.; Ferrand, M.; Kearley, G. J. *J. Neutron Res.* **1996**, *4* (1–4), 33.
(27) D. Richard, M. Ferrand, G. J. Kearley. LAMP, the Large Array Manipulation Program.

(28) Rodríguez-Carvajal, J. *Phys. B Condens. Matter* **1993**, *192* (1), 55.
(29) Hohenberg, P.; Kohn, W. *Phys. Rev.* **1964**, *136* (3B), B864.
(30) P.; Burke P; J., K.; Ernzerhof. *Phys. Rev. Lett.* **1996**, *77*, 3865.
(31) Blöchl, P. E.; Jepsen, O.; Andersen, O. K. *Phys. Rev. B* **1994**, *49*, 16223.
(32) Kresse, G.; Furthmüller, J. *Comput. Mater. Sci.* **1996**, *6* (1), 15.
(33) Kresse, G.; Furthmüller, J. *Phys. Rev. B* **1996**, *54* (16), 11169.
(34) Mączka, M.; Pietraszko, A.; Macalik, L.; Sieradzki, A.; Trzmiel, J.; Pikul, A. *Dalton Trans.* **2014**, *43* (45), 17075.
(35) Mączka, M.; Ptak, M.; Macalik, L. *Vib. Spectrosc.* **2014**, *71*, 98.
(36) Steiner, T. *Angew. Chem. Int. Ed.* **2002**, *41* (1), 48.
(37) Perrin, C.L.; Nielson, J.B. *Annu. Rev. Phys. Chem.* **1997**, 48, 511.
(38) Kwan Eugene. H-Bonding Seminar with transitions, 2009.
(39) Baber, R. A.; Charmant, J. P. H.; Norman, N. C.; Orpen, A. G.; Rossi, J. *Acta Crystallogr. Sect. E Struct. Rep. Online* **2004**, *60* (6), 1086.
(40) Diallo, W.; Gueye, N.; Crochet, A.; Plasseraud, L.; Cattey, H. *Acta Crystallogr. Sect. E Crystallogr. Commun.* **2015**, *71* (5), 473.
(41) Xu, H.-B.; Wang, Z.-M.; Liu, T.; Gao, S. *Inorg. Chem.* **2007**, *46* (8), 3089.
(42) Carlin, R. L.; Duyneveldt, A. J. van. In *Magnetic Properties of Transition Metal Compounds*; Inorganic Chemistry Concepts; Springer Berlin Heidelberg, 1977; pp 54–76.
(43) Carlin, R. L.; Duyneveldt, A. J. van. In *Magnetic Properties of Transition Metal Compounds*; Inorganic Chemistry Concepts; Springer Berlin Heidelberg, 1977; pp 1–22.
(44) Carlin, R. L.; Duyneveldt, A. J. van. In *Magnetic Properties of Transition Metal Compounds*; Inorganic Chemistry Concepts; Springer Berlin Heidelberg, 1977; pp 142–171.
(45) Carlin, R. L.; Duyneveldt, A. J. van. In *Magnetic Properties of Transition Metal Compounds*; Inorganic Chemistry Concepts; Springer Berlin Heidelberg, 1977; pp 109–141.
(46) Crépieux, A.; Lacroix, C. *J. Magn. Magn. Mater.* **1998**, *182* (3), 341.
(47) Rodriguez-Carvajal, J. k-Search program.
(48) Bertaut, E. F.; G. T. Rado and H. Shul,. *Magnetism, vol. III, Ch. 4,*; Academic Press,: New York, 1963.
(49) Rodriguez-Carvajal, J. BasIreps program.
(50) Stokes, H. T; Campbell, B. J; Cordes, R. *Acta Cryst.* **2013**, No. A69, 388.
(51) Aroyo, M. I.; Capillas, C.; Wondratschek, H.; J. M. Perez-Mato. *Acta Crystallogr. Sect.* **2006**, *A62*, 115.
(52) Aroyo, M. I.; Perez-Mato, J. M.; Capillas, C.; Kroumova, E.; Ivantchev, S.; Madariaga, G.; Kirov, A.; Wondratschek, H. *Z. Für Krist. - Cryst. Mater.* **2009**, *221* (1), 15.
(53) Mesbah, A.; Sibille, R.; Mazet, T.; Malaman, B.; Lebègue, S.; François, M. *J. Mater. Chem.* **2010**, *20* (42), 9386.
(54) Fabelo, O.; Cañadillas-Delgado, L.; Pasán, J.; Díaz-Gallifa, P.; Ruiz-Pérez, C.; Lloret, F.; Julve, M.; Puente Orench, I.; Campo, J.; Rodríguez-Carvajal, J. *Inorg. Chem.* **2013**, *52* (21), 12818.
(55) Sibille, R.; Mazet, T.; Elkaïm, E.; Malaman, B.; François, M. *Inorg. Chem.* **2013**, *52* (2), 608.
(56) Sibille, R.; Mazet, T.; Malaman, B.; Wang, Q.; Didelot, E.; François, M. *Chem. Mater.* **2015**, *27* (1), 133.

(57) Díaz-Gallifa, P.; Fabelo, O.; Pasán, J.; Cañadillas-Delgado, L.; Rodríguez-Carvajal, J.; Lloret, F.; Julve, M.; Ruiz-Pérez, C. *Inorg. Chem.* **2014**, *53* (11), 5674.
(58) Sieradzki, A.; Pawlus, S.; N. Tripathy, S.; Gągor, A.; Ciupa, A.; Mączka, M.; Paluch, M. *Phys. Chem. Chem. Phys.* **2016**, *18* (12), 8462.

Chapter 4
$[CH_3NH_3][M^{II}(HCOO)_3]$ compounds

Introduction

The major part of this research has been dedicated to the study of a specific family of metal organic frameworks (MOF) with a perovskite architecture. In this chapter, we will discuss about their crystallographic and magnetic properties, as well as about the possible coexistence of two or more ferroic orders, through which we established their multiferroic or magnetoelectric nature. As we mentioned in the previous chapters, the importance of searching this kind of compounds is powered by their rarity[1–4] associated with the possibility to control the fabrication of new functional materials[5,6]. Therefore, the expectation around them is due to the appearance of coupled phenomena which is extremely attractive for new technology trends[4,7,8]. This new generation of materials is called multiferroic metal-organic frameworks[9–18]. In particular, the coexistence of electric order in the same phase in which the long-range magnetic order occurs, although at substantially lower temperatures, is an exciting starting point for the design of new devices based on these new materials[19]. In metal-organic multiferroics, the multiferroic behaviour is achieved by combining an anionic metal-organic framework, responsible of the long-range magnetic order, with a counter ion located in the cavities of the framework. The adequate combination of these two elements could produce a compound with an order/disorder phase transition, frequently involving the hydrogen bond network[4,20–25] resulting in an electric order.

The most representative compounds exhibiting such behaviour are certainly the oxide perovskites with ABO_3 formula[26–31]. The most famous example is the $BiFeO_3$ compound, which is presently the only compound that has magnetic and ferroelectric properties coexisting at room temperature[32], with the 3*d* electrons of the Fe^{3+} cations. The ferroelectricity arises from the hybridization between the oxygen 2*p* orbitals and the empty 6*p* orbital of Bi. Another important material that marked the beginning of the success of this family of compounds is $YMnO_3$, characterized by a multiferroic behaviour where the ferroelectric order derives from geometrical effects[33]. A more recent system in which a different magnetoelectric coupling occurs is $TbMnO_3$ in which ferroelectricity occurs as a consequence of a special kind of magnetic order[34]. Until this moment, the multiferroic materials cited are only inorganic-based perovskites, but a first exception was introduced in literature by *Jain et Al.* with a hybrid inorganic-organic framework

material[35] of general formula ABX_3, in which A is an organic cation, B is a metal centre and X an organic bridging ligand. The presence of organic molecules, contribute to the formation of hydrogen bonds, that are often responsible of structural phase transitions giving to the compound a ferroelectric behavior[4]. The family of compound that we want to present in this chapter is the $[CH_3NH_3][M(HCOO)_3]$ family, where M is Co^{II}, Fe^{II}, Ni^{II}, Mn^{II} and Cu^{II}, numbered **7**, **8**, **9**, **10** and **11**, respectively (the order adopted for labelling the metals is related to the priority order used for measuring them, and we prefer to keep this order for the sake of clarity).

4.1 Overview of the $[CH_3NH_3][M^{II}(HCOO)_3]$ family

Keeping in mind the formate-based heterometallic compounds exposed in chapter **3**, we have continued the research work by studying the different characteristics observed when the two metal centres are substituted by a unique one (homometallic case) and the replacement of the diethylammonium counterion with the smaller size methylammonium cation. The $[CH_3NH_3][M^{II}(HCOO)_3]$ family investigated is constituted by molecular-based perovskite-like materials, that refer to the mineral $CaTiO_3$ adopting the ABX_3 three-dimensional (3-D) structural framework where, in our case, A is the methylammonium cation, B is the metal centre and X is the organic formate ligand. In the ideal crystal structure, the cubic ABX_3 perovskite is be made up of metal ions sit at the corners of cubes and linked to each other through the coordination bonding oxygen anions, forming a corner-sharing MX_6 octahedral framework. The large cavity between octahedra is an empty space becoming filled by a second cation achieving the electro-neutrality condition (see Figure 1).

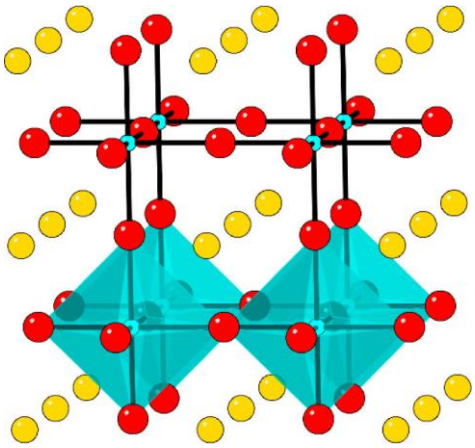

Figure 1: Representations of the 3-D cubic ABX_3 (*Pm*3*m*) perovskite structure.

The perovskite structure is normally slightly distorted depending on the relative size of cation and anions. As a consequence, lower than *Pm*3*m* symmetry space groups are needed to describe the crystal structure[36]. In fact, differently from the linear CN^- and N_3^- bridging ligands that generally form cubic perovskite compounds at room temperature, the coordination polymers based on the formate group, which is a "V-shaped bridge", has a preference to crystallize in lower symmetry space groups. Moreover, until now, there is not formate-bridged perovskite compound crystallizing in the cubic crystal system[22].

Generally, the formate-based complexes present magnetic ordering due to the ability of the well-known formate ligand to mediate ferro- or antiferromagnetic coupling between metal ions depending on the coordination modes of the ligand, as we have seen in the previous chapter. The formate compounds have predilection for a $4^{12}\cdot6^3$-**pcu** topology (primitive cubic net topology), where the formate group acts as bis-monodentate in *anti-anti* coordination mode. This coordination gives rise to structures with medium size cavities where an adequate guest molecule can be located in order to promote electric order, in contrast with the well-known Prussian-blue analogues presenting a compact NaCl framework[37–41]. The maximum size of the counterions to keep the $4^{12}\cdot6^3$-**pcu** perovskite-like topology is of three non-hydrogen atoms, except for the ring-type counterions, like azetidinium and imidazolium. For bigger counterions, the inner chemical pressure precludes the formation of this topology. Other important difference comparing the formate-based compounds with those compounds based on linear bridging ligands (CN^- and N_3^-), is the extended hydrogen-bond network that normally is observed in the formate-based compounds. The occurrence of an intricate H-bond network is mainly due to the ability of the formate anion to act as a proton acceptor. Small changes in the H-bond network can trigger structural phase transitions as was observed in the previous chapter. This tunability can produce remarkable changes in the physical properties, mainly due to order-disorder phase transitions, and therefore they are excellent candidates to be type I multiferroic materials[42–45].

4.2 Objectives

In the present chapter we have investigated the crystal structure, the sequence of phase transitions, the magnetic structure and dielectric properties of $[CH_3NH_3][Co(COOH)_3]$ (**7**) perovskite-like metal-organic compound[46–48] through variable-temperature single-crystal and neutron/X-ray powder diffraction and relative permittivity measurements. Along this chapter we are going to extensively describe the cobalt-based compound as an archetype and the obtained results will be extended to other members of the series [Fe^{II}(**8**), Ni^{II}(**9**), Mn^{II} (**10**) and Cu^{II}(**11**)]. The magnetic properties of compounds **9** , **10**, **11**, based on magnetometry measurements, have been recently reported[47,49]. For the sake of clarity a brief summary of the magnetic properties of this series will be included hereafter.

As mentioned before, this chapter will be centred mainly on the description of compound **7** taken as the main reference. In particular, among the first row transition metal ions containing unpaired electrons, the magnetochemistry of cobalt (II) systems is interesting due to their high anisotropy and d^7 electronic configuration, with occurrence of non-negligible spin-orbit coupling in the ground state.

In fact, the crystal structure of the reported compounds present a sequence of phase transitions as function of temperature. In order to set up the structure of this chapter we are going to describe the different phase transitions as function of temperature for the cobalt-based compound. Each of these phases will be described in detail in the further sections along this chapter.

At room temperature, all members of this series crystallize in the orthorhombic *Pnma* space group (hereafter called phase **I**). The decreasing of the temperature in the Co-based compound gives rise to a first phase transition from the *Pnma* (phase **I**) space group to an incommensurate phase (hereafter called phase **II**), this incommensurate phase evolves into a second phase with a clear change in the modulation vector, this second incommensurate phase will be called phase **III**. At lower temperatures, the Co-based compound becomes again commensurate and the crystal structure can be described in a monoclinic space group (phase **IV**). Finally, all the compounds become magnetically ordered with Néel temperatures ranging from 8 to 33 K. A detailed description of the different magnetic structures based on the representation analysis technique is discussed in the last sections of this chapter.

4.3 Experimental Section

4.3.1 Synthesis of compounds 7 to 11

The synthesis of compound from **7** to **10** has been carried out using aqueous solutions of $MCl_2 \cdot xH_2O$ (3mL, 0.33 M), CH_3NH_3Cl (3 mL, 0.33 M) and NaHCOO (2 mL, 1.5 M), were mixed together with 8 mL of N-methylformamide ($HCONHCH_3$). The resulting solution was sealed in a Teflon-lined stainless steel vessel (43 mL), heated at 140 ºC for 3 days under autogenous pressure, and then cooled to room temperature. After slow cooling, large prismatic pink crystals of $[CH_3NH_3][Co(COOH)_3]$, beige crystalline powder of $[CH_3NH_3][Fe(COOH)_3]$, medium size green crystals of $[CH_3NH_3][Ni(COOH)_3]$ and colourless crystalline powder of $[CH_3NH_3][Mn(COOH)_3]$, suitable for X-ray single crystal and powder diffraction were obtained with a yield of about 88%, 67%, 71%, 68%. The crystals were filtered, washed with ethanol (10 mL) and dried at room temperature. In Figure 2 it is shown a single crystal of compound **7**, which is suitable for neutron single crystal diffraction.

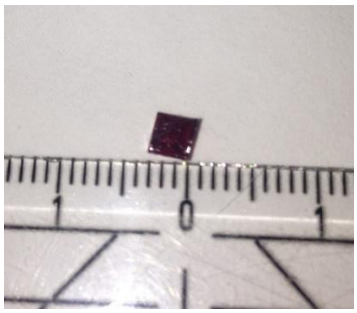

Figure 2: Picture of a large red-prism single crystal of the **7** compound.

Regarding the synthesis of compound **11** it has been prepared using a slow diffusion method. On the bottom of a glass tube 5 ml, it was introduced a methanol solution containing 0.07 g (0.5 mmol) of $CuCl_2$. On top of this, it was carefully layered 5 ml of

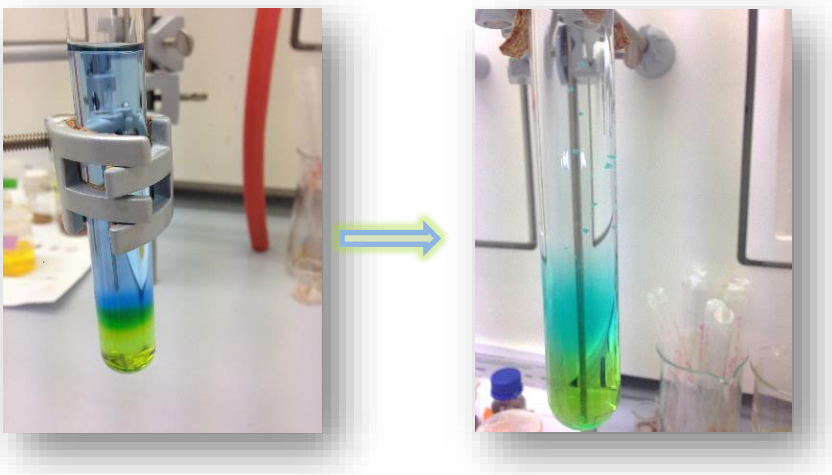

Figure 3: Picture of the slow diffusion synthesis for compound **11**. On the right, the first day of preparation. On the left, after a week result. It is possible to observe the diffusion of the metal solution from the bottom to the top, getting a clear colour due to the gradual dilution until it reaches the ligand solution, producing the crystallization.

MeOH in order to well separate the solution containing the metal and the second one containing the ligand. The ligand solution was carefully layered on top of the previous one, and it was prepared with a methanol solution of a 0.5 M of HCOOH (1.25 ml) and a 0.5 M solution of CH_3NH_3 (98µl), see Figure 3. After a week, green/blue single crystals were collected and washed with methanol. The yield was 55% based on the Cu metal ion. The slow diffusion method permitted to obtain large prism-shape crystals.

4.3.2 Dielectric Measurements

Dielectric measurements on the $[CH_3NH_3][Co(COOH)_3]$ compound were performed by measuring the complex impedance of a 4 mm diameter pressed pellet with a thickness of around 300 µm, made from selected ground single crystals using a commercial Agilent E4980 LCR-meter. Four coaxial cables linked to the electronic devices allow the measurements of the complex impedance. In order to extract the dielectric permittivity constant proportional to the capacitance of the sample, we used a model of capacitor and resistance in parallel.

Metallic electrodes were formed using silver paste on the parallel faces of the pellet. The best conditions of measurement ruling out extrinsic effects, established by systematic checks of the amplitude and frequency dependence, gives rise to an amplitude voltage of 1 V and a frequency of 10 kHz for the temperature range from 5 to 250 K. The relative permittivity as function of T was measured with a heating/cooling rate of 5 K/min.

4.3.3 Heat Capacity

Physical Properties Measurement System (PPMS) from Quantum Design, was used to measure the heat capacity on a single crystal sample of the $[CH_3NH_3][Co(COOH)_3]$ compound. We mounted the sample on a standard sample holder with a small amount of grease. The signal produced for this amount of grease was subtracted in the final data.

4.3.4 Powder X-ray Diffraction Measurements

We collected High-resolution powder diffraction (HRPD) data on the BM25-A Spanish CRG Beamline at ESRF synchrotron (Grenoble, France). A few milligrams of sample were placed inside a Ø 1 mm-diameter capillary. Data collection was done with a fixed wavelength of 0.62173 Å in a continuous 2θ scan transmission mode, between 2-40° range (except for **11** that has been measured in the 5-20º range in 2θ with 100◦ steps and 0.5 s acquisition), with 200° steps and 1 s acquisition time per point. The point detector was a

Cyberstar NaI (Tl) scintillator. We measured the samples from **7** to **11** except compound **10**, which was not yet prepared at that time. For compound **7** we collected six different data sets, while for the others members of the series only two data sets at 298 K and at 80 K. Basically from this experiments we will report just the high temperature data.

Figure 4 : The powder sample of compound **7** mounted on a glass capillary used during the powder diffraction measurements at ALBA synchrotron (Spain).

Powder diffraction patterns were collected also on the BL04-MSPD high resolution powder diffraction beamline at ALBA synchrotron (Barcelona, Spain), equipped with a 13-channel Si(111) multi-analyzer detector with high-angular resolution. The exploration of the high resolution powder diffraction data, using a helium based cryostat, allowing us cooling down 80 K were carried out using a Ø 0.7 mm glass cylinder as sample holder, see Figure 4. For all compounds were performed measurements above and below the crystallographic phase transitions. Specifically, for compound **7** height data sets in the 1-59.5º range in 2θ were collected at 30, 45, 60, 75, 90, 105, 120, 135 K. For compound **8** were recorded ten data sets at 15, 30, 45, 60, 75, 90, 105, 120, 135 and 250 K. For compound **9** were collected five data sets at 15, 30, 45, 60, and 75 K. For compound **10** were recorded height data sets at 25, 45, 65, 85, 125, 145, 165, and 240 K. Additional data measurements were made by ramps exploration in a cooling and warming rates as function of temperature in order to follow the change of the cell parameters variations and the phase transitions for compounds **7** to **10**. All measurements were performed with a wavelength of 0.4948 Å and the data analysis were carried out using the FullProf Suite[50].

4.3.5 Neutron Powder Diffraction Measurements

Neutron powder diffraction experiments were performed on the high intensity diffractometer D1B equipped with variable temperature environment at the Institut Laue Langevin (ILL, Grenoble, France). The samples were put in a Ø 6 mm cylindrical vanadium can and placed inside an Orange Cryostat. The diffraction patterns were recorded using λ = 2.52 Å wavelength, above and below the magnetic order temperature, at 20 and 2 K for compound **7**, 26 and 2 K for compound **8**, 40 and 2 K for compound **9**, 30 and 2 K for compound **10**, and 60 and 10 K for compound **11**, respectively. Moreover, a thermodiffractogram in the 2- 300 K ranges has been collected in order to obtain the

global temperature dependent diffraction pattern of the sample. The crystal structure refinements as well as the magnetic structure calculations were carried out using the FullProf Suite of programs[50].

4.3.6 Single Crystal X-ray Structure Determination and Refinement

Single crystal X-ray diffraction of the $[CH_3NH_3][Co(COOH)_3]$ compound at 300 and 45 K was performed on the CRISTAL beamline at SOLEIL synchrotron (Saclay, France) with λ = 0.67165 Å equipped with a helium stream. A single ϕ-scan was collected at 300 K to check the crystal structure before the phase transition. At low temperature, a combination of ϕ- and ω-scans were collected in order to increase the data completeness. After decreasing the temperature, the crystal suffered a structural phase transition and became a multi-component twin (phase **IV** of compound **7**). The indexing and integration protocol implemented in CrysAlis Pro program[51] permitted to obtain a reasonable model of the RT and the low temperature phases. The structures of both phases were solved by direct methods using the SHELXS97 program[52]. All non-hydrogen atoms were refined anisotropically by full-matrix least squares technique based on F^2 using SHELXL97. The hydrogen atoms were positioned geometrically and refined with AFIX43 constraint code. The final geometrical calculations and the graphical manipulations were carried out with PARST95[53], PLATON[54] and DIAMOND[55] programs.

4.3.7 Neutron Single Crystal Diffraction Measurements

In order to establish the hydrogen bond networks of the compounds **7** and **9**, single crystals of about 36 and 40 mm^3 of compounds **7** and **9**, respectively, (see Figure 5) were mounted onto a displex system in four-circle configuration on the monochromatic neutron thermal diffractometer D19 at the Institut Laue Langevin (ILL). We measured the samples

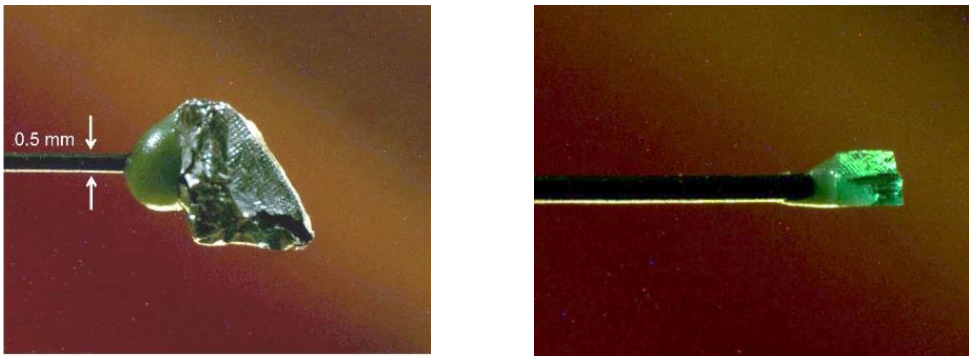

Figure 5: Left, the single crystal of compound **7** used during the neutron diffraction experiment was wrapped in an aluminum foil to avoid damage. Right, single crystal of compound **9.**

at different temperatures RT, 135, 122, 115, 106, 90 and 86 K for compound **7**, and 45 K for compound **9**, in order to elucidate the crystal structure in the different phases. It deserves to be noted that large single crystals for the Fe^{II}- and Mn^{II}-based compounds have not been obtained until now.

To solve the structures in the orthorhombic phase at RT and 135K for compound **7**, we collected data using a wavelength of 0.949Å. However, at lower temperatures, satellite reflections or reflections from two different twin domains appeared and, in order to separate properly the reflections, we changed the wavelength to 1.454 Å. The measurement strategy consists of several omega (ω) scans with steps of 0.07° at different χ and φ positions. The Multi-Detector Acquisition Data Software (MAD) from ILL was used for data collection. Unit cell determinations were done by using PFIND and DIRAX programs, and processing of the raw data was applied using RETREAT and RAFD19 programs. Absorption correction was applied using D19ABS program. The structures at RT and 135 K were solved by direct methods using SHELXL[52]. Full matrix least squares refinement on $|F^2|$ using SHELXL-2014/76 as implemented in WINGX program was used for structure refinement, while at 45 K, for compound **7** phase **IV**, the refinement was performed with JANA2006 program[56,57]. In the twinned phase each domain contributes 50% to the total intensity and they are related by a rotation of 180º around the *a**-axis. It should be noted that it is the same twin-law observed in the single crystal X-ray experiments. After this measurement, the crystal was warmed up and the phase (**7**) was recovered without any evidence of damage in the sample.

For data collected in the temperature range corresponding to phase **II** and **III**, D19 was operated with a wavelength of 1.456 Å, which is a good compromise between instrumental resolution, data completeness and the overlapping of neighbouring reflections. The incommensurate nuclear structures were solved at 122, 115, 106, 90 and 86 K, respectively, while three short (ω) scans where collected at 128, 126, 124, 102, 100 and 98 K temperatures in order to explore the evolution of the modulation vector. The superspace formalism included in JANA2006 program[56,57] was used to perform the data refinement. The program Diamond[55] was used for graphical representations.

4.3.8 Crystallographic tables of the compounds from **7** to **11**

Crystal data and details of the structure determination by X-Ray and neutron diffraction for the compound **7**.

Compound	$[CH_3NH_3][Co(COOH)_3]$ (**7**)				
Formula	$C_4H_9CoNO_6$			$C_4H_9CoNO_6$	
M	226.05			226.05	
Crystal system	Orthorhombic			Monoclinic	
Space group	*Pnma*			$P2_1/n$	
Radiation	*X-rays*	*Neutrons*		*X-rays*	*Neutrons*
***T*(K)**	RT	RT	135(2)	45(2)	45(2)
***a*, Å**	8.40770(10)	8.3940(2)	8.2827(2)	8.1750(3)	8.1621(3)
***b*, Å**	11.7215(4)	11.7181(3)	11.6735(2)	8.2710(3)	8.2487(3)
***c*, Å**	8.11090(10)	8.1068(2)	8.1543(2)	11.6730(5)	11.6584(4)
β, deg	-	-	-	91.883(3)	91.891(3)
***V*, Å^3**	799.34(3)	797.40(3)	788.42(3)	788.85(7)	784.49(5)
Z	4	4	4	4	4
ρ_{calc} (Mg m^{-3})	1.878	1.883	1.904	1.903	1.914
λ (Å)	0.67165	0.94905	0.94905	0.67165	1.454
μ (mm^{-1})	1.746	0.03884	0.03884	1.769	0.03884
***R*$_1$, *I* > 2σ(*I*) (all)**	0.0289 (0.0311)	0.0502 (0.0752)	0.0341 (0.0371)	0.0415 (0.0781)	0.0848 (0.0893)
w*R*$_2$, *I* > 2σ(*I*) (all)	0.0810 (0.0849)	0.1351 (0.1435)	0.0806 (0.0821)	0.0940 (0.1023)	0.1235 (0.1243)
Absorption Correction	Multi-scan	Numerical	Numerical	Multi-scan	Numerical
Independent reflections	1228	2703	2413	3006	1980

Crystal data and details of the structure determination with X-Ray diffraction for the compound **8** and **9**.

Compound	$[CH_3NH_3][Fe(COOH)_3]$ (**8**)
Formula	$C_4H_9FeNO_6$
M	226.05
Crystal system	Orthorhombic
Space group	*Pnma (62)*
Radiation	*X-rays*
***T*(K)**	RT
***a*, Å**	8.480403(7)
***b*, Å**	11.824332(9)
***c*, Å**	8.132253(6)
***β*, deg**	-
***V*, Å^3**	815.4625(11)
Z	4
ρ_{calc} (Mg m^{-3})	1.742
λ (Å)	0.494800
μ (mm^{-1})	0.673
***R*$_F$**	8.70
Gof	2.7
χ^2	7.36

Compound	$[CH_3NH_3][Ni(COOH)_3]$ (**9**)
Formula	$C_4H_9NiNO_6$
M	225.81
Crystal system	Orthorhombic
Space group	*Pnma (62)*
Radiation	*X-rays*
***T*(K)**	RT
***a*, Å**	8.30813(4)
***b*, Å**	11.6009(11)
***c*, Å**	8.05334(4)
***β*, deg**	-
***V*, Å^3**	776.198(12)
Z	4
ρ_{calc} (Mg m^{-3})	1.932
λ (Å)	0.621730
μ (mm^{-1})	2.492
***R*$_F$**	7.67
Gof	1.4
χ^2	2.06

Crystal data and details of the structure determination with X-Ray diffraction for the compound **10** and **11**.

Compound	$[CH_3NH_3][Mn(COOH)_3]$ (**10**)
Formula	$C_4H_9MnNO_6$
M	222.055
Crystal system	Orthorhombic
Space group	*Pnma (62)*
Radiation	*X-rays*
***T*(K)**	RT
***a*, Å**	8.622695(9)
***b*, Å**	11.937059(13)
***c*, Å**	8.199142(9)
***β*, deg**	-
***V*, Å^3**	843.9345(16)
Z	4
ρ_{calc} (Mg m^{-3})	1.748
λ (Å)	0.494800
μ (mm^{-1})	1.558
***R*$_F$**	6.73
Gof	1.9
χ^2	3.83

Compound	$[CH_3NH_3][Cu(COOH)_3]$ (**11**)
Formula	$C_4H_9CuNO_6$
M	230.6631.922
Crystal system	Orthorhombic
Space group	*Pnma (62)*
Radiation	*X-rays*
***T*(K)**	RT
***a*, Å**	8.56950(1)
***b*, Å**	11.45531(2)
***c*, Å**	8.11542(1)
***β*, deg**	-
***V*, Å^3**	796.800(2)
Z	4
ρ_{calc} (Mg m^{-3})	1.847
λ (Å)	0.494800
μ (mm^{-1})	1.897
***R*$_F$**	12.8
Gof	1.9
χ^2	4.29

4.3.9 FTIR- Measurements

The measurement of the infrared spectrum of the compounds from **7** to **11** has been performed using a JASCO FT/IR-4600 Mid-IR optical bench (7800 to 350 cm^{-1}) equipped with a monolithic diamond ATR accessory. The spectrum, recorded at room temperature (see Figure 6), shows the characteristic vibrational modes of the formate group and of the protonated amine. The stretching of υ(N−H) bond is at *ca.* 3000 cm^{-1} with a very weak signal and shoulder shape. The υ(CH_3) stretching bands are located at *ca.* 2860, 1456 and 1420 cm^{-1}.

Table 1. Vibrational modes of compounds from **7** to **11.**

	7	**8**	**9**	**10**	**11**
*υ*N−H	3025sh	3000sh	3088sh	3095sh	3064sh
υCH_3	2865w	2873w	2857w	2860w	2870w
$\upsilon_s/_{as}$ N−H	2775 w	2772 w	2763w	2776w	2769w
δ_{as} N−H	1642w	1636w	1644sh	1644sh	16437sh
υ_{as}OCO	1555s	1570s	1573s	1571s	1560s
υCH3	1457w	1458w	1458w	1457w	1458w
υCH3	1419w	1420w	1420w	1420w	1421w
δ_{as}OCO	1374 w	1376w	1379w	1380w	1377w
υ_sOCO	1352s	1354s	1351s	1351s	1345s
υ_{as}C−N	971w	970w	968w	969w	982w
δ_sOCO	804s	796s	793s	794s	806s

Key codes*: sh = shoulder, br = broad, w = weak, m = medium, s = strong*

The υ(C−N) asymmetric stretching bands with medium intensity have values of frequencies from *ca.* 1000 and 971 cm^{-1}. The typical bands of sodium formate spectrum are also present, showing a small shift in the frequency. The same effect is observed in the bands corresponding to the protonated amine. The υ(OCO) symmetric and stretching bands are observed at *ca.* 1560 and 135 cm^{-1}, the bending at *ca.* 1374 and 800 cm^{-1} showing the strongest intensities. These observed transmission bands are in agreement with those previously reported

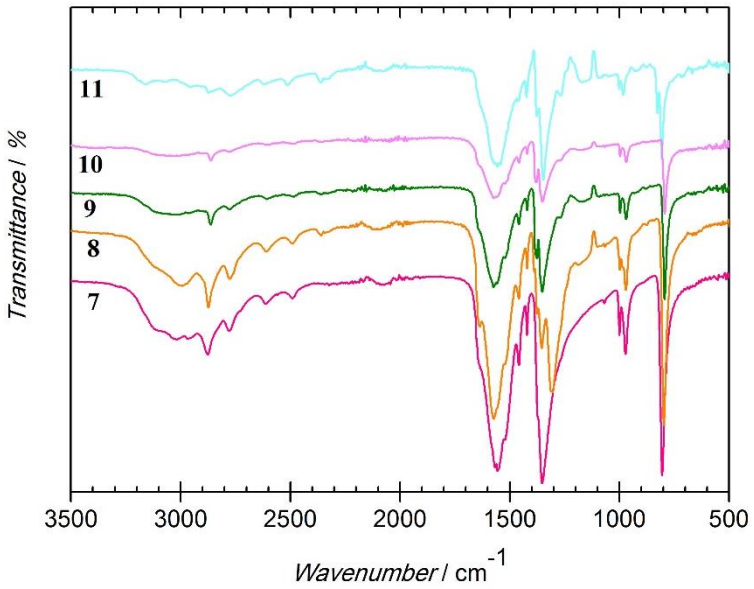

Figure 6: Infrared spectra of compounds from **7** to **11** recorded at room temperature.

4.3.10 Heat Capacity results

The heat capacity data of the compound **7**, only reveal a λ-shaped peak at 15 K, corresponding to the magnetic ordering. At higher temperature the heat capacity has been explored, but there is no signal that could be associated with the structural phase transitions. This absence of signal can be attributed to low energetic phase transitions, which can be present in an extended range of temperatures. The low temperature peak in the heat capacity suggests the compound has a 2D or 3D magnetic dimensionality[58]. In order to study the entropy related with the magnetic transition, we carried out a

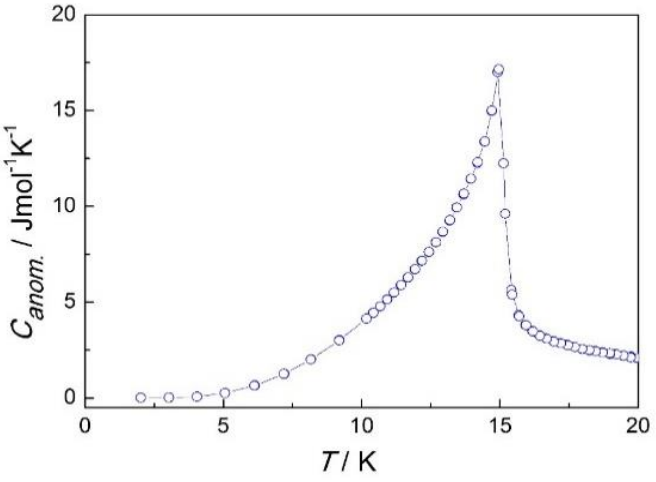

Figure 7: Anomalous heat capacity of $[(CH_3NH_3)][Co(COOH)_3]$ compound corresponding to the long-range magnetic ordering transition (see main text).

background correction by subtracting the phonon contribution (AT^3 term) (see Figure 7). The value of A was fixed to give no magnetic contribution well above the magnetic transition (above 20 K). The magnetic entropy was derived by integration of the C_p/T versus T plot up to 20 K, once the AT^3 contribution subtracted. The value of the entropy approaches 5.86 J mol^{-1} K^{-1} (per cobalt atom), half of the expected 11.5 J mol^{-1} K^{-1} for the magnetic entropy $R\cdot\ln(2s + 1)$ if s = 3/2. Nevertheless, cobalt is known to have s_{eff} = 1/2 at low temperatures[59], thus the value of 5.86 J mol^{-1} K^{-1} is in good agreement with the one expected one for s = 1/2 (5.76 J mol^{-1} K^{-1}).

4.3.11 Dielectric measurements results

The dielectric constant in the form of relative permittivity (ε_r) for compound **7**, is shown in Figure 8a. The relative permittivity decreases linearly from 8.86 at 250 K to 8.54 at 103 K. At this temperature, a clear change in the slope is observed as a drop from 8.54 to 8.47 at 80 K. This anomaly is continuous, which is compatible with second-order or with sluggish first order phase transition. Below this event, the permittivity value decreases in a linear way to reach a value of 8.35 at 6 K. It deserves to be noted that at T_N the relative permittivity remains almost constant, discarding the occurrence of a magneto-electric effect. The shape of the signal suggests the occurrence of an antiferroelectric-like phase transition at *ca.* 103 K. The variation in the slope of ε_r *vs* T displays a broad jump around transition temperature, indicating that the structural phase transition occurs in a large temperature range.

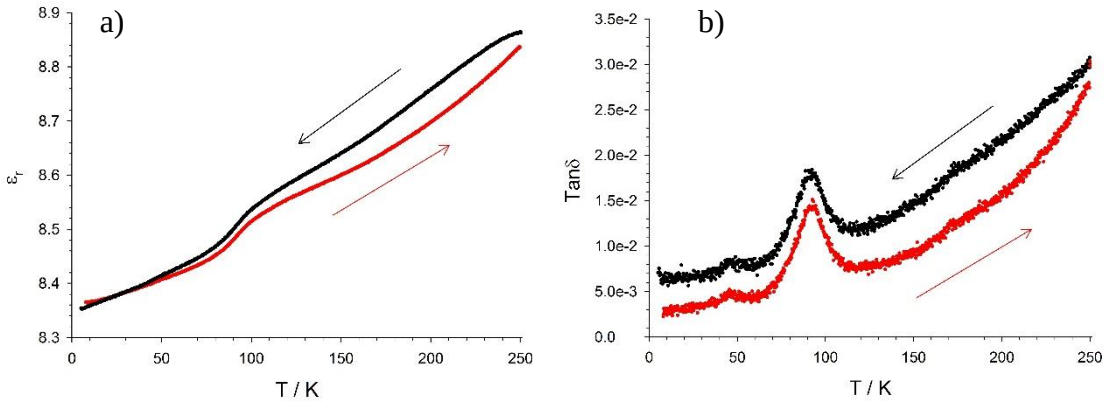

Figure 8: (a) Relative permittivity as a function of temperature (red curve on cooling and black curve on warming). The measurement was done on a pellet sample at 10 kHz, using an amplitude of 1 V. (b) Temperature dependence of the dielectric loss of $[CH_3NH_3][Co(COOH)_3]$ compound, at zero magnetic field. See further details in the experimental section.

Moreover, the powder diffraction data show a non-negligible mixture of phases at low temperature that depends of the cooling/warming process. This, together with the occurrence of two different incommensurate phases during the cooling down, can be at the origin of the changes observed in the permittivity curves. A correlation between nuclear phase transitions and the changes in the permittivity will be discussed in the forthcoming sections.

4.4 Crystal structure of the Phase **I**

The crystal structure of the $[CH_3NH_3][M^{2+}(HCOO)_3]$ series, where M is Co^{II}, Fe^{II}, Ni^{II}, Mn^{II} and Cu^{II} (**7**, **8, 9**, **10** and **11**, respectively), have been investigated using different diffraction techniques; single crystal neutron and X-ray diffraction, and synchrotron powder diffraction. At room temperature, all the compounds, from **7** to **11**, crystallize in the orthorhombic space group *Pnma* and all of them are isomorphs.

The crystal structures at RT can be depicted as a 3D anionic $[M(HCOO)_3]^-$ framework with a $4^{12}6^3$-**pcu** perovskite-like topology (in Schläfli notation). In order to achieve the electroneutrality, the framework cavities are filled with methylammonium cations $[CH_3NH_3]^+$. The compounds can be described as a molecular perovskite-like structure, following the ABX_3 formula, where the A and B sites are occupied by two different cations and the X_3 positions are occupied by anions, which act as bridges between the B sites. These perovskite-like structures can be related with our network being the $[NH_3CH_3]^+$ cation, the M(II) atoms and the formate ligand, the A, B and X_3 sites,

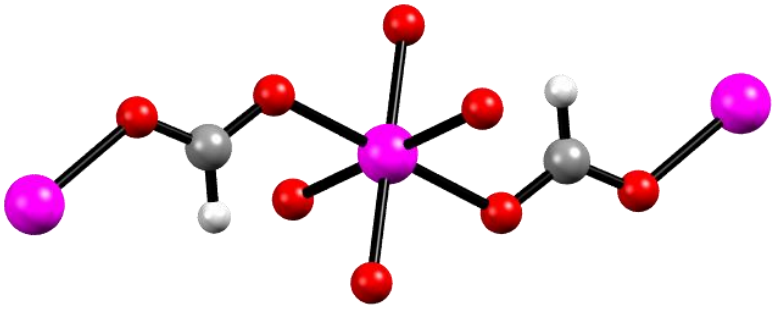

Figure 9: View of a fragment of the structure of **7** (phase **I**) together with the atom numbering, obtained from the single crystal neutron refinement at 135 K. Octahedral Co(1) atom has been represented in pink. The oxygen, carbon and hydrogen atoms have been represented in red, grey and light-gray, respectively. The methylammonium counter ions have been omitted for the sake of clarity.

respectively. In these compounds the anionic framework form cavities about 204-208 $Å^3$ (for compound **7**), which are filled by the $[NH_3CH_3]^+$ cation (A site).

The B site is occupied by the divalent metal ions. In the *Pnma* space group there is only one crystallographically independent metal ion site, which is located at an inversion centre.

Table 2: Selected bond lengths (Å) and angles (º) of compounds **7** phase **I**, measured at ALBA (X-Ray data) and at ILL (Neutron data).

Compound 7 (phase **I**)	X-rays	Neutrons	
Temperature [K]	RT	RT	135 K
Distances [Å]			
M─O1/O1$^{(II)}$	2.0932(6)	2.0945(7)	2.0893(5)
M─O2$^{(I)}$/O2$^{(III)}$	2.1191(6)	2.1169(7)	2.1135(4)
M─O3/O3$^{(II)}$	2.1054(8)	2.1045(7)	2.1002(5)
C1─O1	1.2444(11)	1.2423(9)	1.2467(6)
C1─O2	1.2602(10)	1.2574(9)	1.2628(6)
C2─O3	1.2499(9)	1.2511(8)	1.2556(5)
Angles [°]			
O1─M─O3 O1$^{(II)}$–M–O3$^{(II)}$	88.12(3)	87.95(2)	88.16(3)
O1─M─O3$^{(II)}$ O1$^{(II)}$─M─O3	91.88(3)	92.05(2)	91.84(3)
O1─M─O2$^{(III)}$ O1$^{(II)}$─M─O2$^{(I)}$	87.35(2)	86.89(2)	87.24(3)
O1─M–O2$^{(I)}$ O1$^{(II)}$─M─O2$^{(III)}$	92.65(2)	93.11(2)	92.76(3)
O2$^{(III)}$─M─O3 O2$^{(I)}$─M─O3$^{(II)}$	92.15(3)	92.27(2)	92.14(3)
O2$^{(I)}$─M─O3 O2$^{(III)}$─M─O3$^{(II)}$	87.85(3)	87.73(2)	87.86(3)

Symmetry codes: (I): 3/2−*x*,−*y*,−1/2+*z*, (II): 1-*x*, −*y*, −*z*, (III): −1/2+*x*,*y*,1/2−*z*.

Table 3: Selected geometric parameters of compounds **7** to **11** (Phase **I**) from X-Ray data measured at BM25 beamline at RT.

Compound	**7** (Co)	**8** (Fe)	**9** (Ni)	**10** (Mn)	**11** (Cu)
Temperature [K]	RT	RT	RT	RT	RT
Distances [Å]					
M─O1/O1$^{(II)}$	2.139(5)	2.0959(1)	2.0700(1)	2.1972(1)	1.980(7)
M─O2(I)/O2$^{(III)}$	2.144(4)	2.1638(1)	2.1145(1)	2.2160(1)	2.353(6)
M─O3/O3$^{(II)}$	2.111(4)	2.1201(1)	2.0842(1)	2.2122(1)	2.010(6)
C1─O1	1.184(8)	1.2721(1)	1.2451(1)	1.2422(1)	1.235(11)
C1─O2	1.218(7)	1.2639(1)	1.2500(1)	1.2576(1)	1.234(12)
C2─O3	1.248(5)	1.2682(1)	1.2462(1)	1.2410(1)	1.245(8)
C1─H1	1.099(17)	1.1106(1)	1.0903(1)	1.1239(1)	1.172(19)
C2─H2	1.065(18)	1.0938(1)	1.0842(1)	1.1707(1)	1.04(2)
C3─H3A	1.050(17)	1.0760(1)	1.0675(1)	1.0738(1)	1.06(3)
C3─H3B/H3B$^{(V)}$	1.061(17)	1.0893(1)	1.0681(1)	1.1633(1)	1.051(18)
N1─C3	1.477(12))	1.5192(1)	1.4835(1)	1.5020(1)	1.463(16)
N1─H1N	1.004(18)	1.0227(1)	1.0146(1)	1.0776(1)	1.024(19)
N1─H2N/H2N$^{(V)}$	1.050(16)	1.0578(1)	1.0370(1)	1.0134(1)	1.093(17)
Angles [°]					
O1─M─O3 O1$^{(II)}$─M─O3$^{(II)}$	88.20(17)	88.84(1)	88.27(1)	88.80(1)	88.2(3)
O1─M─O3$^{(II)}$ O1$^{(II)}$─M─O3	91.80(17)	91.16(1)	91.73(1)	91.20(1)	91.8(3)
O1─M─O2$^{(I)}$ O1$^{(II)}$─M─O2$^{(III)}$	92.91(17)	91.98(1)	92.54(1)	91.73(1)	92.5(3)
O1─M─O2$^{(III)}$ O1$^{(II)}$─M─O2$^{(I)}$	87.09(17)	88.02(1)	87.46(1)	88.27(1)	87.5(3)
O2$^{(I)}$─M─O3 O2$^{(III)}$─M─O3$^{(II)}$	88.20(18)	87.59(1)	87.74(1)	87.99(1)	88.2(3)
O2$^{(III)}$─M─O3 O2$^{(I)}$─M─O3$^{(II)}$	91.81(18)	92.41(1)	92.26(1)	92.01(1)	91.9(3)
O1─C1─O2	125.3(5)	124.22(1)	124.34(1)	121.40(1)	127.4(9)
O3─C2─O3$^{(IV)}$	122.9(7)	124.27(1)	123.75(1)	120.51(1)	124.9(10)

Symmetry codes: (I): 3/2-*x*,−*y*,-1/2+*z*, (II): 1-*x*, −*y*, −*z*, (III): −1/2+*x*,*y*,1/2−*z*. (IV): *x*,1/2−*y*,*z*, (V): *x*,1/2−*y*,*z*.

Taking as main example the compound **7**, the Co(II) ion is six-coordinated in almost ideal CO_6 octahedron, Figure 9, with values of the twisting parameter (ϕ) and compression ratio (*s*/*h*), derived from neutron data, of about 60° and 1.3, respectively at RT, (ϕ = 60° and *s*/*h* = 1.22 for an ideal octahedron)[60]. At 135 K, before the first structural phase transition, these values remain almost constant.

The equatorial plane of Co(1) is built up by O1, O3, $O1^{(II)}$ and $O3^{(II)}$ [(II): 1−x, −y, −z] while the axial positions are filled by $O2^{(I)}$ and $O2^{(III)}$ [(I): 3/2−x, −y, −1/2+z; (III): −1/2+x, y, 1/2−z] carboxylate-oxygen atoms (see Figure 9), see Table 2. The metal (II) ions are connected through formate ligands in *anti-anti κOO'* coordination mode along the [1 0 1], [0 1 0] and [1 0 -1] directions, for compounds from **7** to **11**, (see Figure 10). The values of the Co─O─C angle for the carboxylate bridge are in the range from 120.84(5)° to 122.11(4)° for **7** phase **I** at RT, while the Co···Co distances vary from 5.8348(1) to 5.8590(2) Å for **7** phase **I** (see Table 2 for compound **7** and Table 3 for compounds **8** to **11**). Regarding the host framework, there are some slight changes in the M(II) ion octahedral environment. Mainly, all M─O distances of the octahedral environments become shorter with decreasing of temperature, for example in **7**, the equatorial distances change from 2.0945(7) Å at RT [Co1─O1] to 2.0893(5) Å at 135 K [Co1─O1].

Along the series, the M─O bond distances are significantly modified, in particular in compound **11**, where the Jahn-Teller effect of the Cu^{2+} ion plays an important role. A detailed list of the most significant bond distances, at room temperature, is shown in Table 3. The distances in the formate ligands remain almost identical, being in the range from 1.2423(73) Å to 1.2511(7) Å at RT and from 1.2467(1) Å to 1.2628(1) Å at 135 K for compound **7**. However the angles in the ligands become slightly larger from 123.93(8)-124.66(63) deg at RT to 123.485(1)-124.312(1) deg at 135 K.

The hydrogen bonds from RT to 135 K are also shortening dropping down the temperature: the Donor···Acceptor distances are 2.8834(9) at RT and 2.8583(5) Å at 135 K. This contributes to the anchoring of the methylammonium counterion in the cavities as well as to the global crystal structure stabilization (see Figure 10 and Table 4).

Table 4. Possible hydrogen bonds of compounds **7** phase **I** determined from neutron diffraction.

7 (I) at RT	Donor···Acceptor (Å)	H···Acceptor (Å)	Donor-H···Acceptor (º)
N1—H1N···O3/O3$^{(II)}$	3.0448(10)	2.153(3)	144.04(17)
N1—H2N···O1$^{(III)}$	3.3136(9)	2.578(2)	127.55(18)
N1—H2N···O2$^{(III)}$	2.8834(9)	1.851(2)	173.66(19)
7 (I) at 135 K	Donor···Acceptor (Å)	H···Acceptor (Å)	Donor-H···Acceptor (º)
N1—H1N···O3/O3$^{(II)}$	3.0452(7)	2.1494(15)	144.56(7)
N1—H2N···O1$^{(III)}$	3.3207(6)	2.5868(14)	127.07(9)
N1—H2N···O2$^{(III)}$	2.8583(5)	1.8202(13)	173.86(10)

Symmetry codes: (I) 1/2+*x*,*y*,1/2−*z* (II) 1/2+*x*,1/2−*y*,1/2−z, (III) 3/2−*x*,1/2+*y*,-1/2+*z*.

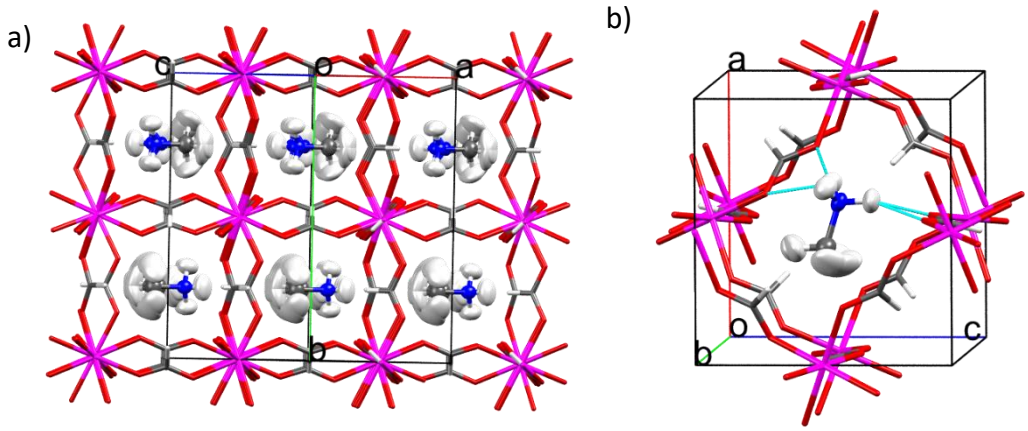

Figure 10: a) View along the [1, 0, 1] direction of a fragment of the structure of **7** (phase **I**), obtained from the single crystal neutron diffraction at RT. b) Detail of the metal-organic cage, where the methylammonium molecule is located, obtained from the single crystal neutron diffraction refinement at 135K. The nitrogen atoms of the methylammonium counterions have been represented in blue. The rest of the atoms follow the same colour codes as in previous figure. The H-bond network of the methylammonium molecules with the framework has been marked as dashed light blue lines.

All these changes in the structure promote that the evolution in temperature of the unit cell parameters does not follow an isotropic diminution with the decreasing of temperature. In fact, the *b*-axis increases slightly upon cooling. The methylammonium molecule is traversed by a mirror plane through the nitrogen and carbon atoms parallel to the *ac*-plane, this feature occurs for all compounds and is important for understanding the hydrogen-bond networks. For example in compound **7** at RT, the hydrogen atoms connected to the carbon atoms are disordered in two positions [H3A, H3B and H3C with

torsion angle H3A─C3─N1─H2N of 51.8(12)°, and H3A, H3C and H3B with torsion angle H3A─C3─N1─H2N of 68.2(12)°]. This disorder can be indicative of a rotation around the C─N axis.

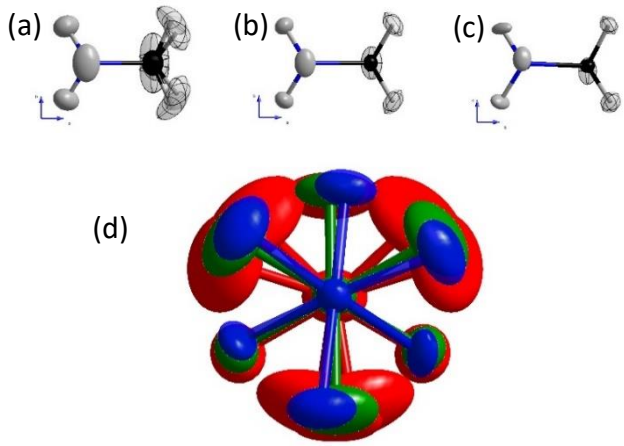

Figure 11. (a-c) Detailed view of the methylammonium molecule at RT and 135 K (phase **I**) and 45 K (phase **IV**, described below) obtained from the single crystal neutron diffraction measurements. The atoms, including the hydrogens, have been represented in ellipsoid mode with a 30% of probability. The hydrogen atoms from the CH_3 groups have been represented in transparent mode together with a principal ellipses. (d) View along the C─N bond of the methylammonium molecule at RT, 135 and 45 K, red, green and blue, respectively

When the system reaches 135 K, the entire molecule sits in a single crystallographic position where the hydrogen atoms bonded to the carbon atom are H3A, H3B and H3B with torsion angle H3A─C3─N1─H2N of 60.01(15)°, indicating that the possible rotation of the hydrogen atoms from the CH_3^- unit disappears, although the ellipsoids of these hydrogen atoms remain bigger than those of the NH_3^- unit (see Figure 11).

In this section, we have described in detail the crystal structure of compound **7**, and some comparisons have been done with compounds **8** to **11**. Before moving to the section describing the low temperature incommensurate phases we would like to show the temperature evolution of compound **11**. The large Jahn-Teller effect of the copper ions, gives rise to a temperature evolution, for this compound, which is significantly different from the sequence of phase transition presented by the archetype Co-based compound. For the sake of clarity, in the next sub-section we are going to describe the temperature dependence of the copper-based compound (**11**) and after that we will continue with the low temperature incommensurate phases.

4.4.1 Temperature evolution of $[CH_3NH_3][Cu(HCOO)_3]$

The substitution of the divalent metal ion by the d^9 Cu^{2+} ion into the previous described network produces a clear change in the lattice parameters. The unit cell parameters obtained from the powder diffraction at RT [a = 8.56950(1), b = 11.45731(2) and c = 8.11542(1) Å, using the orthorhombic *Pnma* space group] show a significant difference with respect to the other compounds of the family mainly in the a- and b-axes. These changes can be attributed to the Jahn-Teller effect that occurs because of the degenerate electronic ground state, which undergoes to a geometrical distortion in order to remove this degeneracy (Figure 12). From the Figure 12a, we observe that the d^9 electron configuration has the e_g orbital set asymmetrically occupied. If the unpaired

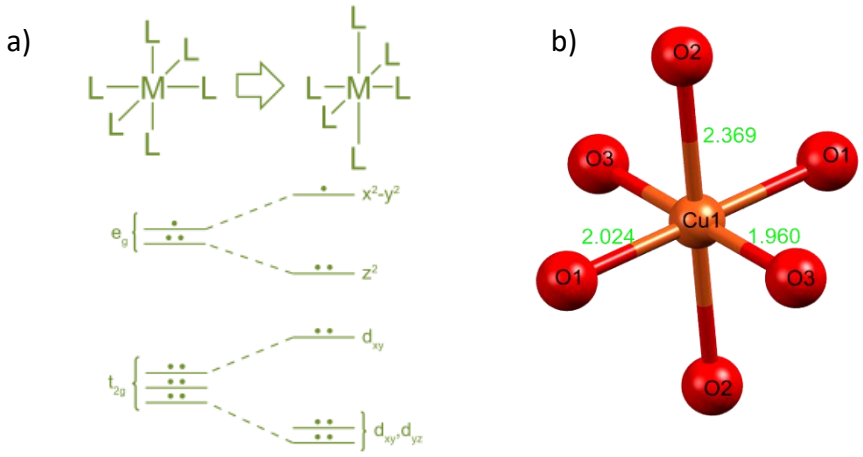

Figure 12: a) Jahn-Teller distortion of a d^9 metal octahedral complex. b) View of the octahedral crystal structure of compound **11**, with a clear Jahn-Teller distortion. The bonds values reported in green are expressed in Å.

electron occupies d_{z2} orbital, between the metal and the z-axis ligands there will be a concentration of the most electron density generating an electrostatic repulsion on the z-axis ligands. In addition, the asymmetric electron density distribution in the e_g orbital may increase the energy of the system. To avoid this effect, the complex suffers an elongation of the z-axis bonds and thus lowers the symmetry. However, the J-T distortions are typically observed in high spin d^4, low spin d^7 and d^9 configurations with octahedral environment. Table 3 above reports the comparison of selected bonds and angles between compound **11** (with Jahn-Teller distortion), and the rest of the other compounds (phase **I**), measured at RT.

The crystal structure of **11** was solved by using EXPO2014[61] and data refinements at RT were performed by using the programs of the FullProf suite[50] in the space group *Pbnm* after trying many different solutions (Figure 13 shows data refinement collected at RT). For example, in the temperature range from RT to 120 °C, the cell parameters (Å) vary from 8.56950(1), 11.45731(2) and 8.11542(1) to 8.63583(6), 11.49475(9) and 8.09947(7) for *a*, *b*, *c* respectively, (see Figure 14). In the low temperature range, from 1.5 to 300 K, neither synchrotron X-ray nor neutron powder diffraction data shows sign of structural phase transitions. A summary of the unit cell evolution in the low temperature region is shown in Table 5.

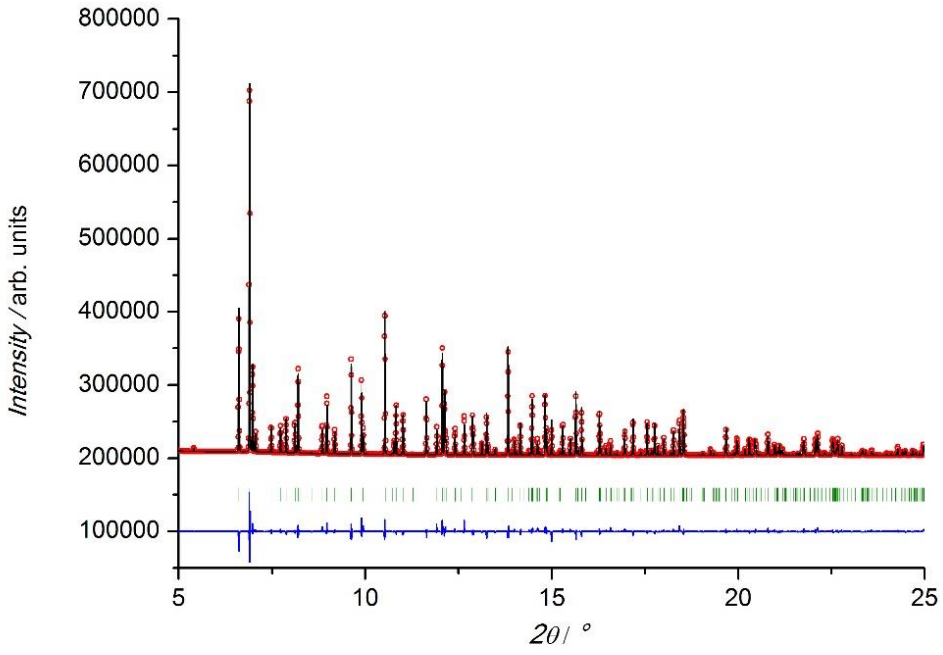

Figure 13: Experimental (open red circles) synchrotron X-ray powder diffraction data and calculated Rietveld refinement (black solid line) pattern for compound **11** at 30 °C (RT) (data collected with λ= 0.4948 Å). The difference between observed and calculated patterns has been represented as a blue line. The vertical green marks represent the position of the Bragg reflections. Refined cell parameters a = 8.56950(1), b = 11.45731(2) and c = 8.11542(1) Å, $\alpha = \beta = \gamma = 90.0°$. The data refinement gives, R_B = 6.29 % and R_F = 5.40 %, as agreement factors.

Table 5: Cell parameters of **11** at different temperatures measured on BM25 and D1B				
Temperature	***a* [Å]**	***b* [Å]**	***c* [Å]**	**V [Å^3]**
BM25				
RT	8.56761(8)	11.45931(11)	8.11778(9)	796.995(14)
150 K	8.48527(6)	11.42183(7)	8.13809(6)	788.722(9)
80 K	8.45906(7)	11.41130(9)	8.14397(7)	786.128(11)
D1B				
300 K	8.5613(8)	11.4550(10)	8.1249(8)	796.82(12)
60 K	8.4541(7)	11.4893(9)	8.2251(6)	798.93(17)
10 K	8.4655(8)	11.4395(13)	8.1700(9)	791.19(15)
2 K	8.4676(8)	11.4500(14)	8.1781(10)	792.90(16)

The above RT temperature evolution of the cell parameters from RT to 170°C, was followed through sequential Rietveld refinements of the synchrotron X-ray data. The *c*-axis length remains almost constant from RT until *ca.* 80 °C, afterwards the length of the axis decreases steadily until 120 °C. This change corresponds to −0.2% of the initial value. While for *a* and *b*-axis basically the behaviour is similar, increasing until a maximum (*ca.* 75 °C) and then after quick drop *ca.* 90 °C, the length starts to increase again constantly. This evolution corresponds to +1.2% for *a* axis and +0.34% for *b*-axis (see Figure 14). Moreover, due to the increasing of the temperature we observed also a net change of the volume that increase from RT reaching the maximum at *ca.* 75 °C and then a drop in the volume is observed between 75 and 90 °C, which correspond with the appearance of a second phase in the X-ray diffraction pattern. This second phase was successfully indexed as metallic copper, and the volume temperature evolution is shown in Figure 15 II.

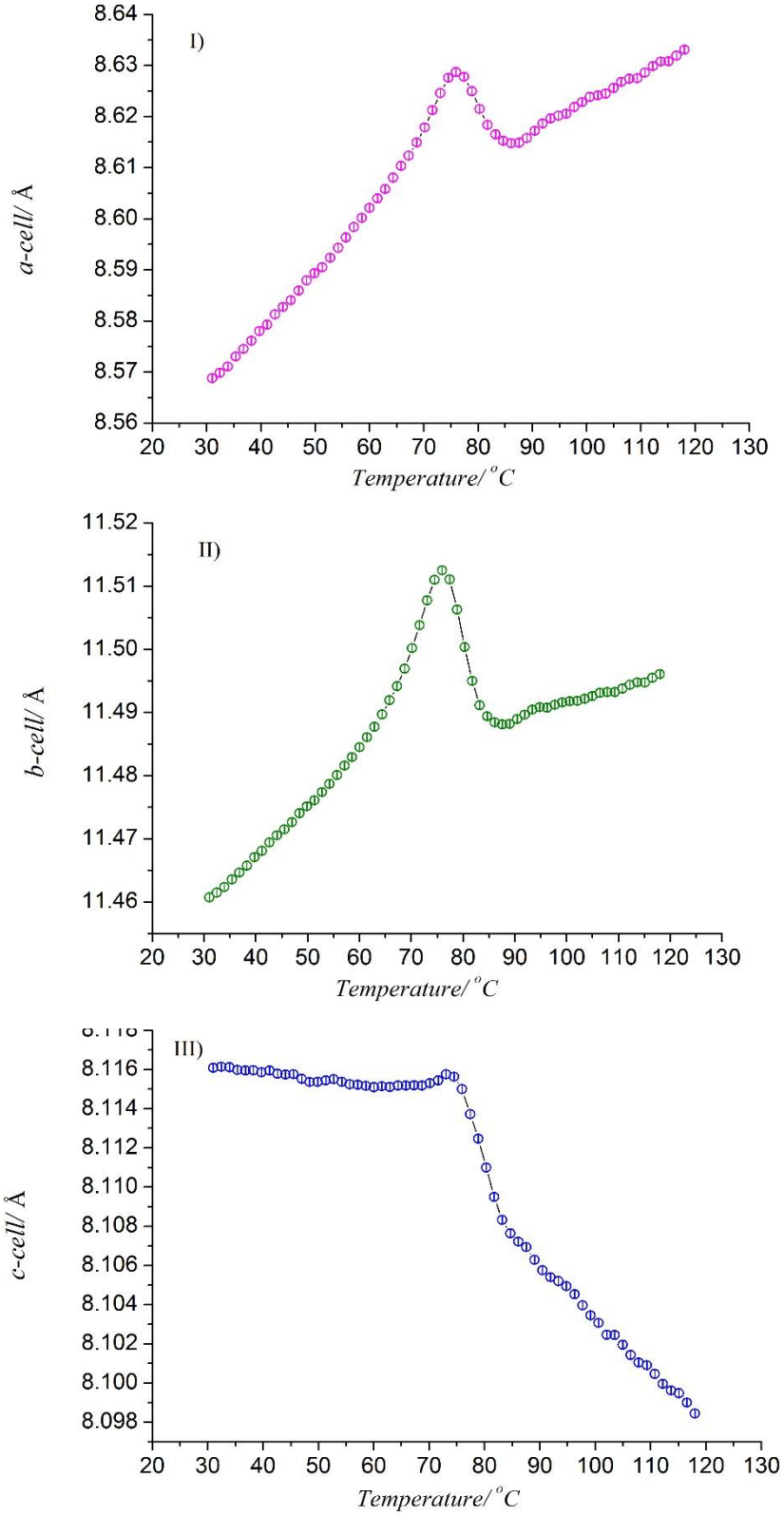

Figure 14: Temperature dependence of **11** lattice parameters *a*, *b*, *c* in the figures I) II) and III) respectively, performed in the range of temperature from 20 to 130 °C.

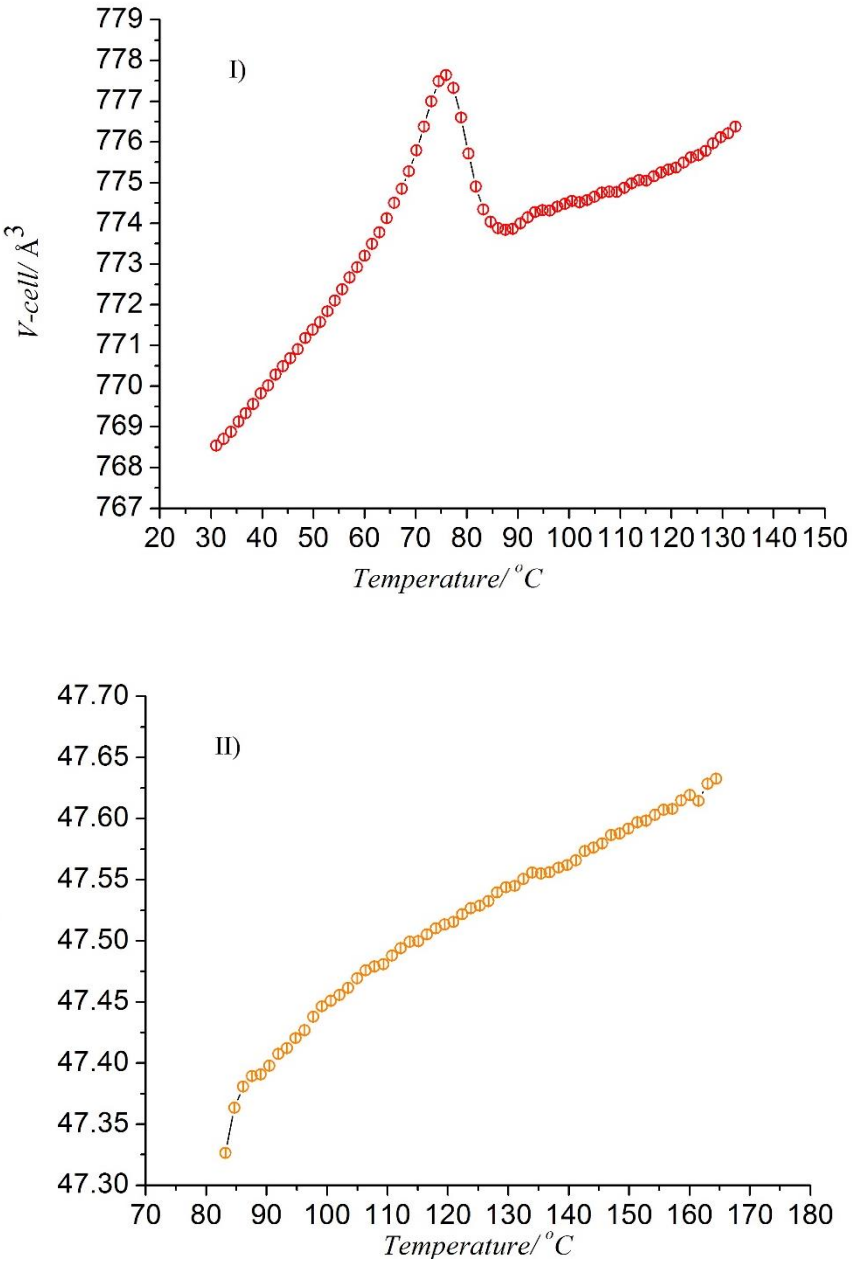

Figure 15: Temperature dependence of **11** volume values I) performed in the range of temperature from 30 to 130 °C and II) 80-170 °C corresponding respectively to the compound **11** and metallic copper.

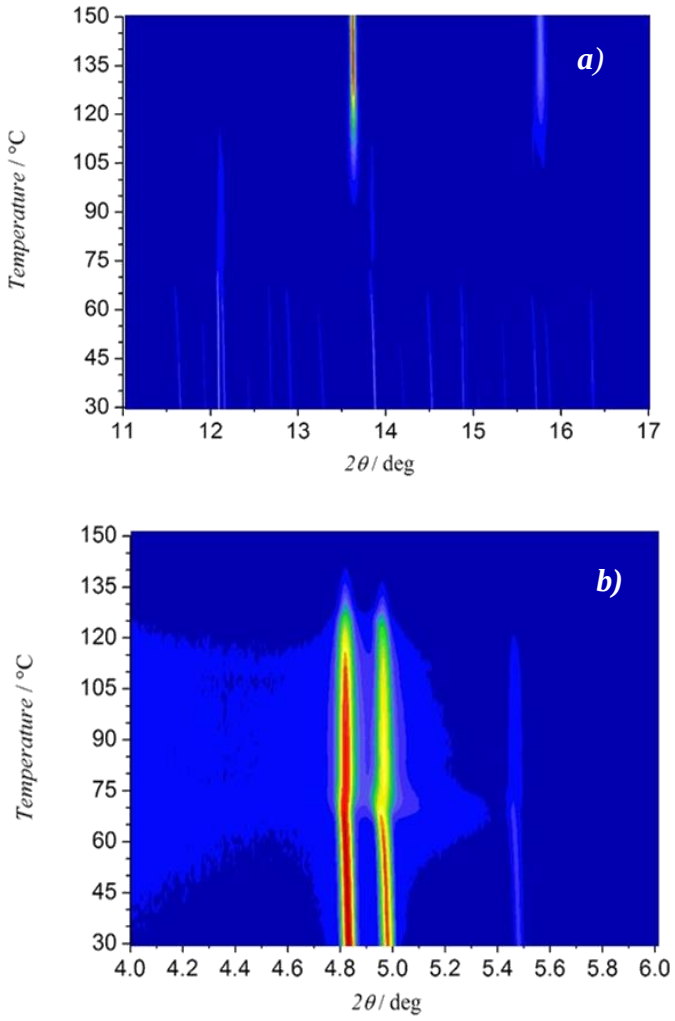

Figure 16: Mesh plot, with the intensities represented with logarithmic scale, collected at the BL04-MSPD (ALBA-Spain) in the temperature range of 30−150°C. The figure a) shows the coexistence of two phases above 13-14 deg of 2θ. The figure b) shows the particular of the starting process of the framework's decomposition, *ca*. below 75 degrees. The decrease in intensity as well as the small shift in the reflections are indicative of the beginning of the

After the appearance of the second phase, the volume of the main phase is increasing again from 90 °C until the sample decomposition *ca*. 150 °C. The maximum change of volume corresponds to 1.6%, which is in agreement with the value expected since a thermal expansion occurred. From 80 to 165 °C, the change of volume of the metallic copper is around the 0.8% (see Figure 15). The coexistence of phases start to be observed above 80 °C as can be seen in Figure 16 .

Figure 17 shows the (0 0 2) reflexion, at 6.98 degrees, "almost" not shifted until 75-80 °C, when the second phase start to be observed. At 7.06 deg. at 30 °C we can observe the (2 1 0) reflection which shows a shift from 7.06 degrees to 7.0 degrees as increasing the temperature. This shift is can be explained due to the elongation of the *a*- and *c*-axes.

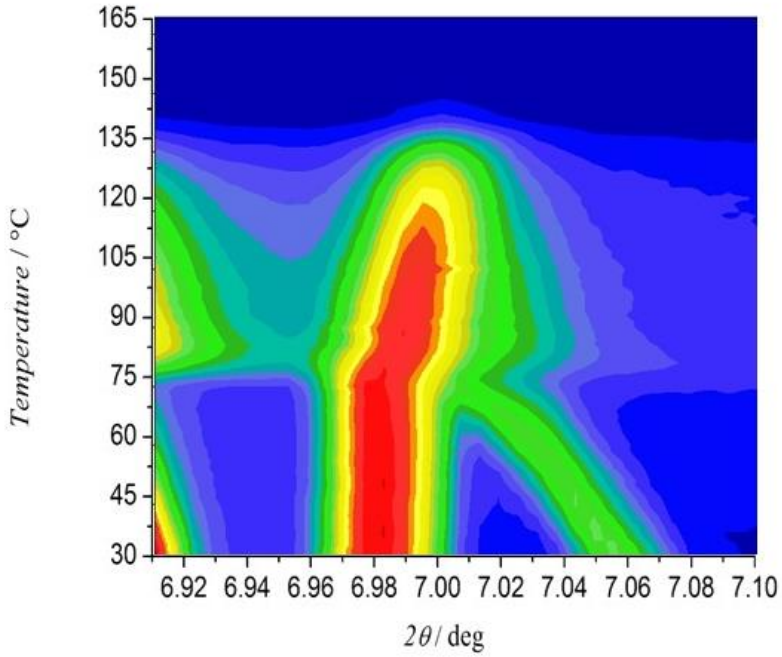

Figure 17: Mesh plot section, from 6.9 and 7.1 degrees range of 2θ, with the intensities represented in logarithmic scale. The figure represents the slight change of the (0 0 2) reflection at 6.98 degrees (2θ) and of the (2 1 0) reflection at ca. 7.06 degrees (2θ) that is particularly affected by a significant displacement to *ca.*7.02 degrees.

After the appearance of the second metallic Cu phase, the behaviour of (0 0 2) reflection implies a shortening of *c*-axis in net contrast with the net increasing of *a*- and *b*-axes, as shown above in Figure 14. In Figure 18, we can appreciate the evolution of the two distinct phases as function of temperature. In the first part is possible to observe only the first phase (copper-based coordination polymer) contribution; heating up the temperature from 20 °C until *ca.* 80 °C a change of the relative phase fraction is observed, so that the second phase (metallic copper) increases at the expense of the initial phase that starts to decompose. In the range between 80 and 138 °C, the first phase is no more observed and only metallic copper is present. The decomposition of the product is compatible with the observations reported on other formate-based compounds containing copper but with different counterions.

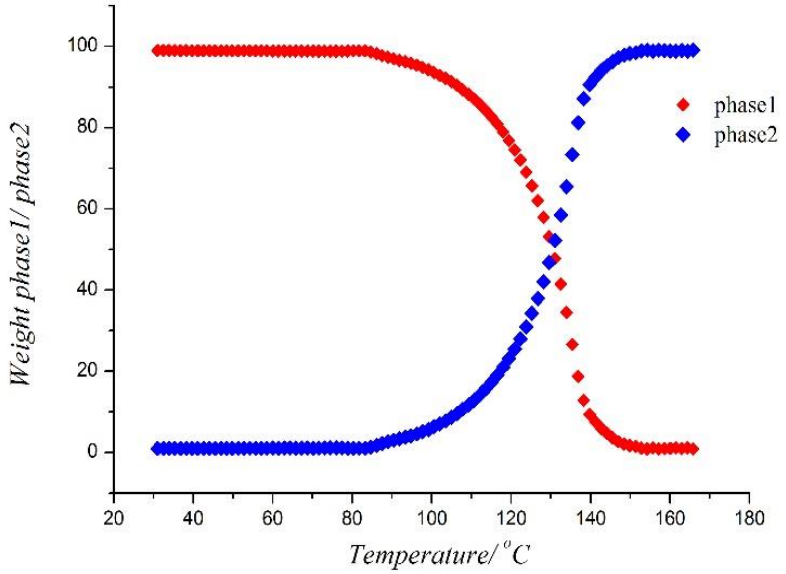

Figure 18: Temperature dependence of the weight fraction of the two distinct phases performed in the range of temperature from 30 to 170 °C. The red and the blue curves correspond to the amount of the main phase and to metallic copper, respectively.

The Bragg reflections of the compound **11** become quite broad due to the presence of microstrains resulting from the presence of defects; however, the *Pnma* structural model fit adequately the data. At 80 °C, in the main phase, the change of the scale factor value is indicative of a mass loss (see Figure 19), which is not a sufficient information in order to reach certain conclusions, but we can attribute it to be the beginning of the

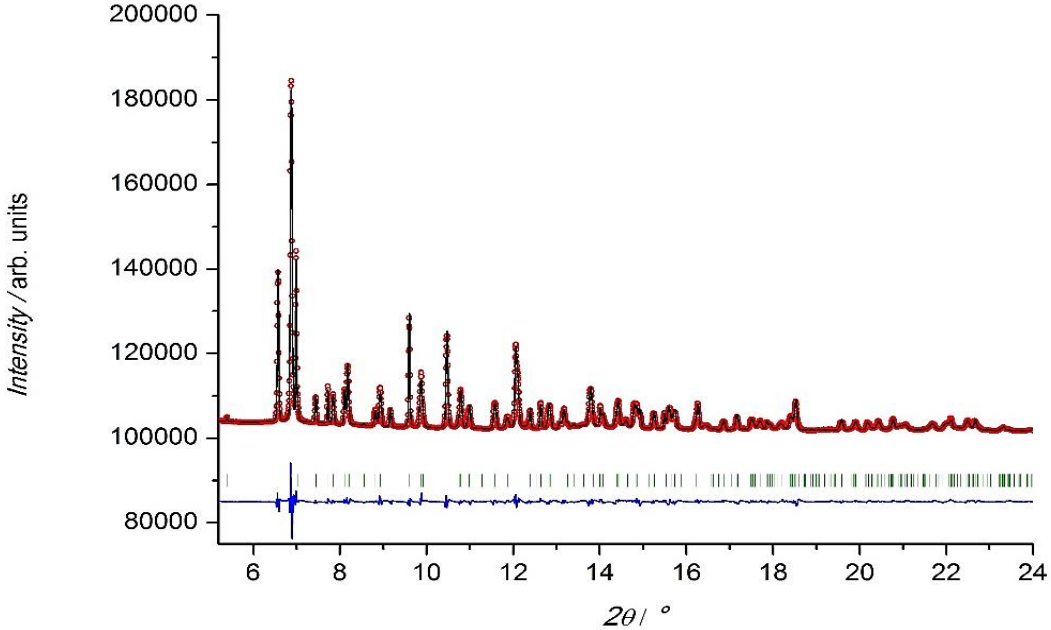

Figure 19: Experimental (open red circles) synchrotron X-ray powder diffraction data and calculated Rietveld refinement (black solid line) pattern for compound **11** at 80 °C (RT) (data collected with λ= 0.4948 Å). The difference between observed and calculated patterns has been represented as a blue line. The vertical green marks represent the position of the Bragg reflections. Refined cell parameters a = 8.62643(4), b = 11.50060(8) and c =8.11079(3) Å, α = β = γ = 90.0°. The data refinement gives, R_B = 5.74 % and R_F = 4.11%, as agreement factors.

decomposition of the initial coordination polymer. The thermal parameters increased significantly with respect to those observed at room temperature. This is in agreement with the fact that the structure vary as function of temperature. Moreover, the thermal parameters of the methylammonium nitrogen atom is "moving" less than the other atoms. The loss of formate ligand as well as of the methylammonium can lead to the collapse of the metal-organic framework architecture[62,63]. In a similar compound reported, the decomposition occurred in different steps[62]. The protonated amines are the first to decompose and successively the groups surrounding the metal centre, represented by the formate groups.

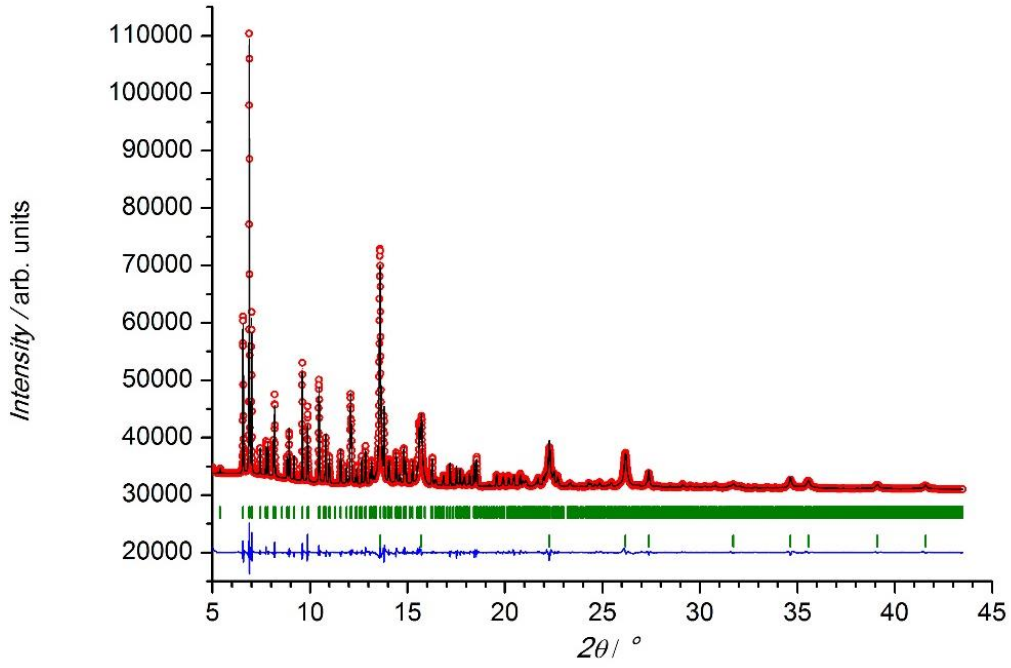

Figure 20: Experimental (open red circles) synchrotron X-ray powder diffraction data and calculated Rietveld refinement (black solid line) pattern for compound **11** at 115 °C (RT) (data collected with λ= 0.4948 Å). The difference between observed and calculated patterns has been represented as a blue line. The vertical green marks represent the position of the Bragg reflections corresponding to two phases. The first one (compound **11**) is refined with cell parameters a = 8.63572(4), b = 11.49460(6) and c = 8.09940(4) Å, $\alpha = \beta = \gamma = 90.0°$. The refinement gives, R_B = 3.61 % and R_F = 1.27%, as agreement factors. The second phase (cubic, metallic Cu) is refined with cell parameter a= 3.62149(2) Å. The data refinement gives, R_B = 1.27% and R_F = 0.909%, as agreement factors.

The structural refinement at 115 °C (Figure 20) shows a mixture of two phases. The first phase corresponds to the structural model of the RT phase together with non-negligible size and strain parameters and the second is metallic copper. Both phases permitted to reach a good final refinement. The coherence length (crystallite/domain size) has different values for each phase. The metallic copper at *ca*. 80 °C is constituted by nano-size particles. As the temperature increases, the nanoparticles of copper show a tendency to agglomerate and recrystallize giving rise to a bigger coherence domain, the

value of the average apparent size obtained from the refinement data increase from 156 Å at 115 K to 3525 Å at 158 K. This is evident in fact, form the decreasing of the width of the reflexions belonging the Cu-phase. In the data refinement at 160 °C (see Figure 21) the metallic copper is observed acquiring a certain crystallinity, so that the crystallite size is above 3000 Å. In order to explain the process of reduction from Cu(II) to Cu(0) few mechanisms have been proposed. This process depends on the presence of oxygen in the surrounding atmosphere. If the reaction occurs in presence of oxygen, it can lead to the oxidation of copper producing CuO. However, in our case, no copper oxide is detected, even thinking that the sample was not sealed in an inert atmosphere. The process of decomposition starts at *ca.* 80 °C resulting finally in the formation of metallic copper via the following reaction:

$$[CH_3NH_3][Cu(HCOO)_3] \xrightarrow{\Delta} Cu_s + 2\,CO_{2_g} + H_{2_g} + CH_3NH_{2_g} + HCOOH_g$$

The formation of H_2 may prevent the formation of copper oxide[62,64]. The interesting aspect of this process is that it does not involve residual presence of formate or methylammonium because they are volatile molecules. This allows thinking that may be a good candidate for using it as inks. In particular, due to the low temperature needed to produce the reaction, to the best of our knowledge the lowest temperature reported until now. In fact, the $[CH_3NH_3][Cu(HCOO)_3]$ compound directly could be mixed as emulsion with a volatile organic solvent to employ it on the surface to treat. Once the evaporation of the solvent is reached, and heating the surface at relatively low temperature, we can achieve the transformation of the layer of ink into a layer of metallic copper.

The use of different materials, including metal-organic-frameworks[65] as electronic conductive inks has already been reported[62–64,66,67]. Particular interests is focused on copper nanoparticles because they are less expensive than others and because they are promising candidates as ink-jet printing coated on flexible organic substrates[62], in order to create electronic circuits, easy to prepare and compatible with a variety of different printing methods[67].

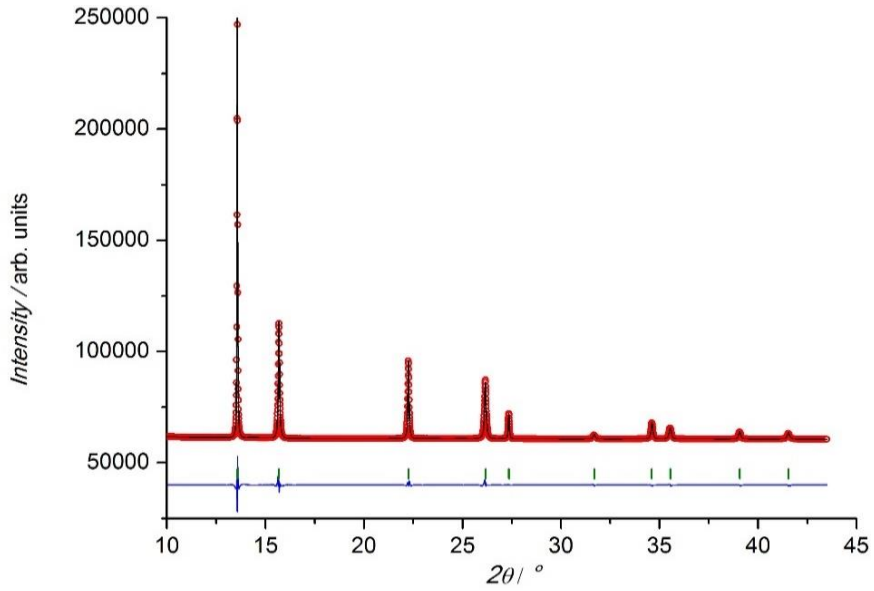

Figure 21: Experimental (open red circles) synchrotron X-ray powder diffraction data and calculated Rietveld refinement (black solid line) pattern for the initial compound **11** that is totally decomposed to metallic Cu at 160 °C (RT) (data collected with λ= 0.4948 Å). The difference between observed and calculated patterns has been represented as a blue line. The vertical green marks represent the position of the Bragg reflections. Refined with cell parameter a = 3.62432(1) Å. The data refinement gives, R_B = 1.89% and R_F = 1%, as agreement factors.

4.5 Incommensurate crystal structures; Phases **II** and **III**

Along this section, we are going to describe the occurrence of different modulated structures, as in the previous section the cobalt-based compound will be used, as the archetype and the rest of the members of the series will be compared with it. The previous described phase (phase **I**) crystallized in the commensurate *Pnma* orthorhombic space group[24,25,46–49,68], however when the temperature decreases some satellite reflections can be identified. The occurrence of these satellite reflections were corroborated with different techniques: synchrotron powder X-ray diffraction, neutron Laue and single crystal neutron diffraction. The combination of these techniques has allowed us to refine structural models with different modulation vectors and well as to suggest a mechanism for the occurrence of this atypical behaviour.

The refinement of modulated structures require the use of the superspace formalism. In the refinement of modulated structures, the deviation $\mathbf{u}(\bar{x}_4)$ from the average atomic position x_i (i = 1 to 3) is refined. The deviation is described in terms of the superposition of atomic modulation functions, which are assumed to be harmonic functions of the internal coordinate $x_4 = \mathbf{q}\,\mathbf{r}_{l\mu}$, where **q** is the modulation vector and $\mathbf{r}_{l\mu}$ is the vector

position of the atom μ in the unit cell *l*). The actual atomic positions of a particular atom (x_i) in the incommensurate phase are thus given as:

$$\boldsymbol{x}(\bar{x}_4) = \bar{\boldsymbol{x}} + \boldsymbol{u}(\bar{x}_4)$$

$$\boldsymbol{u}(\bar{x}_4) = \sum_{1}^{\infty} [\boldsymbol{A}_n \sin(2\pi n \bar{x}_4) + \boldsymbol{B}_n \cos(2\pi n \bar{x}_4)]$$

where $\bar{x}_i$ (i = 1, 2, 3) is the general atomic position in the average structure, $\boldsymbol{A}_n$ and $\boldsymbol{B}_n$ are the amplitudes of the displacement modulation, and *n* is the order of the harmonics in the Fourier series. The deviation $\mathbf{u}(\bar{x}_4)$ from the basic atomic positions x_i (i = 1 to 3), isotropic/anisotropic atomic displacement parameter (ADP), as well as all other parameters considered in the refinement were taking into account in order to refine until a maximum of third-order satellites. It deserves to be noted, that the modulation parameters are usually very sensitive to any deficiency in the average structural model, therefore the average structure should be as accurate as possible. In order to consider all the atoms (including the hydrogen atoms), single crystal neutron diffraction patterns at different temperatures have been collected in order to determine the modulation vectors and the modulated crystal structures of compound **7** phases **II** and **III**. The occurrence of two phases (phase **II** and **III**) is correlated with a change in the wave vector. The determination of the atomic position in each phase is fundamental to understand the mechanism of the modulation. Finally, we have correlated the sequence of phase transitions with the features observed in the dielectric measurements.

4.5.1 $[CH_3NH_3][Co(HCOO)_3]$ (**7**)

The occurrence of an order-disorder phase transition, can involve the blocking of the counterion's libration or the re-organization of these molecules in the framework's cavities. These effects are responsible of a symmetry breaking giving rise to a decrease of the symmetry of the system upon cooling. Moreover, a multiplication of the crystallographic axes are sometimes needed in order to explain the nature of the phase transition[6,18,20,43,44,48,69–75]. However, more complex order-disorder transitions are also possible. Sometimes, the competition between atomic interactions in pure inorganic ABO_3 perovskites is responsible of the occurrence of unusual structural instabilities.

The balance of these interactions can drive to incommensurate structures[76–78]. The atomic interactions responsible of the incommensurate distortions involve both, the A-counterion displacements, as well as antiferrodistorsive motions (mainly the tilting of the oxygen octahedron centred in the B-site)[79]. Among the low number of incommensurate structures reported on the Bilbao Crystallographic Server databases[80] 145 entries (of which 24 are composites)[81], there are no examples of organic-inorganic perovskite-like compounds, although a similar scenario to the pure inorganic perovskites is expected. To the best of our knowledge, the only similar example is the $(C_6H_{11}NH_3)_2[PbI_4]$ compound, which presents a hybrid perovskite-like structure. This compound shows an incommensurate structure below 130 K[82]. The crystal structure was described using the so-called superspace formalism[83] and refined in the superspace group $Pca2_1(\alpha\ ½\ 0)$. The $[CH_3NH_3][Co(COOH)_3]$ compound presents an anomaly in dielectric measurements (section 4.3.10): a broad peak was observed in the dielectric loss, suggesting a reorganization of existing electric dipoles. A detailed exploration in this range of temperatures, using synchrotron powder diffraction, monochromatic single crystal and Laue neutron diffraction, shows the occurrence of satellites reflections, which can be indexed with an incommensurate wave vector. From 300 K to 150 K we have observed no phase transition in the powder sample. The only evident feature is the displacement of Bragg reflections due to the thermal contraction on cooling; see the Figure 22. The temperature evolution of the sample was followed from 45 K to RT using neutron Laue Diffraction at the CYCLOPS diffractometer (Figure 23). In this figure is shown the appearance of satellite reflections below 135 K. The position and intensity of this satellites change as function of the temperature suggesting a change in the modulation wavelength as well as a change in the crystal structure (modulation amplitude). Between 135 K and 120 K the first nuclear phase transition is observed from the orthorhombic *Pnma* space group to an incommensurate structure where first order and second order harmonic reflections are observed (phase **II**). Between 120 and 90 K the intensity of the satellite reflections increases. In this temperature range second and third order harmonic reflections are observed. Below 90 K, a shift in the satellites together with a notable increase of intensity of the first harmonic satellites is manifest. These features suggest a change in the wave vector, and therefore a new incommensurate structure (phase **III**). Below this temperature, the commensurate reflections as well as the second and above order harmonics loses intensity, while the first order satellites increase. Below *ca.* 75 K, (Figure 23 f) the patterns can be indexed with a twined monoclinic

crystal. The detailed description of this new commensurate phase (phase **IV**) will be presented in a further section.

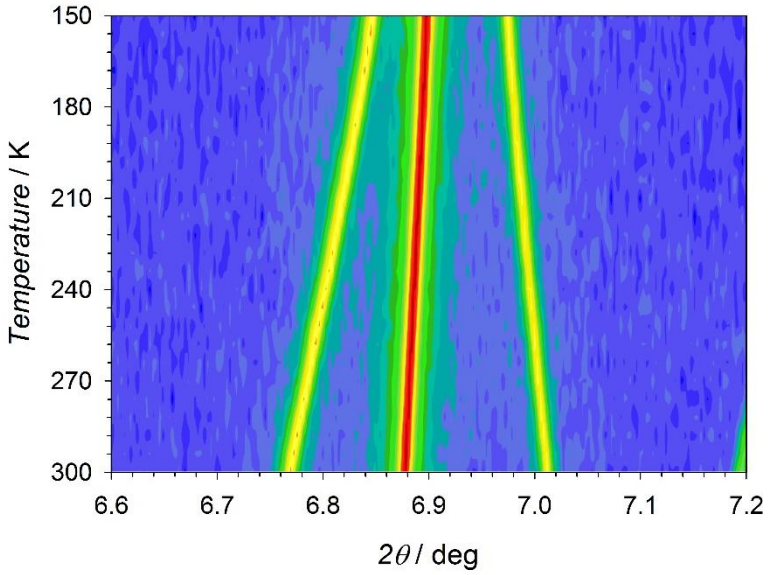

Figure 22: Mesh plot of the Bragg reflections as function of temperature collected as cooling down ramp in the temperature range from 300 to 150 K at BL04-MSPD beam line at ALBA (Spain).

The synchrotron powder diffraction data, between 135 and 30 K, show a behaviour, which is clearly dependent of the cooling/warming history. If we cool down using a slow protocol, following a ramp of 2 K/min plus *ca.* 45 min of acquisition time at each

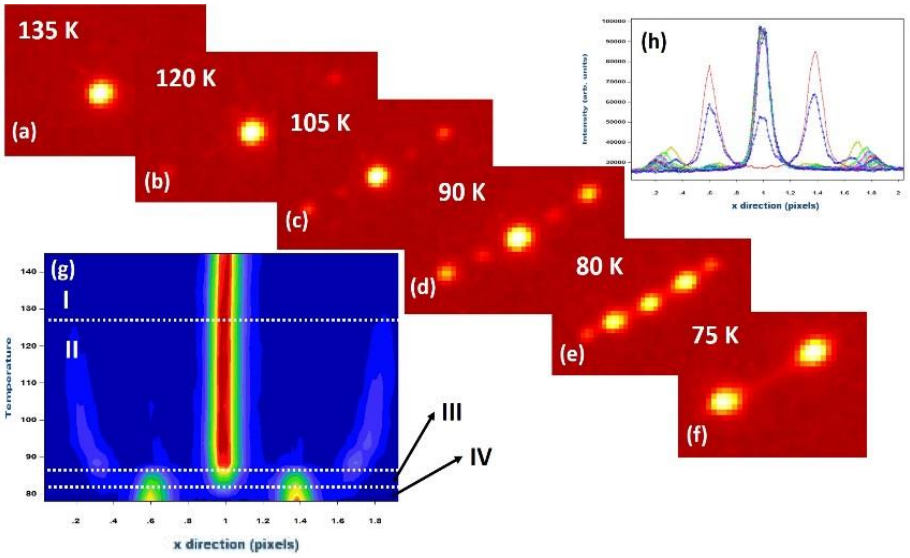

Figure 23: Selected reflection as function of the temperature at Cyclops Laue diffractometer [from a) to f)]. The selected images show the occurrence of two incommensurate structures [see the intensities of the satellite reflections in figures h) and g)] and the low temperature phase (*ca.* 75K) where the crystal became twinned. In the g) figure the temperature evolution of the (a)-(f) images have been represented in a mesh plot together with and the different phases observed. The h) picture is a representation in 2D of the integrated intensities as function of T in which is better understandable the structural transition that present the $[CH_3NH_3][Co(HCOO)_3]$ compound.

temperature (135, 120, 105, 90, 75, 60, 45 and 30 K) we observe that only one modulation vector exists in the full range of temperature.

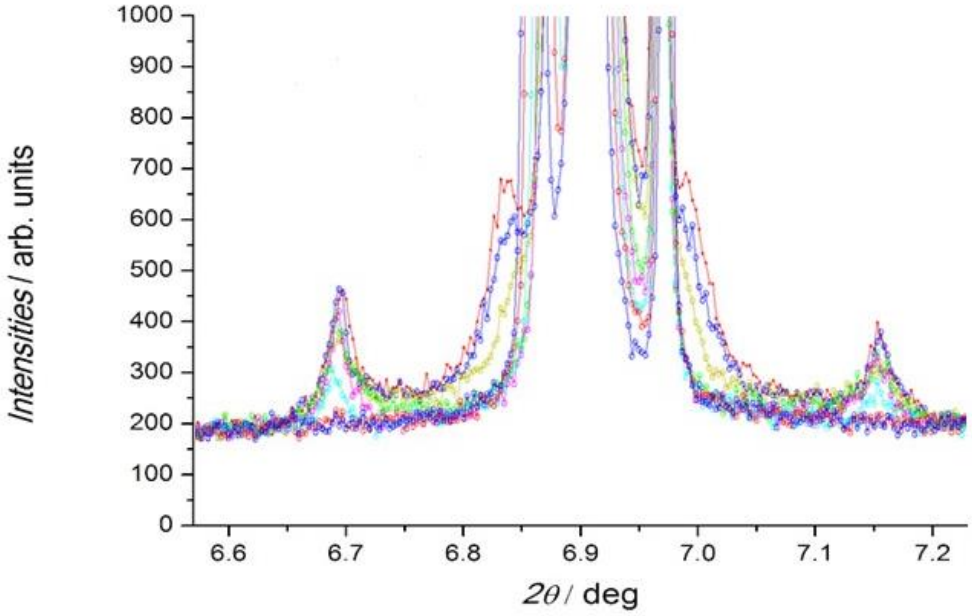

Figure 24: Representation in 2D of the integrated intensities as function of temperature collected as cooling down ramp in the temperature range from 135 K to 30 K at BL04-MSPD beam line at ALBA (Spain).

The superstructure reflections at 6.68 and 7.16 deg. in Figure 24 is observed for temperatures below 120 K and remain present at 30 K. If the cooling is done in a fast way at 5 K/min from high temperature to directly 15 K, depending of the temperature range the system is not able to cool down following the programed ramp, but even in this case

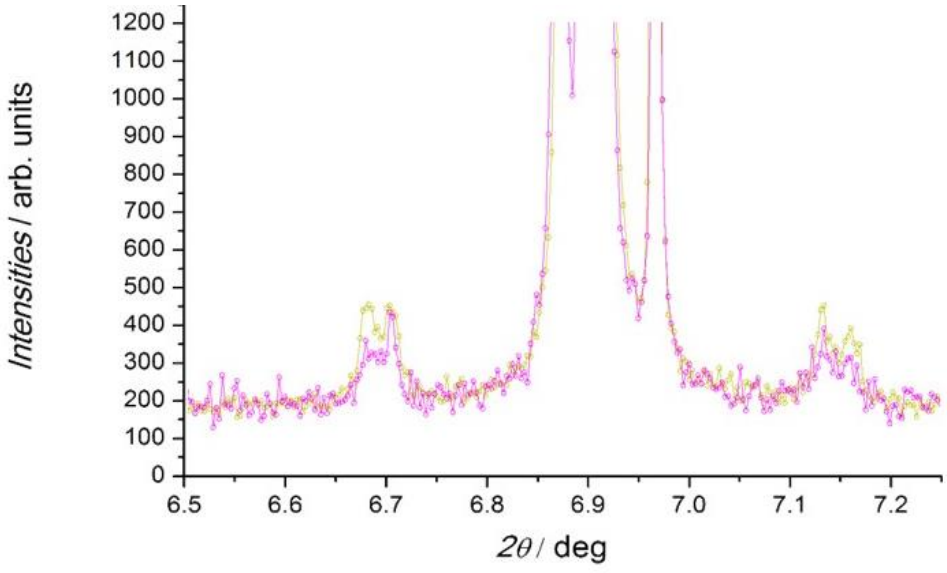

Figure 25: Representation in 2D of the integrated intensities showing the coexistence of modulation vectors, in the same temperature range.

the cooling is much faster than in the previous cooling. In that way, we observe the occurrence of different modulation vectors, which can coexist in the same temperature range, see Figure 25. Finally, we warmed up, from 15 K to 135 K with stabilization temperatures at (15, 30, 45, 60, 75, 90, 105, 120 and 135 K), see Figure 26, during this warming up only one modulation vector has been observed (the temperature range is consistent with the single crystal data). It deserves to be noted that, in the powder data the monoclinic phase (phase **IV**) observed in the single crystal (see section 4.6) data is not obtained as a single phase. A detailed description of these results are shown in 4.6. The modulation vector can be indexed using the powder data, in most of the patterns all satellites reflections can be indexed with a single propagation vector along the *c**-axis. It deserves to be noted that, during the fast cooling, a mixture of two propagation vectors is observed. These **q**-vectors correspond to $q_z \approx 1/7$ or $\approx 1/8$, phase **II** or **III**, respectively. Therefore, the length of the *c*-axis as well as the unit cell volume, in the incommensurate phases (from 130 to 90 K), is close to 7-fold or 8-fold larger than in the commensurate orthorhombic phase (*Pnma* phase **I**). Values which are similar to those reported for the inorganic $PbZrO_3$ perovskite structure[84].

The results obtained from the Laue and synchrotron powder diffraction are not good enough to determine the complete crystal structures in the different incommensurate

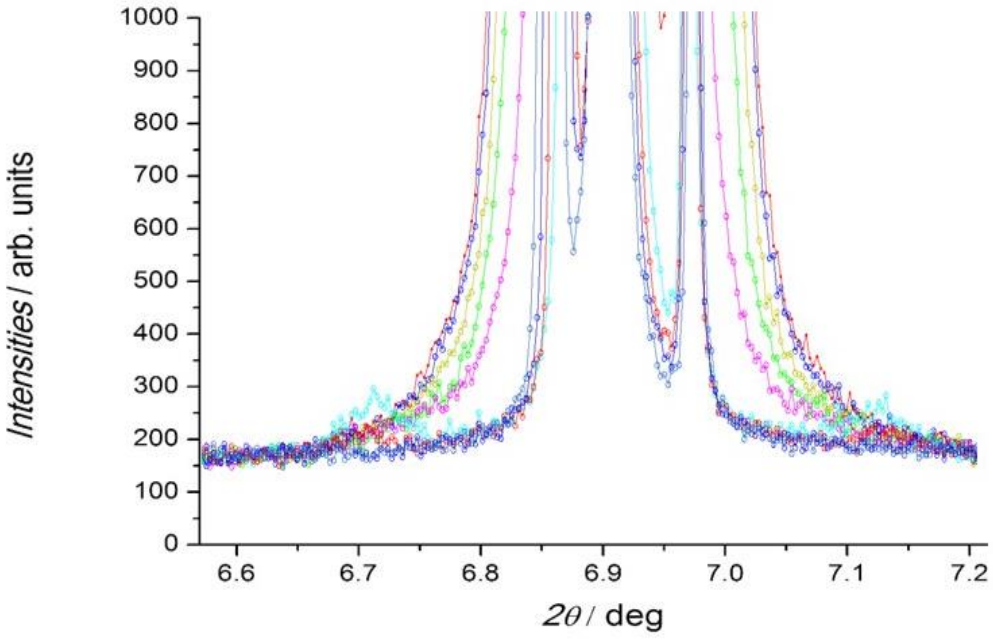

Figure 26: Representation in 2D of the integrated intensities measured warming up the sample from 15 K to 135 K, showing the broadening due to the mixture between monoclinic and orthorhombic phases, as well as the occurrence of satellites (cyan curve).

phases. Therefore, in order to overcome this problem, neutron diffraction on a large single crystal, has been used to increase the number and the quality of satellite reflections.

In order to separate the satellite from the principal reflections, D19 was operated with a wavelength of 1.456 Å, which is a good compromise between instrumental resolution, data completeness and the overlapping of neighbouring reflections. Due to the current limitations of the integration software, the indexing of reflections was done using a super-cell, in order to index until the second order harmonics.

The modulation vector was determined using a large number satellites, including the high-order satellites. The observed satellites are compatible with modulation vector **q**: (0, 0, γ) with γ being values very close to 1/7 or 1/8 depending on the sample temperature. The decomposition into main and satellite reflections (principal, first-, second- and third-order reflections) was done using the D19 software SATELLITE.

The absorption correction, mainly due to the hydrogen content of the sample was carried out after the data integration. The identification of reflection conditions and superspace groups, as well as the crystal structure solution in all possible superspace groups was done using SUPERFLIP. [85] Using the superspace formalism, the best data fit was carried out using the superspace group *Pnma*(00γ)0s0.

The D19 data are grouped in two different sets, those used to full refine the structural model which were collected at 122, 115, 106, 90 and 86 K (see Table 6), and those data collected in order to follow the temperature evolution of the modulation vector. These last scans, consist of three short omega scans, collected in a specific region of the reciprocal space which allows us the determination of the modulation vector. These short-scans were collected at intermediate temperatures between full-data sets. The results derived from these scans correspond to the green light columns in Table 7.

Table 6. Experimental and crystallographic data, measured at D19 diffractometer for compound **7**.

***T*, K**	**122(2)**	**115(2)**	**106(2)**	**90(2)**	**86(2)**
Formula	$C_4H_9CoNO_6$	$C_4H_9CoNO_6$	$C_4H_9CoNO_6$	$C_4H_9CoNO_6$	$C_4H_9CoNO_6$
M	226.05	226.05	226.05	226.05	226.05
Crystal system	Orthorhombic	Orthorhombic	Orthorhombic	Orthorhombic	Orthorhombic
Space group	*Pnma*(00γ)0*s*0	*Pnma*(00γ)0*s*0	*Pnma*(00γ)0*s*0	*Pnma*(00γ)0*s*0	*Pnma*(00γ)0*s*0
***a*, Å**	8.2674(2)	8.2792(4)	8.2556(2)	8.2702(3)	8.2548(3)
***b*, Å**	11.6600(4)	11.6797(6)	11.6519(3)	11.6766(4)	11.6547(6)
***c*, Å**	8.1483(2)	8.1636(5)	8.1508(3)	8.1631(6)	8.1521(3)
α, deg	90.00	90.00	90.00	90.00	90.00
β, deg	90.00	90.00	90.00	90.00	90.00
γ, deg	90.00	90.00	90.00	90.00	90.00
Wavevector	**q** = 0.143**c***	**q** = 0.143**c***	**q** = 0.143**c***	**q** = 0.1247**c***	**q** = 0.1247**c***
***V*, Å^3**	785.48(4)	789.41(8)	784.05(4)	788.29(7)	784.29(6)
Z	4	4	4	4	4
ρ_{calc}, mg m^{-3}	1.9115	1.902	1.915	1.9047	1.9144
λ, Å	1.4569	1.4569	1.4569	1.4569	1.4569
μ, mm^{-1}	0.2414	0.2414	0.2414	0.2414	0.2414
***R*$_1$, *I* > 2σ(*I*) (all)**	0.0880(0.1189)	0.1086(0.2620)	0.0836(0.1012)	0.1030(0.1449)	0.1098(0.1468)
w*R*$_2$, *I* > 2σ(*I*) (all)	0.1048(0.1067)	0.1215(0.1307)	0.0965(0.0982)	0.1293(0.1326)	0.1297(0.1326)
Absorption Correction	Numerical	Numerical	Numerical	Numerical	Numerical
Independent reflections	3543	3226	3544	4617	4920
No. of main refl.	734	661	735	473	745
No. of 1st order satellite reflections	1330	1223	1330	1336	1340
No. of 2st order satellite refl.	1479	1342	1479	1470	1491
No. of 3st order satellite refl.	-	-	-	1338	1344

Table 7. Temperature evolution, from RT to 45 K, of the modulation vector on the single crystal sample of **7** at D19 diffractometer. Columns in light green refers to explorative scans.

T, K	**RT**	**135**	**128**	**126**	**124**	**122**	**115**
Space group	*Pnma*	*Pnma*	*Pnma*(00γ)0s0	*Pnma*(00γ)0s0	*Pnma*(00γ)0s0	*Pnma*(00γ)0s0	*Pnma*(00γ)0s0
a, Å	8.3940(2)	8.2827(2)	8.3100	8.3178	8.3350	8.2674(2)	8.2792(4)
b, Å	11.7181(3)	11.6735(2)	11.6755	11.6743	11.6899	11.6600(4)	11.6797(6)
c, Å	8.1068(2)	8.1543(2)	8.1669	8.1664	8.1726	8.1483(2)	8.1636(5)
α, deg	90.00	90.00	90.00	90.00	90.00	90.00	90.00
β, deg	90.00	90.00	90.00	90.00	90.00	90.00	90.00
γ, deg	90.00	90.00	90.00	90.00	90.00	90.00	90.00
q	(0, 0, 0)	(0, 0, 0)	(0, 0, 0.1428)	(0, 0, 0.1429)	(0, 0, 0.143)	(0, 0, 0.143)	(0, 0, 0.143)
V, Å^3	797.40(3)	788.42(3)	792.3624	792.9772	796.2842	785.48(4)	789.41(8)
A, Å	-	-	-	-	-	0.147	0.198

T, K	**106**	**104**	**102**	**100**	**98**	**90**	**86**	**45**
Space group	*Pnma*(00γ)0s0	*Pnma*(00γ)0s0	*Pnma*(00γ)0s0	*Pnma*(00γ)0s0	*Pnma*(00γ)0s0	*Pnma*(00γ)0s0	*Pnma*(00γ)0s0	$P2_1/c$
a, Å	8.2827(2)	8.3121	8.2605(41)	8.2557(42)	8.2566(40)	8.2702(3)	8.2548(3)	8.1621(3)
b, Å	11.6735(2)	11.6659	11.6521(29)	11.6516(29)	11.6507(26)	11.6766(6)	11.6547(6)	8.2487(3)
c, Å	8.1543(2)	8.1688	8.1638(16)	8.1647(18)	8.1627(18)	8.1631(4)	8.1521(3)	11.6584(4)
α,deg	90.00	90.00	90.00	90.00	90.00	90.00	90.00	90.00
β,deg	90.00	90.00	90.00	90.00	90.00	90.00	90.00	91.891(3)
γ, deg	90.00	90.00	90.00	90.00	90.00	90.00	90.00	90.00
q	(0, 0, 0.143)	(0, 0, 0.1428)	(0, 0, 0.1247)	(0, 0, 0.1245)	(0, 0, 0.1247)	(0, 0, 0.1247)	(0, 0, 0.1247)	(0, 0, 0)
V, Å^3	788.42(3)	792.0997	792.1396	795.9282	796.5082	788.29(7)	784.29(6)	784.49(5)
A, Å	0.251	-	-	-	-	0.342	0.361	-

Being *A* (Å), the maxima refined amplitude for the cobalt atom.

As it can be derived from Table 7, four well differentiated phases have been determined in the single crystal neutron diffraction experiment. The first phase (phase **I**), correspond to the orthorhombic *Pnma* previously described. Between 128 and 104 K, the system become incommensurate (phase **II**) with a modulation vector **q** = (0, 0, ≈1/7). Between 102 and 86 K, the propagation vector is changed from **q** = (0, 0, ≈1/7) to **q** = (0, 0, ≈1/8). This transformation produce a change in the position of the satellite reflections as well as a notable modification of the intensities. Therefore, the increasing of the modulation wavelength from ca 57.2 to 65.6 Å, together with the change in the modulation functions, suggests that in this temperature range, the system can be described as a new incommensurate phase (phase **III**), even if the superspace group remains the same. Therefore, both incommensurate phases (**II** and **III**) can be described in the superspace group *Pnma*(00γ)0s0, with γ ≈1/7, for **II** and 1/8, for **III**. The dependence of the modulation vector with temperature can be consulted in Table 7. Below 86 K, the crystal structure becomes again commensurate, giving rise to a twined crystal. The description of this last structural phase transition can be consulted in the section 4.6 of this chapter.

In order to solve the crystal structure of these incommensurate phases (**II** and **III**) we use the SUPERFLIP program[85]. SUPERFLIP was used only to determine the cobalt atom position, while the position of the other atoms including the H-atoms where located using the difference Fourier map. The refinements using the superspace formalism were carried out with JANA2006[57], which for the moment is the only available program able to handle this formalism. The exploration of the 3D + 1 Fourier density maps clearly indicates a displacive character close to harmonicity for both framework and counterion. Therefore, in the next step, the displacement parameters of the different atoms were refined. After the convergence of the model, all atoms including the hydrogen atoms were refined with anisotropic displacement parameters (ADP's). After that, the first- and second-order harmonic waves of the ADP's were introduced into the model, taking into account the changes in the crystal structure modulation. The final R values are in the range from 8.28 to 9.85 % considering only the main reflections [R_{main}(obs)], and in the range of 7.61 to 14.50 % for the first satellites reflections [R_{sat}(obs)], see Table 8.

Table 8. R-factors of the incommensurate structure refinements at four different temperatures for compound **7.**

	122 K	**106 K**	**90 K**	**86 K**
$\mathbf{R_{all}}$, $\mathbf{wR_{all}}$	11.89, 10.67	10.12, 9.82	14.49, 13.26	14.68, 13.26
$\mathbf{R_{obs}}$, $\mathbf{wR_{obs}}$	8.80, 10.48	8.36, 9.65	10.3, 8.80	10.98, 12.97
$\mathbf{R_{obs}}$, $\mathbf{R_{all}}$, $\mathbf{wR_{all}}$ *(Main reflections)*	8.32, 8.35, 9.85	8.28, 8.33, 9.65	8.80, 9.09, 9.71	8.97, 9.43, 11.28
$\mathbf{R_{obs}}$, $\mathbf{R_{all}}$, $\mathbf{wR_{all}}$ *(First-order satellite reflect.)*	9.70, 12.31, 11.76	7.61, 8.47, 9.36	9.90, 10.94, 14.54	10.26, 11.41, 13.01
$\mathbf{R_{obs}}$, $\mathbf{R_{all}}$, $\mathbf{wR_{all}}$ *(Second-order satellite reflect.)*	15.53, 65.51, 23.29	12.72, 27.27, 13.68	12.97, 20.96, 13.43	16.50, 23.7, 16.23
$\mathbf{R_{obs}}$, $\mathbf{R_{all}}$, $\mathbf{wR_{all}}$ *(Third-order satellite reflect.)*	-	-	27.58, 68.62, 36.58	38.36, 76.96, 41.40
$\mathbf{GoF_{obs}}$, $\mathbf{GoF_{all}}$	6.60, 4.66	5.91, 4.79	7.08, 5.06	7.71, 5.59

Table 9. Comparative study of the **q** vector as function of temperature for compound **7**.

T (K)	Cell parameters (Å)	**q** (r.l.u.)	Modulation length (Å)
128	8.3100(2), 11.6755(4), 8.1669(3)	(0, 0, 0.1428)	57.19
126	8.3178(3), 11.6743(2), 8.1664(2)	(0, 0, 0.1429)	57.14
124	8.3350(2), 11.6899(4), 8.1726(3)	(0, 0, 0.143)	57.15
122	8.2674(2), 11.6600(4), 8.1483(2)	(0, 0, 0.143)	56.98
115	8.2792(4), 11.6797(6), 8.1636(5)	(0, 0, 0.143)	57.09
106	8.2827(2), 11.6735(2), 8.1543(2)	(0, 0, 0.143)	57.02
104	8.3121(2), 11.6659(2), 8.1688(2)	(0, 0, 0.1428)	57.20
102	8.2605(4), 11.6521(3), 8.1638(2)	(0, 0, 0.1247)	65.47
100	8.2557(4), 11.6516(3), 8.1647(2)	(0, 0, 0.1245)	65.57
98	8.2566(4), 11.6507(3), 8.1627(2)	(0, 0, 0.1247)	65.46
90	8.2702(3), 11.6766(6), 8.1631(4)	(0, 0, 0.1247)	65.46
86	8.2548(3), 11.6547(6), 8.1521(3)	(0, 0, 0.1247)	65.37

The ratio between main and satellites reflections is of 0.26, for the 122, 115 and 106 K data-sets and 0.11 and 0.18 for the 90 and 86 K data-sets. This variation is due to the occurrence of third-order reflections when the wave vector is **q** = (0, 0, ≈1/8). The number of refined parameters is of 333 for both the incommensurate structures [**q** = (0, 0, ≈1/7) or (0, 0, ≈1/8)]. In the incommensurate phase, the refined models consist of modulated structures with the modulation vector running along the *c**-axis (using the orthorhombic space group as base), with a modulation length [c/q_z] of 56.98(1), 57.09(2), 57.02(2), 65.46(2) and 65.37(2) Å, for 122, 115, 106, 90 and 86 K, respectively, see also Table 9. Both incommensurate phases (**II** and **III**) are "almost" commensurate. Therefore, instead of working in the superspace group *Pnma*(00γ)0*s*0, the data were transformed into a commensurate super-cell that can be treated using the three-dimensional $P2_12_12_1$ space group. It deserves to be noted that this approach involve the assumption that the structure is strictly commensurate (7-fold or 8-fold along the *c*-axis). However, the refined model using the three-dimensional space group is less stable and only after applying constrains the convergence is achieved. Therefore, even thinking that the phase **II** and **III** are almost commensurate, the quality of the data are significantly better if we use the superspace group formalism. Therefore, this formalism will be used to describe the incommensurate crystal structures hereafter.

In the superspace description, each atom follows a curve forming the so called "atomic domain". This curve, defined as a modulation function, can be described by a periodic function characterized by set of refined parameters. After each refinement, a four-dimensional density map can be calculated and different two-dimensional sections through a specific atom can be calculated. The modulation function must coincide with the atomic domain in the Fourier map. The shape of the modulation function reproduce the modulation of the atomic domain in the Fourier maps, therefore it must not be over or underestimated. The over-parametrization of our data can produce spurious effects, as noise or waiving effects in the modulation function. The refined modulation function exhibits a sinusoidal behaviour, as can be seen in the section of the four-dimensional Fourier map, the modulation function of the Co(II) atoms at different temperatures can be seen in Figure 27. The modulation function for the cobalt atom, represented as a green curve in Figure 27, is in a good agreement with the experimental (F_{obs}) Fourier maps. The shape of this modulation suggests a continuous character, with an increase of the displacive modulation with decreasing temperature.

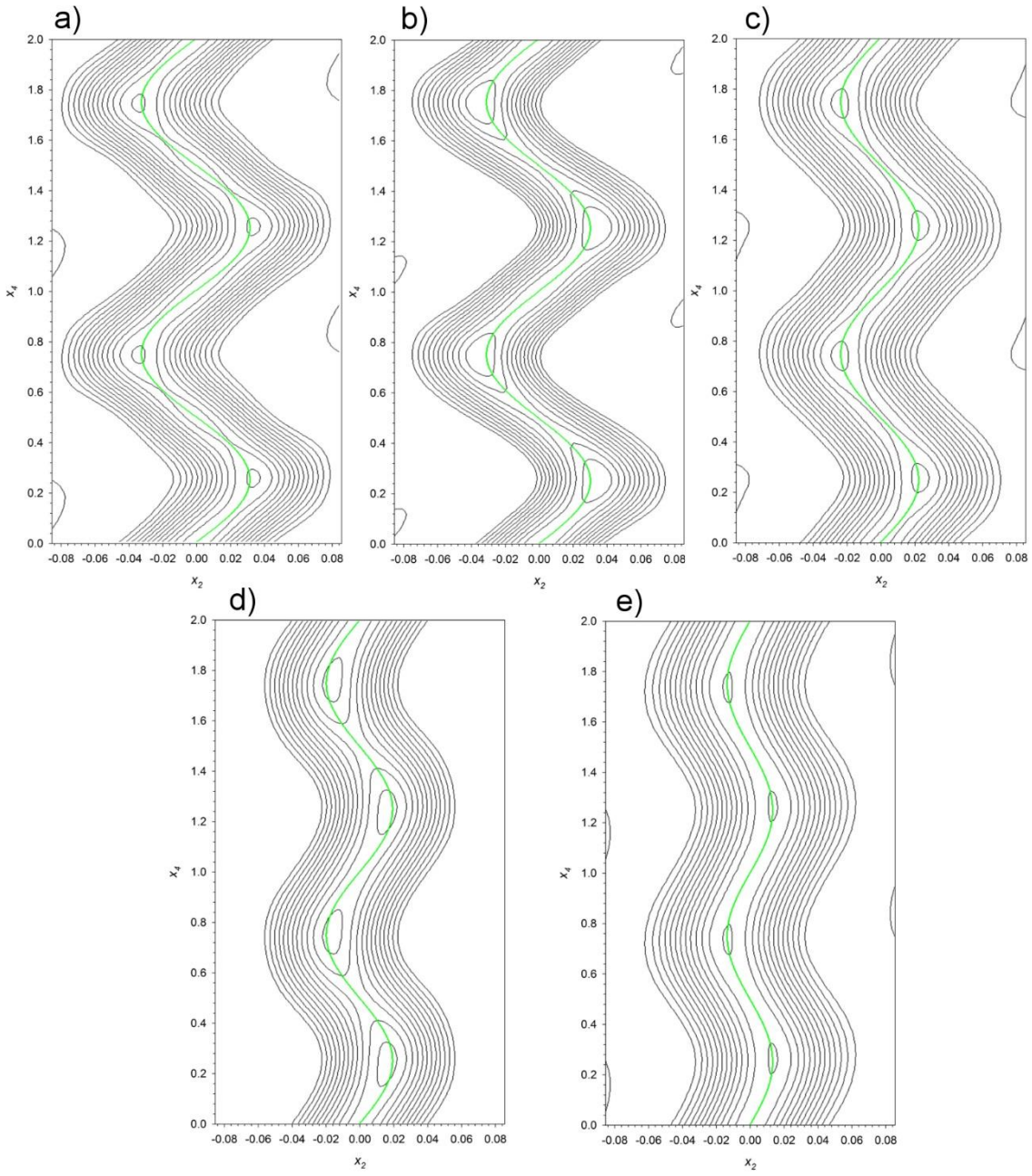

Figure 27: (a-e) Contour plot of the x_4-x_2 two-dimensional sections calculated fixing x_1 = 0.5 and x_3 = 0, corresponding to the atomic domain of the cobalt atom. The 86, 90, 106, 115 and 122 K atomic domains contour plot, together with the refined modulation function, represented as a solid green line, are represented from (*a)* to (*e)*, respectively.

The refined model shows that the amplitudes of the displacive modulation have the main components along the *b*-axis (corresponding to the component along *b* of the sine term of the Fourier coefficients ($A_{y,s,n}$), with n = 0, 1, 2 and 3 for main, first, second and third-order reflections[82,83,86], as seen before in Table 8. A resume of the refined amplitude displacement for cobalt and the C and N of the methylammonium counterion can be consulted in Table 10 and Table 11.

Table 10. Amplitude displacements of the Co1 atom (*sin* term)

	122 K	115 K	106 K	90 K	86 K
x	−0.0011(5)	−0.0051(14)	−0.0022(5)	−0.0027(7)	−0.0034(7)
y	0.0134(4)	0.0196(7)	0.0229(4)	0.0306(6)	0.0322(5)
z	−0.0004(5)	0.0023(15)	0.0004(5)	0.0016(8)	0.0002(6)

Table 11. Amplitude displacement from the sine and cosine terms of the N and C atoms from the dimethylammonium molecule

		q_m	122 K	115 K	106 K	90 K	86 K
N1 *cos*	*x*	1	0	0	0	0	0
	y	1	0.00339(13)	0.0053(3)	0.00602(13)	0.00763(16)	0.00751(17)
	z	1	0	0	0	0	0
N1 *cos*	*x*	2	−0.0009(4)	−0.0023(7)	−0.0001(3)	0.0000(3)	0.0004(3)
	y	2	0	0	0	0	0
	z	2	−0.0009(4)	−0.0046(7)	−0.0003(2)	−0.0008(3)	0.0002(2)
N1 *sin*	*x*	1	0	0	0	0	0
	y	1	0.01261(13)	0.0170(3)	0.02153(13)	0.02946(18)	0.03092(18)
	z	1	0	0	0	0	0
N1 *sin*	*x*	2	−0.0004(4)	−0.0010(7)	−0.0003(3)	−0.0007(3)	−0.0006(3)
	y	2	0	0	0	0	0
	z	2	0.0005(4)	0.0017(7)	0.0005(3)	−0.0006(3)	−0.0002(2)
C3 *cos*	*x*	1	0	0	0	0	0
	y	1	0.00067(19)	0.0006(4)	0.00151(18)	0.0019(2)	0.0015(3)
	z	1	0	0	0	0	0
C3 *cos*	*x*	2	−0.0004(6)	−0.0021(10)	0.0008(4)	0.0002(4)	0.0001(4)
	y	2	0	0	0	0	0
	z	2	−0.0005(6)	0.0005(11)	−0.0007(4)	−0.0009(4)	0.0000(4)
C3 *sin*	*x*	1	0	0	0	0	0
	y	1	0.01261(19)	0.0152(4)	0.02164(19)	0.0297(3)	0.0311(3)
	z	1	0	0	0	0	0
C3 *sin*	*x*	2	0.0000(6)	0.0018(11)	0.0008(4)	−0.0001(4)	0.0003(4)
	y	2	0	0	0	0	0
	z	2	0.0004(6)	−0.0004(11)	0.0003(4)	0.0002(4)	0.0009(4)

Based on the atomic positions present in the average structure, 8*d*, 4*c* or 4*b* Wyckoff positions, symmetry constrains are applied to the sine or cosine terms of the Fourier coefficients. This involve that a slight tilts or distortions of the CoO_6 octahedra are allowed by symmetry. However, these terms are notably smaller than those responsible of the modulation along the *b*-axis. Therefore, the final model present small differences between the modulation of the $[Co(COOH)_3]^-$ framework and the $[CH_3NH_3]^+$ counterions.

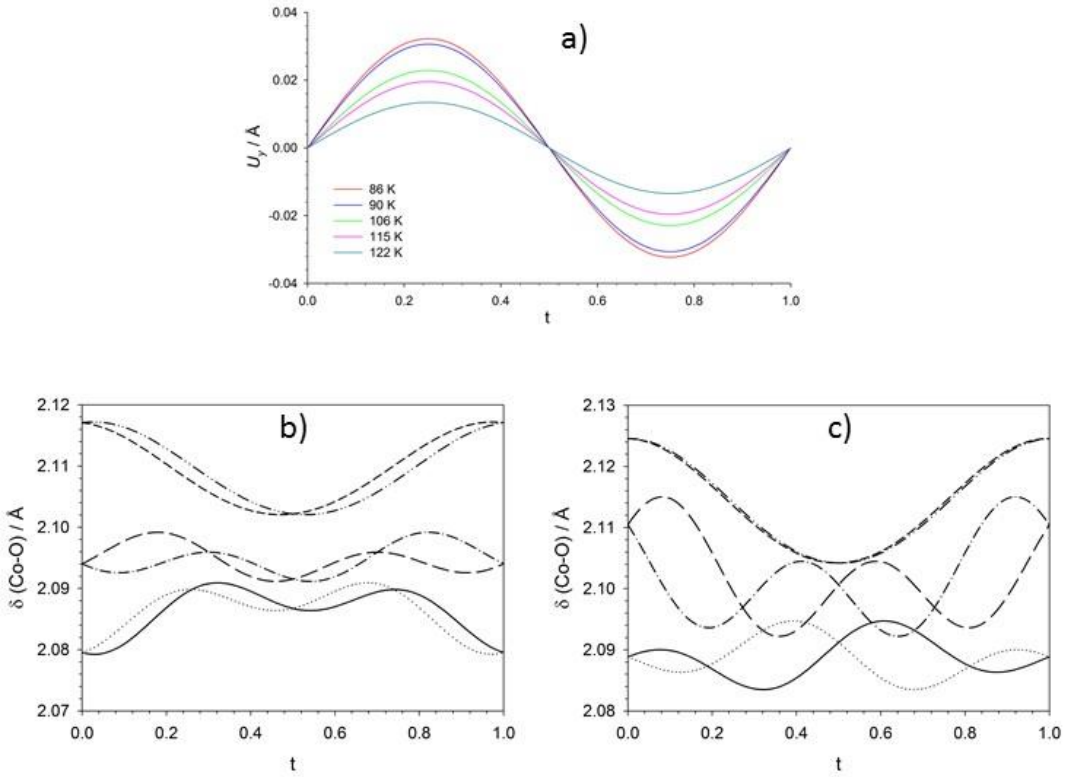

Figure 28*:* (a) Temperature evolution of the modulation function of the cobalt atom. (b-c) Selection of the bond lengths between the cobalt and the oxygen atoms at 106 and 90 K, corresponding to phase **II** and phase **III**, respectively.

The distortion of the CoO_6 octahedra [average Co─O bond distances Å ranged from *ca.* 2.09 to 2.11 Å] are much smaller than the displacement of this octahedra due to the modulated displacement [*ca.* 0.04 Å] see Figure 28 a.

A graphical representation of the bond distance modulation for each Co-─O bond distance at 106 and 90 K, phase **II** and **III** respectively, is shown in Figure 28 b-c. It deserves to be noted that the phase transition temperature is between this two temperatures. It is interesting to observe that at any *t* (=x_4-$\mathbf{qr}_\mu$) value, all the Co─O bond distances are in the range from 2.119 to 2.079 Å from phase **I** and 2.125 to 2.084 Å from phase **II**. This denote that the CoO_6 octahedra remains an almost ideal octahedral environment in the all range of *t*. However the modulation of the bond distances are completely different, this is related with the change in the modulation wavelength from (0, 0, ≈1/7) for phase **II** to (0, 0, ≈1/8) for phase **III**. The same effect is observed in the $[CH_3NH_3]^+$ counterions, the variation in the individual N─C, C─H and N─H bond length, as well as the variation in the C─N─H or H─C─N angles are much smaller than the average displacement values. A graphical description of the modulated structure for each phase, **II** (106 K) and **III** (86 K), is represented in Figure 29. The graphical representation has been carried out considering a super-cell (10-fold along the *c*-axis), in order to include at least a complete period.

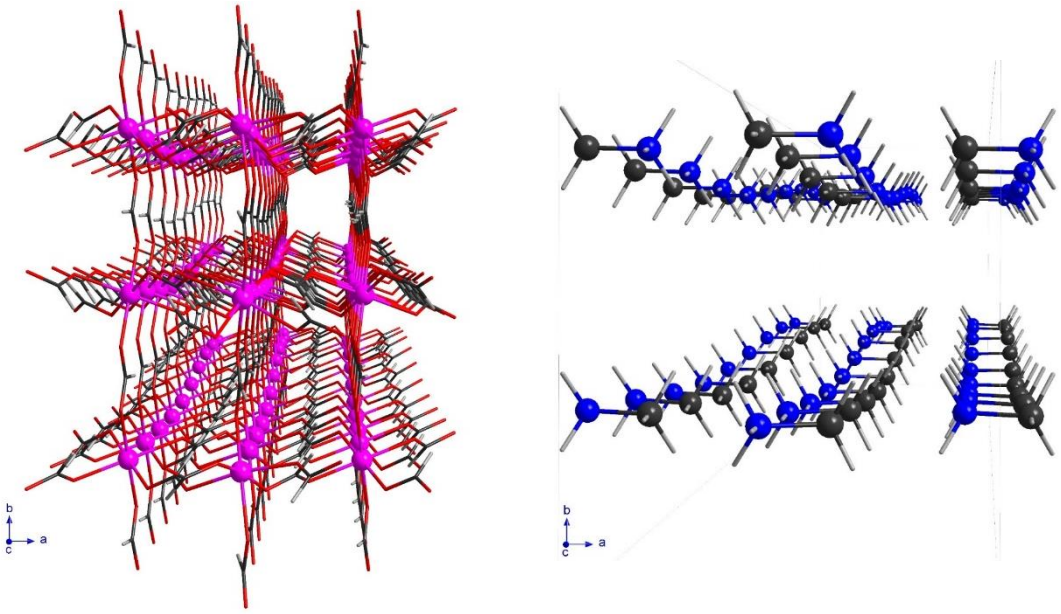

Figure 29: View along *c*-axis of the superstructure solved at 86 K. The cobalt , the oxygen, carbon and hydrogen atoms have been represented in pink, red, black and light-gray, respectively. The graphical representation has been carried out considering a supercell (10 times of the average structure along the *c*-axis), in order to include at least a complete period On the left, the view of the methylammonium modulation inside the cavity, reported in a separated figure for the sake of clarity.

The Table 12-16 shows the possible H-bonds defined along the incommensurate structure using a fraction of the *t* parameter ($t = x_4 - \mathbf{qr}_\mu$), for temperatures from 122 K to 86 K. Along *t*, not all D···A distances correspond to the expected range for an ideal H-bond. Those distances and angles farther which can be considered that do not correspond to a possible H-bond have been denoted in green colour in the next tables. As can be seen, the distances elongates as function of increasing temperature, which is compatible with the increase due to the thermal expansion. However, close to the 106 K, is observed a slight alteration of this tendency. It deserve to be noted that around this temperature the change of modulation wavelength occurs, from (0, 0, ≈1/7) to (0, 0, ≈1/8). For example at 106 K, N1─H1n and N1─H2n decrease from 2.315(11) and 1.845(9) Å (at 90 K), to 2.288(7) and 1.842(7) respectively.

Table 12. Selected distances (Å) and angles (º) involving the ammonium group of **7** at 122 K. Distances and angles farther from the ideal hydrogen bond geometry have been denoted in green colour.

		N1─H1n···O3#s4t0,0,-1			N1─H1n···O3#s6t0,0,-1			N1─H2n···O2#s2t1,0,0		
		H···A	D···A	D─H···A	H···A	D···A	D─H···A	H···A	D···A	D─H···A
122 K	t=0.000	2.080(11)	2.992(6)	153.1(6)	2.247(11)	3.073(5)	140.6(5)	1.835(9)	2.860(3)	173.4(9)
	t=0.100	2.075(11)	3.007(6)	150.1(7)	2.224(11)	3.077(6)	139.8(5)	1.837(9)	2.858(3)	174.0(9)
	t=0.200	2.106(11)	3.030(6)	144.9(7)	2.178(11)	3.064(6)	140.3(6)	1.835(9)	2.860(3)	174.9(9)
	t=0.300	2.166(11)	3.048(6)	142.2(6)	2.133(11)	3.032(6)	144.4(6)	1.829(9)	2.860(3)	174.4(9)
	t=0.400	2.225(11)	3.061(6)	141.5(5)	2.101(11)	3.001(6)	150.5(6)	1.821(9)	2.856(3)	172.0(9)
	t=0.500	2.247(11)	3.073(5)	140.6(5)	2.080(11)	2.992(6)	153.1(6)	1.815(9)	2.850(3)	170.7(9)
	t=0.600	2.224(11)	3.077(6)	139.8(5)	2.075(11)	3.007(6)	150.1(7)	1.814(9)	2.848(3)	172.1(9)
	t=0.700	2.178(11)	3.064(6)	140.3(6)	2.106(11)	3.030(6)	144.9(7)	1.818(9)	2.852(3)	174.4(9)
	t=0.800	2.133(11)	3.032(6)	144.4(6)	2.166(11)	3.048(6)	142.2(6)	1.824(9)	2.859(3)	175.0(8)
	t=0.900	2.101(11)	3.001(6)	150.5(6)	2.225(11)	3.061(6)	141.5(5)	1.830(9)	2.861(3)	174.2(9)

Table 13. Selected distances (Å) and angles (º) involving the ammonium group of **7** at **115 K**. Distances and angles farther from the ideal hydrogen bond geometry have been denoted in grey colour.

		N1─H1n···O3#s4t0,0,-1			N1─H1n···O3#s6t0,0,-1			N1─H2n···O2#s2t1,0,0		
		H···A	D···A	D─H···A	H···A	D···A	D─H···A	H···A	D···A	D─H···A
115 K	t=0.000	2.12(2)	2.954(12)	154.7(12)	2.32(2)	3.060(11)	140.7(10)	1.809(17)	2.877(6)	173.5(16)
	t=0.100	2.08(2)	3.005(12)	149.2(11)	2.26(2)	3.111(12)	139.7(10)	1.864(17)	2.870(6)	172.5(16)
	t=0.200	2.07(2)	3.066(12)	143.4(10)	2.16(2)	3.132(12)	140.8(10)	1.888(17)	2.868(6)	171.8(16)
	t=0.300	2.15(2)	3.073(12)	141.4(9)	2.11(2)	3.075(12)	146.4(10)	1.856(17)	2.871(6)	174.5(16)
	t=0.400	2.27(2)	3.049(12)	141.2(9)	2.12(2)	2.985(12)	153.3(11)	1.817(17)	2.868(6)	175.0(17)
	t=0.500	2.32(2)	3.060(11)	140.7(10)	2.12(2)	2.954(12)	154.7(12)	1.823(17)	2.854(6)	171.0(17)
	t=0.600	2.26(2)	3.111(12)	139.7(10)	2.08(2)	3.005(12)	149.2(11)	1.857(17)	2.840(6)	171.9(17)
	t=0.700	2.16(2)	3.132(12)	140.8(10)	2.07(2)	3.066(12)	143.4(10)	1.861(17)	2.843(6)	173.0(16)
	t=0.800	2.11(2)	3.075(12)	146.4(10)	2.15(2)	3.073(12)	141.4(9)	1.821(17)	2.860(6)	174.3(16)
	t=0.900	2.12(2)	2.985(12)	153.3(11)	2.27(2)	3.049(12)	141.2(9)	1.787(17)	2.876(6)	176.2(15)

Table 14. Selected distances (Å) and angles (º) involving the ammonium group of **7** at **106 K**. Distances and angles farther from the ideal hydrogen bonds geometry have been denoted in green colour.

		N1─H1n···O3#s4t0,0,-1			N1─H1n···O3#s6t0,0,-1			N1─H2n···O2#s2t1,0,0		
		H···A	D···A	D─H···A	H···A	D···A	D─H···A	H···A	D···A	D─H···A
106 K	t=0.000	2.009(8)	2.967(4)	153.9(5)	2.288(7)	3.111(4)	136.1(4)	1.842(7)	2.868(3)	174.2(7)
	t=0.100	2.022(8)	2.985(4)	152.6(5)	2.262(7)	3.110(4)	137.4(4)	1.839(7)	2.865(3)	174.2(7)
	t=0.200	2.097(8)	3.018(4)	148.2(5)	2.206(7)	3.074(4)	141.4(5)	1.831(7)	2.860(3)	173.9(7)
	t=0.300	2.195(8)	3.053(4)	142.5(5)	2.132(8)	3.021(4)	146.7(5)	1.826(7)	2.855(3)	172.9(7)
	t=0.400	2.267(7)	3.087(4)	138.0(4)	2.057(8)	2.978(4)	151.5(5)	1.824(7)	2.849(3)	171.7(7)
	t=0.500	2.288(7)	3.111(4)	136.1(4)	2.009(8)	2.967(4)	153.9(5)	1.821(7)	2.842(3)	171.6(7)
	t=0.600	2.262(7)	3.110(4)	137.4(4)	2.022(8)	2.985(4)	152.6(5)	1.816(7)	2.839(3)	172.7(7)
	t=0.700	2.206(7)	3.074(4)	141.4(5)	2.097(8)	3.018(4)	148.2(5)	1.815(7)	2.845(3)	174.0(7)
	t=0.800	2.132(8)	3.021(4)	146.7(5)	2.195(8)	3.053(4)	142.5(5)	1.823(7)	2.856(3)	174.4(7)
	t=0.900	2.057(8)	2.978(4)	151.5(5)	2.267(7)	3.087(4)	138.0(4)	1.835(7)	2.866(3)	174.4(7)

Table 15. Selected distances (Å) and angles (º) involving the ammonium group of **7** at **90 K**. Distances and angles farther from the ideal hydrogen bonds geometry have been denoted in green colour.

		N1─H1n···O3#s4t0,0,-1			N1─H1n···O3#s6t0,0,-1			N1─H2n···O2#s2t1,0,0		
		H···A	D···A	D─H···A	H···A	D···A	D─H···A	H···A	D···A	D─H···A
90 K	t=0.000	1.973(12)	2.944(6)	156.3(7)	2.315(11)	3.118(6)	134.0(5)	1.845(9)	2.879(3)	173.3(8)
	t=0.100	2.007(12)	2.963(6)	154.2(7)	2.303(11)	3.122(6)	136.0(5)	1.837(9)	2.877(3)	173.7(8)
	t=0.200	2.089(12)	3.015(6)	147.9(6)	2.228(11)	3.099(6)	140.9(6)	1.828(9)	2.868(3)	174.9(8)
	t=0.300	2.186(11)	3.066(6)	140.8(6)	2.113(12)	3.043(6)	147.2(6)	1.827(9)	2.858(3)	174.7(8)
	t=0.400	2.269(11)	3.099(6)	135.7(6)	2.012(12)	2.977(6)	153.3(7)	1.830(9)	2.849(3)	172.2(8)
	t=0.500	2.315(11)	3.118(6)	134.0(5)	1.973(12)	2.944(6)	156.3(7)	1.823(9)	2.841(3)	169.8(8)
	t=0.600	2.303(11)	3.122(6)	136.0(5)	2.007(12)	2.963(6)	154.2(7)	1.808(9)	2.837(3)	170.3(8)
	t=0.700	2.228(11)	3.099(6)	140.9(6)	2.089(12)	3.015(6)	147.9(6)	1.803(9)	2.841(3)	173.4(8)
	t=0.800	2.113(12)	3.043(6)	147.2(6)	2.186(11)	3.066(6)	140.8(6)	1.817(9)	2.855(3)	175.7(8)
	t=0.900	2.012(12)	2.977(6)	153.3(7)	2.269(11)	3.099(6)	135.7(6)	1.837(9)	2.870(3)	174.6(8)

Table 16. Selected distances (Å) and angles (º) involving the ammonium group of **7** at **86 K**. Distances and angles farther from the ideal hydrogen bonds geometry have been denoted in green colour.

		N1─H1n···O3#s4t0,0,-1			N1─H1n···O3#s6t0,0,-1			N1─H2n···O2#s2t1,0,0		
		H···A	D···A	D─H···A	H···A	D···A	D─H···A	H···A	D···A	D─H···A
86 K	t=0.000	1.987(8)	2.957(5)	155.2(6)	2.324(8)	3.129(5)	133.9(5)	1.848(9)	2.875(3)	172.3(8)
	t=0.100	2.010(8)	2.974(5)	154.1(6)	2.292(8)	3.123(5)	136.4(5)	1.842(9)	2.869(3)	173.5(8)
	t=0.200	2.099(8)	3.017(5)	148.3(6)	2.218(8)	3.085(5)	141.5(5)	1.834(9)	2.859(3)	174.7(8)
	t=0.300	2.212(8)	3.067(5)	140.8(5)	2.123(8)	3.028(5)	147.3(6)	1.826(9)	2.849(3)	174.3(8)
	t=0.400	2.297(8)	3.108(5)	135.4(5)	2.034(8)	2.977(5)	152.3(6)	1.817(9)	2.840(3)	173.0(8)
	t=0.500	2.324(8)	3.129(5)	133.9(5)	1.987(8)	2.957(5)	155.2(6)	1.809(9)	2.834(3)	171.7(8)
	t=0.600	2.292(8)	3.123(5)	136.4(5)	2.010(8)	2.974(5)	154.1(6)	1.807(9)	2.834(3)	171.5(8)
	t=0.700	2.218(8)	3.085(5)	141.5(5)	2.099(8)	3.017(5)	148.3(6)	1.815(9)	2.843(3)	172.8(8)
	t=0.800	2.123(8)	3.028(5)	147.3(6)	2.212(8)	3.067(5)	140.8(5)	1.831(9)	2.858(3)	174.4(8)
	t=0.900	2.034(8)	2.977(5)	152.3(6)	2.297(8)	3.108(5)	135.4(5)	1.844(9)	2.871(3)	173.3(8)

The slight variations in the H-bond network, which is agreement with the subtle changes in angles and distances, significantly contribute to the explanation to the occurrence of two incommensurate phase transitions. In the Tables above, we can see as the N1─H1n···O3 hydrogen bond is established with a hydrogen bond interaction with the O3s4 atom or with O3s6. Probably, in certain zones of the structure it is mostly established the contact of N1─H1n···O3s4, while on others the N1─H1n···O3s6. This can be seen as a flip-flop in the H-bond network, and therefore the competition between the inner strength with the weak interactions as are the H-bond, should be the final responsible of the change of the modulation vectors. Finally, we would like to correlate the sequences of phase transitions described before with the signals observed in the

relative permittivity (ε_r) as well as in the dielectric loss curve. The temperature dependence of the nuclear phase transitions from commensurate (**I**) to incommensurate (**II**), from incommensurate (**II**) to incommensurate (**III**) and from incommensurate (**III**) to commensurate (**IV**) phases, should be closely related with the different signal observed in the relative permittivity and in the dielectric loss curve. The relative permittivity measurements shows a behaviour, which is strongly dependent of the direction and therefore anisotropic. However, our data were collected in a pellet (powder sample), which preclude an accurate comparison of the reported results. Therefore, further measurements using a pre-oriented single crystal should be carried out. The temperature dependence of the ε_r when the electric field is applied shows a drop, which is compatible with the occurrence of a paraelectric-antiferroelectric transition due to the reorganization of the dipoles.

The slope in the relative permittivity curve below 130 K is related with the continuous variation in the amplitudes of the displacive modulation, which have been observed in the crystallographic studies. The occurrence of the incommensurate-incommensurate phase transition is not clearly observed in the relative permittivity curve. However, the dielectric loss curve shows a broad peak, which in part can be attributed to the dipoles movements due to the incommensurate to incommensurate phase transition. Nevertheless as will be show in the 4.6 section an important mixture of phases occurs in the powder samples.

Therefore, the broadening in the dielectric loss curve, in part can be related to this effect. Below 70 K, a second transition is observed which have been associated with the structural phase transition to the commensurate monoclinic space group (phase **IV**). The decrease of the dielectric losses with the temperature, from RT to 130 K, just above the incommensurate phase **II** can be related with a decreasing of movement of the $[CH_3NH_3]^+$ counterions, which become almost frozen in a single position at 135 K. The slight decrease of the unit cell volume during the cooling enhance the weak interactions between the guest molecule and the framework, mainly Van der Walls and H-bond interactions, decreasing in dipole friction and therefore the dielectric losses. After the commensurate-incommensurate phase transition (from **I** to **II**) the scenario is not the same. The dipole friction is increasing due to the crystal structure modulation and therefore the dielectric losses increase notably.

The dielectric loss does not decrease again down to the second incommensurate structure (**III**) is stabilized below 90 K, below this temperature the friction between dielectric dipoles is decreasing, due to the "stable" crystal structure, and therefore the dielectric loss follow the same tendency. A similar effect is observed in the 40-80 K temperature range, where the incommensurate (**III**) to monoclinic (**IV**) phase is observed. However, the variation in the dielectric losses is much weaker than in the first transition, suggesting a smooth transition. This is in agreement with the diffraction data, since the first order satellites became the main reflections in the monoclinic phase, confirming the continuous behaviour of this transition.

4.5.2 Phases **II** and **III** from 8 to 10

As already noticed at the beginning of this chapter, compound **7** has a special behaviour compared to the other members of the series. In fact, it is the only one showing an additional transition below the incommensurate phase (*ca.* 75 K) giving rise to a commensurate monoclinic structure, described in the section below 4.6. Resuming, the sequence of phase transitions while decreasing the temperature, for the cobalt compound **7,** is as follow: first commensurate to the incommensurate phase (**I** to **II**), the incommensurate phase can be indexed with a $\mathbf{q}_1$ modulation vector. Decreasing the temperature, the modulation vector changes giving rise to a second modulation vector $\mathbf{q}_2$ (phase **III**) then at a lower temperature, it changes again to a commensurate structure. We will describe in detail this sequence in the next section. The analysis of the other compounds **8** to **10** confirms the occurrence of the transition from the commensurate orthorhombic phase to incommensurate orthorhombic phases. Ideally, these incommensurate phases should be defined by unique propagation vectors.

Table 17. Comparative study of the **q** vector as function of temperature of compound **8**. In blue is marked the transition temperature.

T (K)	Cell parameters (Å)		**q** (r.l.u.)	Modulation length (Å)
250	8.48040(1), 11.82433(1), 8.13225(1)	main	(0, 0, 0)	0
135	8.40991(3), 11.81052 (4), 8.15723 (3)	main	(0, 0, 0)	0
	8.38653(2), 11.80651(1), 8.18546(6)	$\mathbf{q}_1$	(0, 0, 0.14501(1))	56.44
	8.38480(7), 11.79979(9), 8.17121(8)	$\mathbf{q}_2$	(0, 0, 0.16508(2))	49.49
120	8.40272(3), 11.80972(4), 8.15912(4)	main	(0, 0, 0)	0
	8.38624(2), 11.80729(1), 8.17957(5)	$\mathbf{q}_1$	(0, 0, 0.14500 (1))	56.41
	8.38399(5), 11.80340(8), 8.16944(6)	$\mathbf{q}_2$	(0, 0, 0.16029(2))	50.96
105	8.39863(3), 11.80773(4), 8.16027(3)	main	(0, 0, 0)	0
	8.38553(1), 11.80581(6), 8.17202(4)	$\mathbf{q}_1$	(0, 0, 0.15750(1))	51.88
	8.38553(1), 11.80581(6), 8.17202(4)	$\mathbf{q}_2$	(0, 0, 0.14273(2))	57.25
	8.38553(1), 11.80581(6), 8.17192(4)	$\mathbf{q}_3$	(0, 0, 0.17012(2))	48.04
75	8.39432(4), 11.80498(4), 8.16039(4)	main	(0, 0, 0)	0
	8.37225(1), 11.80410(7), 8.17401(5)	$\mathbf{q}_1$	(0, 0, 0.14275(2))	57.26
	8.38657(6), 11.80896(1), 8.15854(9)	$\mathbf{q}_3$	(0, 0, 0.16899(2))	48.27
45	8.38131(3), 11.80603(4), 8.16340(3)	main	(0, 0, 0)	0
	8.37831(1), 11.80651(7), 8.16417(8)	$\mathbf{q}_1$	(0, 0, 0.14257 (2))	57.26
	8.37912(1), 11.80368(1), 8.16500(8)	$\mathbf{q}_2$	(0, 0, 0.16820(2))	48.54
30	8.37760(4), 11.80465(4), 8.16422(3)	main	(0, 0, 0)	0
	8.37602(1), 11.80583(7), 8.16345(8)	$\mathbf{q}_1$	(0, 0, 0.14316(2))	57.02
	8.37807(1), 11.80382(1), 8.16552(1)	$\mathbf{q}_2$	(0, 0, 0.16799(3))	48.60

However, as it has been shown for the cobalt-based powder data, the phase transitions behaviour is rather different from the observations in the single crystal sample. Unfortunately, only for compounds **7** and **9** we have succeeded to grow, big enough, single crystals for neutron experiments. Moreover, the decision of characterizing them by synchrotron powder diffraction was due to the fact that single crystal neutron experiments imply very long acquisition times and the neutron beam time is very limited. Powder

diffraction measurements of **8** to **10** in the low temperature range, were performed in the BL04-MSPD high-resolution powder diffraction beamline at ALBA synchrotron. The transition from the commensurate to incommensurate phase occurs at 135 K, 45 K and 145 K for compounds **8**, **9** and **10** respectively. The Rietveld method was used considering only the "average structure", defined as the *Pnma* phase. While the refinement of the integrated intensities of the satellite peaks has been performed by adding a second phase in Le Bail fit mode with the same cell parameters as the *Pnma* space group, and with a **q** vector (labelled $\mathbf{q}_1$, to $\mathbf{q}_n$ referring to the number of phase), see Table 17, Table 18, Table 19, for **8**, **9** and **10**, respectively.

Table 18. Comparative study of the **q** vector as function of temperature of compound **9**. In blue is marked the transition temperature.

T (K)	Cell parameters (Å)		**q** (r.l.u.)	Modulation length (Å)
75	8.20989(1), 11.55038(1), 8.09960(1)	main	(0, 0, 0)	0
60	8.20075(1), 11.54798(2), 8.10325(1)	main	(0, 0, 0)	0
45	8.19328(2), 11.54645(3), 8.10505(2)	main	(0, 0, 0)	0
	8.19328(2), 11.54645(3), 8.10505(2)	$\mathbf{q}_1$	(0, 0, 0.15372(1))	52.73
30	8.18864(2), 11.54579(3), 8.10533(2)	main	(0, 0, 0)	0
	8.18864(2), 11.54579(3), 8.10533(2)	$\mathbf{q}_1$	(0, 0, 0.15228(4))	53.23
15	8.18517(2), 11.54562(3), 8.10429(2)	main	(0, 0, 0)	0
	8.18464(2), 11.54571(2), 8.10501(3)	$\mathbf{q}_1$	(0, 0, 0.15204(4))	53.31

Table 19. Comparative study of the **q** vector as function of temperature of compound **10**. In blue is marked the transition temperature.

T (K)	Cell parameters (Å)		**q** (r.l.u.)	Modulation length (Å)
240	8.62272(1), 11.93709(1), 8.19917(1)	main	(0, 0, 0)	0
165	8.56416(2), 11.92096(1), 8.23396(1)	main	(0, 0, 0)	0
145	8.54811(3), 11.91816(2),8.24209(2)	main	(0, 0, 0)	0
	8.54811(3), 11.91816(2),8.24209(2)	$\mathbf{q}_1$	(0, 0, 0.14267(9))	57.77
125	8.53452(4), 11.91413(3), 8.24845(3)	main	(0, 0, 0)	0
	8.55798 (6), 11.90384(7), 8.23972(5)	$\mathbf{q}_1$	(0, 0, 0.12422(2))	66.33
	8.55798(6), 11.90384(7), 8.23972(3)	$\mathbf{q}_2$	(0, 0, 0.14307(2))	57.59
	8.53452(4), 11.91419(3), 8.24832(3)	$\mathbf{q}_3$	(0, 0, 0.16365(1))	50.40
85	8.51435(6), 11.90707(3), 8.25748(4)	main	(0, 0, 0)	0
	8.51435(6), 11.90707(3), 8.25748(4)	$\mathbf{q}_1$	(0, 0, 0.11852(9))	69.67
	8.51435(6), 11.90707(3), 8.25748(4)	$\mathbf{q}_2$	(0, 0, 0.13816(2))	59.76
	8.51435(6), 11.90707(3), 8.25748(4)	$\mathbf{q}_3$	(0, 0, 0.16406(1))	50.33
65	8.50611(6), 11.90469(3), 8.26123(4)	main	(0, 0, 0)	0
	8.50611(6), 11.90469(3), 8.26123(4)	$\mathbf{q}_1$	(0, 0, 0.14390(14))	57.41
	8.50611(6), 11.90469(3), 8.26123(4)	$\mathbf{q}_2$	(0, 0, 0.11637(15))	70.99
	8.50611(6), 11.90469(3), 8.26123(4)	$\mathbf{q}_3$	(0, 0, 0.16179(9))	51.06
45	8.50025(6), 11.90324(3), 8.26457(4)	main	(0, 0, 0)	0
	8.50025(6), 11.90324(3), 8.26457(4)	$\mathbf{q}_1$	(0, 0, 0.11872(1))	69.61
	8.50025(6), 11.90324(3), 8.26457(4)	$\mathbf{q}_2$	(0, 0, 0.14671(3))	56.33
	8.50025(6), 11.90324(3), 8.26457(4)	$\mathbf{q}_3$	(0, 0, 0.16459(8))	50.21
25	8.49523(6), 11.90244(4), 8.26661(5)	main	(0, 0, 0)	0
	8.50195(3), 11.90373(2), 8.26549(3)	$\mathbf{q}_1$	(0, 0, 0.16416(7))	50.35
	8.50195(3), 11.90373(2), 8.26549(3)	$\mathbf{q}_2$	(0, 0, 0.11662(3))	70.87
	8.50016(6), 11.90331(4), 8.26449(5)	$\mathbf{q}_3$	(0, 0, 0.14633(3))	56.47

At lower temperature, for compound **8** and **10**, (*ca.* 135 K and 125 K respectively) the profile matching of the satellites can only be achieved with a mixture of **q** vectors ($\mathbf{q}_1$ to $\mathbf{q}_3$), coexisting simultaneously, except for **9** that can be refined with a unique **q** vector (see Table 17, Table 18, and Table 19).

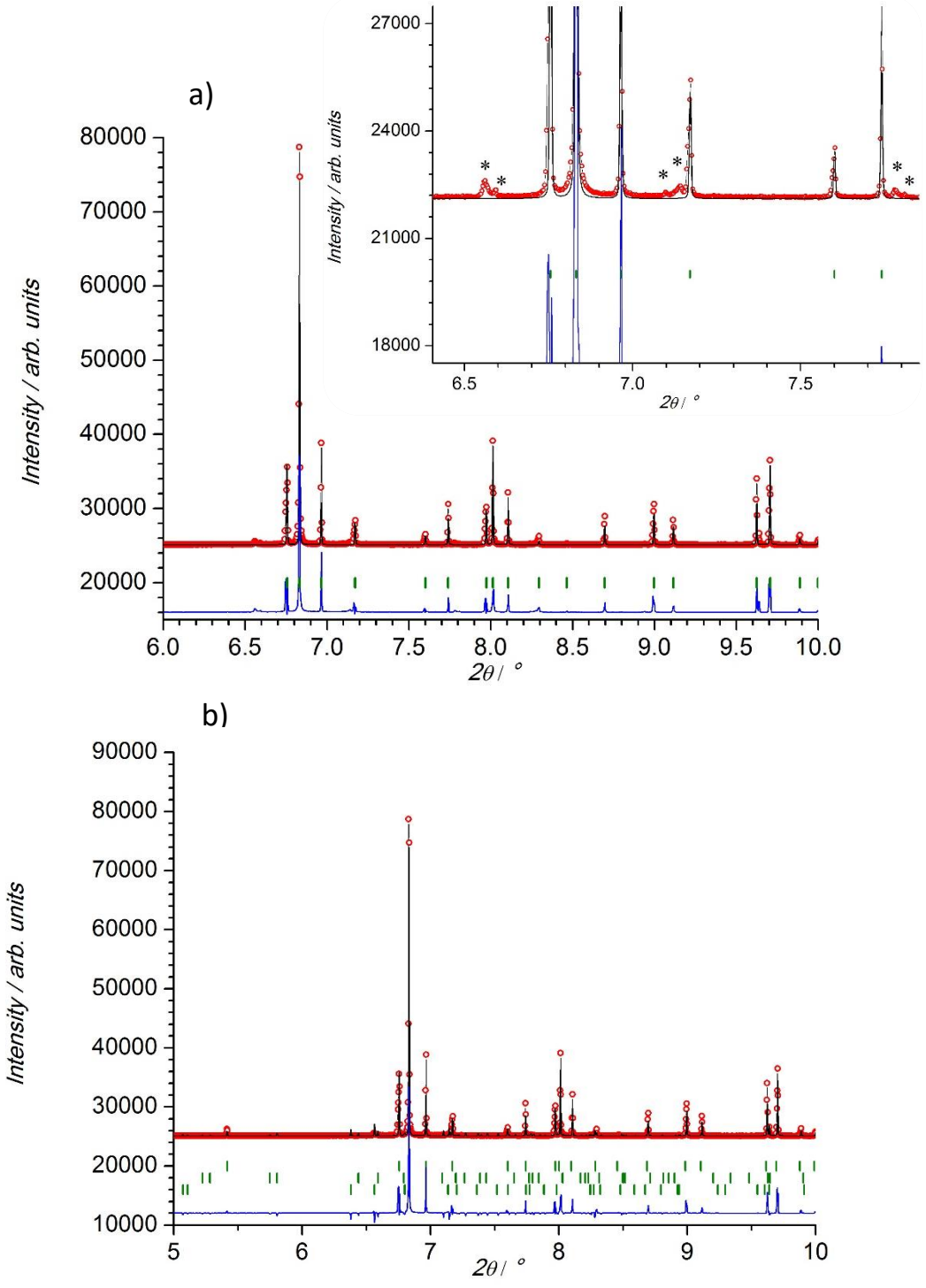

Figure 30. a) Experimental (open red circles) synchrotron X-ray powder diffraction data and calculated Rietveld refinement (black solid line) pattern for compound **8** at 135 K (data collected with λ= 0.4948 Å). The vertical green marks represent the position of the Bragg reflections. The inset shows a zoom of the low-angle region. It should be noted that the satellite reflections have not been taken into account in the refinement and are marked with * symbol. Figure b) shows the (open red circles) synchrotron X-ray powder diffraction data and calculated Rietveld refinement (black solid line) pattern with the indexed satellites after introducing $\mathbf{q}_1$, $\mathbf{q}_2$, and $\mathbf{q}_3$. The upper row of vertical green marks represent the position of the Bragg reflections for the orthorhombic phase. While the lower rows correspond to the position of satellites corresponding to the second and third profile matching phases, respectively.

The behaviour of these phases depends of the temperature cooling/warming protocol however in all cases we observe a displacement effect of the propagation vectors related to the decreasing of the temperature. In Figure 30 it is shown the synchrotron X-ray powder diffraction pattern of compound **8** at 135 K corresponding to the orthorhombic phase (Figure 30 a) refined by the Rietveld method when the transition to the incommensurate phase is already occurred (for compound **8** it is below 135 K, see Table 17). In order to reproduce the experimental data, three different propagation vectors are needed, and even in this case the broadening of the satellites reflections preclude a good fit of these reflections (see Figure 30 b).

As can be seen in Table 18, the nickel-based compound **9** is the only powder sample which show a single modulation vector in the full range of temperature below commensurate to incommensurate phase transition. The quality of the diffraction pattern permit not only the modulation vector determination, but also a Rietveld refinement of the incommensurate structure. It should be noted that compound **8**, in the incommensurate phase transition, shows always a mixture of modulation vectors which preclude to carry out a good Rietveld refinement. This is also the case for compound **10**, where only in the incommensurate phase transition at 145 K, there is a single propagation vector. Therefore, only at this temperature the Rietveld refinement using the superspace formalism is

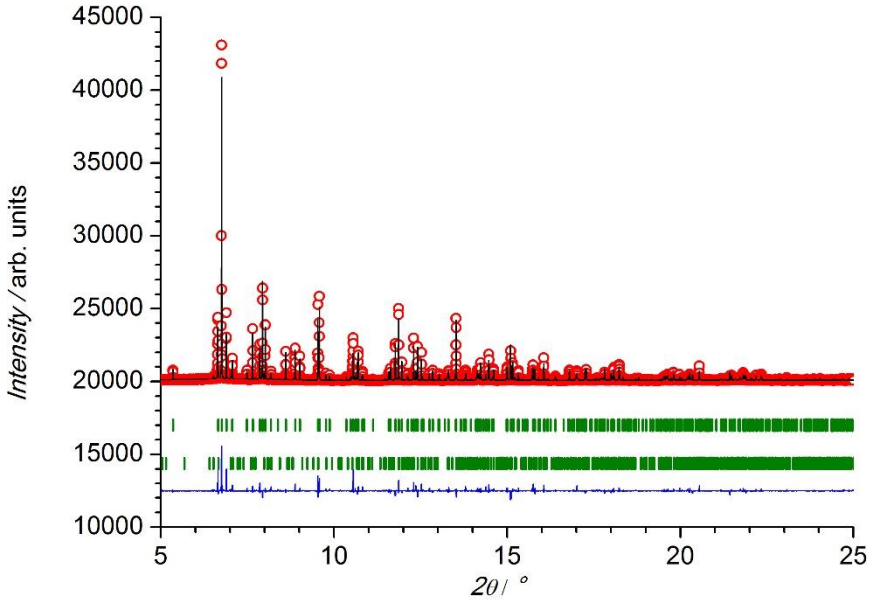

Figure 31: Experimental (open red circles) synchrotron X-ray powder diffraction data and calculated Rietveld refinement (black solid line) pattern for compound **10** at 145K (data collected with λ= 0.4948 Å). The difference between observed and calculated patterns has been represented as a blue line. The vertical green marks represent the position of the Bragg reflections. Refined cell parameters a = 8.56950(1), b = 11.45731(2) and c = 8.11542(1) Å, $\alpha = \beta = \gamma$ = 90.0°. The data refinement for phase1 gives, R_B = 10.9 % and R_F = 6.85 %, as agreement factors, and for the phase2 corresponding to a profile matching gives, R_B = 0.7 % and R_F = 0.6 %.

reasonable. As the modulation vector at 145 K is almost 1/7 ($\gamma \approx 0.14267(9)$), we have used as starting point the model derived from the cobalt-base compound in phase **II**.

After refining the modulation vector, all the satellite reflections are well indexed, however, the satellites reflections are not only very weak in comparison with the main reflections, but they are also notably broadened. This suggests a short correlation length of the incommensurate modulation. In the final refinement all atoms except hydrogens (not included in the model) were refined with isotropic displacement parameters. Only first-order harmonic waves were introduced into the model in order to improve the refinement. The refinement converges only if the atomic modulation function is not refined. A detail of the data fit, including all these parameters is shown in Figure 31. The crystal structure of **9**, was solved by synchrotron X-ray powder diffraction using the same superspace group as in the case of the cobalt-based compound (**II** and **III**). Therefore, the *Pnma*(00γ)0s0 superspace group is also confirmed for the nickel-based compound. In this compound only a single modulation vector is observed in the full range of the incommensurate phase, with a value of $\gamma \approx 0.152$. Unlike the cobalt-based compound this modulation vector correspond to a modulation wavelength of *ca.* 6.5·*c*, which is far from the ≈7·*c* or ≈ 8·*c* observed in the **II** and **III** phases of the cobalt compound. It deserves to be noted, that this modulation vector, remains constant down to 15 K (see Figure 32), which was the lowest temperature accessible using X-ray

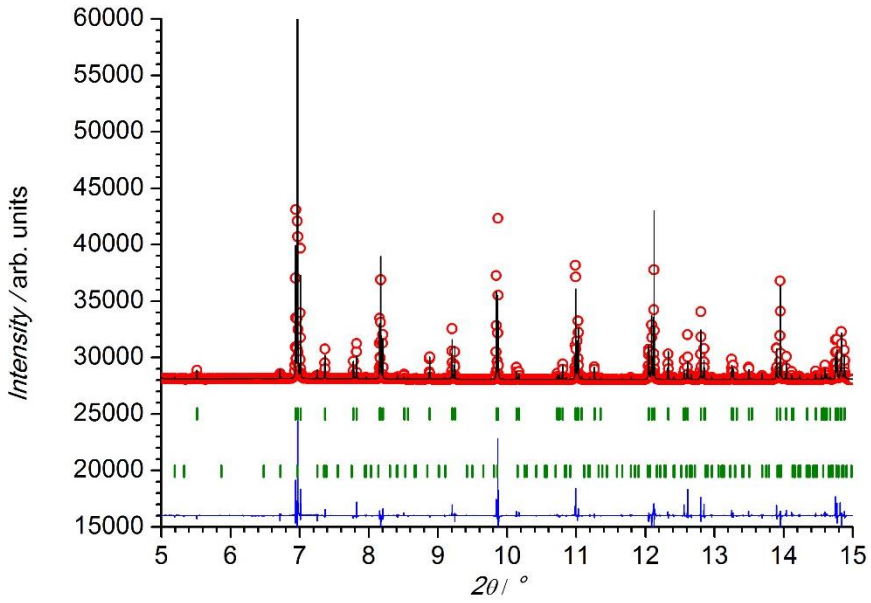

Figure 32: Experimental (open red circles) synchrotron X-ray powder diffraction data and calculated Rietveld refinement (black solid line) pattern for compound **9** at 15 K (data collected with λ= 0.4948 Å). The difference between observed and calculated patterns has been represented as a blue line. The vertical green marks represent the position of the Bragg reflections. Refined cell parameters a = 8.56950(1), b = 11.45731(2) and c = 8.11542(1) Å, $\alpha = \beta = \gamma$ = 90.0°. The data refinement for phase1 gives, R_B = 9.34 % and R_F = 6.55 %, as agreement factors, and for the phase2 corresponding to a profile matching gives, R_B = 0.8 % and R_F = 0.7 %.

diffraction, and therefore below T_N. The nickel-based compound could be synthesized as large single crystals, so we have carried out also a single crystal neutron diffraction acquisition at 45 K to be in the incommensurate phase and well above T_N. Here below, we report the main results obtained by monochromatic neutron single crystal diffraction. As in the cobalt-based compound, D19 was operating with a wavelength of 1.456 Å, which give us a good compromise between instrumental resolution and peak separation. It deserve to be noted that the detector-sample distance is fixed, and therefore only the right selection of the wavelength can help us to separate the reflections. As in the case of

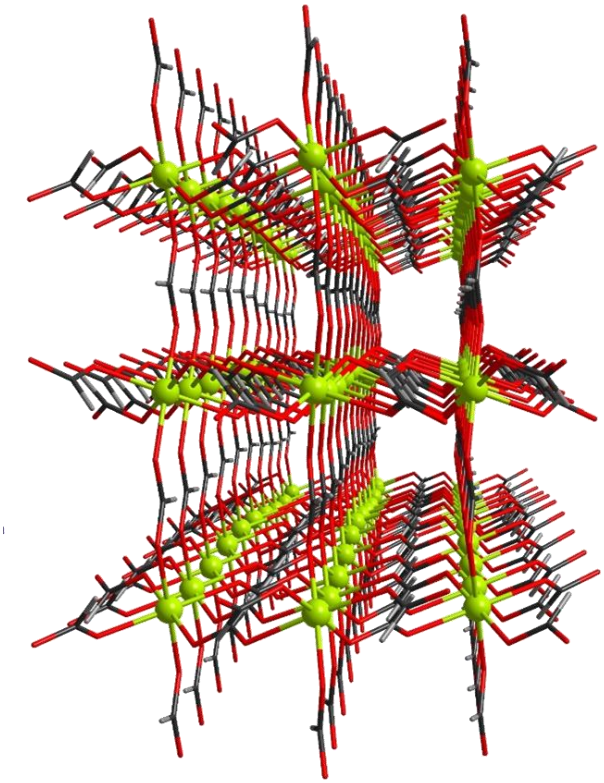

Figure 33: View along the *c*-axis of the modulated structure of **9** at 45 K on D19. The nickel atoms have been represented in green. The oxygen, carbon and nitrogen atoms have been represented in red, black and blue respectively. The graphical representation has been carried out considering a super-cell (10 times the average structure along the *c*-axis), in order to include at least a complete period, the methylammonium cation has been omitted for sake of clarity.

compound **7**, we used the superspace formalism, moreover with a modulation length of 6.5·*c**, it is not anymore reasonable use a 3D space group to approach the incommensurate structure by a commensurate approximant. Therefore, from the single-crystal data at 45 K, we have obtained a modulation vector **q** = (0, 0, 0.151981), which is consistent with the one obtained from powder diffraction. The space group determination is also compatible with the superspace group *Pnma*(00γ)0s0 as was derived from the powder data, and in agreement with the superspace group obtained in the cobalt-based compound (see Figure 33).

Table 20. R-factors of refinement at 45 K for the single crystal sample of **9** at D19 diffractometer

	45 K
$\mathbf{R_{all}}$, $\mathbf{\mathit{w}R_{all}}$	16.39, 13.31
$\mathbf{R_{obs}}$, $\mathbf{\mathit{w}R_{obs}}$	11.39, 12.82
$\mathbf{R_{obs}}$, $\mathbf{R_{all}}$, $\mathbf{\mathit{w}R_{all}}$ *(main reflections)*	8.90, 9.66, 10.85
$\mathbf{R_{obs}}$, $\mathbf{R_{all}}$, $\mathbf{\mathit{w}R_{all}}$ *(first-order satellite reflect.)*	15.18, 22.05, 16.34
$\mathbf{R_{obs}}$, $\mathbf{R_{all}}$, $\mathbf{\mathit{w}R_{all}}$ *(second-order satellite reflect.)*	20.07, 52.13, 24.11
$\mathbf{GoF_{obs}}$, $\mathbf{GoF_{all}}$	7.28, 4.94

SUPERFLIP program[85] was used to determine the nickel atom position, the position of the other atoms including the H-atoms where located using the difference Fourier map. In the final refinement, all atoms including the hydrogen atoms were refined with anisotropic displacement parameters (ADP's), which was not possible in the previous X-rays powder data refinement. At the final stage of refinement, the first- and second-order harmonic waves of the ADP's were introduced into the model, which take into account the changes in the crystal structure modulation. A view of the final 3D+1 model, where ten average unit cells have been drawn in order to emphasize the crystal modulation, is depicted in Figure 33. The refined amplitude displacements for some selected atoms are shown in Table 21. The final *R* values are in the range from 8.9 to 11%, considering only the main reflections [R_{main}(obs)], and in the range of 15 to 22 % for the first satellites reflections [R_{sat}(obs)], see Table 20. As in the case of the cobalt-based compound, the distortion of the NiO_6 octahedra is not significant, the variation of the Ni─O bond distances in the *t* range ($0 < t < 1$), as defined before, is ranged from 2.043(4) to 2.059(4) for Ni(1)─O(1), from 2.063(4) to 2.082(4) for Ni(1)─O(2) and from 2.049(4)to 2.061(4) for Ni(1)─O(3), which denote an almost ideal NiO_6 octahedra.

Table 21. Amplitude displacements of **9**, from the sine and cosine terms of the Ni1 atom (only *sin* term, because the cos is null), and of the N and C atoms from the dimethylammonium molecule.

		q	45 K
Ni1 sin	*x*	1	0.0027(3)
	y	1	−0.0213(2)
	z	1	0.0005(3)
N1 cos	*x*	1	0
	y	1	0.0053(3)
	z	1	0
N1 sin	*x*	1	0
	y	1	−0.0195(3)
	z	1	0
C3 cos	*x*	1	0.0006(4)
	y	1	0.0012(2)
	z	1	0.0013(3)
C3 sin	*x*	1	0.0020(3)
	y	1	−0.0202(2)
	z	1	0.0007(3)

In Table 22, the possible H-bonds of the incommensurate structure **9** are reported as a function of *t* parameter at 45 K. The refined distances are in agreement with those obtained previously for the compound **7**. As in the cobalt case, there is a flip-flop in the H-bond, the distances elongates as function of *t*, from $t = 0$ to $t = 0.7$ the N1─H1n···O3#s2t0,1,0 distance increase from 2.145(5) to 2.249(8) Å, after the $t = 0.7$ the distance invert its tendency decreasing at $t = 1$ down to 2.052(8) Å. The boxes

Table 22. Selected distances (Å) and angles (º) involving the ammonium group of **9** at 45 K. Distances and angles farther from the ideal hydrogen bond geometry have been denoted in green colour.

		N1─H1n···O3#s2t0,1,0			N1─H2n···O3#s3t1,0,0		
		H···A	D···A	D─H···A	H···A	D···A	D─H···A
45 K	t=0.000	2.145(5)	3.050(3)	144.3(2)	1.840(8)	2.859(5)	175.0(6)
	t=0.100	2.032(8)	2.990(4)	151.8(7)	1.833(8)	2.853(5)	174.6(6)
	t=0.200	2.052(8)	3.003(4)	150.7(7)	1.822(8)	2.844(5)	174.4(6)
	t=0.300	2.108(8)	3.034(4)	147.1(7)	1.812(8)	2.836(5)	174.0(6)
	t=0.400	2.183(8)	3.073(4)	142.4(7)	1.807(8)	2.833(5)	173.3(6)
	t=0.500	2.249(8)	3.106(4)	138.6(7)	1.808(8)	2.835(5)	172.7(6)
	t=0.600	2.275(8)	3.117(4)	136.9(7)	1.815(8)	2.841(5)	172.9(6)
	t=0.700	2.249(8)	3.102(4)	138.0(7)	1.825(8)	2.850(4)	173.8(6)
	t=0.800	2.184(8)	3.067(4)	141.5(7)	1.835(8)	2.858(4)	175.0(6)
	t=0.900	2.109(8)	3.028(4)	146.2(7)	1.840(8)	2.861(5)	175.4(6)
	t=1.000	2.052(8)	3.000(4)	150.2(7)	1.840(8)	2.859(5)	175.0(6)

highlighted in green in Table 22, correspond with those distances or angles which are far from the ideal H-bond contact.

Based on the previous described results we can conclude that the nickel-based compound is the only one showing completely consistent behaviour between powder and single crystal data. Therefore, suggesting that, unlike the other members of this series, the competition between weak interactions do not play an important role in this compound.

While for the iron- (**8**) and manganese-based compound (**10**), the results suggest a behaviour similar to those of the cobalt powder-sample. For iron-compound, the results show the occurrence of a multi-domain behaviour. In our opinion, this can be understood in the sense that a part of the sample has a $\mathbf{q}_1$ modulation vector, part has a $\mathbf{q}_2$, and part has a $\mathbf{q}_3$. This scenario is more plausible than a complex incommensurate structure with three modulation vectors. This situation is the same for the manganese-based compound, below 145 K. This assumption is supported by the single crystal data on the cobalt-compound, which show two propagation vectors but never a mixture of both. However, in order to shed light into this problem, we plan to made single crystal measurements as function of the temperature. As growing large single crystals to carry out neutron diffraction data is a difficult task, we will try to explore the sequence of phase transition using low temperature X-ray diffraction.

4.6 Monoclinic phase (**IV**)

The neutron and X-ray single crystal data carried out at 45 K, show the occurrence of a further phase transition. This phase transition is accompanied of a twinning of the sample so that reflections from two different twin domains appear. Therefore, in order to resolve the crystal structure, both component of the twin should be considered. Each twin contributes *ca.* 50% to the total intensity and they are related by a rotation of 180° around the *a**-axis. It should be noted that the same twin-law observed was observed in the single crystal X-ray and neutron experiments. A reconstruction of the reciprocal space plane (*h* 1 *l*) above and below the phase transition for the single-crystal X-ray diffraction is shown in Figure 34, where the two twin components are clearly observed.

Therefore, based on the single crystal analysis, compound **7** present a phase transition from the incommensurate phase *Pnma*(00γ)0s0 (**7** phase **III**) to a monoclinic phase **IV**. The analysis of the possible space groups of this new phase suggests that the crystal

structure can be solved in the $P2_1/n$ monoclinic space group. Structurally, compound **7 (**phase **IV**) present a crystal structure description very similar to those previously described. However, in order to facilitate the comparison, along this section, we are going to compare the low temperature phase (**IV**) mainly with the commensurate *Pnma* phase (**I**). The crystal structure was solved in the $P2_1/c$ standard group with unit cell dimensions of a = 8.175(5), b = 8.269 (5), c = 14.465(5) Å, β = 126.270(5)º (basis change from *Pnma* space group defined by –**c**, **-a**, **b**+**c**; 0, 1/2, 1/2).

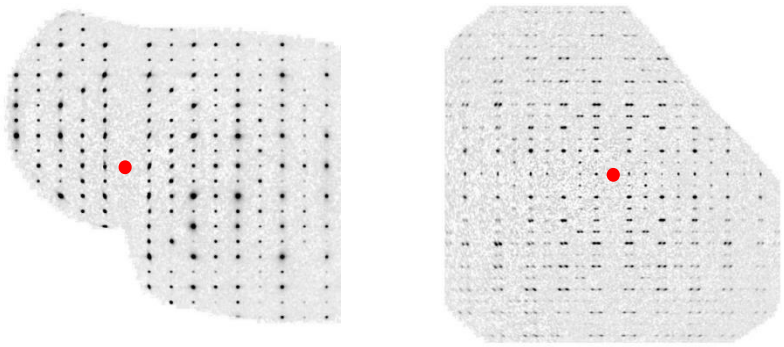

Figure 34: View of the reconstruction of the reciprocal space plane (*h 1 l*) at RT (top) and at 45 K (bottom), obtained from the synchrotron X-ray single crystal data . The splitting of the reflection in the low temperature plane, is due to the occurrence of two domains. The twin domains are related by a rotation of ca. 180 deg. with respect [1 0 0] direction. In both figures *h* is increasing from the red point to right and *l* from the red point to the top. The red point correspond to the (0 1 0) reflection position.

However, along this section, for the sake of clarity in the comparison of the crystallographic structures previously described, we will keep the $P2_1/n$ non-standard space group with β = 91.89º. Which is the closest description to the previous described orthorhombic phases. The phase transition between *Pnma* and $P2_1/n$ non-standard group implies an overall permutation of the three crystallographic axis in the sense $a^{RT}=-b^{LT}$, $b^{RT}=-c^{LT}$ and $c^{RT}=a^{LT}$, together with a change on the β angle of 1.89º, keeping almost invariant its cell volume. Therefore, there is a group-subgroup relation between the orthorhombic *Pnma* and the monoclinic $P2_1/n$ space groups, even thinking that between these two phases there are two intermediate incommensurate phases. Considering that the incommensurate phases were solved in the *Pnma*(00γ)0s0 superspace group, which in fact, is a (super)-sub-group of the 3D orthorhombic space group *Pnma*, therefore it is compatible with a second order kind (continuous) phase transition. However the coexistence of phases in the powder samples at low temperature (see below), points to a weak first-order character. This behaviour is not common for formate complexes

presenting an order-disorder phase transition[87].The topology of phase (**IV**) remains invariable, therefore as in the previous phase the 3D framework $4^{12}6^3$-**pcu** perovskite-like topology is conserved.

However, due to the breaking of symmetry, and contrarily to the orthorhombic phase **I**, in phase **IV**, there are two crystallographically independent cobalt(II) ions [Co1 and Co2],

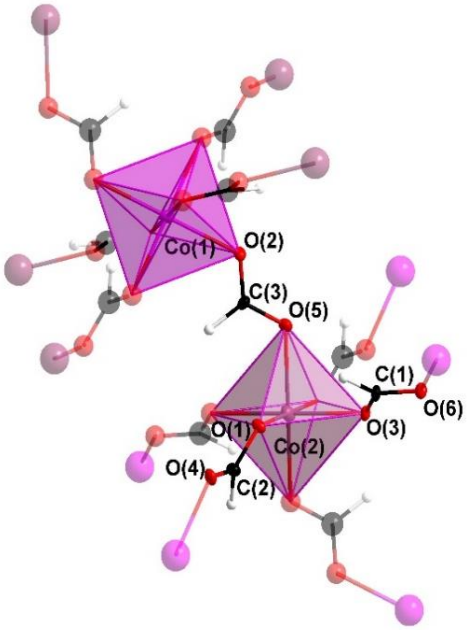

Figure 35: View of a fragment of the structure of **7**(**IV**) together with the atom numbering, obtained from the single crystal neutron refinement at 45 K. The octahedral Co(1) and Co(2) atoms have been represented in pink and purple, respectively. The oxygen, carbon and hydrogen atoms have been represented in red, black and light-gray, respectively. The ORTEP representation (50% ellipsoid probability) has been used to denote the asymmetric unit. The transparent mode was used to represent the atoms generated by symmetry operations. The methylammonium counter ions have been omitted for the sake of clarity.

both located in inversion centres. Each Co1 is surrounded by six Co2, and every Co2 is surrounded by six Co1 ions, building in both cases an octahedral perovskite-like framework (see Figure 35). At low temperature, the metal (II) ions are connected through *anti-anti* formate ligands along the [−1 1 0], [1 1 0] and [0 0 1] directions for **7** (**IV**) (see Figure 36). The values of the Co-O-C angle for the carboxylate bridge are in the range from 120.02(24)° to 122.27(19)° while the Co···Co distances vary from 5.8022(1) to 5.8292(1) Å (see Table 23). Regarding the octahedral environments of the metal atom at low temperature, as noticed above, all the bond distances become shorter, except for

the apical distance of the Co2 site, which changes from 2.1135(4) Å at 135 K [Co1─O2b$^{(I)}$] to 2.1212(1) Å at 45 K [Co2─O5$^{(V)}$].

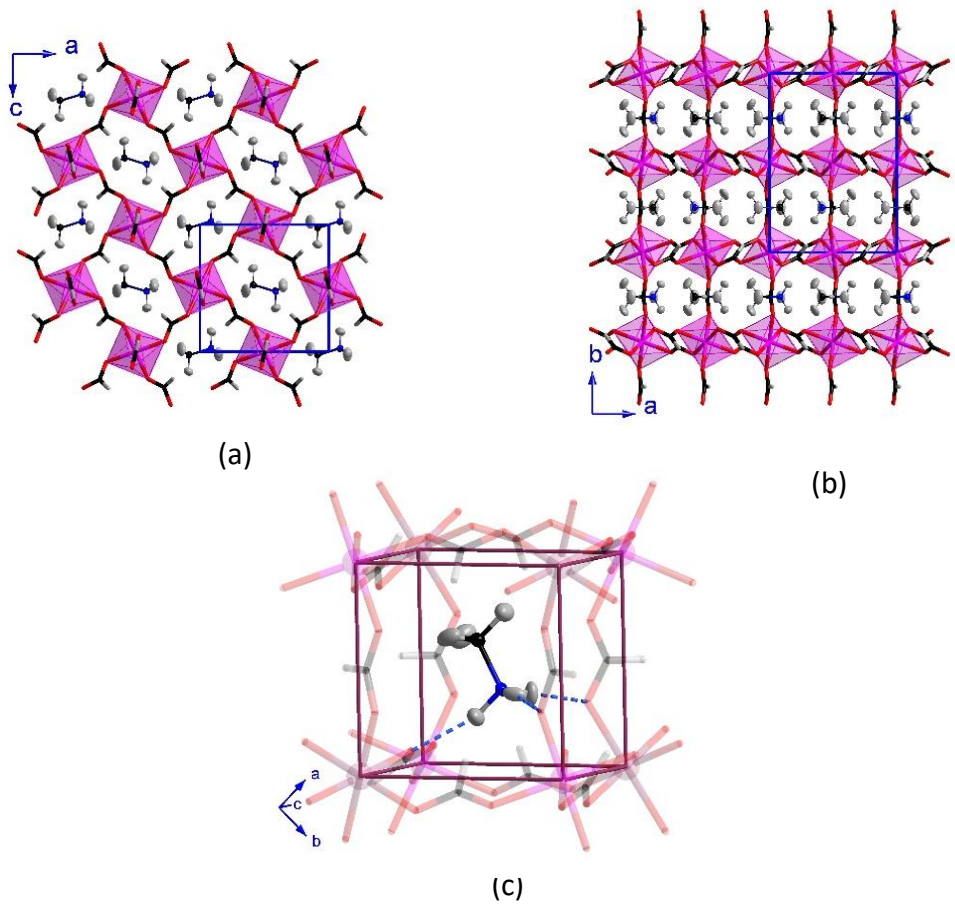

Figure 36: (a) and (b) correspond to views along the *b*- and *c*-axis, respectively of **7** (**IV**) at 45K. (c) Figure shows a detail of the metal-organic cage, where the methylammonium molecule, is located at 45 K, respectively. The nitrogen atoms of the methylammonium counterions have been represented in blue. The rest of the atoms follow the same colour codes as in previous figure. The H-bond network of the methylammonium molecules with the framework has been represented as dashed blue lines. The purple (c) bonds are only a guide to the eye.

Furthermore, the apical distances of the Co(1) ion in compound **7** (**IV**) [Co1─O6$^{(V)}$ = 2.096(3) Å] is shortened, reaching almost the same value as one of the equatorial distances [Co1─O4$^{(I)}$ = 2.096(3) Å], see Table 2 and Table 23. The distances in the formate ligands remain almost identical being in the range from 1.2467(1) Å to 1.2628(1) Å at 135 K and in the range from 1.246(3) Å to 1.268(4) Å at 45 K. However the angles in the ligands become slightly larger from 123.485(1)-124.312(1) at 135 K to 123.7(2)-124.7(3) at 45 K.

Table 23. Selected bond lengths (Å) and angles (º) of compound (**7IV**).

45K	**(7IV)**		Neutrons	45K	**(7IV)**		X−rays
Co1−O2	2.090(3)	Co2−O1	2.083(3)	Co1−O2	2.1005(16)	Co2−O1	2.0811(16)
Co1−O4$^{(I)}$	2.096(3)	Co2−O3	2.102(3)	Co1−O4$^{(I)}$	2.1073(16)	Co2−O3	2.1048(15)
Co1−O6$^{(II)}$	2.097(3)	Co2−O5	2.102(3)	Co1−O6$^{(II)}$	2.0967(16)	Co2−O5	2.1210(16)
Co1−O4$^{(III)}$	2.096(3)	Co2−O1$^{(VI)}$	2.121(3)	Co1−O4$^{(III)}$	2.1073(16)	Co2−O1$^{(VI)}$	2.0811(16)
Co1−O2$^{(IV)}$	2.090(3)	Co2−O3$^{(VI)}$	2.102(3)	Co1−O2$^{(IV)}$	2.1005(16)	Co2−O3$^{(VI)}$	2.1048(15)
Co1−O6$^{(V)}$	2.097(3)	Co2−O5$^{(VI)}$	2.121(3)	Co1−O6$^{(V)}$	2.0967(16)	Co2−O5$^{(VI)}$	2.1210(16)
Co1$^{(VII)}$−O4−C2	120.02(24)	Co2−O5−C3	120.04(24)	Co1$^{(VII)}$−O4−C2	120.47(15)	Co2−O5−C3	119.49(15)
Co1−O2−C3	120.92(23)	Co2−O3−C1	120.26(18)	Co1−O2−C3	120.53(14)	Co2−O3−C1	120.36(15)
Co1$^{(VIII)}$−O6−C1	122.27(19)	Co2−O1−C2	121.44(22)	Co1$^{(VIII)}$−O6−C1	122.10(15)	Co2−O1−C2	121.66(15)
Co1···Co2	5.8022(1)	Co1···Co2$^{(III)}$	5.8292(2)	Co1···Co2	5.8022(1)	Co1···Co2$^{(III)}$	5.8292(2)
Co1···Co2$^{(V)}$	5.8022(1)			Co1···Co2$^{(V)}$	5.8022(1)		

Symmetry code (**7IV**): (I) *x*,1+*y*,*z*, (II) 1/2−*x*,1/2+*y*,1/2−*z*, (III) −*x*,−*y*,−*z*, (IV) −*x*,1−*y*,−*z*, (V) −1/2+*x*,1/2−*y*,−1/2+*z*, (VI) 1−*x*,−*y*,−*z*, (VII) *x*,−1+*y*,*z*, (VIII) 1/2−*x*,−1/2+*y*,1/2−*z*

Due to the thermal contraction, the accessible space filled by the $[NH_3CH_3]^+$ cation within the 3-dimensional framework is 190-191 $Å^3$ per unit cell at 45K, value which is smaller if compared with the previous phase **I** values. Other effects as the occurrence of a slight reorientation of the methylammonium ions into the cavities as well as a small distortion of the framework, in a sort of displacive transition (see Figure 36) are also partially responsible of this shrinking.

In the orthorhombic phase **I** the methylammonium molecule was traversed by a mirror plane through the nitrogen and carbon atoms parallel to the *ac*-plane. However, once in the monoclinic phase **IV**, this mirror plane is lost, and therefore, six crystallographically independent hydrogen atoms [H6, H9 and H5 in the CH_3^- unit and H1, H2 and H8 in the NH_3^+], are observed in this low temperature phase. All these variations imply slight changes in hydrogen bond network of the guest-methylammonium molecule with the host-framework, involving distances and angles. Details of the most significant H-bonds are reported in Table 24.

Table 24. Possible hydrogen bonds of compounds **7** (**IV**) determined from neutron diffraction.

7 (**IV**) at 45 K	Donor···Acceptor (Å)	H···Acceptor (Å)	Donor-H···Acceptor (º)
N1─H2···O5	2.845(3)	1.828(7)	174.9(5)
N1─H8···O4$^{(I)}$	2.876(3)	1.834(7)	172.3(5)
N1─H1···O3$^{(II)}$	2.955(4)	1.991(7)	153.2(5)

Symmetry code **7B**: (I): $-x+1/2, y+1/2, -z+1/2$; (II): $-x+3/2, y+1/2, -z+1/2$

Due to the small distortion of the framework together with the reorientation of the methylammonium counter ions, the number of hydrogen bonds in the monoclinic phase (**IV**) is larger than those observed in the orthorhombic phase **I**, being the Donor···Acceptor distances 2.8834(9) at (**I**) and in the range of 2.845(3) and 2.955(4) Å at 45 K (**IV**). Although the described scenario is compatible for both, single crystal neutron and X-ray diffraction, the synchrotron X-ray powder data of compound **7** show a more complex situation. The diffraction patterns collected below the incommensurate structural phase transitions show more reflections than expected for a single monoclinic phase (see the inset in Figure 37). Moreover, some of the narrow reflections observed at RT become very broad at 45 K. This suggests a non-negligible occurrence of strains after the phase transition. It should be noted that at RT the model in *Pnma* space group fits well the experimental data (see Figure 37). The indexing of the low temperature pattern using a single phase was unsuccessful, and the best refinement model was obtained with a mixture between phases **I** and **IV**. It deserves to be noted that this mixture of two phases was not observed in neither the single crystal X-ray nor the single crystal neutron diffraction patterns. In order to take into account anisotropic broadening, a quartic form in (*h k l*) for the strain was used in the fit (see Figure 37).

Figure 38 shows the comparison of the micro-strain results between high- and low-temperature phases, suggesting an increase of strain after the phase transition. The occurrence of strain in the sample can be consequence of the atomic displacement, giving rise to the monoclinic twin-domains observed in the single crystal data.

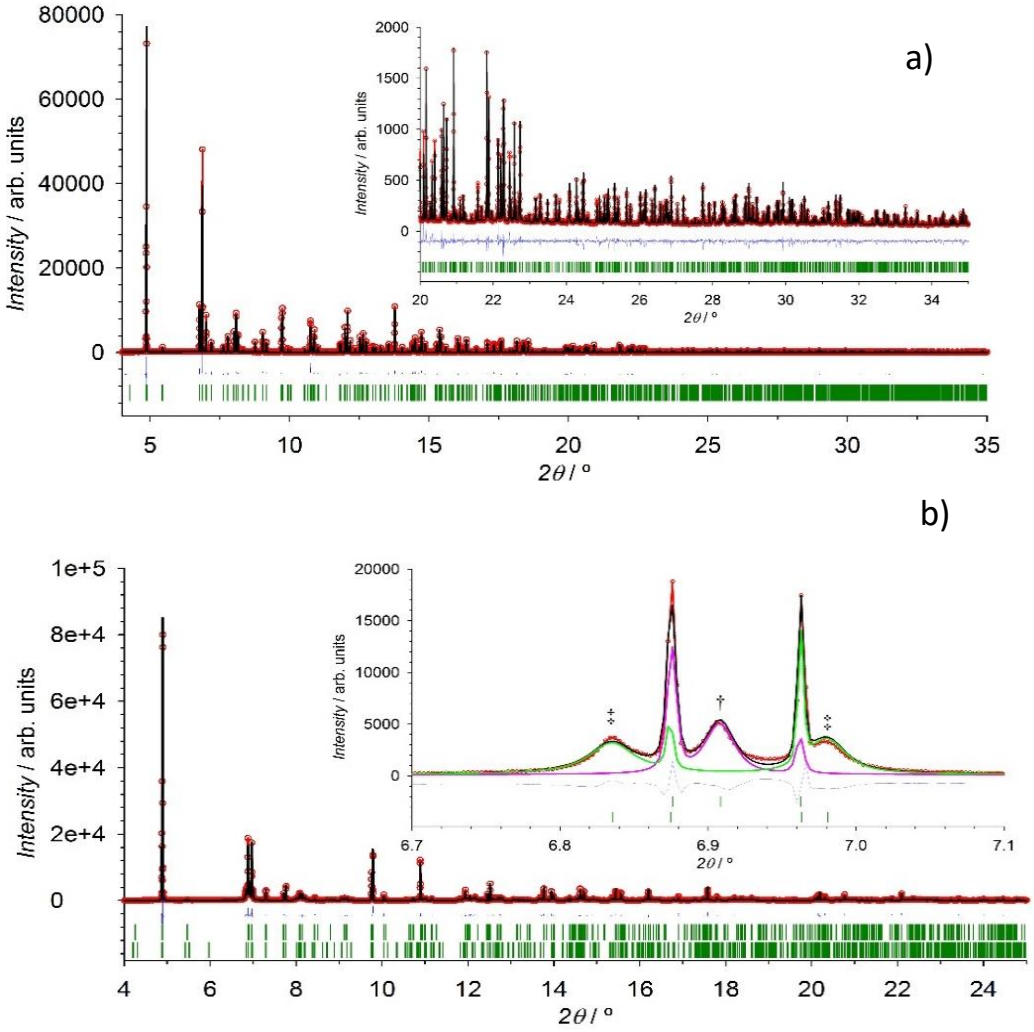

Figure 37. a) Experimental (open red circles) synchrotron X-ray powder diffraction data and calculated Rietveld refinement (black solid line) pattern for compound **7** at RT (data collected with λ= 0.4948 Å). The difference between observed and calculated patterns has been represented as a blue line. The vertical green marks represent the position of the Bragg reflections. The inset shows a zoom of the high-angle region. Refined cell parameters a = 8.392869(8), b = 11.707005(8) and c = 8.104255(7) Å. The data refinement gives, R_B = 9.40 % and R_F = 5.55 %, as agreement factors. (b) Le Bail fit of the same sample collected at 45 K. The code of colours has the same meaning that in (a). The upper raw of vertical green marks represent the position of the Bragg reflections for the orthorhombic phase. While the lower raw shows the position corresponding to the monoclinic phase, with refined cell parameters of a = 8.26226(3), b = 11.6471(2) and c = 8.15991(3) Å and a = 8.16148(2), b = 8.26332(1) and c = 11.65342(7) Å, β = 91.676(1)° for the orthorhombic and monoclinic phase, respectively. The inset shows in detail the contribution of each phase. The intensity corresponding to the orthorhombic and monoclinic phases is represented by pink and green solid lines, respectively. It should be noted that the orthorhombic (1 2 1) reflection, marked with † symbol is split into the (−1 1 2) and (1 1 2) reflections in the monoclinic phase, marked with ‡ symbols in the figure.

Two different samples were measured at low temperature (*ca.* 45K,), and although both are similar, the differences suggest a temperature dependence of the strain pattern as well as in the ratio between the orthorhombic and monoclinic phases.

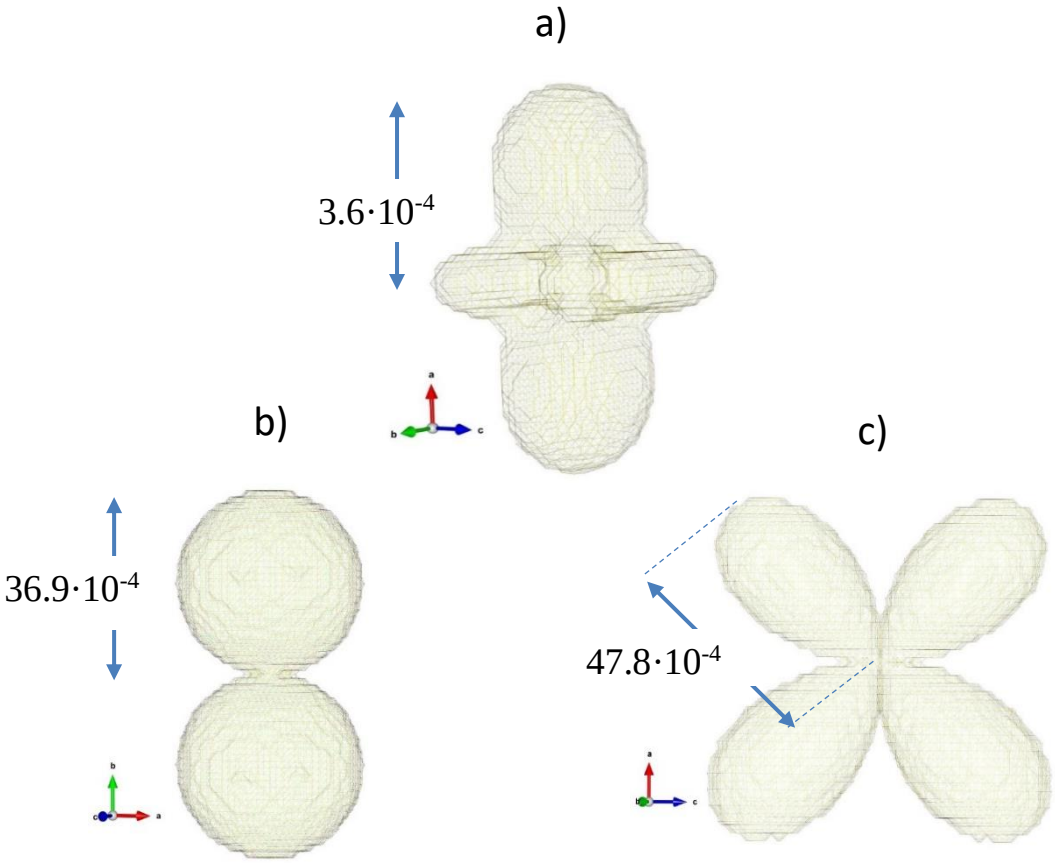

Figure 38: Visualization of micro-strain results[75] of the refinement at RT a) and at 45 K (b and c). At RT the refinement have been done using the orthorhombic phase, while at 45 K a multiphase refinement combing the orthorhombic and monoclinic unit cells was necessary (see main text).

Due to the large overlapping between the orthorhombic and monoclinic phases (related by a group-subgroup relation) together with the broadening of some reflections, the Rietveld refinement including both phases is not stable and therefore we have limited our analysis of the powder sample to the described Le Bail fit, Figure 39.

Further studies to elucidate the influence of the temperature cooling/warming protocol, as well as to try to obtain a pure monoclinic phase are needed. However, due to the range of temperature of this effect these experiments cannot be done using a standard laboratory diffractometer.

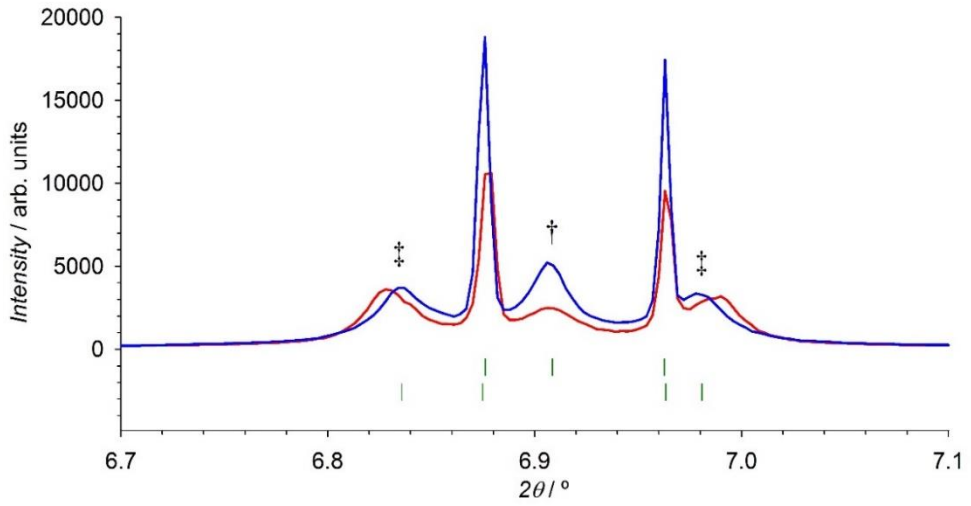

Figure 39: Comparative of two different cobalt-based samples collected at BL04-MSPD high-resolution powder diffraction beamline at ALBA synchrotron at 45 K, with a wavelength of 0.4948 Å. The vertical green marks represent the position of the Bragg reflections for the orthorhombic and monoclinic phases, top and bottom, respectively. The highlighted reflections correspond to the orthorhombic (1 2 1) reflection, marked with † symbol, which is split into the (−1 1 2) and (1 1 2) reflections in the monoclinic phase, marked with ‡ symbols in the figure. The difference in the intensity of the peaks are related with the ratio between the orthorhombic and monoclinic phases.

4.7 Magnetic studies of compounds 7 to 10

4.7.1 Magnetometry measurements

Along this section, we are going to describe the macroscopic magnetic behaviour of the compounds **7** to **11**. Although the SQUID measurements, on single crystal and powder samples, for some of these compounds have been previously reported,[47,49] a brief description will be included in this section in order to help the readers to understand the magnetic structure determination described later. The preliminary measurements published by *Pato-Doldán et al.*[49], reveal a global antiferromagnetic behaviour for compounds **7**, **9**, **10** and **11**. To the best of our knowledge, the magnetometry measurements of the iron-based compound (**8**) have not been reported in the literature, therefore it will be presented here for the first time.

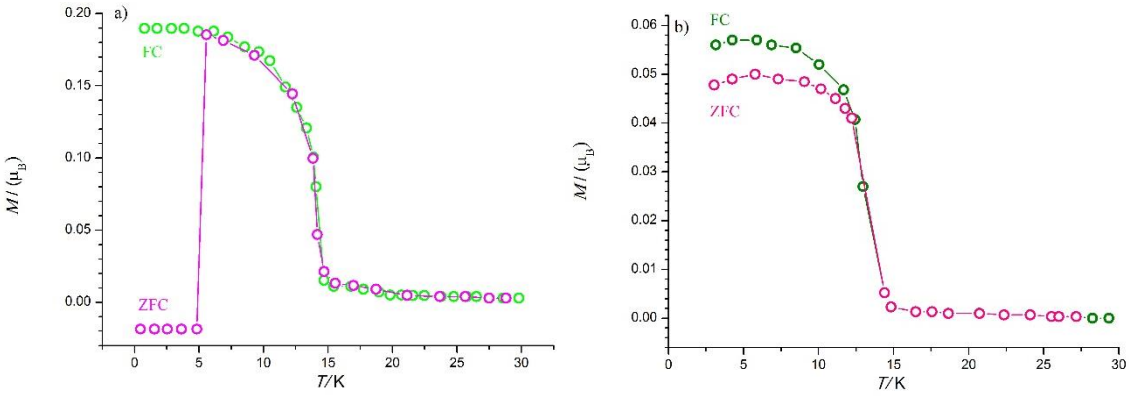

Figure 40: a) magnetization curve of **7** (Co-based) single crystal oriented along [010] direction showing the spin-flop at 14.5 T. Right, Zero-field cooled (ZFC) and field cooled (FC) magnetization M as a function of temperature measured with different magnetic fields (here it is reported only at 1000 Oe) in (b) polycrystals at 1000 Oe. Data obtained from Ref. [47,49]

The magnetometry measurements of compound **7** were studied on single crystal and powder samples[47,49] revealing a global antiferromagnetic behaviour with a ferromagnetic component below 15.9 K. The single crystal analyses show that this ferromagnetic contribution accounts for 0.19 μ_B along the [0 1 0] direction (in the orthorhombic *Pnma* description). This behaviour is compatible with a weak-spin canting or due to the non-compensation of the magnetic moments in the network (Figure 40). It deserves to be noted that the structural phase transition from orthorhombic to monoclinic was unknown when the magnetometry measurements were reported. Therefore, the orbit splitting of the cobalt ions was not known. Therefore, *Aguirre et al.* suggested the Dzyaloshinskii–Moriya interactions could be responsible of the spin canting effect. This option will be explored combining the neutron diffraction analysis with *ab initio* electronic structure calculation (see section 4.7.2). Finally this compound present a magneto-electric behaviour which is correlated with a possible spin-flop under strong magnetic fields (*ca.* 14.5 T). Although, the magnetic structure determination under magnetic field has not been the objective of this thesis, the representational analysis carried out in the next section can be used to propose a magnetic phase transition under applied external field.

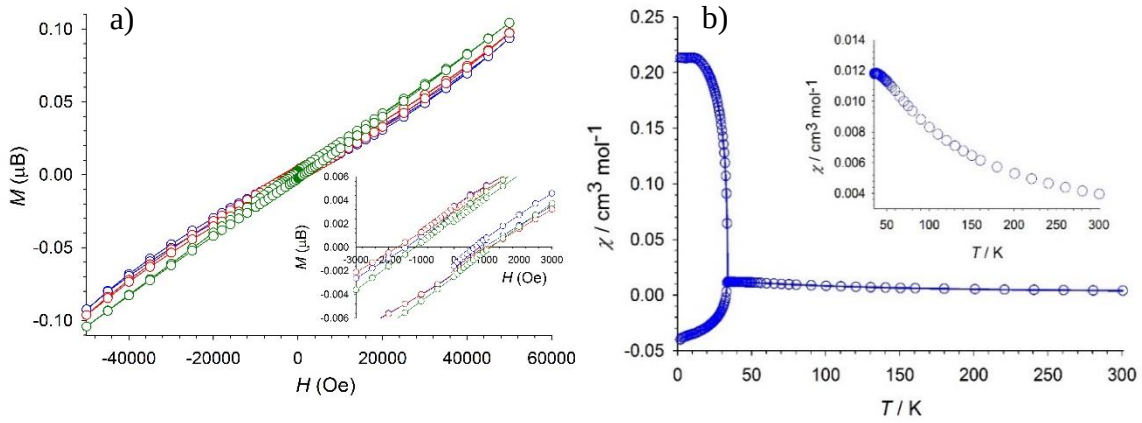

Figure 41: Left, Magnetization vs applied field at different temperature points, (red) 2 K, (blue) 15 K, (green) 30 K for compound **9** (Ni-based). Right, view of the temperature dependence of χ measured in the ZFC-FC regime. The inset detail of the 30 to 300 K region, collected under an external magnetic field of 5000 Oe.

The compound **9** present a very similar magnetic behaviour. As is observed in Figure 41, the susceptibility curve presents a first maximum around 33 K which is an indication of antiferromagnetic behaviour. The jump in the susceptibility below this temperature, as in the case of compound **7**, is related with the presence of a ferromagnetic signal. This ferromagnetic signal can be due to the non-compensation of the magnetic moments of due to the occurrence of a weak spin-canting. In Figure 41, there is a negative magnetization in the zero field cooled (ZFC) measurement. It deserves to be noted that this signal is not symmetric with respect to the field cooled (FC) measurements, therefore it suggest that this signal should come from a weak residual magnetic field in the superconducting magnet. As a result of this residual magnetic field, the ferromagnetic component of the sample orders in the opposite direction giving rise to a global negative magnetization. The ability to change the sense of the ferromagnetic component even at the very weak magnetic fields (remnant magnetic field), is a signature of the weak anisotropy of this compound. The field-dependent isothermal magnetization measurements were obtained at three different temperatures, 2, 15 and 30 K all bellow T_N. Neither in our measurements nor in those reported by *Aguirre et al.*, there is signal of jumps or concavities. Therefore, at variance to the cobalt-based compound, a spin-flop transition is not expected for the nickel compound. Finally, it deserves to be noted that, in the different hysteresis loops (2, 15 and 30 K), the coercive field is almost invariant with a value around 1000 Oe. So that it is confirmed that this compound is a weak-ferromagnet below 33 K. This weak-ferromagnetic should be due to a spin canting that can be explained by the Dzyaloshinskii–Moriya interaction, which favour no-collinear spin arrangements.

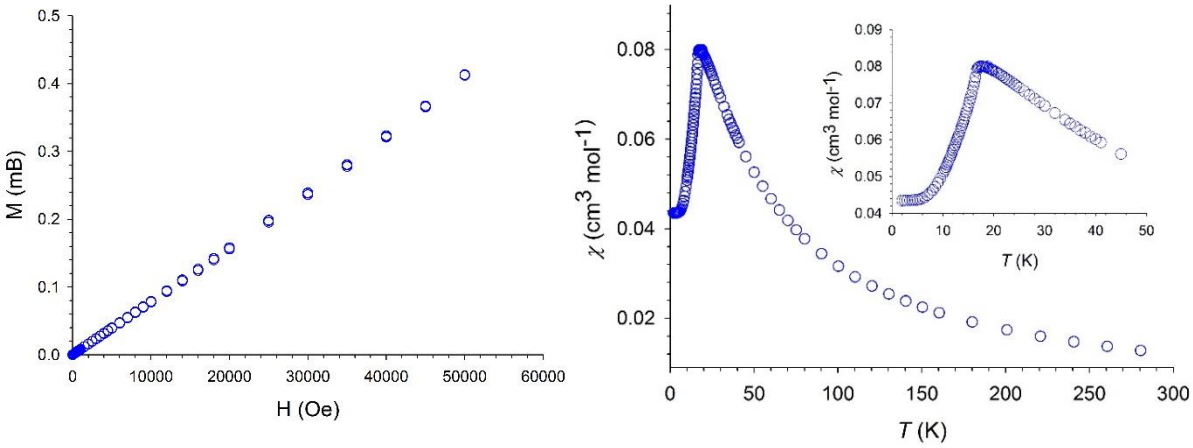

Figure 42: (Left) View of the magnetization plot versus magnetic field. (Right) Temperature dependence of the magnetic susceptibility for compound **8** (Fe-based). The inset shows a detail of the low temperature region.

The magnetometry measurements of compound **8** and **10** are slightly different to those previously described. The global behaviour of both compounds, as in the previous cases, is antiferromagnetic, but at variance to the cobalt- and nickel-based compounds neither in the temperature evolution of the magnetization nor in the field-dependent magnetization curves there is an indication of ferromagnetic signals. Therefore, the compounds **8** and **10** do not show any hysteresis cycle. Figure 42 shows the temperature dependence of the magnetization curve, for compound **8** measured in an external magnetic field of 500 Oe. This compound under the FC regime, displays a broad peak extended from 10 to 40 K where it reaches the maximum around 18 K confirming the antiferromagnetic ground state. The plateau shape at low temperature it is very close to zero magnetization, this means that in the underlying antiferromagnetic lattice the spins are coupled strictly antiparallel among them, with no signal of spin canting or non-compensated magnetic moments. Figure 42 b shows the isothermal magnetization at 2 K for compound **8**, the linearity as function of the external magnetic field denotes strong antiferromagnetic interactions which are not overcome even at 5 Tesla. The isothermal magnetization for compound **10** (see Figure 43) collected at 4 K (red) and 2.5 K (green) increase linearly form 0 to 10 T. At low magnetic field (*ca.* 0.6 T) a change in the magnetization curve is observed, this can be due to a small spin-reorientation or due to a spin-flop transition (see Figure 43).

A similar effect was observed in compound **7**, but in the previous case the upturn in the magnetization was more remarkable. The temperature dependency of the magnetic susceptibility under FC-ZFC regime, exhibits an antiferromagnetic order with no

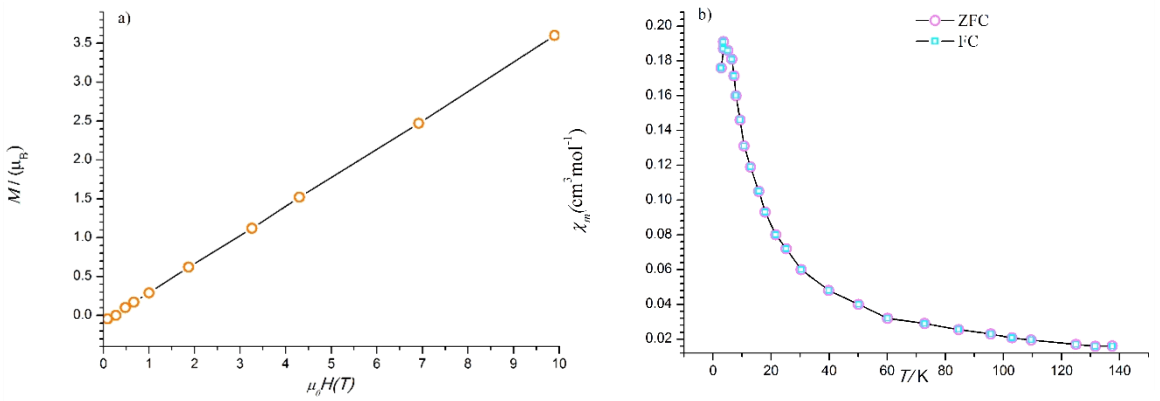

Figure 43: a) Magnetization plot along two different directions at 4 K for compound 10 (Mn-based). Inset: thermal evolution of the magnetization of compound **10**. b) View of the temperature dependence of χ measured in the ZFC-FC regime. Data obtained from Ref.[49]

presence of weak ferromagnetic component, as in the iron-based compound. The susceptibility measurements suggest a long range magnetic order, with a T_N of *ca.* 8 K. Moreover, in comparison with other members of the series, compound **10** is the most isotropic being a d^5 (Mn^{2+}) high-spin ion. The other members of this series, have a non-negligible magnetic anisotropic term, particularly important for the cobalt-based compound, therefore a competition between single ion anisotropy and the Dzyaloshinskii–Moriya interactions is expected.

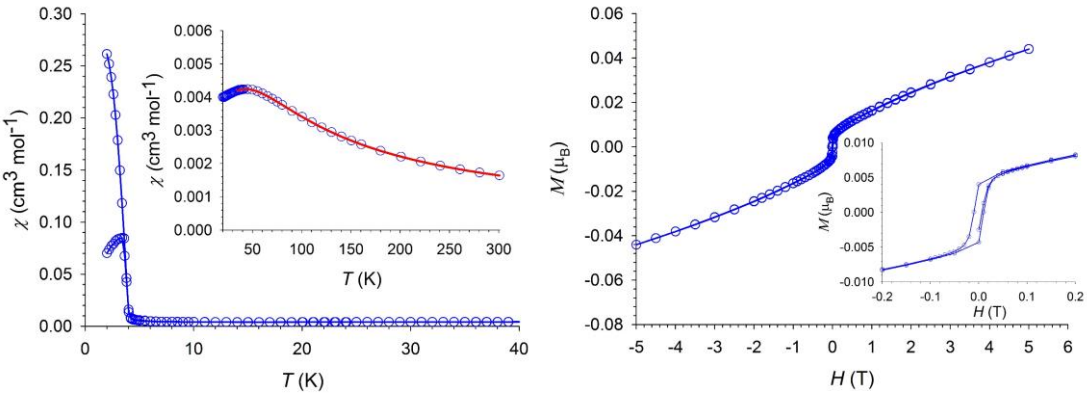

Figure 44: (a) The magnetization as a function of temperature measured in ZFC and FC regimes for compound **11** (Cu-based) by using different magnetic fields 100 Oe (ZFC-FC curve) from 2 to 40 K and 5000 Oe from 35 to 300 K (inset). The solid red line represent the fit to the antiferromagnetic chain model (see main text). (b) Field dependent isothermal magnetization collected at 2K. The inset show a detail of the small coercive field. (Own measurements).

The magnetometry measurements of the copper-based compound (**11**) in the form of susceptibility as function of temperature is shown in the Figure 44. This curve shows two well-differenced features, the first one is a broad maximum around 38 K. The maximum is consistent with the occurrence of a global antiferromagnetic behaviour. However the shape of the susceptibility curve, in particular the maximum, which is extended in a very

large range of temperatures, is a feature of short-range order. If we suppose that the unpaired electron of the Cu(II) ions is on the $d_{x^2-y^2}$ orbital, that means that the 3D structure can be seen as antiferromagnetic chains connected through a carboxylate bridge in *anti-anti* conformation. This chains are running along the *b*-axis (orthorhombic basis) and involving the shortest Cu-O bond distances. Each of these chains is connected to other two adjacent through the apical position of the copper ion, giving rise to the final 3D structure. However, if the magnetic orbital is the d_z^2, which in this case correspond to the apical position of the copper environment, the copper ions are not connected between them. Therefore, in this system there is only two kind of bridges between adjacent copper ions, the one connecting copper ions through the carboxylates ligand occupied the equatorial plane ($d_{x^2-y^2}$ orbital) and those that connect the copper ions through carboxylate groups occupied both equatorial planes ($d_{x^2-y^2}$ orbital) and apical positions (d_z^2 orbital), in this last case due to the orbital overlapping the exchange coupling is not favoured. Based on the topological approach described above, we can propose a magnetic model where the main antiferromagnetic interaction is along the *b*-axis involving the $d_{x^2-y^2}$ orbital, this produce a 1D antiferromagnetic order, which is compatible with the broad peak observed in the susceptibility measurement. In order to estimate the magnetic interaction along the chain we can model the susceptibility data according to the antiferromagnetic chain model proposed by Bonner and Fisher's in the temperature range from 35 to 300 K. The experimental data can be fitted by the following numerical expression:

$$\chi_M = \frac{Ng^2\beta^2}{k(T-\theta)} \frac{0.25 + 0.074875x + 0.075235x^2}{1.0 + 0.9931x + 0.172135x^2 + 0.757825x^3}$$

$$\theta = \frac{zjS(S+1)}{3k}$$

With $x=|J|/kT$, the Hamiltonian defined as $H= -\Sigma\ J\ S_iS_{i+1}$ and J is the exchange integral coupling constant.

The best fit using nonlinear regression analysis leads to $J = -46.5(1)$ cm^{-1} and $g = 2.28(2)$. In order to improve the data fit a Weiss parameter (θ) was included in the fit, giving rise to $j = -11.8(6)$ K, the z parameter take into account the number of metal neighbours. The calculated curve matches well the experimental data in the whole temperature range including the shape of the antiferromagnetic short-ordering peak. The calculated model have been represented as the solid red line in Figure 44. A second magnetic transition (*ca.* 4.0 K) is observed in the Figure 44. This remain us the ferromagnetic signal observed

in the cobalt- and nickel-based compounds. Therefore, it can be understood as a long range order due to the inter-chain interactions. Although there is a ferromagnetic signal, the magnetization curve show a very weak ferromagnetic component, therefore the antiferromagnetic order within the chains should be maintained. The origin of this ferromagnetic signal, as in the previous case should be related with a weak spin canting or due to the non-compensation of the magnetic moments. However, this compound does not present any structural phase transition at low temperature, so there is only one copper orbit and the non-compensation of the different networks consequently can be discarded. To finish with the magnetic properties of this compound, let us present the temperature evolution of the neutron diffraction pattern. Three long acquisitions at 60, 10 and 2 K

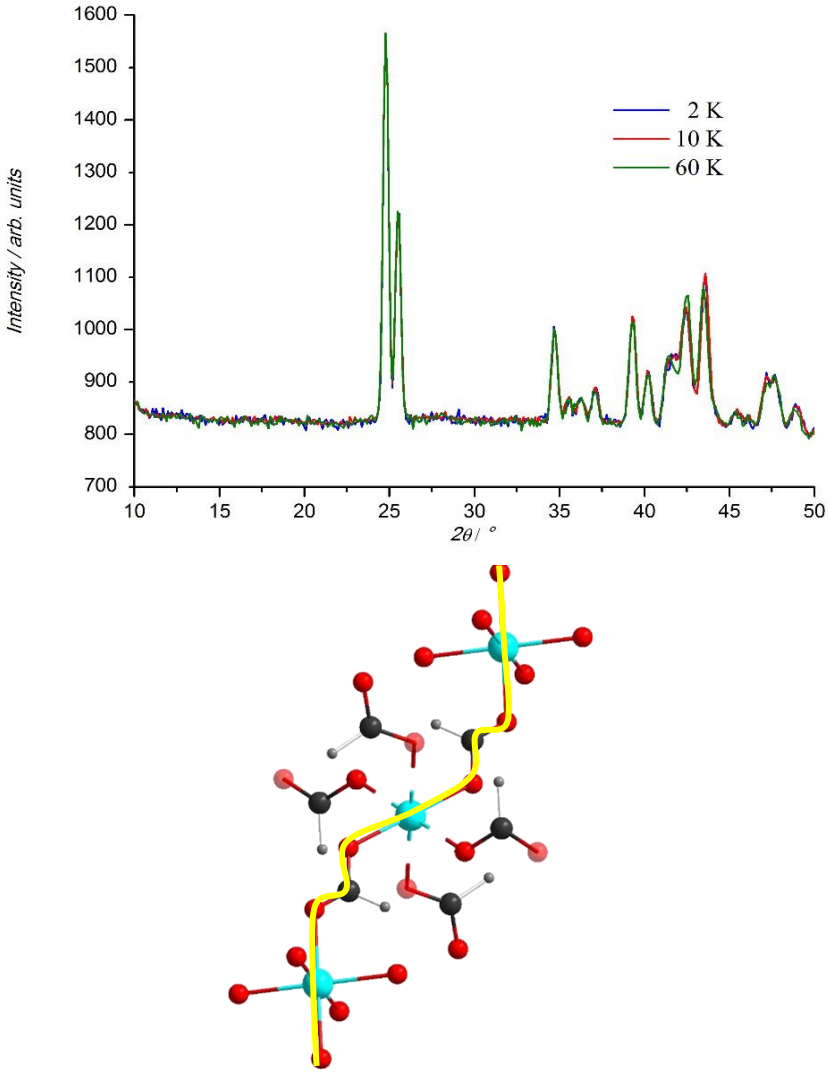

Figure 45: Comparative analysis of compound **11** between three patterns collected at D1B high flux diffractometer (blue) 2 K and (red) 10 K and (green) 60 K, showing that no magnetic peaks appear by neutron experiments while it has been possible to detect the two phase transitions by macroscopic measurements (see main text) occurring at 2 and 45 K. Below, it is shown the 1-dimensional chain that favours the antiferromagnetic interactions involving the shortest Cu─O distance, it means the unpaired electron of the Cu(II) ions in the $dx^2–y^2$ orbitals through the formate anions. In fact, when the magnetic orbital is the dz^2 the copper ions are not interacting among them, (for this reason, the oxygen is marked in transparent red colour.)

were carried out (Figure 45). The 60 K correspond with the paramagnetic phase, well above the broad peak observed at *ca.* 38 K. The second pattern was collected at 10 K, where only the 1D order may be observed. Finally, the last pattern was collected at 2 K below the long-range 3D magnetic order. However, even after a long acquisition there are not signal of short- or long-range magnetic order. It deserves to be noted that the copper ion have s = 1/2, so the magnetic signal is expected to be weak. This together with the large background due to the hydrogen atoms content preclude to obtain a pattern where the magnetic reflections are clearly observed. In order to diminish the influence of the hydrogen atoms, we will try to explore the low temperature phase using single crystal Laue diffraction, if not, polarized neutron diffraction measurements can be carried out in order to separate the incoherent signal from the magnetic signal. Therefore, further work in this compound is needed in order to ambiguously determine if there is really 3D magnetic ordering.

4.7.2 Neutron data analysis

Along this section we are going to describe the neutron diffraction data, with the final objective to propose a magnetic structure model for each member of this series. As we have discussed in preliminary sections, the powder diffraction data present an important mixture of phase; as a consequence, some simplifying approximations will be used throughout this section in order to shed light into the understanding of the magnetic structures of these compounds. All the results presented in this section are based on data coming from the high flux and medium resolution D1B powder diffractometer. This instrument has a very low intrinsic background and a large flux which allow us to explore the full range of temperatures in a reasonable period of time. Finally, as in the structural description we are going to use the cobalt-based compound as the archetype and after describing the magnetic structure of this compound the results will be extended to the other members of this series.

4.7.2.1 $[CH_3NH_3][Co(COOH)_3]$ (7)

The temperature evolution of the neutron diffraction patterns of compound **7** collected in the range: 300−20 K, show a progressive increase of intensity on some Bragg reflections when the temperature decreases. This increase of intensity should be related with some distortion in the structure, probably due to the motion of the methyl group of the methylammonium counterions. From the single crystal neutron diffraction we have observed that the libration of the methyl group is frozen below 135 K, value which correspond with the maximum in the intensity of the reflection at *ca.* 42 degrees in Figure 46 a (observed maximum at *ca.* 130 K). Below this temperature this reflection decrease continuously until *ca.* 80 K, where a drastic decreasing of intensity is observed.

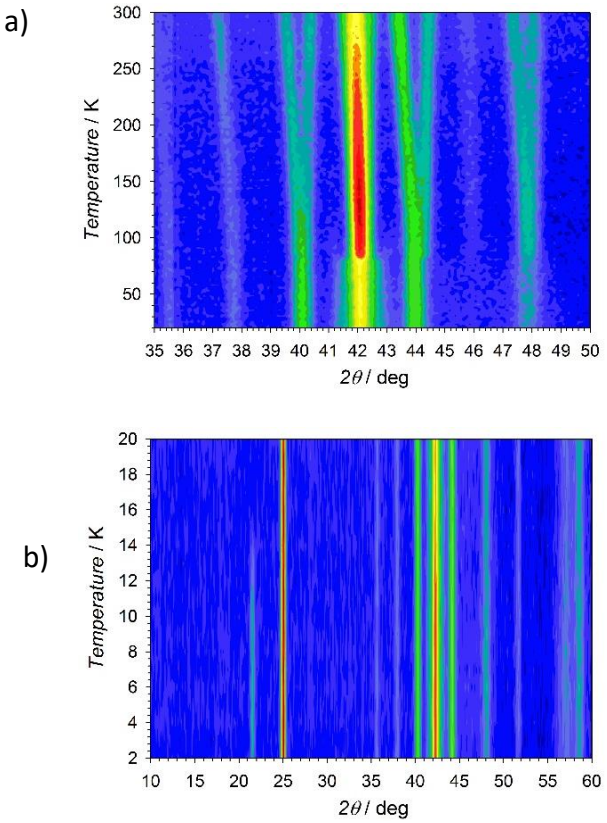

Figure 46: (a) Mesh plot of compound **7** (Co-based), with the intensities represented in logarithmic scale, of the thermodiffractogram collected at D1B in the temperature range of 20–300 K. (b) Mesh plot of the thermodiffractogram in the temperature range of 2–20 K.

This temperature, correspond with the nuclear phase transition from the phase **III** to phase **IV**, therefore from the incommensurate to the monoclinic structure. The broadening of the reflections below this temperature is associated with a mixture of phase **I** and phase **IV**, as was also observed in the powder X-ray diffraction. This mixture of phases is persistent even at lower temperatures; therefore, it should be taken into account in the magnetic structural analysis. As the cobalt-based compound is the only one presenting

orthorhombic and monoclinic phases below the Neél temperature, the analysis carried out for the cobalt-based compound can be extended to the other members of the series which are simpler. Figure 46 b, shows a detail of the low temperature range from 20 to 2 K. In this thermodiffractogram the occurrence of new reflections is observed below 15 K, this corresponds to the occurrence of a long-range magnetic ordering. The T_N obtained from the neutron diffraction data is in good agreement with the value observed from the magnetometry measurements. The magnetic contributions are also observed on the top of the nuclear Bragg reflections, which is indicative of a **k** = (0, 0, 0), magnetic propagation vector[47]. In order to determine the possible magnetic structures at zero applied magnetic field, a series of high-statistics neutron diffraction measurements above and below the ordering temperature have been carried out. Due to the weak magnetic contribution, the overlap between nuclear reflections and the considerable background produced by the high number of hydrogen atoms in the sample, our data preclude an accurate refinement of the crystal and magnetic structure at the same time. We have subtracted the nuclear contribution from the low temperature pattern at 2 K, using the pure nuclear intensity of the paramagnetic phase measured at 20 K. Both diffraction patterns were normalized to the same monitor count in order to obtain the best difference pattern. This difference pattern isolates the magnetic contribution and therefore, a more accurate indexing of the magnetic reflections as well as a simpler data treatment of the magnetic structure can be

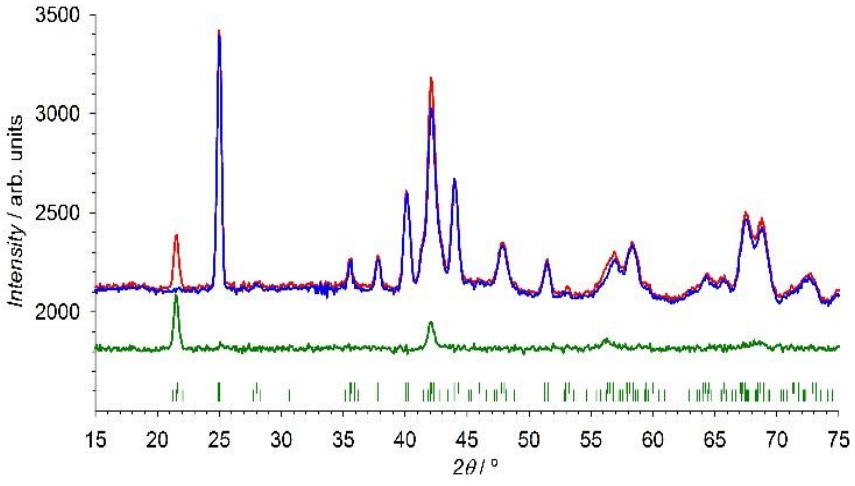

Figure 47: Neutron powder patterns of **7** (Co-based) collected at 2 K (red) and 20 K (blue) using the high flux D1B diffractometer. The difference diffraction pattern has been represented in green. The intensity of the calculated difference pattern has been shifted to an arbitrary value in order to achieve a similar background as those observed in the original patterns. The vertical lines represent the Bragg positions for compound **7** (**I**) (top) and **7** (**IV**) (bottom).

undertaken (see Figure 47). The same approach will be applied to determine the magnetic structure of the other members of the series.

As described before, and in contrast with the single crystal measurements, at low temperature (below ca 80 K) the powder diffraction measurements show the occurrence of both phases **7** (**I**) and **7** (**IV**), *Pnma* and $P2_1/n$, respectively. Therefore, in order to accomplish the symmetry analyses, we have considered both phases separately. Considering first, the parent *Pnma* space group, four irreducible representations are compatible with the Wyckoff position of the Co(II) atoms (4*b* Wyckoff position) and the propagation vector **k** = (0, 0, 0). These four representations correspond to four magnetic groups; *Pnm'a', Pnma, Pn'm'a* and *Pn'ma'* (see Figure 48) and all them were tested to fit the difference pattern.

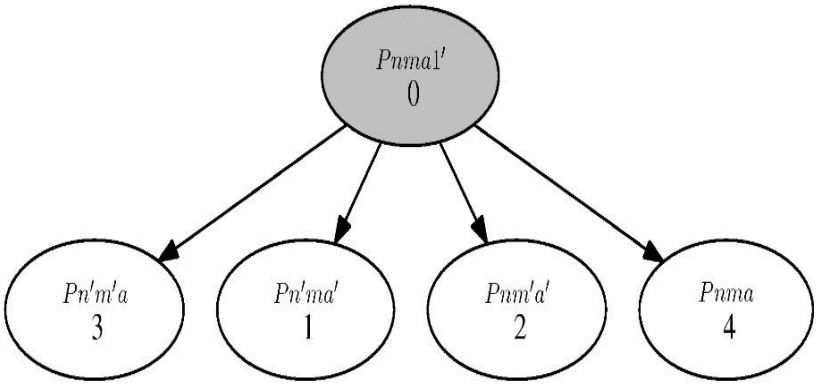

Figure 48: Graph and list of the k-maximal symmetries for the parent space group *Pnma* and **k** = (0,0,0). In this case, the condition of the magnetic site being *4b* does not restrict further the list.

The four irreducible one-dimensional representations of the group G_k , (Γ_1-Γ_4) and a simple set of basis vectors for each irreducible representation (*irreps*) can be determined using the program BasIreps[50] for *Pnma* parent space group. The representational analysis provides the expression of the Fourier vector coefficients (in this case equivalent to magnetic moments) as linear combinations of basis functions. The basis vectors describe the possible magnetic structures. The magnetic representation Γ_M for each magnetic site [Wyckoff position 4*b*] can be decomposed as the direct sum of the *irreps*, Γ_1 to Γ_4, by applying the great orthogonality theorem. Each *irrep* appears three-times for 4*b* site. In the present case [where **k** = (0, 0, 0)], all the Fourier coefficients must be real:

$$\Gamma_M(4b) = 3\Gamma_1 \oplus 3\Gamma_2 \oplus 3\Gamma_3 \oplus 3\Gamma_4$$

The *Pnm'a'* magnetic model can be discarded since it is far from fitting properly the neutron experimental data, and, as we will see hereafter, this is also applied to the iron-(**8**), nickel-(**9**), and manganese-based (**10**) compounds. The *Pnma* model can reproduce the experimental data, but the obtained magnetic model agrees with a strictly antiferromagnetic structure, in contrast with the magnetometry measurements, which show a clear ferromagnetic contribution. Therefore, the *Pnma* magnetic space group is not allowed by symmetry, neither for the cobalt- nor for the nickel-based compound, both presenting a weak ferromagnetic signal below T_N. The *Pn'm'a* and *Pn'ma'* magnetic groups are also in agreement with the neutron experimental data, and both allow a ferromagnetic component. If in a first approach, we considered only the orthorhombic contribution in the difference pattern of the cobalt ion. The best fit by using the *Pn'm'a* magnetic model to the neutron data provides an antiferromagnetic structure with a small ferromagnetic contribution along the *c*-axis [*c* = 8.1543(2) Å] of 0.44 μ_B per Co(II) ion. This ferromagnetic component can be seen as the spin canting observed in the magnetometry measurements. However, from magnetization as function of the different crystal orientations, *Aguirre et al.*[47] have shown that the ferromagnetic signal should be along the *b*-axis. This model does not allow ferromagnetic contribution along the *b*-axis, being strictly antiferromagnetic in this direction, so that we can discard it. The refined model by using the *Pn'ma'* group presents a ferromagnetic contribution along the orthorhombic *b*-axis [*b* = 11.6735(2) Å] and therefore this is the only solution compatible

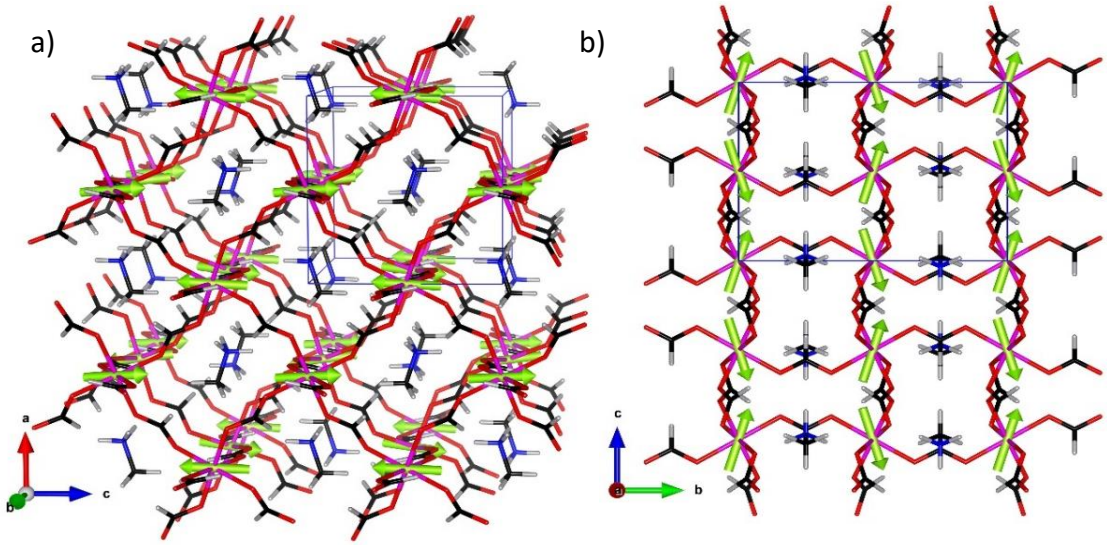

Figure 49: (a) Perspective view along the *b*-axis of the magnetic structure refined in the *Pn'ma'* Shubnikov space group. (b) Detail view along the *a*-axis. The crystal and magnetic unit cell [**k** = (0, 0, 0)], has been represented in blue and the magnetic moments in light green. The nuclear structure has been represented using the same code of colours than in the previous figures. The atoms follow the same colour codes as in previous figures.

with the macroscopic measurements (see Figure 49). Moreover, this magnetic space group fits better than the others the experimental data. The refined ferromagnetic component in the *Pn'ma'* magnetic space group, have a contribution about 0.68(12) μ_B per Co(II) ion, which is higher than the signal encountered along this axis in reference[49] (*ca*. 0.19 μ_B). However, the single crystal diffraction data at 45 K showed that once the sample of **7 (IV)** achieves the phase transition it becomes a twinned crystal. Depending on the relation between the twin domains, the magnetic contribution can change. The twin domains observed in the single crystal experiments (neutrons and X-ray) are related by a rotation of 180º with respect to the shortest axis (*a*-axis in the orthorhombic base), that means, perpendicular to the ferromagnetic component. As a consequence of these twin-domains, the ferromagnetic contribution obtained from the single-crystal magnetometry measurements can be underestimated depending on the twin-domain balance. The refined value for the Co(II) magnetic moment, using this first approach, is of 2.9(2) μ_B, which is reasonable for a high-pin divalent cobalt ion.

Considering now, as parent the $P2_1/n$ monoclinic space group, the magnetic representation Γ_M for each magnetic site [Wyckoff position 2*b* for Co(1) and for 2*c* for Co(2)] can be decomposed as the direct sum of the *irreps*, Γ_1 and Γ_3. Each *irrep* appears three-times for 2*b* and 2*c* sites.

$$\Gamma_M(2b) = 3\Gamma_1 \oplus 3\Gamma_3 \qquad (2)$$

$$\Gamma_M(2c) = 3\Gamma_1 \oplus 3\Gamma_3 \qquad (3)$$

There are two independent magnetic sites [Co(1) and Co(2)], so there are six degrees of freedom to refine these magnetic structures. The number of parameters can be reduced assuming the same magnetic moment for both magnetic sites. The Shubnikov groups corresponding to Γ_1 and Γ_3 are $P2_1/n$ and $P2_1'/n'$ [with (**a**, **b**, **a**+**c**; 0, 0, 0) transformation to the $P2_1'/c'$ standard magnetic space group], respectively. The $P2_1/n$ model gives a magnetic structure where the magnetic moments are almost antiferromagnetically coupled in all directions, which does not explain the ferromagnetic signal in the magnetometry measurements. Moreover, it is not able to fit properly the experimental data. The best fit is obtained with the $P2_1'/n'$ model that gives a magnetic structure permitting the occurrence of weak ferromagnetism, and therefore it is in agreement with the magnetometry measurements.

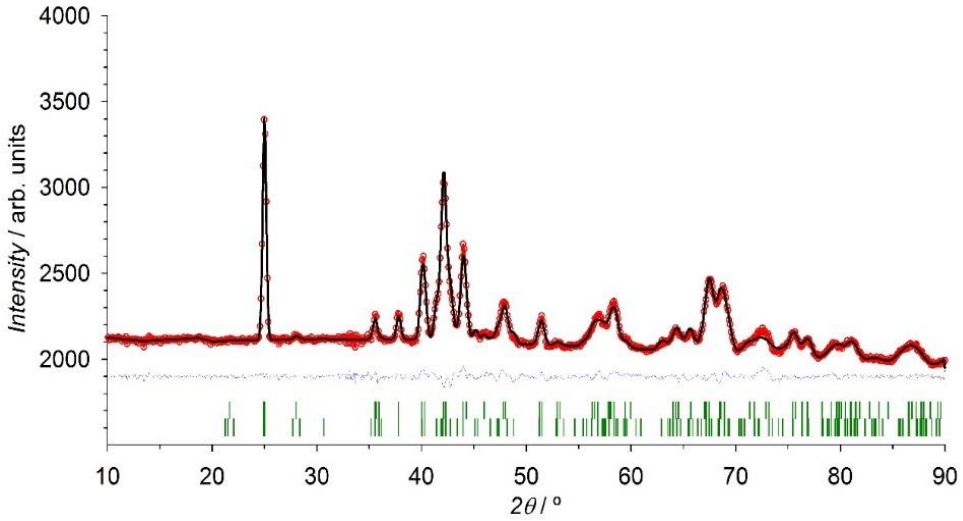

Figure 50: Rietveld refinement of compound **7** (Co-based) collected at 20 K (paramagnetic) using the high flux D1B diffractometer. The experimental data have been represented as open red circles, the calculated Rietveld refinement is represented as black solid line and the difference between observed and calculated patterns has been represented as a blue line. The vertical green marks represent the position of the Bragg reflections, orthorhombic (upper marks) and monoclinic phase (bottom marks). Giving rise to a refined value of the orthorhombic and monoclinic fraction of 56 and 44 %, respectively

Due to the contribution of both phases in the cobalt-based compound, with a ratio between orthorhombic and monoclinic phases of 56 and 44%, respectively (Figure 50). Derived from the Rietveld refinement of the paramagnetic phase, including both phases. The magnetic structure refinement have been carried out combining the two possible magnetic space groups. As the monoclinic distortion is not very large and in order to avoid over-parametrization, in the initial refinements both magnetic structures were restrained to be the same. This constraint is supported by the observation of magnetic intensities only on top of the reflections coming from the orthorhombic space group. Therefore, some constraints were added to the monoclinic $P2_1'/n'$ magnetic space group to reproduce the magnetic structure of the orthorhombic *Pn'ma'* magnetic space group. Only in the last refinement, the monoclinic phase has been refined independently. Due to the low number of magnetic reflections, the *a*- and *b*-components of the two magnetic sites of the monoclinic phase have been constrained to be antiferromagnetically coupled, as was observed in the orthorhombic phase (*a*- and *c*-component in the orthorhombic space group). The refined magnetic moment of Co(1) and Co(2) are equal within the experimental error, with a value of 2.9(2) μ_B. Concerning the magnetic interactions, the strongest must be those due to the Co(II)-formate-Co(II) super exchange pathways resulting in a 3-dimensional magnetic network.

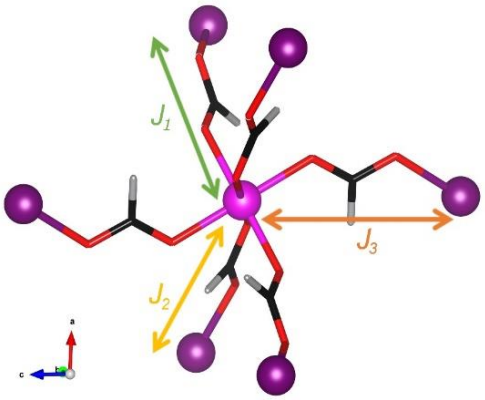

Figure 51: View of the three possible magnetic interactions J_1-J_3 between Co(1) (pink) and Co(2) (purple) ions in **7** (**IV**).

In such magnetic network, each Co(II) ion is coupled with other four Co(II) ions in the *ab*-plane, using the monoclinic description (or *ac*-plane in the orthorhombic space group), by two magnetic interactions J_1 and J_2, and with two other Co(II) ions along the *c* direction by a J_3 magnetic interaction (see Figure 51). These three magnetic interactions are expected to be of the same order of magnitude, due to their very similar magnetic pathway geometries, and antiferromagnetic in nature. Due to the slight distortion after the structural phase transition, this scenario is also valid for the monoclinic space group. Since there is no frustration in the magnetic network, an antiferromagnetic collinear structure should be expected at low temperature, which is in disagreement with the ferromagnetic signal observed in the magnetometry measurements. A possible origin for this ferromagnetic signal is the existence of a non-negligible single-ion magnetic anisotropy for the Co(II) ions, which can produce a non-collinear magnetic structure. In order to investigate this possibility we computed the value of the zero-field splitting D tensor for the two different Co(II) ions by *ab initio* calculations. The main results of the *ab initio* calculations for the lowest symmetry space group ($P2_1/n$) are shown in Table 25. In both Co(II) ions, the $s = 3/2$ ground state multiplet is split up in two doublet states separated by a large energy gap due to a large uniaxial D value. This D value is positive, indicating Z-plane magnetic anisotropy. In addition, although much smaller than the D value, the non-zero orthorhombic E value shows that there is also a relevant magnetic anisotropy on the easy plane.

Table 25. Uniaxial (D) and orthorhombic (E) anisotropy terms. Energy gap between the two lowest doublet states (energies are given in Kelvin units).

Ion	Energy gap (K)	D(K)	E(K)
Co(1)	293.9	144.1	8.0
Co(2)	294.3	144.7	8.0

In both Co(II) ions the hard axis is almost along a pseudo S_6 axis of the distorted octahedral environment around the Co(II) ions, pointing towards one formate molecule, whereas the easy axis is almost along the projection of one Co-O bond on the easy plane (see Figure 52). Here, it is interesting to remark that in the unit cell there are two Co(1) ions and two Co(2) ions. The symmetry operations relating the two Co(1) ions, or the two Co(2) ions, do not conserve the orientation of the main single-ion magnetic anisotropy axes, resulting in four different orientations of these axes in the unit cell, two for the Co(1) ions and two for the Co(2) ions.

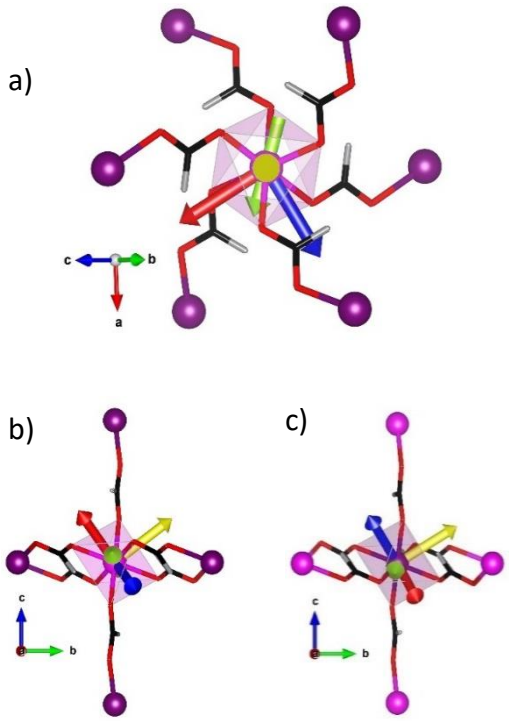

Figure 52: (a) View of the single-ion magnetic anisotropy axes seen along the pseudo S_6 axis of the distorted octahedral environment around the Co(1) ion. Hard axis (yellow), easy axis (red) and intermediate axis (blue). The refined magnetic moment has been represented in light green. (b-c) View of the superposition of the experimental model and the single-ion magnetic anisotropy axes for Co(1) and Co(2) ions along the crystallographic *a*-axis (in the $P2_1'/n'$ magnetic space group). Methylammonium molecules have not been included for the sake of clarity.

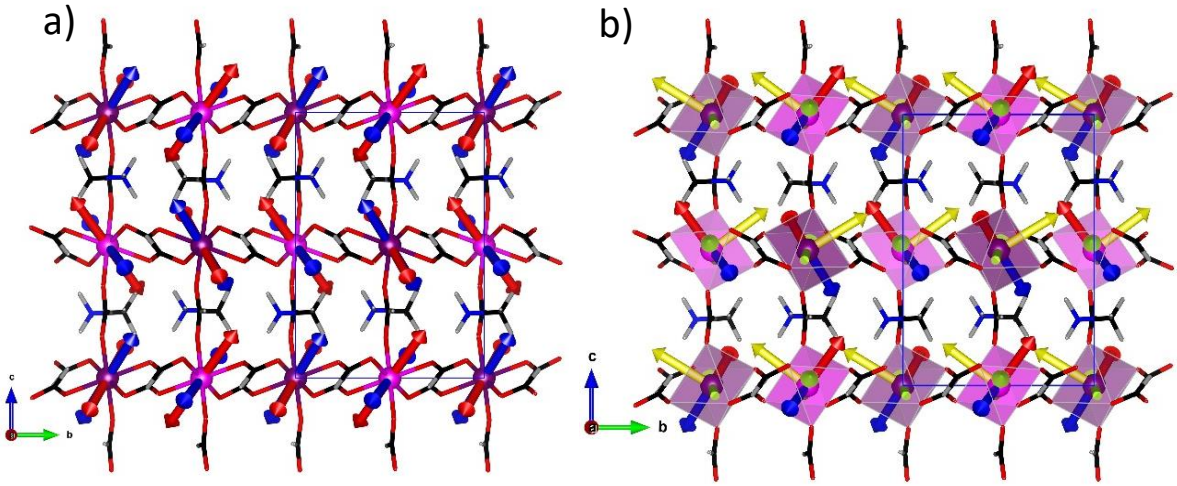

Figure 53. a) Easy (red) and intermediate (blue) single-ion magnetic anisotropy axes seen along the crystallographic *a*-axis. (b) Easy single-ion magnetic anisotropy axes for each Co(II) ion, pink for Co(1) and purple for Co(2). The direction of the arrow indicates the direction towards which the magnetic moment would deviate from an antiferromagnetic arrangement along the crystallographic *a*-axis. The calculated hard axis is represented in yellow, while the refined magnetic moments are represented in light-green.

The energies involved in the magnetic interactions must be of the same order of magnitude as the magnetic transition temperature (*ca.* 15 K). Therefore, due to the large uniaxial (D) magnetic anisotropy values, the magnetic moment of each Co(II) ion should almost lay on its easy magnetic anisotropy plane. A representation of these planes is given in Figure 53 a) where we show the easy magnetic anisotropy axis and the intermediate one for all the Co(II) ions in the unit cell, both of them defining the easy anisotropy plane. Although the four different easy planes are not coplanar, all of them almost contain the *a*-axis (*c*-axis in the orthorhombic phase). Therefore, in the case of no magnetic anisotropy in the easy magnetic plane (E = 0), the magnetic moments should be collinear along the *a*-axis and antiferromagnetically coupled. However, the non-zero magnetic anisotropy in the easy magnetic anisotropy plane (E = 8.0 K) would produce a deviation of the magnetic moments from the *a*-axis towards the easy magnetic anisotropy axis of each Co(II) ion. Taking into account the antiferromagnetic order along the *a*-axis, the previous deviation of the magnetic moment gives rise to a global non-compensated component along the *c*-axis (in the monoclinic space group) (see Figure 53 and Figure 54 b). Moreover, the magnetic components along the *b*-axis would be compensated resulting in a zero magnetic moment along that axis. Therefore, these results are in agreement with both, magnetometry measurements and the refined magnetic structures.

4.7.2.2 $[CH_3NH_3][Fe(COOH)_3]$ (8)

The Figure 54 shows the temperature evolution of the iron-based (**8**) compound, collected from 2 to 26 K and from 26 to 300 K (Figure 54). From RT to 26 K, only a slight shift of the reflections due to the thermal contraction is observed. At variance to the cobalt-based data, the intensity of the nuclear reflections is not significantly modified, suggesting that the counterion libration is much less important than in the previous case. Moreover, the abrupt change in the intensity at *ca.* 80 K, in the cobalt- compound, is not observed here. Therefore, we can discard the occurrence of a monoclinic phase at low temperature. A slight broadening of some reflections can be observed when the temperature decrease, which could be related with the incommensurability of this compound at low temperature. However, due to the large background and to the high hydrogen content, the satellite reflections are not visible.

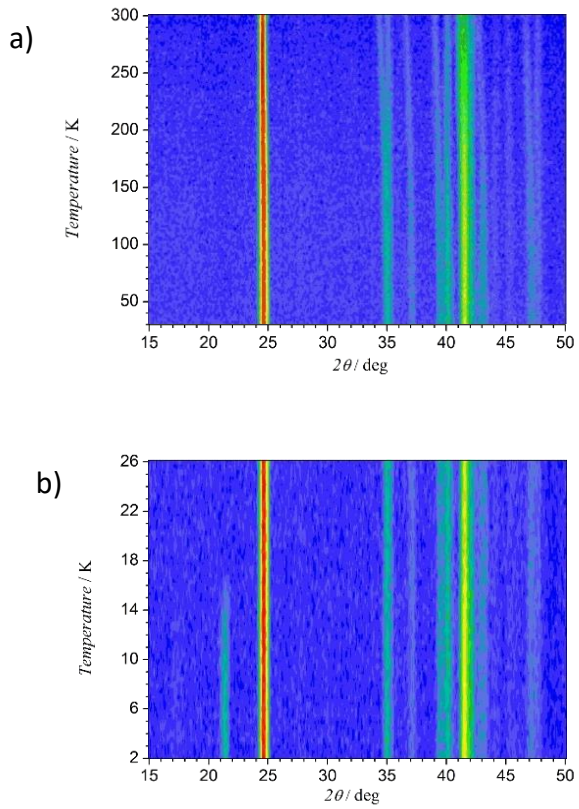

Figure 54: (a) Mesh plot of compound **8** (Fe-based) with the intensities represented in logarithmic scale, of the thermodiffractogram collected at D1B in the temperature range of 30−300 K. The figure shows the changes of intensities of the nuclear reflections from RT to the phase transition temperature at *ca.* 200 K. Below this temperature the orthorhombic phase become incommensurate. (b) Mesh plot of the thermodiffractogram in the temperature range of 2−26 K. The appearance of new reflections and the increase of intensity on the top of the nuclear reflections below 17 K, is in agreement with the reported T_N of this compound.

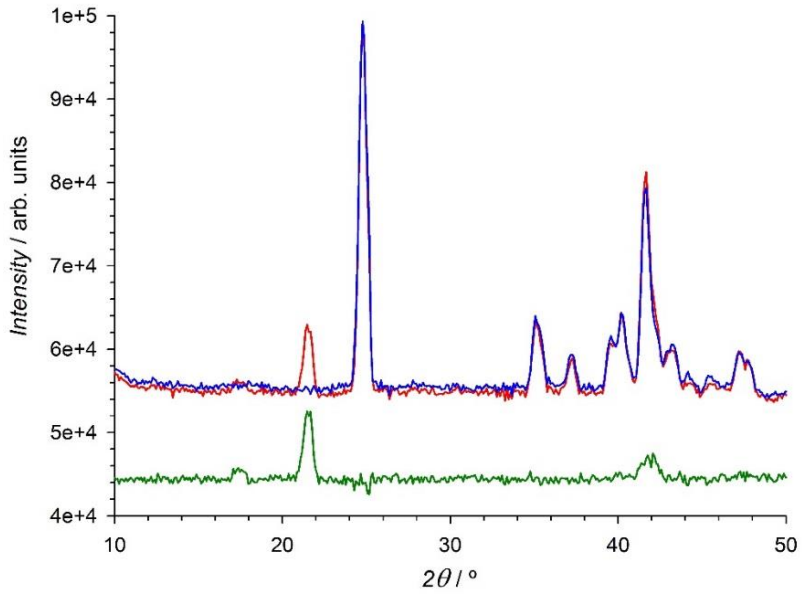

Figure 55: Neutron powder patterns of compound **8** (Fe-based) collected at 2 K (red) and 26 K (blue) using the high flux D1B diffractometer. The difference diffraction pattern has been represented as a solid green line.

The low temperature range from 26 to 2 K is shown in the Figure 54 b. In this thermodifractogram, the occurrence of new reflections is observed below 17 K, as in the previous case these reflections can be indexed with a **k** = (0, 0, 0) propagation vector. It was also confirmed with the indexing of the magnetic reflections using the program K-search included in the FullProf distribution. The strongest magnetic reflection, as in the compound **7**, corresponds to the (1 1 0) reflection, which is observed at 21.7 degrees (2θ). Although the difference pattern show the occurrence of three sets of magnetic reflections, located around the 2θ values of 17.5, 21.5 and 42.2 degrees. In order to work only with the magnetic contribution, the nuclear contribution has been subtracted from the low temperature pattern at 2 K (see Figure 55). Based on the previous described representational analysis, considering the *Pnma* as parent group the Fe(II) Wyckoff position (4*b* Wyckoff positon) and the propagation vector **k** = (0, 0, 0). We obtain the same four irreducible representations corresponding to the four Shubnikov magnetic groups; *Pnm'a', Pnma, Pn'm'a* and *Pn'ma'* (see Figure 48). The magnetometry measurements of compound **8** shows a global antiferromagnetic behaviour, but at difference to the cobalt-based compound no signal of ferromagnetism is observed in the iron-compound. Therefore, the four magnetic space groups are potential solutions. In order to discriminate among them, we have carried the fit of the data using the four magnetic space group. The refinement carried out in the *Pnm'a'* magnetic space group is not able to fit properly the magnetic reflections, in particular only the (1 0 0) reflection is well fitted using this model.

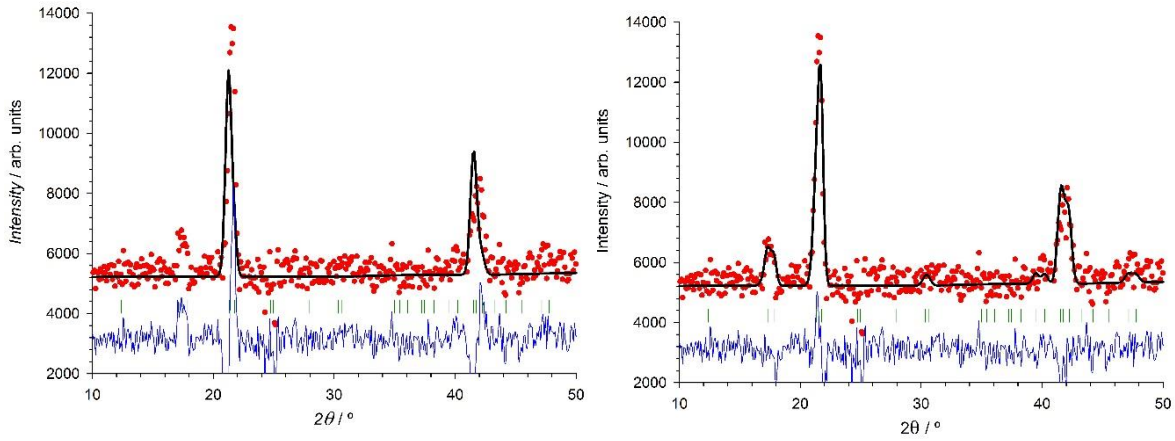

Figure 56*:* Fit of the difference pattern of compound **8** (Fe-based) in the *Pn'ma*' (left) and in the *Pnma* magnetic space group (right). Experimental data have been represented as red circles, calculated Rietveld patterns are shown as solid black lines, and difference between observed and calculated patterns have been plotted as solid blue lines. Vertical green marks represent the position of the Bragg reflections. The data refinement for the *Pnma* magnetic space group gives, R_B = 27.4% and R_F = 15.8%, as agreement factors.

Therefore it can be discarded. The *Pn'm'a* and *Pn'ma'* magnetic groups allows ferromagnetic component along the *c*-and and *b*-axes, respectively. However, if this component are fixed to zero both models can be considered as a possible magnetic space group. The fit carried out in the *Pn'm'a* Shubnikov group, presents a pure antiferromagnetic structure after fixing the component along the *c*-axis to zero, in agreement with the experimental data. The magnetic structure can be seen as an antiferromagnetic structure with the main component of the magnetic moments antiferromagnitcally coupled along the *b*-axis. The component along the *a*-axis produce a weak tilting of these magnetic moments which are also antiferromagnetically coupled along this axis. However, the R_f factor is slightly large, being above the 20 %. The fit using the *Pn'ma'* magnetic space group, gives rise to a good fit with the lowest R_f factor which is around the 15 % (but notice that the reflections with calculated zero intensities do not contribute to the R-factor). However, this model does not fit the first set magnetic reflections, corresponding to the (0 0 1) and (1 0 0) (see Figure 56). Moreover the value of the refined magnetic moments [*ca.* 3.6(1) μ_B] is slightly lower than that expected for a Fe(II) compound.The last magnetic model correspond to the *Pnma* (see Figure 56). It is the only space group that provide a global antiferromagnetic structure. For the refinement the component along the *c*-axis was fixed to zero.

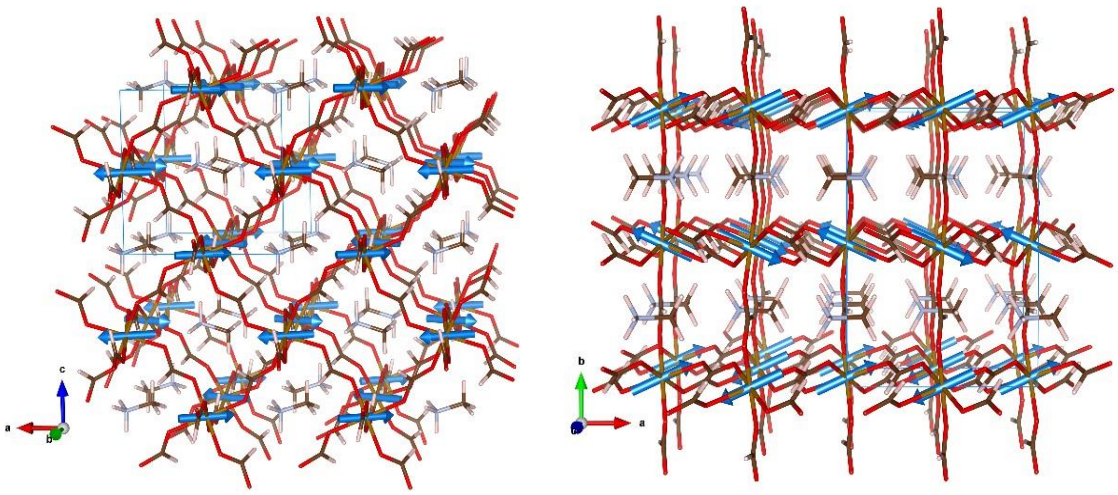

Figure 57: (left) Perspective view along the *b*-axis of the magnetic structure refined in the *Pnma* Shubnikov space group for compound **8** (Fe-based). (right) Perspective view along the *c*-axis. The crystal and magnetic unit cell [**k** = (0, 0, 0)], has been represented in blue and the magnetic moments in light blue. The nuclear structure has been represented using the same code of colours than in the previous figures, except for Fe ions that are represented in brown.

The magnetic structure can be described as antiferromagnetic layers, with the magnetic moments coupled antiferromagnetically mainly along the *a*-axis. The refined component along the *b*-axis produces a tilt of these magnetic moments outside the *ac*-plane, being by symmetry antiferromagnetically coupled (see Figure 57). This model reproduce well the full set of observations, and R_f = 16 % is close to that obtained with the *Pn'ma'* magnetic space group. The refined value of the magnetic moment [4.2(1) μ_B] that within the error is almost theoretical value for a high-spin Fe(II)-based compounds (s = 2). Therefore, among the four possible magnetic space groups we consider than the *Pnma* is the most plausible magnetic space group for this compound. The relatively high R-factors, even if the model is correct, is due to the noisy character of the patterns.

*4.7.2.3 $[CH_3NH_3][Ni(COOH)_3]$ (**9**)*

The temperature evolution of compound **9** in the range from 40−300 K is shows in see Figure 58 a. In this temperature range, only a slight shift of the reflections due to the thermal contraction is observed. Contrary to the cobalt-based data, the intensity of the nuclear reflections is not significantly modified, suggesting that the molecular libration is almost negligible. As in the iron-based compound (**8**) there not sign of structural phase transition, therefore the occurrence of a monoclinic phase at low temperature can be discarded, in good agreement with the X-ray diffraction data. Finally, due to the hydrogen content the incommensurability of this compound at low temperature is not visible.

In the low temperature range, from 40 to 2 K the thermodiffractogram shows (see Figure 58 b) the occurrence of new reflections. These can correspond to (1 1 0) or to (0 1 1) which are almost overlapped. The intensity increase of this reflections occurs around 34 K, which is in a good agreement with the magnetometry measurements, and therefore these reflections should have a magnetic character. The indexing of these magnetic reflections were carried out using the K-search program, giving rise to a **k** = (0, 0, 0) propagation vector, which is also in agreement with the other members of this series.

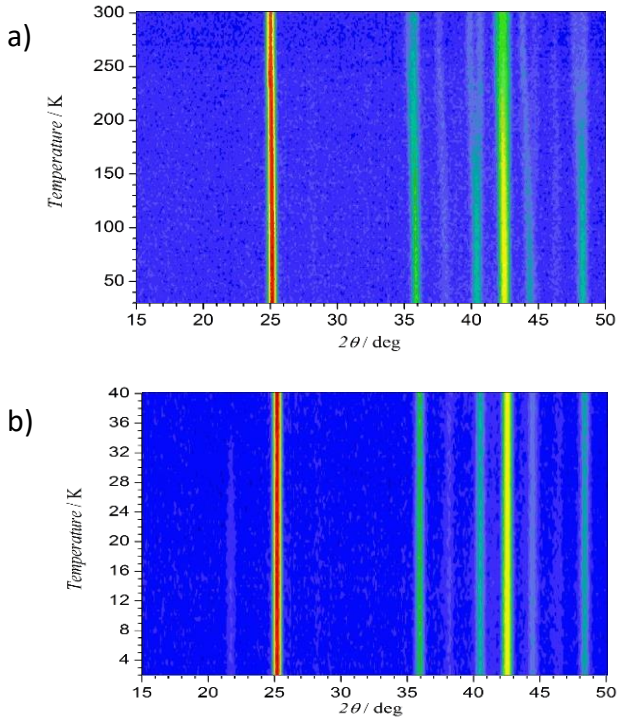

Figure 58: a) Mesh plot of compound **9**, with the intensities represented in logarithmic scale, of the thermodiffractogram collected at D1B in the temperature range of 40−300 K. The figure shows the changes of intensities of the nuclear reflections from RT to the phase transition temperature at *ca.* 200 K. Below this temperature the orthorhombic phase become incommensurate. b) Mesh plot of the thermodiffractogram in the temperature range of 2−40 K. The appearance of new reflections and the increase of intensity on the top of the nuclear reflections below 33 K, is in agreement with the reported T_N of this compound.

As in the previous case, the difference pattern, between ordered and paramagnetic, have been carried out to refine the possible magnetic structures. However, from the difference pattern, only one clear set of magnetic reflections are observed (see Figure 59). The low number of magnetic observations is in part related to the spin value of the Nickel(II) at high spin, which is $s = 1$, and therefore it have only two unpaired electrons. The susceptibly measurements of compound **9** are similar to the cobalt-based compound. In the full range of temperatures the magnetic interaction among the metal centres have an antiferromagnetic behaviour, with the occurrence of a ferromagnetic signal below T_N

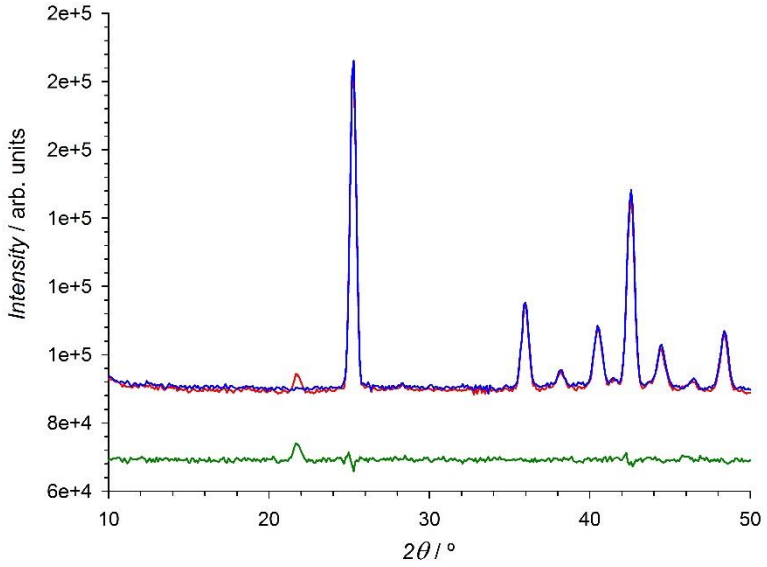

Figure 59: Neutron powder patterns of compound **9** (Ni-based) collected in the ordered phase at 2 K (red), and in the paramagnetic phases, at 40 K (blue). The difference pattern has been represented as a solid green line.

(see a detailed explanation in the previous section or in the ref.[49]. Therefore, as in the cobalt-based compound, those maximal space groups which preclude by symmetry the occurrence of a ferromagnetic component can be directly discarded as possible solution. In this particular case, the only that does not allow a ferromagnetic component is the *Pnma*, and can be excluded. Moreover the data refinement using this magnetic space group is not satisfactory. The other three maximal space groups, *Pnm'a', Pn'm'a* and *Pn'ma'* were refined against the experimental data. The *Pnm'a'* space group is not able to fit the experimental data and therefore was also discarded. Among the other two models, there are not significant differences, mainly due to the occurrence of a single set of observations. The refinement in the *Pn'm'a* give a magnetic structure with the magnetic moments along the *b*-axis, and antiferromagnetically coupled with all the adjacent neighbours. Although this model allow a ferromagnetic component along the *c*-axis, our data do not allow us to refine this component. The refined value of the magnetic moments using this model give rise to a value of 2.03(5) μ_B with a R_f factor of *ca.* 2 %. However, from the single crystal magnetometry measurements presented by Pato-Doldán et *al*.[49] we know that the easy axis in this compound is along the *b*-axis. That means that the ferromagnetic component, due to the spin canting should be along this axis. Therefore, this model, should be discarded even if the data refinement is in agreement with the model.

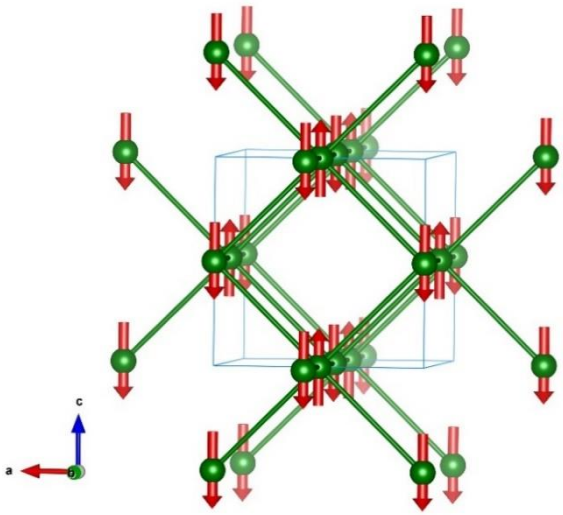

Figure 61: Perspective view along the *b*-axis of the magnetic structure refined in the *Pn'ma'* Shubnikov space group for compound **9**, where only the magnetic sites have been represented. The crystal and magnetic unit cell has been represented in blue, the nickel atoms in green and the magnetic moments as red arrows. The green bonds between nickels atoms are only a guide for the eye.

The fit carried out using the *Pn'ma'* magnetic group give rise to a magnetic structure, where the magnetic moments are along the *c*-axis, and as in the previous case, each magnetic moment is antiferromagnetically coupled with the adjacent ones (see Figure 60). This magnetic space group allows a ferromagnetic component along the *b*-axis, which is compatible with the previous magnetometry measurements. However, due to the low number of observations, this component has been fixed to zero. The refined value of the magnetic moments using this model give rise to a value of 2.04(5) μ_B with a R_f factor of *ca.* 2 % (see Figure 61).

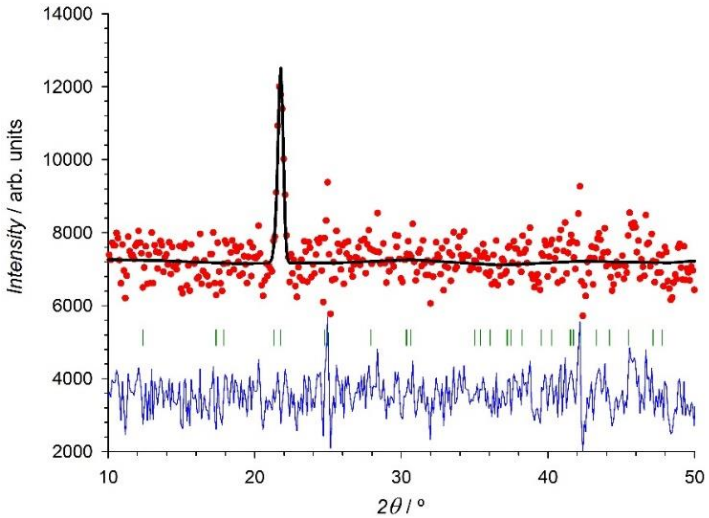

Figure 60: Fit of the difference pattern of compound **9** (Ni-Based) in the *Pn'ma*' magnetic space group. Experimental data have been represented as red circles, calculated Rietveld pattern is shown as a solid black line, and difference between observed and calculated patterns has been plotted as a solid blue line. Vertical green marks represent the position of the Bragg reflections. The data refinement gives, R_B = 3.05% and R_F = 1.87 %, as agreement factors.

4.7.2.4 $[CH_3NH_3][Mn(COOH)_3]$ (**10**)

The thermodiffractogram of compound **10** (see Figure 62) collected in the temperature range from 200 to 10 K, shows mainly the contraction of the cell parameters due to the thermal effect. As in the iron-based compound the intensity of the nuclear reflections is not significantly modified in this range of temperatures, suggesting that the counterion libration is much less important than in the Co-case. It deserves to be noted that iron- and manganese-based compounds do not present this increase of intensity while cobalt- and nickel-based compounds present this effect. Therefore, this can be related with the ionic radius of the metal transition, being 0.83, 0.78, 0.745, and 0.69 Å for Mn(II), Fe(II), Co(II) and Ni(II). Therefore, for values below 0.78 Å this effect is observed.

As in compounds **8** and **9**, the monoclinic phase is not observed. The symmetry analysis study will be carried out using the parent *Pnma* space group. Even considering that

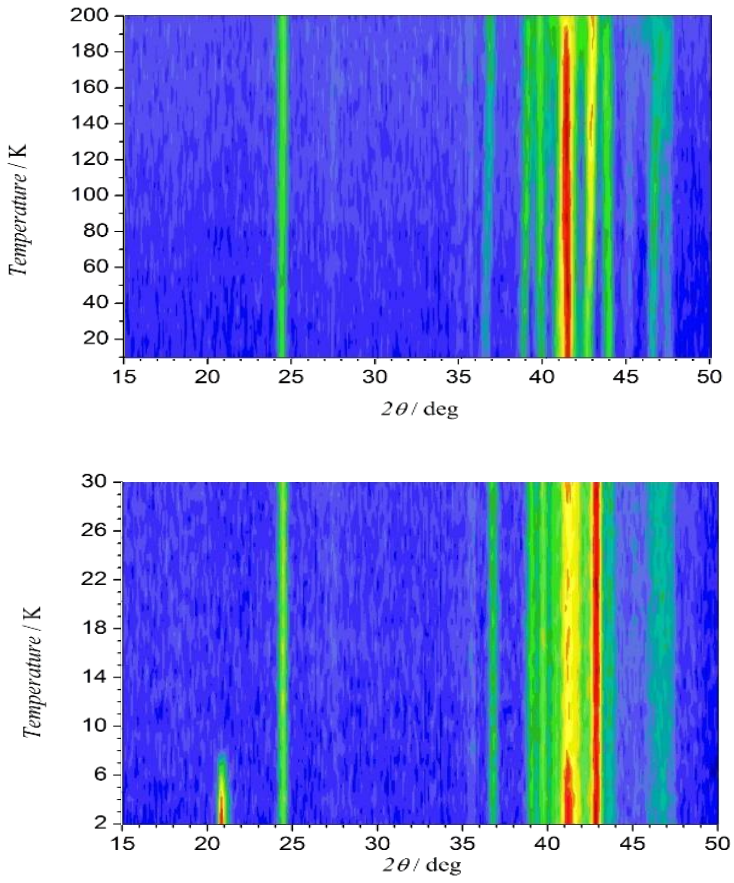

Figure 62: (a) Mesh plot of compound **10** (Mn-based), with the intensities represented in logarithmic scale, of the thermodiffractogram collected at D1B in the temperature range of 10−200 K. The figure shows the changes of intensities of the nuclear reflections from RT to the phase transition temperature at *ca.* 200 K. Below this temperature the orthorhombic phase become incommensurate. (b) Mesh plot of the thermodiffractogram in the temperature range of 2−30 K. The appearance of new reflections and the increase of intensity on the top of the nuclear reflections below 8 K, is in agreement with the reported T_N of this compound.

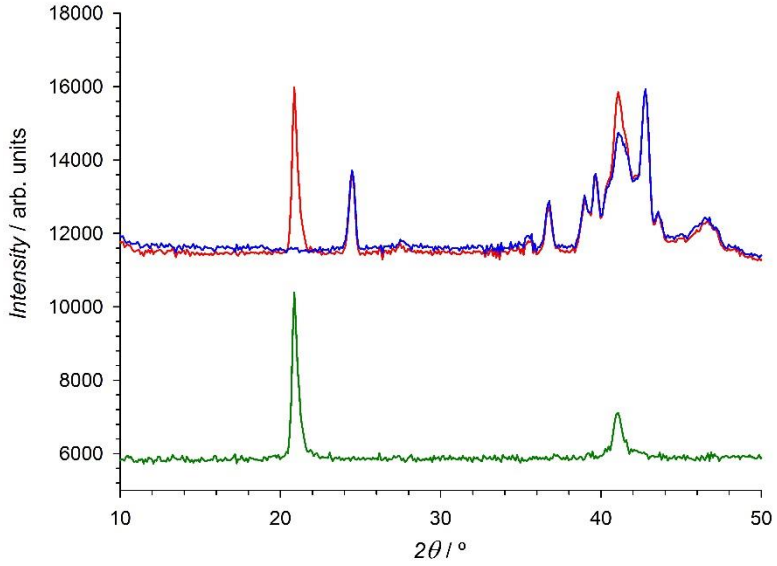

Figure 63: Neutron powder patterns of compound **10** (Mn-based) collected in the ordered phase at 2 K (red), and in the paramagnetic phases, at 30 K (blue). The difference pattern has been represented as a solid green line.

compound **10** remains incommensurate at low temperatures, the super-structure reflections are not visible in this neutron diffraction data, mainly due to the large hydrogen content and the weakness of the satellites. In the low temperature range, from 30 to 2 K, some new reflections are observed. As in the previous cases this reflections can be indexed with a **k** = (0, 0, 0) propagation vector. Two sets of magnetic reflection, at *ca.* 21.10 and 41.18 degrees, are observed. In order to eliminate the influence of the nuclear structure, the magnetic structure refinement has been carried out using the difference pattern. The difference pattern has been calculated subtracting the nuclear contribution, obtained for a long acquisition pattern at 30 K (in paramagnetic state), to the same pattern collected at 2 K with the same collection time, where the system is well below of T_N (see Figure 63). The macroscopic magnetic behaviour of compound **10** is similar to that of compound **8**. It shows a global antiferromagnetic behaviour without the occurrence of any ferromagnetic signal. Therefore, as in compound **8** the four magnetic space groups are potential solutions. The compound **10**, present a T_N around 8 K, which is in good agreement with the magnetometry measurements. Comparing the neutron diffraction data at 2 K between compound **8** and compound **10**, there is an important difference. In the iron-based compound (**8**), there was a weak set of magnetic reflections, corresponding to the (0 0 1) and (1 0 0), at low 2θ. The magnetic contribution on top of these reflections was used to discard the *Pn'ma'* space group. In this sample, the four magnetic space groups are possible, therefore hereafter we are going to describe the fit using each of these space groups.

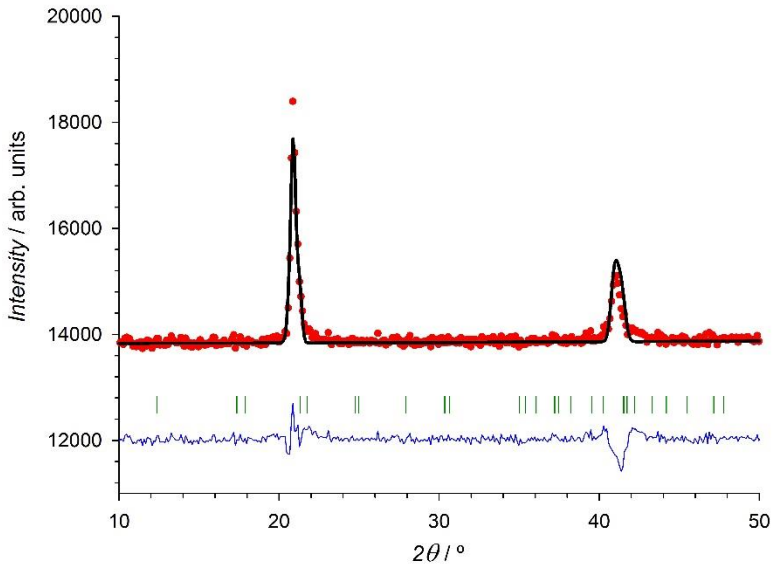

Figure 64: Fit of the difference pattern of compound **10** (Mn-based) in the *Pn'ma'* magnetic space group. Experimental data have been represented as red circles, calculated Rietveld pattern is shown as a solid black line, and difference between observed and calculated patterns has been plotted as a solid blue line. Vertical green marks represent the position of the Bragg reflections. The data refinement gives, R_B = 13.02% and R_F = 9.91 %, as agreement factors. It deserves to be noted that the (0 0 1) and (1 0 0) reflections are not illuminated differently than in compound **8**.

The refinement carried out in the *Pnm'a'* magnetic space group is far to fit the experimental data, and therefore it can be rejected as a possible solution. The *Pnma* space group is the only one which allow a pure antiferromagnetic structure based on symmetry, that means without apply any additional restriction. However, in this case, the refinement using this space group give a result which is also far to be acceptable, with a R_f above 30 %. Similar result is obtained if the *Pn'm'a* magnetic groups is used; moreover, in order to avoid a global ferromagnetic behaviour the component of the magnetic moment along the *c*-axis has been fixed to zero. The refined component of the magnetic moments using this Shubnikov space group give a value of 5.3(1) μ_B which is slightly high for a Mn(II)-based compound.

The last refinement was carried out in the *Pn'ma'* magnetic group (see Figure 64), which allows a ferromagnetic component along the *b*-axis. In order to be in agreement with the magnetometry measurements, this component was fixed to zero during the refinements. Moreover, the component along the *a*-axis, contribute mainly to the (1 1 1) reflection positioned at 27.59 degrees, where only noise coming from the background is observed. Based on that, the component of the magnetic moment along the *a*-axis has also been fixed to zero.

Therefore, the magnetic structure can be seen as a collinear antiferromagnetic structure where the magnetic moments are along the *c*-axis, and coupled antiferromagnetically

within the *ac*-plane and between adjacent planes along the *b*-axis (see Figure 65). The refined magnetic moments give a value of 5.1(1) μ_B which is almost the theoretical value for a s = 5/2. Therefore, at variance to the iron-based compound, this model reproduces well the experimental data giving an R_f factor of 9.9 %.

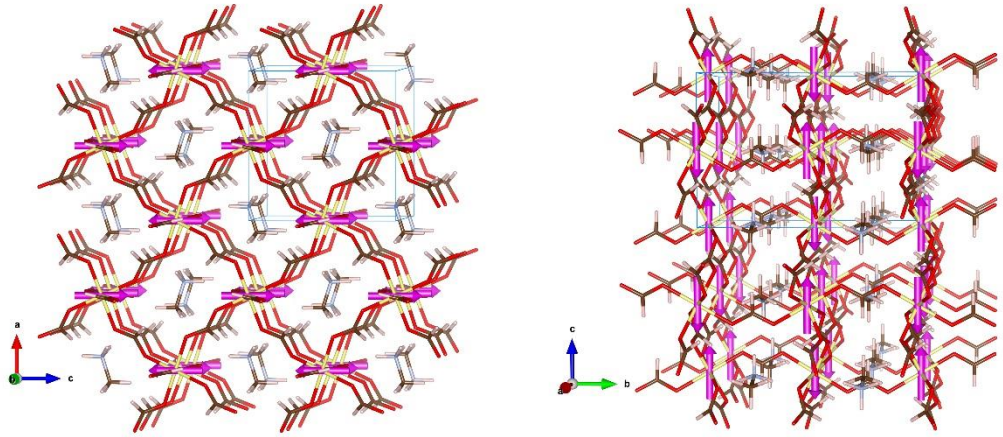

Figure 65: (Left) Perspective view along the *b*-axis of the magnetic structure refined in the *Pn'ma'* magnetic space group for compound **10** (Mn-based). (Right) Perspective view along the *a*-axis. The crystal unit cell, coincident with the magnetic unit cell because **k** = (0, 0, 0), has been represented in blue and the magnetic moments as pink arrows. The nuclear structure has been represented using the same code of colours than in the previous figures, except for Mn(II) ions that are represented in yellow.

4.7.3 Influence of the nuclear incommensurability on the magnetic structure

As it was described at the beginning of this section, the magnetic structures determined here above for compounds from **8** to **10**, have been obtained using the average nuclear structures. However, as it was described in the previous sections at low temperatures these compounds become incommensurables. Unfortunately, the superspace magnetic group formalism has not been included until now in the used refinement programs and the incommensurate satellites are too weak in the neutron powder patterns. In this last section, we are going to describe, based in the symmetry analysis, the influence of a nuclear modulation into the magnetic structure description.

In order to present a general overview of this subject, we are going to consider that at low temperatures, there is only one modulation vector (**q**), which means that the coexistence of different vectors will be considered as a mixture of several modulated structures with different modulation vectors, as was discussed in the 4.5 section.

Based on that, we can use the ISODISTORT suite (Version 6.3.5, June 2017) to evaluate the combination of displacive and magnetic distortions both together. In order to calculate the *irreps* to describe the full list of possible superspace magnetic groups. The calculation will be done using two independent modulation vectors, one related to the nuclear distortion and the second one related to the magnetic contribution. For the magnetic contribution **k**= (0, 0, 0), because all the magnetic signals are on top of nuclear reflections, in fact there is no magnetic signal on the top of the nuclear satellites. The second modulation vector is **q** = (0, 0, γ), which is characterizing the nuclear modulation. The γ parameter has the values described in the previous section 4.5.

Table 26. List of the possible super magnetic space groups compatible with the distortion modes obtained from considering **k** = (0, 0, 0) and **q** = (0, 0, γ) as modulation vectors for the magnetic and nuclear distortions, respectively.

	origin		origin
Pnma(0,0,γ)000,	(0,0,0,0)	*Pnma*(0,0, γ)0s0	(0,0,0,0)
Pmn2_1(0,0,γ)000,	(−1/4,1/4,0,0)	*Pmn*2_1(0,0, γ)s0s	(−1/4,1/4,0,0)
Pn'm'a(0,0,γ)000	(0,0,0,0)	*Pn'm'a*(0,0, γ)0s0	(0,0,0,0)
Pm'n'2_1(0,0, γ)000,	(−1/4,1/4,0,0)	*Pm'n'*2_1(0,0, γ)s0s	(−1/4,1/4,0,0)
Pnm'a'(0,0, γ)000	(0,0,0,0)	*Pnm'a'*(0,0, γ)0s0	(0,0,0,0)
Pm'n2_1'(0,0, γ)000	(−1/4,1/4,0,0)	*Pm'n*2_1'(0,0, γ)s0s	(−1/4,1/4,0,0)
Pn'ma'(0,0, γ)000	(0,0,0,0)	*Pn'ma'*(0,0, γ)0s0	(0,0,0,0)
Pmn'2_1'(0,0, γ)000,	(−1/4,1/4,0,0)	*Pmn'*2_1'(0,0, γ)s0s	(−1/4,1/4,0,0)
Pnma(0,0, γ)0s0,	(0,0,0,3/4)	*Pnma*(0,0, γ)000	(0,0,0,3/4)
Pmn2_1(0,0, γ)s0s	(−1/4,1/4,0,0)	*Pmn*2_1(0,0, γ)000	(−1/4,1/4,0,0)
Pn'm'a(0,0, γ)0s0,	(0,0,0,3/4)	*Pn'm'a*(0,0, γ)000	(0,0,0,3/4)
Pm'n'2_1(0,0, γ)s0s,	(−1/4,1/4,0,0)	*Pm'n'*2_1(0,0, γ)000	(−1/4,1/4,0,0)
Pnm'a'(0,0, γ)0s0,	(0,0,0,3/4)	*Pnm'a'*(0,0, γ)000	(0,0,0,3/4)
Pm'n2_1'(0,0, γ)s0s	(−1/4,1/4,0,0)	*Pm'n*2_1'(0,0, γ)000	(−1/4,1/4,0,0)
Pn'ma'(0,0, γ)0s0,	(0,0,0,3/4)	*Pn'ma'*(0,0, γ)000	(0,0,0,3/4)
Pmn'2_1'(0,0, γ)s0s	(−1/4,1/4,0,0)	*Pmn'*2_1'(0,0, γ)000	(−1/4,1/4,0,0

The choice of each particular *irrep* affects the symmetry of the atomic displacements (nuclear or magnetic). In this particular case, the combination of the different *irreps*, give rise to a list of 32 possible superspace magnetic groups (see Table 26).

Based on the refined magnetic space group for compound **8** to **10**, *Pnma* for compound **8** and *Pn'ma'* for compounds **9** and **10,** together with the obtained incommensurate superspace group, which was *Pnma*(0,0, γ)0s0. We can assume that the most probable

superspace magnetic groups are *Pnma*(0,0, γ)0s0 for compound **8** and *Pn'ma'*(0,0, γ)0s0 for compounds **9** and **10**. In order to see the influence of considering the nuclear incommensurability into the magnetic structure description, we describe below the different modes which are active is we consider the *Pn'ma'*(0,0, γ)0s0 as superspace magnetic group, which should be the one for compound **9** and **10**.

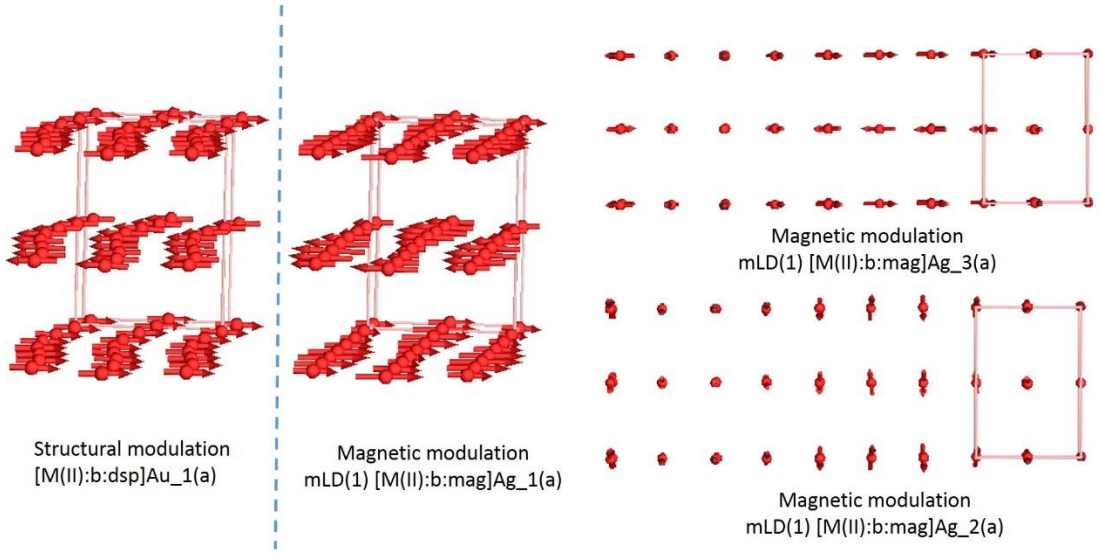

Figure 66: (left) View of the influence of one displacive modes to the metal centre considering the *Pnma* parent space group. (right) Detail of the three displacive magnetic modes for the same metal centre

In the *Pn'ma'*(0,0, γ)0s0 as superspace magnetic group, there are twelve free parameters, which are divided on displacive, magnetic, and strain modes. There are three strain models, each strain mode is a linear combination of the six strain components, and for our analysis these modes are affecting only positions of the Bragg peaks. Three other modes correspond to nuclear displacive modes. These modes, are able to reproduce the nuclear modulation, each mode represents a modulation along one direction (see Figure 66 left). With these three modes we can reproduce fully the paramagnetic incommensurate structure. Three additional modes are pure magnetic and allow to obtain the relative orientation and magnitude of the magnetic moments. If we consider only these modes, this is equivalent to the refinement of the magnetic moments in the average structure. Finally, there are also three other modes which takes into account the displacive effects into the magnetic sites. This last block, is not accessible at refining the average magnetic structure. In order to display these modes graphically, in the right part of the Figure 66 we can see the influence of one displacive nuclear mode and three displacive magnetic modes. For the sake of clarity we have represented only the metal centre.

It should be noted, that the influence of these magnetic modulation modes, are mainly observed in the change of intensity in the satellite reflections. However, in the neutron powder diffraction pattern presented in the previous sections these satellites are not distinguished from the background. In order to explore the influence of these modulation, we plan to carry out low temperature single crystal neutron diffraction experiments on the nickel-based compound, to accurately study the intensity of the satellites reflections above and below T_N.

Conclusion and discussion

The crystal structure analysis of compound **7** has revealed unreported phases transitions from *Pnma* space group at RT **7** (**I**) to $P2_1/n$ space group (non-standard setting of space group of $P2_1/c$) at low temperature **7** (**IV**). This transition takes place through two additional incommensurate phase transitions: one when the observed satellites are compatible with the modulation vector **q** = (0, 0, γ) with γ being very close to 1/7 (**III**) and the second one when **q** is close to 1/8 (**IV**). The sequence of transitions on cooling the single crystal is (RT)**I**→(*ca.* 128 K)**II**→(*ca.* 85 K)**III**→(*ca.* 78 K)**IV**.

The transition from RT to the lowest temperature involves slight changes in the orientation of the methylammonium counterions, which are weakly anchored into the cavities, as well as in the Co(II) octahedral environments. These modifications in the structure are associated with the occurrence of an electric phase transition from the paraelectric state to the antiferroelectric-like state. The studies carried out on powder samples show a notable mixture of orthorhombic and monoclinic phases, even at the lowest temperature (*ca.* 2K), differently to the single crystal case. Moreover, the broadening of some reflections after the structural transition denotes an important strain contribution certainly due to the presence of extended defects.

Compound **7** is quite sensitive to the temperature changes and also to the cooling or warming rate employed in the experiments. The weight fraction between the different phases at low temperature depends on the thermal history. The incommensurate phase, in the powder sample, can be maintained below 30 K much lower than the incommensurate-commensurate transition temperature observed in the single crystal studies. In the incommensurate phase there are also different phases, which can be stabilized by cooling or heating the sample. In some cases, both phases being coexistent. These phases evolve from one to another depending on the temperature; however, the narrow temperature range in which they appear, it makes difficult to separate them. At lower temperatures, the powder sample, evolves into a mixture of orthorhombic and monoclinic phases. The splitting of the reflection (1 2 1) of the orthorhombic phase in the doublet (−1 1 2) / (1 1 2) of the monoclinic phase is a clear indicator of this phase transition. The powder diffraction pattern of the monoclinic phase can be refined with the same model as that obtained from the single crystal data, where the mixture of phase has not been observed. While the small contribution of the orthorhombic phase, that remain

after the phase transition, is remarkably different from that refined at high temperature. The Rietveld refinement using a multiphase approach, is not good enough to validate the orthorhombic structure at low temperature.

Regarding the others members of this series, iron-based (**8**), nickel-based (**9**) and manganese-based (**10**) compounds, all of them display only one phase transition from the orthorhombic phase to the orthorhombic incommensurate phase, with different modulation vectors, keeping the latter phase down to the lowest temperature. It deserves to be noted that the monoclinic phase for these compounds, has not been detected neither in powder nor in single crystal for those of which single crystal measurements were carried out. The coexistence of different modulation vectors, in powder samples, has been observed for all members of this series, with the exception of the copper-based compound which does not present the incommensurate phase. As it has been discussed in the cobalt-based compound, the phase transitions of these compounds are weakly first-order or nearly second order, the coexistence of different phases can be explained by a sluggish transition where different part of the sample are transiting to different incommensurate structures. Although the temperature is the "trigger" parameter for the phase transition other parameters as particle size, crystallinity, strains, etc. are also involved. The competition among all these parameters, can produce that some regions of the bulk sample (powder sample) transit to the incommensurate phase with a particular wave vector while other regions do it with a different one. This is the most plausible scenario, however a second possibility is also imaginable. This second scenario, involve a multi-**q** incommensurate structure, where in order to reproduce the incommensurability more than one modulation vector is needed. However, from the single crystal data on the cobalt- and nickel-based compounds this scenario could not be confirmed.

Regarding the Cu-based compound (**11**), we observed the occurrence of a significant change in the lattice parameters, with respect to the others members of the series, which have been attributed to the Jahn-Teller effect of the copper ion. The only transformation detected, as function of the temperature, has been the thermal decomposition into the metallic copper, at above room temperatures. The temperature evolution of this decomposition as well as a possible mechanism of decomposition have been discussed along this chapter.

As decreasing the temperature all members of this series show a global antiferromagnetic behaviour, the compounds **7**, **8**, **9**, and **10** present a long-range magnetic order at about 15.7, 16.8, 33 and 8 K respectively. For compound **7** the ordering is characterized by the occurrence of a non-collinear antiferromagnetic structure where magnetic moments are not strictly compensated. Therefore, below 15 K this material shows the coexistence of an antiferroelectric-like behaviour originated from a structural phase transition, non-significantly coupled with the weak ferromagnetism arising from the non-compensation of the non-collinear antiferromagnetic structure of the metal-organic host framework. Even if weak ferromagnetism is commonly attributed to the Dzyaloshinskii-Moriya interaction, the *ab initio* calculations indicate that the single-ion anisotropy of Co(II) ions is the dominant term in this case. The magnetic reflections in the neutron measurements at 2 K are compatible with *Pn'ma'* and $P2_1'/n'$ magnetic models. The best refined models give rise to magnetic structures where the magnetic moments are antiferromagnetically coupled, with a small non-compensated component of the magnetic moment, in agreement with the *ab initio* calculations. Moreover, the obtained magnetic structures at zero-field are not compatible with the magneto-electric behaviour previously observed on this compound, therefore, in order to explain this magneto-electric behaviour the occurrence of a field-induced phase transition is needed. The magnetic structure determination under external magnetic field is needed to understand the origin of the magneto-electric coupling. The magnetometry measurements of compound **8**, shows that the system becomes antiferromagnetically ordered. The neutron diffraction data show that the magnetic structure corresponds with the *Pnma* magnetic space group. This magnetic space group is the only one which give rise to a global antiferromagnetic structure without adding non-symmetry constrains in the magnetic moments. The magnetic structure can be described as antiferromagnetic layers, with the magnetic moments coupled antiferromagnetically mainly along the *a*-axis. A small component along the *b*-axis is also present; however by symmetry this component is also antiferromagnetically coupled.

The magnetic structure of the compounds from **9** to **10** were solved in the *Pn'ma'* magnetic space group. The result of our measurements as shown in the magnetic studies section. The weak ferromagnetic interaction observed in compound **9**, in the magnetometry measurements cannot be derived from the neutron diffraction data because the contribution to the scattered intensity is too small. It deserves to be noticed that

compound **9** (nickel-based compound) produces a very small magnetic contribution to the diffraction pattern, mainly due to the low expected magnetic moment (s = 1) of less than 2 μ_B. Therefore, the refined magnetic model is the same that for the manganese-based compound (**10**), which does not show any ferromagnetic contribution in the magnetometry measurements. The best refined models give rise to a magnetic structure where the magnetic moments are coupled antiferromagnetically in a collinear structure along *c*-axis.

Bibliography

(1) Cheong, S.-W.; Mostovoy, M. *Nat. Mater.* **2007**, *6* (1), 13.
(2) Khomskii, D. *Phys. Online J.* **2009**, *2*, 20.
(3) Ramesh, R.; Spaldin, N. A. *Nat. Mater.* **2007**, *6* (1), 21.
(4) Ramesh, R. *Nature* **2009**, *461* (7268), 1218.
(5) Yaghi, O. M.; O'Keeffe, M.; Ockwig, N. W.; Chae, H. K.; Eddaoudi, M.; Kim, J. *Nature* **2003**, *423* (6941), 705.
(6) Zhou, H.-C. "Joe"; Kitagawa, S. *Chem. Soc. Rev.* **2014**, *43* (16), 5415.
(7) Spaldin, N. A.; Fiebig, M. *Science* **2005**, *309* (5733), 391.
(8) Kreisel, J.; Kenzelmann, M. 2009, pp 17–20.
(9) Thomson, R. I.; Jain, P.; Cheetham, A. K.; Carpenter, M. A. *Phys. Rev. B* **2012**, *86* (21), 214304.
(10) Liu, B.; Shang, R.; Hu, K.-L.; Wang, Z.-M.; Gao, S. *Inorg. Chem.* **2012**, *51* (24), 13363.
(11) Tan, J.-C.; Jain, P.; Cheetham, A. K. *Dalton Trans.* **2012**, *41* (14), 3949.
(12) Stroppa, A.; Barone, P.; Jain, P.; Perez-Mato, J. M.; Picozzi, S. *Adv. Mater.* **2013**, *25* (16), 2284.
(13) Stroppa, A.; Jain, P.; Barone, P.; Marsman, M.; Perez-Mato, J. M.; Cheetham, A. K.; Kroto, H. W.; Picozzi, S. *Angew. Chem. Int. Ed.* **2011**, *50* (26), 5847.
(14) Polyakov, A. O.; Arkenbout, A. H.; Baas, J.; Blake, G. R.; Meetsma, A.; Caretta, A.; van Loosdrecht, P. H. M.; Palstra, T. T. M. *Chem. Mater.* **2012**, *24* (1), 133.
(15) Guo, M.; Cai, H.-L.; Xiong, R.-G. *Inorg. Chem. Commun.* **2010**, *13* (12), 1590.
(16) Rogez, G.; Viart, N.; Drillon, M. *Angew. Chem. Int. Ed.* **2010**, *49* (11), 1921.
(17) Jain, P.; Ramachandran, V.; Clark, R. J.; Zhou, H. D.; Toby, B. H.; Dalal, N. S.; Kroto, H. W.; Cheetham, A. K. *J. Am. Chem. Soc.* **2009**, *131* (38), 13625.
(18) Fu, D.-W.; Zhang, W.; Cai, H.-L.; Zhang, Y.; Ge, J.-Z.; Xiong, R.-G.; Huang, S. D.; Nakamura, T. *Angew. Chem. Int. Ed.* **2011**, *50* (50), 11947.
(19) Chu, Y.-H.; Martin, L. W.; Holcomb, M. B.; Gajek, M.; Han, S.-J.; He, Q.; Balke, N.; Yang, C.-H.; Lee, D.; Hu, W.; Zhan, Q.; Yang, P.-L.; Fraile-Rodríguez, A.; Scholl, A.; Wang, S. X.; Ramesh, R. *Nat. Mater.* **2008**, *7* (6), 478.
(20) Jain, P.; Ramachandran, V.; Clark, R. J.; Zhou, H. D.; Toby, B. H.; Dalal, N. S.; Kroto, H. W.; Cheetham, A. K. *J. Am. Chem. Soc.* **2009**, *131* (38), 13625.
(21) Pardo, E.; Train, C.; Liu, H.; Chamoreau, L.-M.; Dkhil, B.; Boubekeur, K.; Lloret, F.; Nakatani, K.; Tokoro, H.; Ohkoshi, S.; Verdaguer, M. *Angew. Chem. Int. Ed.* **2012**, *51* (33), 8356.
(22) Xu, W.-J.; Du, Z.-Y.; Zhang, W.-X.; Chen, X.-M. *CrystEngComm* **2016**, *18* (41), 7915.
(23) Gómez-Aguirre, L. C.; Pato-Doldán, B.; Stroppa, A.; Yáñez-Vilar, S.; Bayarjargal, L.; Winkler, B.; Castro-García, S.; Mira, J.; Sánchez-Andújar, M.; Señarís-Rodríguez, M. A. *Inorg. Chem.* **2015**, *54* (5), 2109.
(24) Mączka, M.; Ciupa, A.; Gągor, A.; Sieradzki, A.; Pikul, A.; Macalik, B.; Drozd, M. *Inorg. Chem.* **2014**, *53* (10), 5260.
(25) Mączka, M.; Gągor, A.; Macalik, B.; Pikul, A.; Ptak, M.; Hanuza, J. *Inorg. Chem.* **2014**, *53* (1), 457.
(26) Shang, M.; Zhang, C.; Zhang, T.; Yuan, L.; Ge, L.; Yuan, H.; Feng, S. *Appl. Phys. Lett.* **2013**, *102* (6), 062903.
(27) Van Aken, B. B.; Palstra, T. T. M.; Filippetti, A.; Spaldin, N. A. *Nat. Mater.* **2004**, *3* (3), 164.
(28) Vrejoiu, I.; Alexe, M.; Hesse, D.; Gösele, U. *Adv. Funct. Mater.* **2008**, *18* (24), 3892.

(29) Rout, D.; Moon, K.-S.; Kang, S.-J. L. *J. Raman Spectrosc.* **2009**, *40* (6), 618.
(30) Khomchenko, V. A.; Paixão, J. A.; Costa, B. F. O.; Karpinsky, D. V.; Kholkin, A. L.; Troyanchuk, I. O.; Shvartsman, V. V.; Borisov, P.; Kleemann, W. *Cryst. Res. Technol.* **2011**, *46* (3), 238.
(31) Catalan, G.; Scott, J. F. *Adv. Mater.* **2009**, *21* (24), 2463.
(32) Lebeugle, D.; Colson, D.; Forget, A.; Viret, M.; Bataille, A. M.; Gukasov, A. *Phys. Rev. Lett.* **2008**, *100* (22), 227602.
(33) Van Aken, B. B.; Palstra, T. T. M.; Filippetti, A.; Spaldin, N. A. *Nat. Mater.* **2004**, *3* (3), 164.
(34) Kenzelmann, M.; Harris, A. B.; Jonas, S.; Broholm, C.; Schefer, J.; Kim, S. B.; Zhang, C. L.; Cheong, S.-W.; Vajk, O. P.; Lynn, J. W. *Phys. Rev. Lett.* **2005**, *95* (8), 087206.
(35) Jain, P.; Dalal, N. S.; Toby, B. H.; Kroto, H. W.; Cheetham, A. K. *J. Am. Chem. Soc.* **2008**, *130* (32), 10450.
(36) Saparov, B.; Mitzi, D. B. *Chem. Rev.* **2016**, *116* (7), 4558.
(37) Entley, W. R.; Girolami, G. S. *Inorg. Chem.* **1994**, *33* (23), 5165.
(38) Sato, O.; Iyoda, T.; Fujishima, A.; Hashimoto, K. *Science* **1996**, *271* (5245), 49.
(39) Ferlay, S.; Mallah, T.; Ouahès, R.; Veillet, P.; Verdaguer, M. *Nature* **1995**, *378* (6558), 701.
(40) Ferlay, S.; Mallah, T.; Ouahès, R.; Veillet, P.; Verdaguer, M. *Inorg. Chem.* **1999**, *38* (2), 229.
(41) Dong, W.; Zhu, L.-N.; Song, H.-B.; Liao, D.-Z.; Jiang, Z.-H.; Yan, S.-P.; Cheng, P.; Gao, S. *Inorg. Chem.* **2004**, *43* (8), 2465.
(42) Wang, Z.; Zhang, B.; Inoue, K.; Fujiwara, H.; Otsuka, T.; Kobayashi, H.; Kurmoo, M. *Inorg. Chem.* **2007**, *46* (2), 437.
(43) Xu, G.-C.; Zhang, W.; Ma, X.-M.; Chen, Y.-H.; Zhang, L.; Cai, H.-L.; Wang, Z.-M.; Xiong, R.-G.; Gao, S. *J. Am. Chem. Soc.* **2011**, *133* (38), 14948.
(44) Cañadillas-Delgado, L.; Fabelo, O.; Rodríguez-Velamazán, J. A.; Lemée-Cailleau, M.-H.; Mason, S. A.; Pardo, E.; Lloret, F.; Zhao, J.-P.; Bu, X.-H.; Simonet, V.; Colin, C. V.; Rodríguez-Carvajal, J. *J. Am. Chem. Soc.* **2012**, *134* (48), 19772.
(45) Mączka, M.; Ciupa, A.; Gągor, A.; Sieradzki, A.; Pikul, A.; Ptak, M. *J. Mater. Chem. C* **2016**, *4* (6), 1186.
(46) Boča, M.; Svoboda, I.; Renz, F.; Fuess, H. *Acta Crystallogr. C* **2004**, *60* (12), m631.
(47) Gómez-Aguirre, L. C.; Pato-Doldán, B.; Mira, J.; Castro-García, S.; Señarís-Rodríguez, M. A.; Sánchez-Andújar, M.; Singleton, J.; Zapf, V. S. *J. Am. Chem. Soc.* **2016**, *138* (4), 1122.
(48) Mazzuca, L.; Canadillas-Delgado, L.; Fabelo, O.; Rodriguez-Velamazan, J. A. berto; Luzon, J.; Vallcorba, O.; Simonet, V.; Colin, C. V.; Rodriguez-Carvajal, J. *Chem. – Eur. J.* n/a.
(49) Pato-Doldán, B.; Gómez-Aguirre, L. C.; Hansen, A. P.; Mira, J.; Castro-García, S.; Sánchez-Andújar, M.; Señarís-Rodríguez, M. A.; Zapf, V. S.; Singleton, J. *J. Mater. Chem. C* **2016**, *4* (47), 11164.
(50) Rodríguez-Carvajal, J. *Phys. B Condens. Matter* **1993**, *192* (1), 55.
(51) Agilent Technologies UK Ltd. Agilent, CrysAlis PRO.
(52) Sheldrick, G. M. *Acta Crystallogr. Sect. C Struct. Chem.* **2015**, *71* (1), 3.
(53) Nardelli, M. *J. Appl. Crystallogr.* **1995**, *28* (5), 659.
(54) Spek, A. L. *J. Appl. Crystallogr.* **2003**, *36* (1), 7.
(55) Brandenburg & H. Putz. DIAMOND 2.1d, Crystal Impact GbR, CRYSTAL IMPACT, K.

(56) Pinheiro, C. B.; Abakumov, A. M. *IUCrJ* **2015**, *2* (1), 137.
(57) Petříček, V.; Dušek, M.; Palatinus, L. *Z. Für Krist. - Cryst. Mater.* **2014**, *229* (5), 345.
(58) Jongh, L. J. de; Miedema, A. R. *Adv. Phys.* **1974**, *23* (1), 1.
(59) L.J. de Jongh. *Magnetic Properties of Layered Transition Metal Compounds*; Springer, 1990.
(60) Stiefel, E. I.; Brown, G. F. *Inorg. Chem.* **1972**, *11* (2), 434.
(61) Altomare, A.; Cuocci, C.; Giacovazzo, C.; Moliterni, A.; Rizzi, R.; Corriero, N.; Falcicchio, A. *J. Appl. Crystallogr.* **2013**, *46* (4), 1231.
(62) Yabuki, A.; Arriffin, N.; Yanase, M. *Thin Solid Films* **2011**, *519* (19), 6530.
(63) Kim, S. J.; Lee, J.; Choi, Y.-H.; Yeon, D.-H.; Byun, Y. *Thin Solid Films* **2012**, *520* (7), 2731.
(64) Yabuki, A.; Arriffin, N. *Thin Solid Films* **2010**, *518* (23), 7033.
(65) Rozenberg, G. G.; Bresler, E.; Speakman, S. P.; Jeynes, C.; Steinke, J. H. G. *Appl. Phys. Lett.* **2002**, *81* (27), 5249.
(66) Park, B. K.; Kim, D.; Jeong, S.; Moon, J.; Kim, J. S. *Thin Solid Films* **2007**, *515* (19), 7706.
(67) Paquet, C.; Lacelle, T.; Deore, B.; J. Kell, A.; Liu, X.; Korobkov, I.; L. Malenfant, P. R. *Chem. Commun.* **2016**, *52* (12), 2605.
(68) Wang, Z.; Zhang, B.; Otsuka, T.; Inoue, K.; Kobayashi, H.; Kurmoo, M. *Dalton Trans.* **2004**, *0* (15), 2209.
(69) Spencer, E. C.; Kiran, M. S. R. N.; Li, W.; Ramamurty, U.; Ross, N. L.; Cheetham, A. K. *Angew. Chem.* **2014**, *126* (22), 5689.
(70) Li, W.; Probert, M. R.; Kosa, M.; Bennett, T. D.; Thirumurugan, A.; Burwood, R. P.; Parinello, M.; Howard, J. A. K.; Cheetham, A. K. *J. Am. Chem. Soc.* **2012**, *134* (29), 11940.
(71) Li, W.; Thirumurugan, A.; Barton, P. T.; Lin, Z.; Henke, S.; Yeung, H. H.-M.; Wharmby, M. T.; Bithell, E. G.; Howard, C. J.; Cheetham, A. K. *J. Am. Chem. Soc.* **2014**, *136* (22), 7801.
(72) Sánchez-Andújar, M.; Presedo, S.; Yáñez-Vilar, S.; Castro-García, S.; Shamir, J.; Señarís-Rodríguez, M. A. *Inorg. Chem.* **2010**, *49* (4), 1510.
(73) Shang, R.; Xu, G.-C.; Wang, Z.-M.; Gao, S. *Chem. – Eur. J.* **2014**, *20* (4), 1146.
(74) Chen, S.; Shang, R.; Hu, K.-L.; Wang, Z.-M.; Gao, S. *Inorg. Chem. Front.* **2014**, *1* (1), 83.
(75) Li, M.-Y.; Kurmoo, M.; Wang, Z.-M.; Gao, S. *Chem. – Asian J.* **2011**, *6* (11), 3084.
(76) Baldinozzi, G.; Calvarin, G.; Sciau, P.; Grebille, D.; Suard, E. *Acta Crystallogr. B* **2000**, *56* (4), 570.
(77) Baldinozzi, G.; Grebille, D.; Sciau, P.; Kiat, J.-M.; Moret, J.; Bérar, J.-F. *J. Phys. Condens. Matter* **1998**, *10* (29), 6461.
(78) Tamura, H. *Ferroelectrics* **1978**, *21* (1), 449.
(79) Patel, K.; Prosandeev, S.; Yang, Y.; Xu, B.; Íñiguez, J.; Bellaiche, L. *Phys. Rev. B* **2016**, *94* (5), 054107.
(80) B-IncStrDB - The Bilbao Incommensurate Structures Database http://b-incstrdb.ehu.es/incstrdb/index.php (accessed Sep 24, 2017).
(81) Aroyo, M. I.; Capillas, C.; Wondratschek, H.; J. M. Perez-Mato. *Acta Crystallogr. Sect.* **2006**, *A62*, 115.
(82) Yangui, A.; Pillet, S.; Mlayah, A.; Lusson, A.; Bouchez, G.; Triki, S.; Abid, Y.; Boukheddaden, K. *J. Chem. Phys.* **2015**, *143* (22), 224201.
(83) Elcoro, L.; Perez-Mato, J. M.; Friese, K.; Petříček, V.; Balić-Žunić, T.; Olsen, L. A. *Acta Crystallogr. B* **2008**, *64* (6), 684.

(84) Jona, F.; Shirane, G.; Mazzi, F.; Pepinsky, R. *Phys. Rev.* **1957**, *105* (3), 849.
(85) Palatinus, L.; Chapuis, G. *J. Appl. Crystallogr.* **2007**, *40* (4), 786.
(86) Wagner, T.; Schönleber, A. *Acta Crystallogr. B* **2009**, *65* (Pt 3), 249.
(87) Li, M.; Liu, B.; Wang, B.; Wang, Z.; Gao, S.; Kurmoo, M. *Dalton Trans.* **2011**, *40* (22), 6038.

Chapter 5
$[NH_4][Mn(HCOO)_3]$ compound

Introduction

The subject of this last chapter is the crystal and magnetic characterization of $[NH_4][Mn(HCOO)_3]$ compound **12** by neutron diffraction techniques. The synthesis, the X-Ray crystallographic studies, including IR, UV-Vis and the macroscopic magnetic properties of $[NH_4][M(HCOO)_3]$ with (M= Mn, Co, Ni,) were firstly reported by Wang *et al.*[1] and successively followed by the publication of Xu *et al*[2,3] which added to the literature on this compound and its series. The discovery of the coexistence of the magnetic and electric ordering in the $[NH_4][M(HCOO)_3]$ series [M= Mn(II), Fe(II), Co(II), Ni(II) and Zn(II)] of compounds. In this scenario, the approach planned by us, was to provide, by using the high sensitivity of neutron diffraction techniques, a complete study on the crystallographic and magnetic properties of the compounds belonging to this family, up to that moment unexplored by neutron. Lawler *et al.*[4] published, anticipating our objective, an interesting article including the neutron powder diffraction studies on the series [M= Mn(II), Fe(II), Co(II) and Ni(II)] where all the compounds, excepting that of iron-based, were synthetized by using perdeuterated reagents. Compound **12** as well as the others three members of this family, have a magnetic structure exhibiting antiferromagnetic coupling between adjacent metal centres, which are bridged by formate ligands. Nonetheless, here I report our results obtained from the data recorded exclusively for the manganese-based compound (**12**), and I compare it with the results reported on the same compound by Lawler *et al.*[4] using it as the principal reference.

5.1 Overview

The $[NH_4][M(HCOO)_3]$ family possess inorganic-organic components which characterize it as a metal-organic framework. This hybrid nature offers a good potential for the applicability of many different properties and functionalities[5–10]. This series of compounds can be identified as MOF with hexagonal ABX_3 (where A is a large cation, B is a transition metal and X is an organic ligand) structure characterized as a multiferroic compound due to changes into the hydrogen bond newtwork[11,12]. The framework adopted by the ABX_3 family depends particularly on the overall size of the counterion employed in the synthesis[4,13–16]. For the synthesis of the $[NH_4][M(HCOO)_3]$ series the ammonium molecule, the smallest protonated amine,[17] was employed as counterion, giving rise to a

chiral structure. In others cases, the use of bigger amines such as $CH_3NH_3^+$, $(CH_3)_2NH_2^+$ etc., give rise to the typical perovskite architectures[14,18–20]. As it is shown below in the crystallographic section, the counterion NH_4^+ is located in the cavities of the framework and it can influence the topology of the crystal structure by introducing functionalities such as ferroelectricity in coexistence with long-range magnetic order[1]. All studied compounds[2,3,21,22] among this series show a paraelectric to ferroelectric phase transition generated by the order- disorder state of the NH_4^+ cation[1,2,4].

In order to better understand the trigonal disorder of the cation, the high sensitivity of neutron diffraction has been significant for obtaining a good refinement at the low temperature of the crystallographic structure, getting an accurate model including the hydrogen atoms positions.

Regarding the magnetic properties, the experimental data evidenced an antiferromagnetic ordering at 8 K for compound **12,** while the others members of the family show a weak ferromagnetism due the presence of a possible spin canting[1,4].

5.2 Experimental section

5.2.1 Synthesis

Compound **12** has been prepared using a slow diffusion method. On the bottom of a glass tube, 8 ml of a solution 0.8 M prepared by using formic acid neutralized by ammonia in methanol were introduced. 8 ml of a solution containing 0.8 g (0.4 mmol) of $MnCl_2{\cdot}4H_2O$ were carefully layered on top of the previous solution. After two days, pale pink single crystals were collected and washed with methanol (see Figure 1). The yield was 68% based on the manganese. The slow diffusion method permitted to obtain big pyramidal crystals. It is interesting to underline that using achiral reactives it has been possible to obtain a chiral product. In general, chiral molecules (due to their big volume) reduce the possibility to observe a long magnetic order because they dilute the coupling among the spins[1]. By the way, in this case being the ammonium small enough this behaviour is

Figure 1: View of the crystals grown in the mono-tube obtained by slow diffusion method.

equilibrated. If we compare this synthesis with the one used by Lawler *et al.*[21], water has been used as a solvent, in addition, excepting for the Fe-based compound, all powder samples were synthetized by using perdeuterated reagents. The Lawler *et al.*[21] method led to the formation of $Mn(HCOO)\cdot 2H_2O$ impurities, which has been not revealed in our case.

5.2.2 Single-crystal neutron experiments

The single-crystal measurements (D9) were carried out in a sample of 2 × 3 × 3 mm^3, approximately, which was mounted on a standard aluminium pin. The D9 instrument was equipped with a closed-cycle cryostat for low-temperature measurements. The instrument was operated in the four-circle configuration with a wavelength of 0.83220 Å for data collections at zero magnetic field at RT, 15 K (paramagnetic phase) and in the magnetically ordered phase (ca. 1.8 K). The data collections in D9 consist of ω-scans or ω-2θ scans. The program RACER[23] was used to integrate these scans and to correct them for the Lorentz factor. The crystal absorption corrections were made with the DATAP[24] program. The refinement of the crystal and magnetic structures was performed using the program FullProf[25]. Below are reported the experimental parameters and main crystallographic data for compound from **12**.

Formula	**$[NH_4][Mn(HCOO)_3]$**
Empirical Formula	C3H3 MnO6H4N
M_r (g·mol-1)	208.028
Temperature (K)	RT
λ(Å)	0.8322
Crystal system	Hexagonal
Space group (No.)	*$P6_322$* (No.182)
***a* (Å)**	7.28950 (10))
***b* (Å)**	7.28950 (10)
***c* (Å)**	8.39990 (3)
***V* (Å^3)**	386.545 (2)
Z	2
ρ_c (g·cm^{-3})	1.787
Meas. Reflections	704
Parameters/ restraints	27 / 0
Hydrogen treatment	Refined with constraints
Goodness of fit	1.5
R_B (%)	12.77
χ^2	1.18

5.2.3 FTIR-Measurements

Vibrational studies were carried out at room temperature. A list of the band assignments corresponding to the internal vibrations modes of **12** is given in Table 1. The infrared spectrum matches with the previously reported literature data[26] and it is shown in Figure 2. The fundamental internal vibrations of the NH_4^+ cation consist of a triplet, at the high frequencies, which corresponds to the antisymmetric stretching modes 3204, 2980, 2866 cm^{-1}. At 2751 cm^{-1} we observe the C─H in plane bending mode (rocking) while at 1557 cm^{-1} a strong band is descriptive of the antisymmetric stretching of the C─O bond of the $HCOO^-$ group. The bending mode of the NH_4^+ cation is shown at 1435 cm^{-1}. Another band related to the C─H in plane bending (rocking) is observed at 1385 cm^{-1} and at 1022 cm^{-1} as out of plane bending (wagging). The symmetric stretching of the C─O group appears at 1352 cm^{-1}. The O─C─O bending (scissoring) at 790 cm^{-1}.

Table 1: Vibration modes for compounds **12**

υ_{as} NH_4^+	3204 sh 2980 sh 2866 sh
ρ HCOO⁻	2751 w
υ_{as} **HCOO⁻**	1557 s
υ NH_4^+	1435m
ρ HCOO⁻	1385s
***υ* HCOO⁻**	1352s
ρ HCOO⁻	1022w
***δ* HCOO⁻**	790s

Key codes: *sh*: shoulder *w*: weak, *m*: medium, *s*: strong and **υ** stretching, *δ* bending, *ρ* rocking, and $\upsilon_{as/s}$ asymmetric/symmetric stretching.

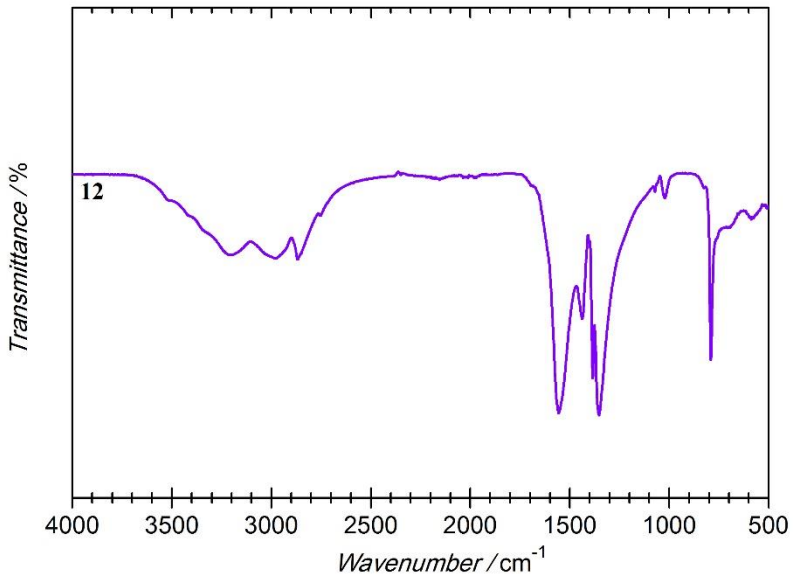

Figure 2: Infrared spectrum of compounds **12** recorded at room temperature.

5.3 Crystal structure description

The crystal structure of compound **12** previously reported[1,2,21,22,27] has been re-examined along this section. The structure of **12a** (HT) belongs to the hexagonal polar $P6_322$ space group[1,2,4,14], while at lower temperature (below 254 K), it undergoes a structural phase transition. The crystal structure can be solved in the $P6_3$ space group **12b** (LT), which is a subgroup of the high temperature phase.

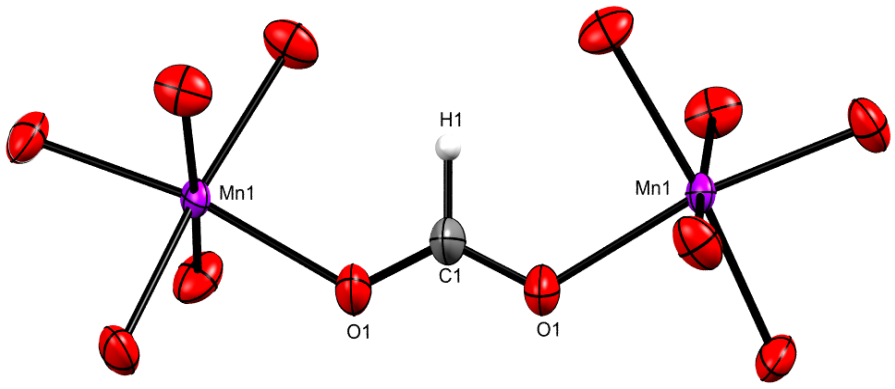

Figure 3: ORTEP- representation of a framework fragment of **12**, at high temperature, consisting of a MnO_6 octahedron bridged by a formate ligand in *anti-anti* conformation**.** Ellipsoids represent a presence probability of 50%.

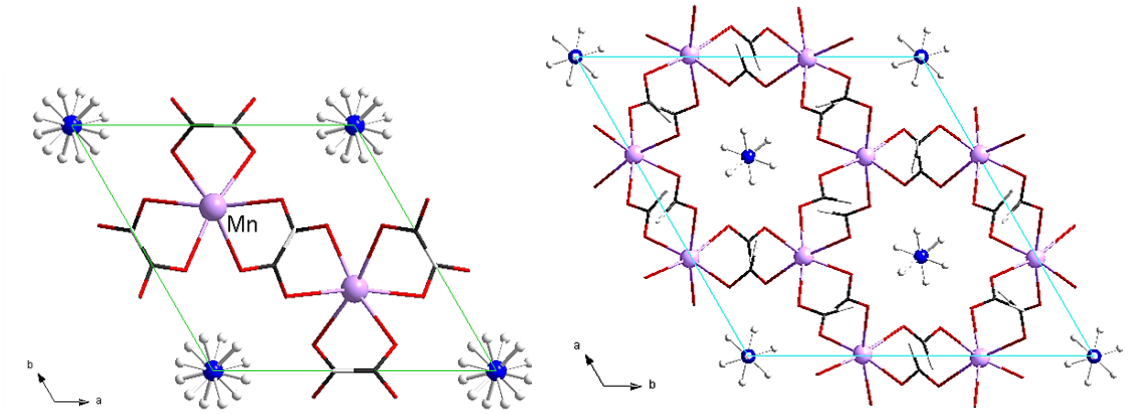

Figure 4*:* View of the crystal structure of **12**a (left) and **12**b (right) in the *ab*-plane. On the left, the HT structure in the $P6_322$ space group, on the right the LT structure in the space group $P6_3$. Note the NH_4^+ trigonal disorder (left) and the ordered array obtained once it transited to the polar crystal structure (right).

The structures consist of an anionic framework $[Mn(HCOO)_3]^-$ where the metal ions are hexa-coordinated and connected via the formate ligands in *anti-anti* mode (Figure 3). The 3-dimensional framework has a $4^9 \cdot 6^6$ topology[28,29] in Schäfli notation, and it consist of channels extended along the *c*-axis direction, which are occupied by the tetrahedral NH_4^+ molecules, showing a trigonal disorder at high temperature (see Figure 4). It is clear

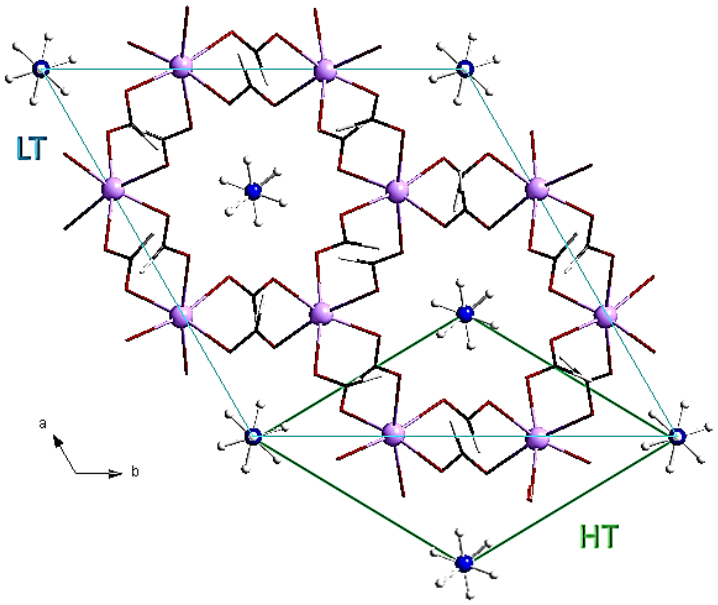

Figure 5: View of the structure for compound **12** along *c*-axis. Green and clear blue cell edges represent the unit cell at HT and LT respectively. The colour code used for the atoms is the following: pink, red, black, blue, white for manganese, oxygen, carbon, nitrogen, hydrogen respectively.

that the ammonium counterion not only balances the charge but also plays a templating role in the formation of this particular framework. At high temperature, the ammonium counterions are contained in the (0, 0, z) channel that after the transition becomes three distinct channels (0, 0, z); (2/3, 1/3, z); (1/3, 2/3, z) in the new cell (see Figure 5).

In fact, a visible change, from $P6_322$ to $P6_3$, it is the mild elongation of the *c*-axis at low temperature while $a'=(a-b)$, and the triplication of the cell volume $V^{LT} = 1175.8$ Å which is almost $3V^{HT}$ (see Table 5).

Moreover, at high temperature, the octahedral geometry of the metal has a distorted conformation probably because the lack of the inversion centre between metal sites due to the presence of the formate linker. Each coordination octahedron of metal ion has a different orientation from its six neighbours, (see Figure 3). The metal-oxygen equatorial and axial bond distances as well as selected distances and angles for both phases (HT and LT), can be consulted in Table 2 and Table 3. By observing the angles values it is easily appreciable the occurrence of the octahedra distortion (see the angles and distances reported in Table 2 and Table 3) at high and low temperature, see Figure 5.

The channels are characterized by a particular zig-zag/helical layout involving the M−O−C−O−M bonds, as shown in Figure 6 (top).

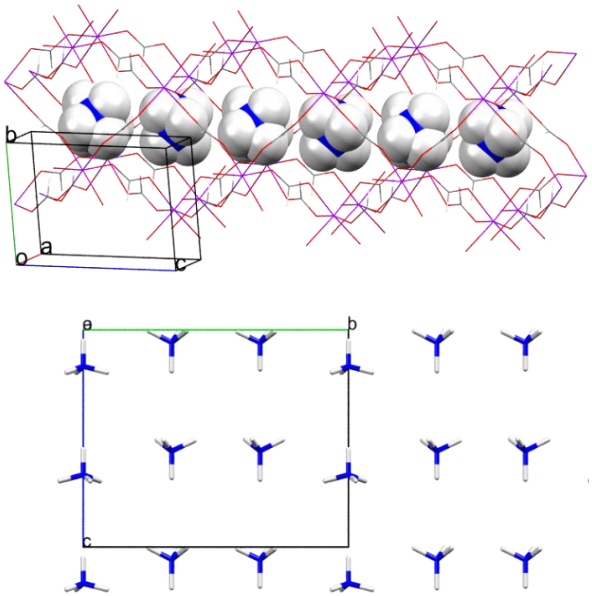

Figure 6: (Top) View of the disordered NH_4^+ cations (space-filling model) located in the helical channels, extended along *c*-axis, at the high temperature structure. (Bottom) View along *b*-axis for more clarity, of the ordered NH_4^+ cations in a capped stick model located in the helical channels, along *c*-axis, at low temperature. In this picture, the framework has been omitted from the figure for the sake of clarity.

Table 2: Selected distances (Å) for **12** from the refinement of data recorded at 290 K and 15 K using the neutron single crystal diffractometer D9.

290 K		**15 K**	
Mn−O1$^{(I)}$	2.164(4)	Mn−O1$^{(I)}$	2.18(4)
		Mn−O2$^{(II)}$	2.23(4)
		Mn−O3$^{(I)}$	2.22(3)
		Mn−O4$^{(III)}$	2.18(3)
		Mn−O5$^{(I)}$	2.17(3)
		Mn−O6$^{(IV)}$	2.15(3)
C−O1$^{(I)}$	1.224(3)	C1−O1$^{(I)}$	1.22(3)
		C1−O2$^{(I)}$	1.22(3)
		C2−O3$^{(I)}$	1.25(3)
		C2−O4$^{(I)}$	1.25(3)
		C3−O5$^{(I)}$	1.22(3)
		C3−O6$^{(I)}$	1.27(3)
C−H$^{(I)}$	1.047(10)	C1−H1$^{(I)}$	1.13(3)
		C2−H2$^{(I)}$	1.10(3)
		C3−H3$^{(I)}$	1.09(2)
		N1−H11$^{(I)}$	1.03(3)
N−H2$^{(I)}$	1.073(12)	N1−H12$^{(I)}$	1.03(5)
N−H2$^{(II)}$	1.070(14)	N2−H21$^{(I)}$	1.05(3)
N−H2 $^{(III)}$	1.071(12)	N2−H22$^{(I)}$	1.11(5)
		N3−H31$^{(I)}$	1.013(19)
		N3−H33$^{(I)}$	0.99(4)

Symmetry codes (structure at 290 K)

(I): *x*, *y*, *z*; (II): 1−*y*,2+*x*−*y*,*z*; (III): 1−*x*+*y*,1−*x*,*z*

Symmetry codes (structure at 15 K)

(I): *x*,*y*,*z*; (II*): x*−*y*,*x*,1/2+*z*; (III):1−*x*,1−*y*,1/2+*z*; (IV): *y*,−*x*+*y*,1/2+*z*

Table 3: Selected angles (°) for **12** from the refinement of data recorded at 290 K and 15 K using the neutron single crystal diffractometer D9.

290 K		15 K	
		O1−Mn−O3$^{(I)}$	90.4(13)
		O1−Mn−O4$^{(III)}$	83.1(12)
		O1−Mn−O5$^{(I)}$	90.5(13)
		O1−Mn−O6$^{(IV)}$	98.8(12)
***Cis*-O1−Mn−O**$^{(I)}$	82.35(12)	**O2**$^{(II)}$ **−Mn−O3**$^{(I)}$	80.0(11)
***Cis*-O1−Mn−O1**$^{(II)}$	96.77(11)	**O2**$^{(II)}$**−Mn−O4**$^{(III)}$	89.1(13)
***Cis*-O1−Mn−O** $^{(III)}$	90.89(12)	**O2**$^{(II)}$**−Mn−O5**$^{(I)}$	98.2(13)
		O2$^{(II)}$**−Mn−O6**$^{(IV)}$	91.6(14)
		O3 −Mn−O4$^{(III)}$	95.5(11)
		O3−Mn−O5$^{(III)}$	90.3(14)
		O4$^{(III)}$**−Mn−O6**$^{(IV)}$	90.4(14)
		O1−Mn−O2$^{(II)}$	167.0(13)
***Trans*-O1−Mn−O1**$^{(VI)}$	169.86(13)	**O3−Mn−O6**$^{(IV)}$	169.6(16)
		O4$^{(III)}$**−Mn−O5**	171.4(14)
		Mn−O1−C1$^{(I)}$	125.1(15)
		Mn$^{(V)}$**−O2−C1** $^{(I)}$	120.3(14)
Mn−O1−C$^{(V)}$	123.4(2)	**Mn−O3−C2**$^{(I)}$	123.5(13)
		Mn$^{(VI)}$ **−O4−C2**	122.8(14)
		Mn−O5−C3$^{(I)}$	119.7(12)
		Mn$^{(VII)}$ **−O6−C3**	126.8(12)
		O1−C−O2$^{(I)}$	127.7(18)
O1−C−O1$^{(VI)}$	127.3(3)	**O3−C−O4**$^{(I)}$	126.8(16)
		O5−C−O6$^{(I)}$	122.9(15)

Symmetry codes (structure at 290 K)

(I): 1−*y*,1−*x*,1/2−*z*; (II): *x*,1+*x*−*y*,1/2−*z*; (III): 1−*y*,1+*x*−*y*,*z*; (VI): −*x*+*y*,*y*,1/2−*z*; (V): *x*, *y*, *z*; (VI): −*x*,−*x*+*y*,−*z*.

Symmetry codes (structure at 15 K)

(I): *x*,*y*,*z*; (II*): x*−*y*,*x*,1/2+*z*; (III):1−*x*,1−*y*,1/2+*z*; (IV): *y*,−*x*+*y*,1/2+*z* (V): *y*,−*x*+*y*,−1/2+*z*, (VI): 1−*x*,1−*y*,−1/2+*z*; (VII): *x*−*y*,*x*,−1/2+*z*.

Xu et al.[2] carried out DSC (Figure 7) and dielectric measurements (with applied electric field parallel to the *c*-axis) in which they observed the structural phase transition at 254 K, attributed to the change from a paraelectric to ferroelectric phase, triggered by the occurrence of an order-disorder phase transition, involving mainly the hydrogen atoms of the counterion inside the channels.

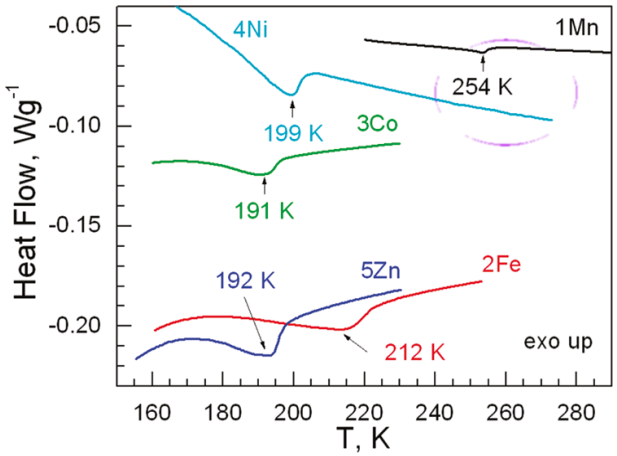

Figure 7: DSC measurements for compound **12,** published by *Xu et al.*[2]

Below the phase transition the compound **12** is ferroelectric in which an electric hysteresis can be displayed below the phase transition temperature, showing an increase of the polarization with decreasing temperature[2]. Moreover, the measured dielectric constant with the electric field parallel to *a*-axis, revealed a weaker response than that obtained with E // *c*. This measurement established that the preferred polarization direction is the *c*-axis with a high anisotropy character. This ferroelectric transition implies a symmetry breaking, resulting in a space group transformation from $P6_322$ (high temperature) to $P6_3$ (low temperature) as shown in Figure 4, as we hinted at the beginning.

Neutron diffraction experiments have been used to prove that the order-disorder phase transition is triggered by the change in the H-bond network at low temperature (Figure 8). Although the H-bond network is notably modified, the framework is slightly modified mainly due to slight distortions of the MO_6 octahedral. Therefore, after the ordering of ammonium counterions no radical structural effects are observed in the metal formate framework.

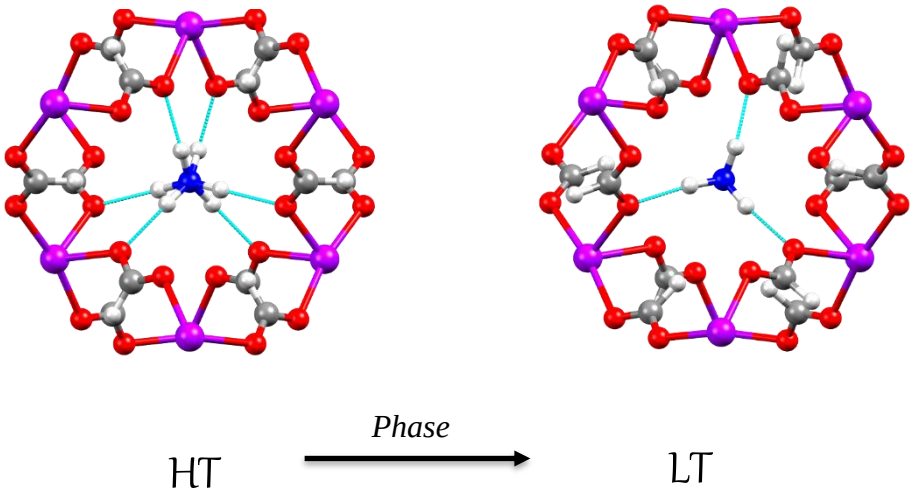

Figure 8*:* (Left), detailed view of the hydrogen bonds involving the trigonal disordered ammonium cation. (Right), view of the hydrogen bonds involving the ordered ammonium cation after the phase transition.

In fact the structural type of new phase is considered as a structural homotype when compared with the HT phase[22]. H-bonds occur between the cation NH_4^+ and the oxygen atoms of the formate framework. NH_4^+ acts as hydrogen bond-donor via the N−H groups while the oxygens of the formate act as acceptors. From the values shown in Table 4, it is possible to observe the shortening of the hydrogen bonds upon cooling, an aspect that favours the occurrence of the structural phase transition.

Table 4: Hydrogen bond distances and angles (Å and °, respectively) for **12** recorded at 290 K and at 15K

D	**H**	**A**	**D-H [Å]**	**H...A [Å]**	**D...A [Å]**	**D-H...A [°]**
			290K			
N1	H2	O1	1.073(12)	1.909(13)	2.947(3)	161.9(10)
			15K			
N1	H11	O1	1.03(3)	1.79(3)	2.811(18)	169(3)
N2	H21	O3	1.05(3)	1.81(3)	2.839(16)	166(3)
N3	H31	O6	1.013(19)	1.82(2)	2.835(15)	176(3)

In addition, at low temperature, the NH_4^+ shows small displacements along the *c*-axis with respect to the high temperature positions, which should be at the origin of the polarization occurring in the material. Due to the occurrence of a group-subgroup phase transition, the crystal used should became in a multi-domain crystal due to the appearance of twins.

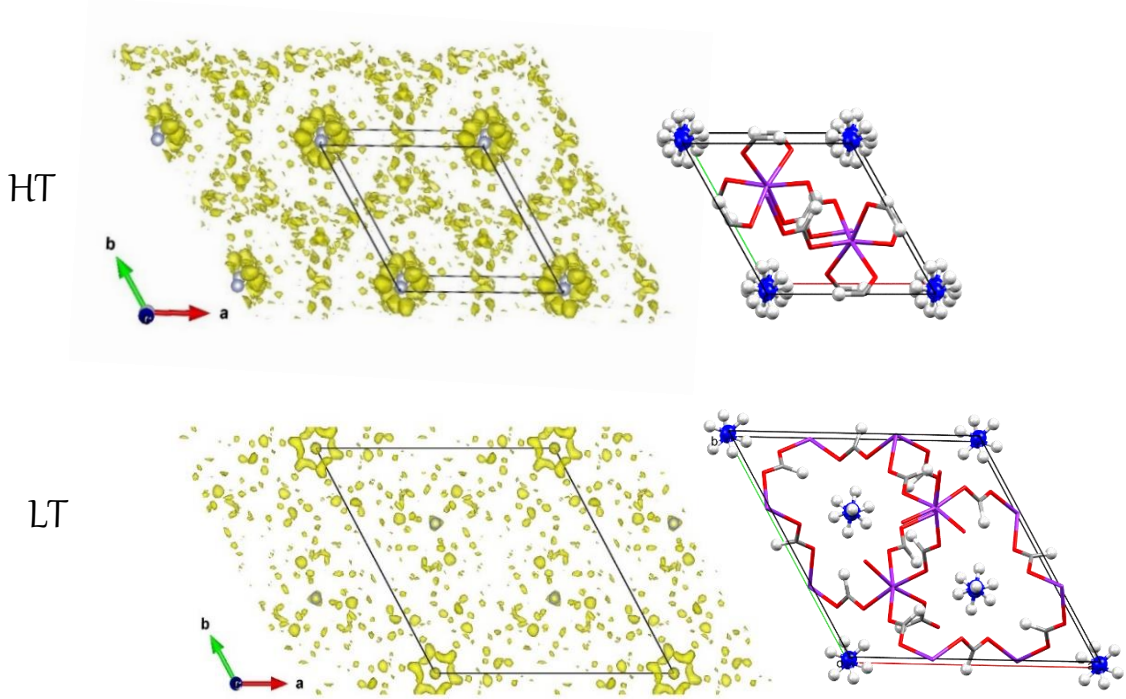

Figure 9: (Top) difference Fourier density map of the compound **12** by using single crystal neutron diffraction data recorded at high temperature. (Bottom) difference Fourier density map of the compound **12** by using single crystal neutron diffraction data recorded at low temperature. In both cases the calculated structure factors was performed without H-atoms.

However, according to our data refinements, this effect was not detected. As the sample was glued directly to the aluminium pin, the strength between the glue and the crystal can be strong enough to produce an unbalance between the different iso-energetic domains. The refinement using different twin-domains gave values close to zero for all domain except for the main one, confirming the absence of twinning problems in the sample. Using difference Fourier map, it was possible to detect the negative density related to the hydrogens and to localize them one by one (see Figure 9). Afterwards, hydrogens were refined anysotropically. The density surrounding the nitrogen atoms is the most distinguishable reason why the related hydrogens were easily located despite the disorder of the cation at high temperature.

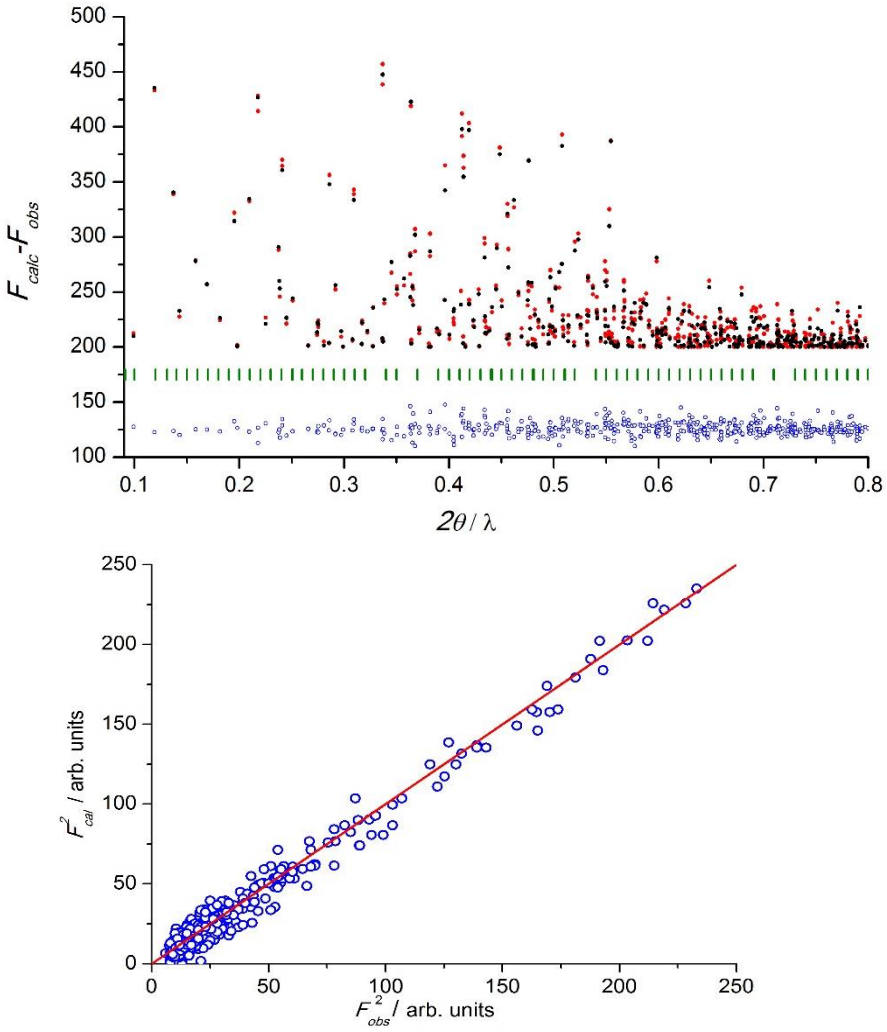

Figure 10: Experimental (open red circles) single crystal neutron diffraction data and calculated Rietveld refinement (black circles) integrated intensities as a function of sin θ/λ for **12**. The difference between observed and calculated intensities are represented as blue circles. The vertical green marks are the positions of the Bragg peak positions. Data of compound **12** were collected at 290 K using the D9 instrument with λ = 0.83220 Å. (Below) Plot of the observed vs calculated square structure factors. The experimental data are represented as open blue circles and the ideal case ($F_{cal}^2 = F_{obs}^2$) is represented as a solid red line. The refinement has been done in the space group $P6_322$ with the associated cell parameters $a = b = 7.2895(5)$ Å, $c = 8.3999(1)$ Å, $\alpha = \beta = 90°$ and $\gamma = 120°$. The multi-pattern data refinement gives the following agreement factors $\chi^2 = 1.18$ and $R_B = 9.27$ %

The cavity volume accessible to the counterion, (calculated by PLATON[30]) is 55.5 Å^3 (14.3%) of the unit cell volume (386.5 Å^3) at high temperature, but at low temperature is 245.8 Å^3 (20.9%) of the unit cell volume (1175.8 Å^3). These values differs from those determined by Xu *et al.*[2], for whom the framework of **12**, at LT, exhibited a contraction. However, an ammonium molecule has a volume[31] of 24.4 Å^3. According to our calculations, the remaining available volume in the channel is 14.5 Å^3 (3.7 % of the total one) at HT while at LT no residual volume is available into the void. The cell parameters values changes from $a = b = 7.2895(5)$ $c = 8.3999(1)$ to $a = b = 12.6125(5)$ $c = 8.5349(2)$ for

the HT and LT respectively. Data refinements at RT and at LT were performed by using Full Prof suite[25].

Data refinements at high temperature gives R_F = 9.27 % (HT), it is possible to appreciate the result of this crystal structure refinement in Figure 10. At low temperature, data refinements gives a value of R_F = 11.3% (HT), the crystal structure refinement is reported in Figure 11.

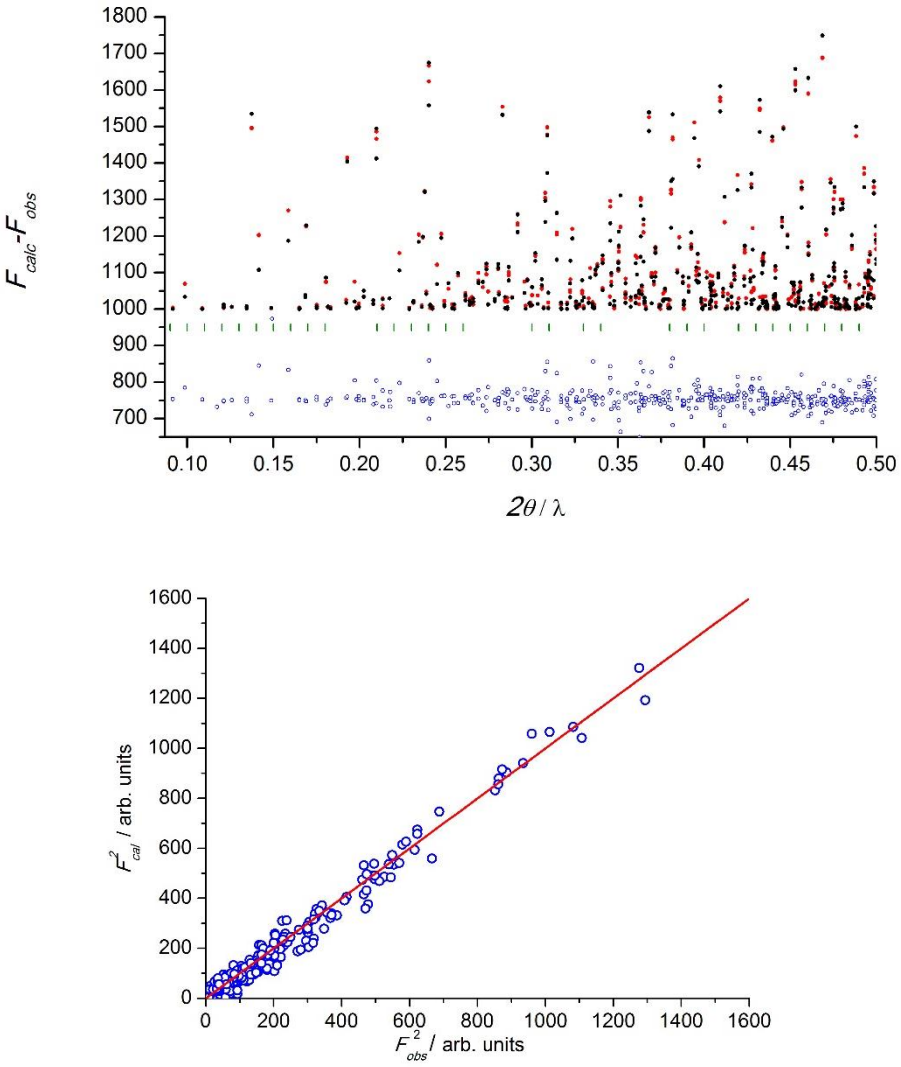

Figure 11: Experimental (open red circles) single crystal neutron diffraction data and calculated Rietveld refinement (black circles) integrated intensities as a function of sin θ/λ for **12**. The difference between observed and calculated intensities are represented as blue circles. The vertical green marks are the positions of the Bragg peak positions. Data of compound **12** were collected at 15 K using the D9 instrument with λ = 0.84160 Å. (Below) Plot of the observed vs calculated square structure factors. The experimental data are represented as open blue circles and the ideal case ($F_{cal}^2 = F_{obs}^2$) is represented as a solid red line. The refinement has been done in the space group $P6_322$ with the associated cell parameters $a = b = 12.6125(5)$ Å, $c = 8.5349(2)$ Å, $\alpha = \beta = 90°$ and $\gamma = 120°$. The multipattern data refinement gives the following agreement factors $\chi^2 = 6.50$ and $R_B = 11.3$ % .

In the table below, we report the crystallographic data for both temperatures.

Table 5: Experimental parameters and main crystallographic data for compound **12** obtained from the single crystal neutron diffraction.

Temperature (K)	**290**	**15**
Empirical Formula	$C_3H_7MnNO_6$	$C_3H_7MnNO_6$
M_r (g·mol^{-1})	208.04	208.04
λ(Å)	0.83220	0.84160
Crystal system	Hexagonal	Hexagonal
Space group (No.)	$P6_322$ (182)	$P6_3$ (173)
a (Å)	7.2895(5)	12.612(5)
b (Å)	7.2895(5)	12.612(5)
c (Å)	8.3999(1)	8.5349(2)
V (Å^3)	386.545	1175.795
Z	2	6
ρ_c (g·cm^{-3})	1.787	1.763
Meas. Reflections/ Unique	1180/ 706	1174/ 477
Parameters refined	34	55
χ^2	1.18	5.566
R_F	9.27	14.41

5.4 Magnetic properties

The magnetic structure of **12** were explored and determined using a single crystal sample, measuring on D9 single crystal diffractometer at ILL, at *ca.* 1.5 K, which is well below the ordering temperature. The first results about the magnetic properties of compound **12** were presented by *Wang et al.*[1] in form of magnetometry measurements. The magnetic susceptibility measurements shown a global antiferromagnetic behaviour. However, in the low temperature region, and increase of susceptibility is observed, suggesting the occurrence of a weak spin canting or the non-compensation of the magnetic networks. The zero field (ZFC) and the field cooling (FC) measurements confirm the occurrence of a weak ferromagnetic order at *ca.* 8 K. However, the isothermal magnetic measurements collected at 2 K did not show any evident hysteresis (see Figure 12). The isomorphic compounds of the same series with Ni(II) and Co(II), exhibit a notable stronger

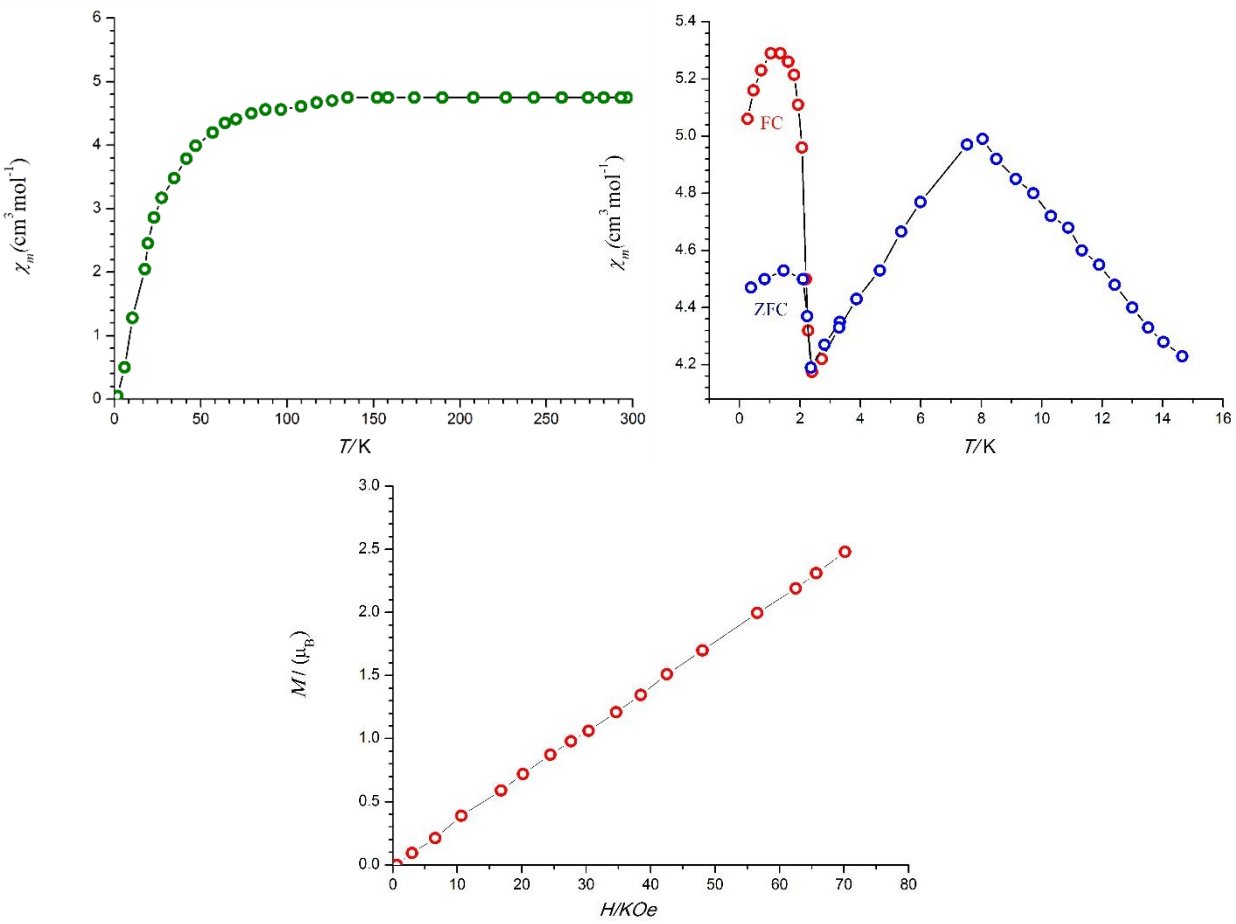

Figure 12: (Top), plots of χT as function of T for **12** in an applied field of 100 Oe. Right, ZFC/FC measurements under 5 Oe field, in the low temperature region, for **12. (**Bottom) the isothermal magnetization of **12**, with an inset showing the low-field region. Pictures published by *Wang et al.*[1]

ferromagnetic signal compared to that of compound **12**, probably due to a larger canting angle or a large difference between the non-compensation of the magnetic moments. Moreover, the magnetic ordering temperature observed in the macroscopic measurements are in agreement with those observed in the neutron diffraction data. The evolution of the (−1 2 0) and the (−1 1 0) reflections, between 16 and 2 K, shows an increase at *ca.* 8 K, (see Figure 13) which correspond with the long range order observed in the macroscopic measurements. The second transition observed at ca. 4 K, however, is not observed in the neutron diffraction data. Finally, it deserves to be noted that the T_N observed for **12**, is very close to those reported for different families of hybrid perovskite compounds containing manganese. For instance, when the ammonium cation is substituted by dimethylammonium[14,15], which suggest a low influence of the selected counterion.

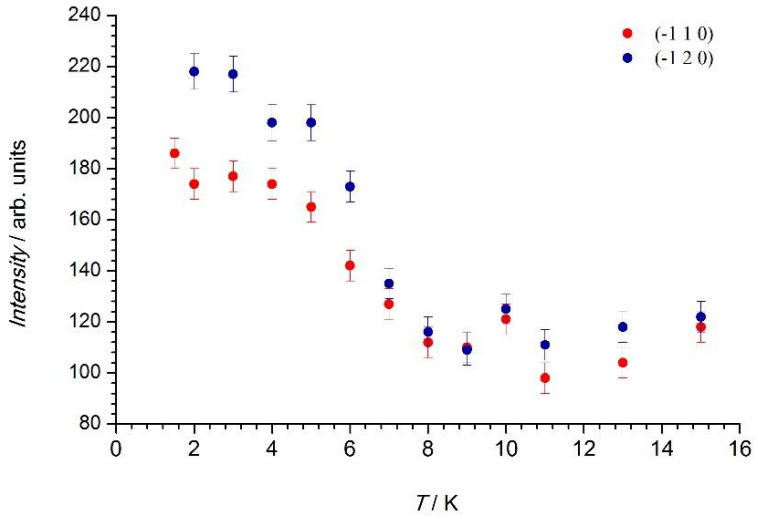

Figure 13: Temperature evolution of the (1 1 0) and the (-1 2 0) reflections collected on D9 single crystal diffractometer from 15 to 1.5 K.

The survey of the reciprocal space, together with the increase of intensity below of T_N of several nuclear reflections confirm the occurrence of a **k** = (0, 0, 0) propagation vector. In order to explore a full space of magnetic structures solutions, we have carried out a simulated annealing (SA) by using 65 magnetic reflections. The magnetic reflections where deduced by subtracting the nuclear intensities of the paramagnetic phase from the ordered one. This approach have been used in order to eliminate the influence of the nuclear model in the magnetic structure determination, moreover this approach give us a better accuracy in the estimation of the magnetic signal. The magnetic data were reduced in *P*1 symmetry to avoid errors due to the merging before the nuclear subtraction. The SA was initially done without symmetry constrains, therefore the six metal sites that fill the unit cell were included in the model with only the identity as symmetry operation. The magnetic moments of the metal sites were varied and they converged (R_F = 21.7%), giving rise to a magnetic structure with the magnetic moments coupled two by two, see Figure 14. This rather symmetric solution, suggest that the magnetic space group has a higher symmetry than *P*1. Therefore, in order to determine the correct magnetic space group we have used the group representation analysis. The magnetic representation Γ_M for the magnetic site [Wyckoff position 6*c*] can be decomposed as a direct sum of *irreps* applying the great orthogonality theorem.

$$\Gamma_M(2c) = 3\,\Gamma_1 \oplus 3\Gamma_2 \oplus 3\Gamma_3\Gamma_5 \oplus 3\Gamma_4\Gamma_6$$

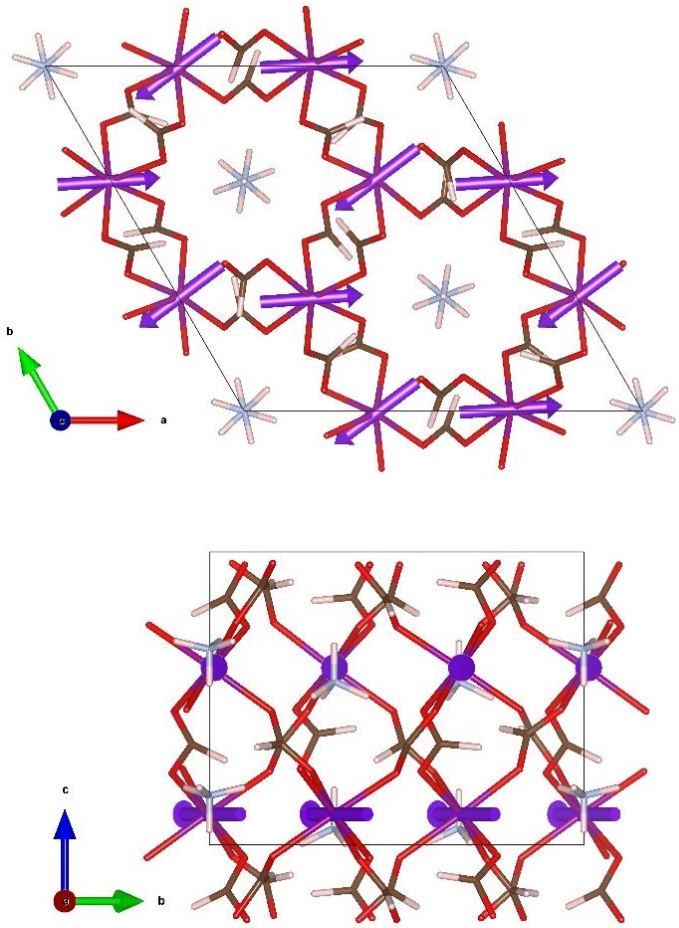

Figure 14: (Top), view in the *ab*-plane of the magnetic structure obtained by simulating annealing. (Bottom), view along the *b*-axis of the magnetic moments.

The complete list of the irreducible representation are shown in Table 6. The magnetic representations (in Table 6) are all possible solutions, but with the propagation vector **k** = (0, 0, 0), all the Fourier coefficients must be real. The *k*-subgroup program available in the Bilbao crystallographic server[7–9] (BCS) was used to obtain the group-subgroup hierarchy for all possible magnetic symmetries of the paramagnetic structure with space group $P6_3$, propagation vector **k** = (0, 0, 0) and magnetic sites occupying the 6*c* Wyckoff position. The magnetic structure of compound **12**, was analysed using the four physically irreducible representations (Γ_1; Γ_2; $\Gamma_3\Gamma_5$; $\Gamma_4\Gamma_6$) and a combination of them. Among them, the maximal magnetic subgroups, $P6'_3$ and $P6_3$, are one-dimensional, while the last two physical irreducible representation are combination of bi-dimensional irreducible representations. In order to obtain the lowest symmetry magnetic space groups, which are subgroups of the parent grey group, a combination two or more physically irreducible representation is needed.

Table 6: Irreducible Representations of the parent space group *P*-31*c* for **k** = (0, 0, 0). The symmetry elements are written according to Seitz's notation.

	(1|000)	(3^{+}_{00z}|000)	(3^{-}_{00z} |000)	(2_{00z}|$00\frac{1}{2}$)	(6^{-}_{00z}|$00\frac{1}{2}$)	(6^{+}_{000}|$00\frac{1}{2}$)
Γ_1	1	1	1	1	1	1
Γ_2	1	1	1	-1	-1	-1
$\Gamma_3\Gamma_5$	$\begin{pmatrix}1 & 0\\0 & 1\end{pmatrix}$	$\begin{pmatrix}-a & b\\-b & -a\end{pmatrix}$	$\begin{pmatrix}-a & -b\\b & -a\end{pmatrix}$	$\begin{pmatrix}1 & 0\\0 & 1\end{pmatrix}$	$\begin{pmatrix}-a & b\\-b & -a\end{pmatrix}$	$\begin{pmatrix}-a & -b\\b & -a\end{pmatrix}$
$\Gamma_4\Gamma_6$	$\begin{pmatrix}1 & 0\\0 & 1\end{pmatrix}$	$\begin{pmatrix}-a & b\\-b & -a\end{pmatrix}$	$\begin{pmatrix}-a & -b\\b & -a\end{pmatrix}$	$\begin{pmatrix}-1 & 0\\0 & -1\end{pmatrix}$	$\begin{pmatrix}a & -b\\b & a\end{pmatrix}$	$\begin{pmatrix}a & b\\-b & a\end{pmatrix}$

a = 1/2 and $b = \sqrt{3}/2$.

All the magnetic groups proposed (see Figure 15) were tested to fit the difference pattern. The fit carried out using the $P6_3$, $P3$ and $P2_1'$, magnetic space groups are discarded based on the large ferromagnetic signal obtained after the refinement, which is not compatible with the almost antiferromagnetic ground state of the compound **12**. Therefore neither of these models are compatible with magnetometry measurements. Moreover the $P6_3'$ magnetic space group, give rise to a strictly antiferromagnetic structure and therefore the weak ferromagnetic signal observed in the macroscopic measurements cannot be explained.

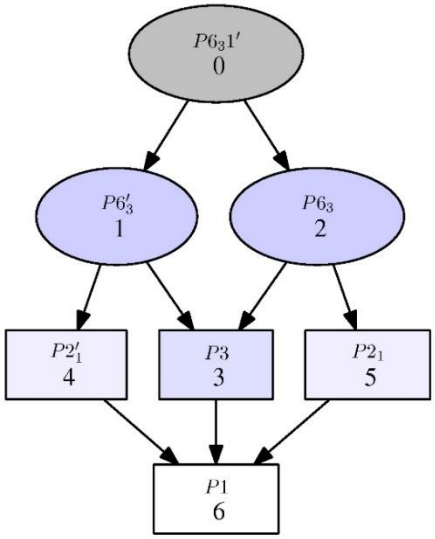

Figure 15: Magnetic subgroups which allow non-zero magnetic moment, calculated from the parent grey group $P6_3$ with the 6c Wyckoff position of the Mn^{II}.

Therefore, only the $P2_1$ magnetic group is compatible with both, experimental neutron data and macroscopic measurements. Although the magnetic space group allows the occurrence of a net ferromagnetic signal along the *c*-axis, the refined component along this direction is zero within the experimental error. Therefore, it have been fix to zero in

the final refinements. The spin arrangements derived from the data refinement, can be described as ferromagnetic layers extended in the *ab*-plane and coupled antiferromagnetically along the *c*-axis. Due to the breaking of symmetry from the parent ($P6_3$) space group to the monoclinic ($P2_1$), the manganese site which occupy a 6*c* Wyckoff position is splitting in three different orbits all of them in a 2*a* Wyckoff position. The magnetic moments of each orbit can be refined independently, however in order to avoid overparametrization the modulus of the magnetic moment for all sites where constrained to be equal. Due to symmetry contractions, even if the modulus of the magnetic moments for each site are not equal, the magnetic model do not allows the occurrence of ferromagnetic signal within the *ab*-plane. This can be derived from the irreducible representations (see table below), the $P2_1$ Shubnikov group is obtained from the combination of the Γ_1 and $\Gamma_3\Gamma_5$, the presence of $\Gamma_3\Gamma_5$ allows the occurrence of a ferromagnetic component. The magnetic moments of the metal sublattices determined by the data refinement, from the difference patterns between the paramagnetic and the magnetically ordered phase, are listed in the Table 7**.**

Table 7: Magnetic moment components in Mb, obtained for the single crystal neutron diffraction data refinement for each atom site using the $P2_1$ Shubnikov group.

	M_a	M_b	M_c	M_{total}
Mn(1-3) (6*c*)	4.342(1)	2.2(3)	0	4.34(9)

The macroscopic magnetic measurements[1,2] of **12** showed the occurrence of an almost strict antiferromagnetic coupling between adjacent metal ions with a very weak spin canting below 4 K. The proposed model, can explain the global antiferromagnetic behaviour of this compound, moreover the occurrence of a weak canting is also allowed by symmetry. However, the value of the canting component is well below to our detection limit and therefore it cannot be determined (see Figure 16). The refined value of the magnetic moments, constrained to be on the *ab*-plane are *ca*. 4.34(9) μ_B, value which is in agreement with other coordination polymers based on Mn^{II} metal ions (s = 5/2). The magnetic moment values obtained for Mn2 and Mn3 are the same than Mn1, in order to obtain the same arrangement, they were constrained to assume the same orientation. Finally I would like to compare this result from the one obtained initially using the simulating annealing protocol. Comparing both models the magnetic interaction between adjacent metallic centres seems to have the same behaviour and therefore both models are

almost equivalent (Figure 14 and Figure 16). However, some slight change in the orientation of the magnetic moments are observed, mainly due to the simulated annealing was carried out without symmetry constrains, and therefore the number of free parameters is larger. This is also the explanation for the small canting observed in the simulated annealing refinement, which cannot be confirmed through the refinement carried out in the $P2_1$ magnetic space group. It deserves to be noted that the proposed magnetic space group is also compatible with the ferroelectricity observed in this compound and therefore although weakly it is connected with the magnetic structure. Further studies to understand the influence of the magnetic field in both, ferroelectricity and in the magnetic structure are needed to completely understand the correlation between both properties.

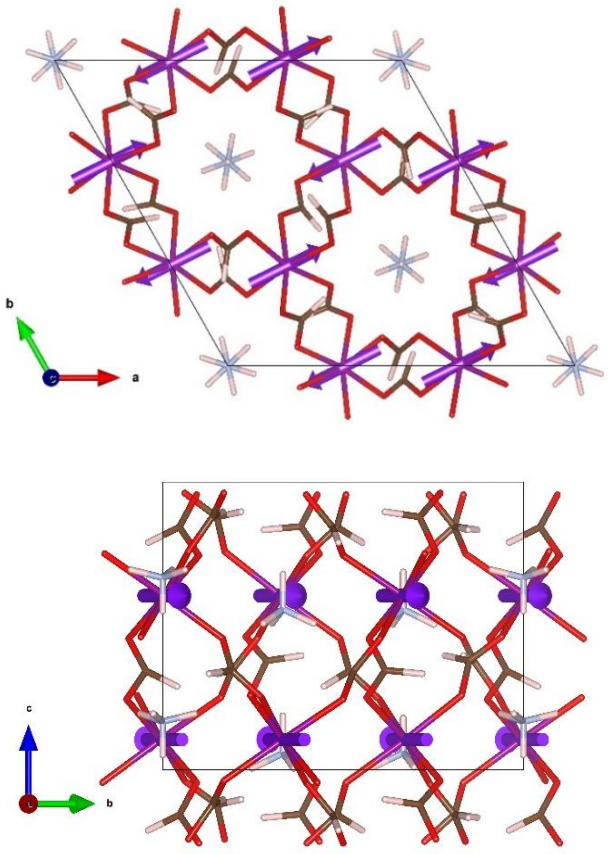

Figure 16: (Top), view in the *ab*-plane of the magnetic structure obtained by single crystal refinement, using the $P2_1$ magnetic space group. (Bottom), view along the *b*-axis of the magnetic structure. The code of colours used for the nuclear structure is the same that in the previous figures.

Conclusion and discussion

In this work we have investigated the crystal and magnetic structure of $[NH_4][Mn(HCOO)_3]$ compound, through single crystal neutron diffraction technique. In the first part of this chapter, we have confirmed the occurrence of a nuclear phase transition, we have localized the hydrogen atoms of the NH_4^+ counter ions above and below phase transition, and we have corroborate that the origin of this phase transition is due to an order-disorder effect of the counterions. The occurrence of a ferroelectric order below the phase transition temperature, suggests that the reorganization of the H-bond network is the responsible of this effect. We have carefully determined the H-bond interaction and proposed the distortion of the counterions as triggering of this ferroelectricity.

In the second part of this chapter, we have determine the hierarchy for all possible magnetic symmetries compatibles with the paramagnetic space group $P6_3$, propagation vector **k** = (0, 0, 0) and Wyckoff position of the metal centres. All possible magnetic space group have been used to fit the experimental data, however the only which is compatible with the magnetometry, polarimetry and with the neutron diffraction data is the $P2_1$ space group. The refined magnetic structure consist on ferromagnetic layers extended in the *ab*-plane coupled antiferromagnetically with the adjacent ones along the *c*-axis. This model is compatible with one of the possible solution proposed by *Lawler et al*.[21] which was obtained using partially deuterated samples and neutron powder diffraction data. It should be noted that, *Lawler et al*.[21] are not able to distinguish between the $P2_1$ and $P2'_1$ magnetic space groups. However the large number of observations obtained from the single crystal data help us to discard the $P2'_1$ magnetic space groups, and therefore the $P2_1$ space group remains the only solution.

We tried to shed light to the weak ferromagnetic signal observed below 4 K, however the temperature evolution of the magnetic reflection don't show any change in the intensity that could be attributed to this transition. Based on the symmetry analysis we can propose a model based in a weak spin canting along the *c*-axis with is the only possible direction where a ferromagnetic component is allowed. However based on our refinements this cannot be confirmed. In order to better understand the nature of the magneto-electric coupling for this compound, a further work may be to measure experimentally the possible magnetic exchange couplings interactions and ultimately its multiferroic behavior. Furthermore, determining the influence in the atomic positions when a magnetic

field is applied, possibly by using a single crystal sample deuterated, would be helpful for clarifying the origin of the magnetic mechanism of this compound.

Bibliography

(1) Wang, Z.; Zhang, B.; Inoue, K.; Fujiwara, H.; Otsuka, T.; Kobayashi, H.; Kurmoo, M. *Inorg. Chem.* **2007**, *46* (2), 437.
(2) Xu, G.-C.; Zhang, W.; Ma, X.-M.; Chen, Y.-H.; Zhang, L.; Cai, H.-L.; Wang, Z.-M.; Xiong, R.-G.; Gao, S. *J. Am. Chem. Soc.* **2011**, *133* (38), 14948.
(3) Xu, G.-C.; Ma, X.-M.; Zhang, L.; Wang, Z.-M.; Gao, S. *J. Am. Chem. Soc.* **2010**, *132* (28), 9588.
(4) Lawler, J. M. M.; Manuel, P.; Thompson, A. L.; Saines, P. J. *Dalton Trans. Camb. Engl. 2003* **2015**, *44* (25), 11613.
(5) W. Eerenstein; N. D. Mathur; J. F. Scott. *Nature* **2006**, *442* (7104), 759.
(6) Scott, J. F. *Nat. Mater.* **2007**, *6* (4), 256.
(7) Miller, J. S. *Elsevier* **2014**, *17* (5), 224.
(8) Coronado, E.; Espallargas, G. M. *Chem. Soc. Rev.* **2013**, *42* (4), 1525.
(9) Wang, W.; Yan, L.-Q.; Cong, J.-Z.; Zhao, Y.-L.; Wang, F.; Shen, S.-P.; Zou, T.; Zhang, D.; Wang, S.-G.; Han, X.-F.; Sun, Y. *Sci. Rep.* **2013**, *3*, 2024.
(10) Schmid, H. *Ferroelectrics* **1994**, *162* (1), 317.
(11) Stroppa, A.; Jain, P.; Barone, P.; Marsman, M.; Perez-Mato, J. M.; Cheetham, A. K.; Kroto, H. W.; Picozzi, S. *Angew. Chem.* **2011**, *123* (26), 5969.
(12) Jain, P.; Ramachandran, V.; Clark, R. J.; Zhou, H. D.; Toby, B. H.; Dalal, N. S.; Kroto, H. W.; Cheetham, A. K. *J. Am. Chem. Soc.* **2009**, *131* (38), 13625.
(13) Liu, B.; Shang, R.; Hu, K.-L.; Wang, Z.-M.; Gao, S. *Inorg. Chem.* **2012**, *51* (24), 13363.
(14) Wang, Z.; Hu, K.; Gao, S.; Kobayashi, H. *Adv. Mater.* **2010**, *22* (13), 1526.
(15) Wang, Z.; Zhang, B.; Otsuka, T.; Inoue, K.; Kobayashi, H.; Kurmoo, M. *Dalton Trans.* **2004**, *0* (15), 2209.
(16) Duan, Z.; Wang, Z.; Gao, S. *Dalton Trans.* **2011**, *40* (17), 4465.
(17) Zhao, T.-M.; Chen, S.; Shang, R.; Wang, B.-W.; Wang, Z.-M.; Gao, S. *Inorg. Chem.* **2016**, *55* (20), 10075.
(18) Weng, D.-F.; Wang, Z.-M.; Gao, S. *Chem. Soc. Rev.* **2011**, *40* (6), 3157.
(19) Mączka, M.; Ciupa, A.; Gągor, A.; Sieradzki, A.; Pikul, A.; Macalik, B.; Drozd, M. *Inorg. Chem.* **2014**, *53* (10), 5260.
(20) Mączka, M.; Gągor, A.; Macalik, B.; Pikul, A.; Ptak, M.; Hanuza, J. *Inorg. Chem.* **2014**, *53* (1), 457.
(21) Lawler, J. M. M.; Manuel, P.; Thompson, A. L.; Saines, P. J. *Dalton Trans.* **2015**, *44* (25), 11613.
(22) Volkova, L. M.; Marinin, D. V. *J. Supercond. Nov. Magn.* **2016**, *29* (11), 2931.
(23) Lehmann, M. S.; Larsen, F. K. *Acta Crystallogr. A* **1974**, *30* (4), 580.
(24) P. Coppens,. *Crystallographic Computing*; F. R.Ahmed (MunksgaardInternational Booksellers and PublishersLtd.: Copenhagen, 1979.
(25) Rodríguez-Carvajal, J. *Phys. B Condens. Matter* **1993**, *192* (1), 55.
(26) Mączka, M.; Szymborska-Małek, K.; Ciupa, A.; Hanuza, J. *Vib. Spectrosc.* **2015**, *77*, 17.
(27) Mączka, M.; Szymborska-Małek, K.; Ciupa, A.; Hanuza, J. *Vib. Spectrosc.* **2015**, *77*, 17.
(28) Batten, S. R.; Robson, R. *Angew. Chem. Int. Ed.* **1998**, *37* (11), 1460.
(29) A.F. Wells. In *Three-Dimensional Nets and Polyhedra*; Wiley: New York, 1977.
(30) Spek, A. L. *J. Appl. Crystallogr.* **2003**, *36* (1), 7.
(31) Calculation of molecular properties and bioactivity score http://www.molinspiration.com/cgi-bin/properties (accessed Sep 9, 2017).

Summary and General Conclusion

The work presented in this thesis deals with the synthesis of metal-organic frameworks, specifically metal formate frameworks, and the characterization of their structural and magneto-electric properties using essentially Neutron and X-Ray diffraction techniques. The investigation of magneto-structural correlations of the metal-organic networks has become the goal of an intense research since their hybrid characteristics; open countless possibilities for the creation of new smart materials. One of the features of MOFs is their versatility but also their diverse topologically crystal structures, many of which are derived from minerals in nature. For this thesis, we focused our investigation on the *niccolite-like structures* with general formula $[A][Fe^{III}M^{II}X_6]$, (mixed-valence compounds where A is a protonated amine M is a divalent metal ion connected to the trivalent iron through X which is the formate linker), that are described in **chapter 3**. And we dedicated the second part of our research to the *perovskite-like structures* with general formula $[A][BX_3]$, (homometallic compounds where A is a protonated amine, M is a divalent metal ion and X the formate linker), which are described in **chapter 4** and **5.**

The studied MOFs were synthesized from a suitable metal salt, formic acid and an amine under solvo-thermal conditions or by slow evaporation or diffusion techniques. The presence and the chemical nature of the protonated amine played a crucial role compensating the charge, but also influencing for example the structure of the network, in terms of size and shape. In addition, the most evident effect is related to the hydrogen-bonding interactions often contributing to the order-disorder phase transitions, which may induce electrical polarization. Specific properties and functions of these target materials were explored by substituting the metal centres and/or the organic counterion. A common formate 3D structure is displayed, in the niccolite and perovskite-like structures of MOFs, with a dense metal network where the formate groups act as bis-monodentate, in an *anti-anti* coordination mode. The magnetic arrangement of these two families of compounds is in general, an antiferromagnetic ordering with weak ferromagnetism. Magnetic properties becomes more varied in the mixed valence system, since the combination of two or more magnetic centres in the same structure can lead to long range magnetic order with ferrimagnetic behaviour or with canted antiferromagnetism, depending on the involved spins.

Based on the general description above, the detailed structural and magnetic properties of these materials have been compared between them and their differences have been discussed in this thesis titled ***«Preparation, structure determination, and physical properties of formate-based molecular compounds»***, (*French translation: «Préparation, détermination de la structure et des propriétés physiques de composés moléculaires basées sur le formiate»).* The main results obtained during the investigation of the last three years' work have been arranged as following:

Chapter 1 concerns the general concepts related to the main topics investigated in this thesis project. A brief review is dedicated to the molecular-based magnetic materials giving particular attention to the subject of metal-organic frameworks and magnetoelectric multiferroics. The exploration of the magnetic properties required to go through the basics of ferromagnetism and ferroelectricity.

Chapter 2 gives a general overview about the different techniques used to synthesize and to characterize the chemical and physical properties, as well as the main characteristics of the instruments used for our experiments in different facilities.

Chapter 3 is focused on the niccolite-like structure of mixed valence metal-formate, $[(CH_3)_2NH_2][Fe^{III}M^{II}(HCOO)_6]$ with M^{II} = Co^{II} (**2**), Mn^{II} (**3**), Ni^{II} (**4**) and Mg^{II} (**5**). The ordering of $Fe^{III}M^{II}$ in the crystal lattice was established by single crystal/powder X-ray diffraction in combination with high resolution neutron diffraction and its influence on the physical properties discussed. The refined structural models have been used as starting point for the refinement of the magnetic structures. The nature of the magnetic ordering has been established by magnetization measurements and by the magnetic structure determination using neutron powder diffraction experiments. This work has been the continuation of a previous investigation on the compound $[(CH_3)_2NH_2][Fe^{III}Fe^{II}(HCOO)_6]$ **1** characterized by a paraelectric to antiferroelectric phase transition[1], characterized by a change of the space group from $P\bar{3}1c$ (Room Temperature) to $R\bar{3}c$. The magnetic order transition (*ca.* 37 K) for **1** evidenced the non-compensation of the interacting local spins giving rise to a weak non-collinear ferrimagnetic structure along the *c-axis*, where the Fe^{II} and Fe^{III} sites are antiferromagnetically coupled. When Fe^{II} is replaced with either Co^{II} (**2**), Mn^{II} (**3**), Ni^{II} (**4**) or Mg^{II} (**5**), no structural phase transition is observed, all compounds retain the $P\bar{3}1c$ space group. Consequently, no change in their electrical properties is detected. Moreover,

the magnetic properties of **2**, **3** and **4** show a general antiferromagnetic behaviour. The *C*2'/*c'* magnetic space group gives rise to a magnetic structure where the magnetic moments of both sites are mainly antiferromagnetically coupled in the *ab*-plane, with a small component along the *c*-axis. For compound **2**, the refined model shows a ferrimagnetic behaviour, mainly in the *ab*-plane, due to the non-compensation of the magnetic moments of each lattice. For compound **3** the refinement shows an antiferromagnetic arrangement with a small spin canting along the *c*-axis, which should be the responsible of the weak ferromagnetic signal observed in the magnetometry measurements. The negative magnetization observed in the compound **1** suggests a magnetic interaction between Fe^{II} and Fe^{III} networks that is not observed in the Co^{II}- or Mn^{II}-based compounds. Moreover the magnetic moments orientation, for the Fe^{II}-based compound is mainly along the *c-axis* while for the Co^{II}- or Mn^{II}-based compounds they are in the *ab*-plane, mainly perpendicular to the direction of the moments obtained for compound **1**. A different magnetic structure is produced when the network is synthesized with the Ni^{II} ion at the divalent metal centre: the non-compensation of the magnetic moments produces a net ferromagnetic component. From the refinement of the neutron data, we have obtained a magnetic structure belonging to the magnetic space group $P\bar{3}1c$', which gives rise to an ordering with the magnetic moments located strictly along the *c*-axis. This conformation is almost the same as that obtained from the data refinement of the compound **1**. Compound **5** (Mg^{II}-based compound), shows a certain disorder in the position of the divalent metal ion, where Fe^{II} is interchanged with Mg^{II}, resulting in a mixed occupation disorder. This evidence leads to think that in some zones of the crystal different coupling interactions between the magnetic divalent metal (Mg^{II}/Fe^{II}) and Fe^{III} may occur. Moreover, the negative magnetization observed for **5** together with the partial substitution of Mg^{II} by Fe^{II} suggested a similar magnetic behaviour to **1**, but diluted. In reality, the contribution of the small $Fe^{III}Fe^{II}$ regions within the $Fe^{III}Mg^{II}$ framework is too small to be detected by neutron diffraction techniques, even after a long acquisition, probably because of the disordered distribution of the metal ions, which preclude a real long-range magnetic order.

Finally, we investigated the influence of the counterion in the chemical and physical properties of $[(CH_3CH_2NH_3)][Fe^{III}Fe^{II}(HCOO)_6]$ (**6**), where the methylammonium counterion used from compound **1** to **5**, is replaced by the larger ethylammonium molecule. The magnetic behaviour is characterized by an antiferromagnetic coupling

along the *c*-axis. The non-compensation of the magnetic moments give rise to a small ferromagnetic component along the *c*-axis.

Chapter 4 consists of a detailed description of the results obtained for the crystal and magnetic structures of $[CH_3NH_3][M^{II}(COOH)_3]$ with M^{II} = Co^{II} (**7**), Fe^{II} (**8**), Ni^{II} (**9**), Mn^{II} (**10**), and Cu^{II} (**11**) with a perovskite-like topology. The investigation was carried by using powder and single crystal diffraction (neutron and X-ray) as function of the temperature. The common point among those compounds is that at room temperature all of them crystallize in the *Pnma* orthorhombic space group. The methylammonium counter-ions are found slightly disordered in the cavities of the framework, which in part can be at the origin of the structural phase transitions of these compounds, except for the cooper-based compound (**11**).

In the specific case of $[CH_3NH_3][Co(COOH)_3]$ (**7**), three nuclear phase transitions have been observed between 135 K and 75 K, from the orthorhombic *Pnma* space group at room temperature to an incommensurate structure where first order and second order harmonic reflections are observed. The observed satellites between the main reflections are compatible with an incommensurate structure with a modulation vector, which is approximately $\mathbf{q} \approx (0, 0, 1/7)$.

At *ca.* 80 K a notable increase of intensity of the first harmonic satellites is manifest. This results in the occurrence of a different modulation vector $\mathbf{q} \approx (0, 0, 1/8)$. Below this temperature, the commensurate reflections as well as the second and above order harmonics lose intensity, while the first order satellites increase. Below *ca.* 75 K, the observed reflections match with the $P2_1/n$ monoclinic space group. Here, it is important to underline a difference when compound **7** is measured using a single crystal or in form of a crystalline powder. A unique commensurate monoclinic phase is observed for the single crystal, while for the powder the coexistence of two commensurate monoclinic and modulated orthorhombic phases is observed.

When the Co^{II} (**7**) metal centre is replaced by Fe^{II} (**8**), Ni^{II} (**9**), Mn^{II} (**10**), and Cu^{II} (**11**), very interesting effects are observed. For example, the compounds **8** to **10** show a unique transition from orthorhombic commensurate to orthorhombic incommensurate phase, keeping the modulated phase down to the lowest temperature. We confirmed this behaviour for compound **9** using single crystal neutron diffraction experiments, obtaining the same results as for the powder sample. For the copper-based compound (**11**) no structural transition from *Pnma* is observed when the temperature is decreased. However,

the compound is characterized by quite different lattice parameters due the Jahn-Teller effect of Cu^{II}. Decomposition occurred at *ca.* 160°C when the sample was heated, forming elemental copper. We suppose that this characteristic might offer an application of **11** to be used as an ink to produce electric circuits.

From the magnetic point of view **7**, **8**, **9**, and **10** present an overall antiferromagnetic coupling with a long-range magnetic order at about 15.7, 16.8, 33 and 8 K, respectively. For compound **7** this is due to the occurrence of a non-collinear antiferromagnetic structure where magnetic moments are not strictly compensated. The magnetic reflections measured by neutron diffraction techniques, at 2 K, are compatible with the orthorhombic magnetic space group *Pn'ma'* and with the monoclinic magnetic space group $P2'_1/n'$, the fit was done mixing two magnetic space groups due to the non-negligible mixture of phases observed in the low temperature powder sample. Compound **8** and **10** are purely antiferromagnetically coupled as predicted by magnetometry measurements, while compound **9** showed weak magnetic signal. Based only in the neutron diffraction data, the weak ferromagnetic component observed in magnetometry cannot be determined, in part due to the weak magnetic contribution and in part due to the large background coming from the hydrogen content. We solved and presented the magnetic structures of **9** and **10** using strictly antiferromagnetically coupling along the *c*-axis in the *Pn'ma'* for both cases. The low temperature neutron diffraction data on compound **8**, shows the occurrence of new reflections which cannot be fitted using the *Pn'ma'* magnetic space group, therefore a change in the magnetic symmetry is observed for the iron-based compound, which was successfully solved using the *Pnma* magnetic space group.

Chapter 5 is centred on the study of the compound with a chiral structure and the following formula $[NH_4][Mn^{II}(HCOO)_3]$ (**12**). This compound crystallize in the hexagonal space group $P6_322$ at room temperature and it shows at 254 K a paraelectric to ferroelectric phase transition associated to a structural phase transition from $P6_322$ to $P6_3$, generated by the order-disorder state of the NH_4^+ cation. In order to understand the trigonal disorder of the cation, the high sensitivity of neutron diffraction has been crucial for obtaining the refinement at the low temperature crystal structure, and to get an accurate model including the positions of the hydrogen atoms. Regarding the magnetic properties, the experimental data evidenced an antiferromagnetic ordering at 8 K combined with a small spin canting. The structural and magnetic phase transitions have been explored by determining the crystal and magnetic structures below T_N. For these

measurements we used single crystal neutron diffraction on the $[NH_4][Mn^{II}(HCOO)_3]$ sample. We confirmed that the magnetic structure consist of ferromagnetic layers extended in the *ab*-plane coupled antiferromagnetically with the adjacent ones along the *c*-axis. The Shubnikov group used for solving the magnetic structure is $P2_1$. Further works are needed in order to assess the super-exchange magnetic interactions occurring in this compound, as well as in all the members of this family. Experiments under applied magnetic field are necessary for completing this work.